Title

Hydride-Supported Actinide—Transition Metal Complexes

Author

Ye, Christopher

Publication Date

2024

Peer reviewed|Thesis/dissertation

Hydride-Supported Actinide–Transition Metal Complexes

By

Christopher Ziyu Ye

A dissertation filed in partial satisfaction of the

requirements for the degree of

Doctor of Philosophy

in

Chemistry

in the

Graduate Division

of the

University of California, Berkeley

Committee in charge:

Professor John Arnold, Chair

Professor Polly L. Arnold

Professor Rebecca J. Abergel

Spring 2024

Hydride-Supported Actinide–Transition Metal Complexes

by

Christopher Ziyu Ye

Chapter 2 was adapted from Ye, C. Z.; Del Rosal, I.; Boreen, M. A.; Ouellette, E. T.; Russo, D. R.; Maron, L.; Arnold, J.; Camp, C. A versatile strategy for the formation of hydride-bridged actinide–iridium multimetallics. *Chem Sci*. **2023**, *14*, 861-868 with permission from The Royal Society of Chemistry.

Chapter 3 was adapted from a submitted manuscript: Ye, C. Z.; Del Rosal, I.; Kelly, S. N.; Brackbill, I. J.; Maron, L.; Camp, C. A; Arnold, J. Photolysis-Driven Bond Activation by Thorium and Uranium Tetraosmate Polyhydride Complexes.

Chapter 4 was adapted from a manuscript in preparation: Ye, C. Z.; Del Rosal, I.; Kelly, S. N.; Ouellette, E. T.; Hohloch, S; Maron, L.; Camp, C. A; Arnold, J. Synthesis, Structure, and Bonding of Actinide–Rhenium Polyhydrides.

Chapter 5 was adapted from a manuscript in preparation: Ye, C. Z.; Del Rosal, I.; Ouellette, E. T.; Maron, L.; Camp, C. A; Arnold, J. Reduction of CS_2 to an Ethanetetrathiolate by a Hydride-Bridged Uranium–Iridium Heterobimetallic

Abstract

Hydride-Supported Actinide–Transition Metal Complexes

by

Christopher Ziyu Ye

Doctor of Philosophy in Chemistry

University of California, Berkeley

Professor John Arnold, Chair

Chapter 1. The field of f-block–transition metal hydride chemistry is introduced and summarized. Key properties of these compounds such as small molecule activation chemistry and H_2 uptake and release are outlined. The dearth of actinide–transition metal species despite their potential for fundamental bonding insight and novel reactivity is highlighted, and the motivations for studying these compounds are stated.

Chapter 2. Reaction of K[Cp*IrH$_3$] with actinide halides led to multimetallic actinide–transition metal hydrides U{(μ-H)$_3$IrCp*}$_4$ and Th{[(μ-H)$_2$(H)IrCp*]$_2$[(μ-H)$_3$IrCp*]$_2$}, respectively. These complexes feature an unexpected, significant discrepancy in hydride bonding modes; the uranium species contains twelve bridging hydrides while the thorium complex contains ten bridging hydrides and two terminal, Ir-bound hydrides. Use of a U(III) starting material with the same potassium iridate resulted in the octanuclear complex {U[(μ_2-H)$_3$IrCp*]$_2$[(μ_3-H)$_2$IrCp*]}$_2$. Computational studies indicate significant bonding character between U/Th and Ir in the tetrairidate compounds, the first reported evidence of actinide-iridium covalency. In addition, these studies attribute the variation in hydride bonding between the tetrairidate complexes to differences in dispersion effects. This work establishes a novel route to synthesizing actinide–transition metal polyhydrides with close metal–metal contacts.

Chapter 3. Conversion of Cp*OsH$_5$ to K[Cp*OsH$_4$] with KBn, followed by reaction with tetravalent actinide halides results in the synthesis of uranium– and thorium–osmium heterometallic polyhydride complexes. Through these species, An–Os bonding and the reactivity of An–Os interactions are studied. These complexes are formally sixteen-coordinate, the highest observed coordination number for uranium and thorium. Computational studies suggest the presence of a significant bonding interaction between the actinide center and the four coordinated osmium centers, the first report of this behavior between osmium and an actinide. Upon photolysis, these complexes underwent intramolecular C–H activation with the formation of an Os–Os bond, while the thorium complex was able to activate an additional C–H bond of the benzene solvent, resulting in a μ-η^1,η^1 phenyl ligand across one Th–Os interaction. These results highlight the

unique reactivity that can arise from actinide and transition metal centers in proximity, and expand the scope of actinide photolysis reactivity.

Chapter 4. The third Cp*-supported transition metal polyhydride – Cp^*ReH_6 – was shown to be a competent partner to actinide hydrides. The synthesis of actinide tetrarhenate complexes completed a series of iridate, osmate, and rhenate polyhydrides, allowing for structural and bonding comparisons. Computational studies examine the bonding interactions, particularly between metals, in these complexes. Several factors affect metal–metal distances and covalency for the actinide tetrametallates, including metal oxidation state, coordination number, and dispersion effects. The osmium and rhenium octametallic U_2M_6 clusters are reported as well, with similar analysis of structure and electronics.

Chapter 5. Reaction of the potassium iridate $K[Cp^*IrH_3]$ with a bulky uranium(III) metallocene yielded a heterobimetallic U(III)–Ir species. Reactivity of this complex with CS_2 is described, resulting in the novel ethanetetrathiolate fragment, as produced *via* hydride insertion and C–C coupling. This demonstrates the ability to combine the hydride insertion chemistry of transition metal hydrides with C–C coupling observed in U(III) compounds by bringing both metal centers in close proximity.

Hydride-Supported Actinide–Transition Metal Complexes

Table of Contents

Acknowledgements

It's not every day that you get the chance to thank the people who have made a difference in your life, and barring any surprise Academy Award wins in my future, this may be one of the best opportunities I will get. So, without further ado, my ~~Oscar~~ Ph.D. speech.

First, I would like to thank my Ph.D. advisor, John Arnold. I likely would not have come to Berkeley if it were not for John and the group, and I am thankful that all of the wonderful things I heard about him while visiting proved to be true through the years of my Ph.D. The environment of collaboration and support fostered in the group started with John and was a major reason that I have reached this point. Balancing a healthy set of hobbies and life outside of chemistry with the drive for results in academia is no mean feat, but John managed it well and gave us the freedom to do so as well. John, I wish you the best as you sail off into retirement, both literally and figuratively.

To Clément, my second advisor from afar, thank you for your ideas and support throughout this process, not to mention the two months I was able to spend in your lab in Lyon. My time in France was a truly unique experience, and I am thankful for your efforts to make it possible. This dissertation would not exist without you, and I look forward to seeing where you take this heterometallic hydride chemistry in the coming years.

I must also credit the educators who originally instilled my passion for chemistry, starting with Siobhan Julian. Ms. Julian was the best high school chemistry teacher a kid could ask for, and I still recall her lessons on redox, which involved a stuffed lion holding a sign (LEO says GER!), and a particularly energetic class where she climbed on a desk to represent an excited electron. You made chemistry exciting to me for the first time, a feeling which has continued to this day.

I was fortunate enough to be advised by equally inspiring professors in my college career at Harvey Mudd, Katherine Van Heuvelen and Adam Johnson. Prof. Van Heuvelen, your patience and guidance were instrumental to building my confidence and abilities as a scientist. I stepped into your lab for the first time as a freshman unsure of whether chemistry was the right path for me, and left prepared to tackle a Ph.D. Thank you for everything you've done and continue to do for the people of Harvey Mudd – professors like you are what made my four years there so wonderful. Prof. Johnson, I will always appreciate your willingness to take me into your lab for a summer (even though I later returned to Prof. Van Heuvelen). Your humor, advice, and blunt honesty were extremely helpful and much appreciated as I faced the question of what to do with my life after Mudd.

In a small group like ours, you get to know each of your lab mates pretty well, each of whom contributed to my time here. First my immense thanks to Michael Boreen, who was an attentive and patient mentor from day 1, answering my endless questions and offering advice whenever it was needed. I can't express how (selfishly) relieved I was when you stayed in our group as a postdoc so that I could rely on your support for a little bit longer. Not only did you mentor me as a chemist, but you became one of my best friends in Berkeley as well. I will always cherish the time we spent together drinking stouts and watching sports, Curb, Jon Bois, or just talking about the latest things happening in our lives. Thank you too for convincing me to get back onto skis, even if I did take a 200-foot tumble along the way.

Mark Straub, thank you for welcoming me into 508 with open arms. I enjoyed the conversations we had about chemistry as well as whatever random topic happened to pique our interest on a given day. To Jade Fostvedt, I have always felt so lucky to have been hosted by you as a visiting student; talking to you cemented my decision to come to Berkeley and join the Arnold lab. Your positivity was inspiring, and talking to you always brightened my day when I needed it most. Erik Ouellette, thank you for braving the floodwaters of 512 with me, I'm sure we'll both never forget that fateful day. I look forward to more skiing and sports trash talk in the future. Sheridon Kelly, I've appreciated the time we've had both on campus and up the hill, and I'll miss talking about books and anything but chemistry during lunch with you. To Joe Brackbill, it's been great having an actinide buddy through the end of our time here in the group. I'm especially grateful to have gotten to know you better these past couple of years. I have been able to count on your support and friendship inside and out the lab, and I appreciate your willingness to share your perspectives on not just chemistry but life as well. Finally, to David, the last bastion of the Arnold group, it's been a pleasure working with you these past couple years. Your energy for research is infectious and helped remind me that discovering new things is really, really cool. I wish you the best of luck as the Last Arnold.

To everyone else I had the privilege of working alongside in Berkeley: Emmanuel Cortes, Anukta Jain, Julian Magdalenski, Franck Ulm, Constantine Kyprianou, and Lucas Rodriguez, thank you for your support and filling the years I spent in this lab with pleasant memories. To my brief coworkers in Lyon: Cynthia Cuevas Chavez, Anthony Vivien, Rosalyn Falconer, Laurent Veyre, and especially Nghia Le, Léon Escomel, and Abdelhak Lachguar, thank you for welcoming me, helping me adjust to a new lab space, and giving me advice on how to make the most of my weekends in France.

I also would not have made it through these past five years without the love and support of numerous people that I am fortunate enough to call my friends. To the Webster crew: Roger Zhang, Robin Zhang, Kyle Xiao, Marco Caiola, James Hu, and Krishna Patel, I am so grateful for your friendship throughout the years. I look forward to many more garbage plates in our futures. To the friends I made at Harvey Mudd: Trevor Fung, Jason Dwyer, Jordan Haack, Nick Draper, Celena Wang, Veronica Show, Celine Wang, Keo Chui, Debbie Lin, and so many more, you all kept me sane during the isolation and loneliness of the pandemic. I feel extremely grateful to have so many people that I have trusted and leant on for support, and each of you played a part in that. To the community at CFC, thank you for reaching out and taking me in as a part of your community. I honestly did not expect to find a church when I first came to Berkeley, but your warmth and kindness turned out to be exactly what I needed. To Hoyun Kim in particular, thank you for being such a friend during my time here. Your caring heart and delicious cooking have tided me through many rough patches over the years. My special thanks to Greg, Traci, and the rest of the Fungs as well for treating me like family during my time in the Bay – I carry the title of honorary Fung with pride and hope to spend more Thanksgivings with you all.

To Nathalie Co, I was fortunate enough to meet you near the end of my time here, and for that I feel like the luckiest man alive. It really is true that love finds you when you least expect it. Every day is better with you, and I can't wait to see what our future holds.

Last and greatest, I owe the most to my family for getting me to where I am today. Thank you Dad, for always believing in me even when I was at my lowest. Your outlook on life and positivity are so inspiring, and have taught me how to be the person I am today. Mom, without your sacrifices, I would never have had the chance to be in this position, or thank all the people mentioned before – you made all of this possible. Daniel, ever since we were little you were the greatest younger brother, and now that you're older it has only become clearer. Thank you for the support, visits, and calls during my years in Berkeley. To 姥姥, 姥爷, 奶奶, 爷爷, 舅舅, 伯伯, and 姑姑, despite our physical distance, thank you for always supporting me and my family. I love you all. And finally, to Grandma Louise and Grandpa Jim, thank you for taking in an immigrant couple as family; your hospitality has left an indelible mark on us all. I dedicate this dissertation to you both.

Chapter 1

A Brief History of f-Block–Transition Metal Hydrides

Introduction

Transition metal (TM) hydrides play a pivotal role in inorganic and organometallic chemistry, delivering fundamental insights into metal bonding character and participating in numerous chemical transformations and catalytic cycles.[1–4] Heterometallic species pairing the transition metal center(s) with other metals are of both fundamental and practical interest, capable of stabilizing reactive metal–metal bonds and holding the potential for cooperative reactivity. One particularly successful strategy has been the pairing of electron-rich transition metal hydrides with electron-poor, Lewis acidic metals. This has been well documented for main-group and cationic coinage metals, yielding complexes capable of H_2 activation, olefin polymerization, and carbonyl reduction.[5,6]

The lanthanides (Ln) and actinides (An) of the f-block are also highly Lewis acidic, positioning them as ideal partners for similar chemistry. Significant progress has been made in the field of Ln–TM heterometallic hydrides, with the development of several routes to access these compounds.[7–11] These complexes have exhibited metal–metal electronic communication,[9–11] hydrogen capture and release properties,[12,13] and carbonyl reduction chemistry.[14–16] Despite the productivity of this lanthanide chemistry, similar studies have not yet been realized for the actinides beyond early pioneering studies on U–Re hydrides by Ephritikhine and coworkers over thirty years ago. Here we will present an overview of the progress that has been made in this field, and motivate the further study of actinide-transition metal hydride species.

Synthetic Strategies for Rare-Earth–Transition Metal Hydrides

The rare-earth (RE) metals largely dominate the landscape of f-block–TM heterometallic hydride chemistry, yielding the first example of such species with Evans and coworkers' report of the trimetallic Y_2Zr tetrahydride **1.1** in 1984 (Figure 1.1).[7] Reaction of the yttrium dimer $[Cp'_2YH(THF)]_2$ (Cp' = C_5H_4Me) with 0.5 equivalents of $[Cp'_2ZrH_2]_2$ yielded the final product, which contains three μ_2-hydrides and one μ_3-hydride coordinated to the three metal centers. The first structurally authenticated RE–TM hydride complexes, $[Cp_2Y(THF)Re_2H_7(PMe_2Ph)_4]$ (**1.2-Y**) and $[Cp_2LuRe_2H_7(PMe_2Ph)_4]$ (**1.2-Lu**), followed in 1990 from a joint effort by the Evans and Caulter groups.[8] In this case, methane elimination from $Cp_2LnMe(THF)$ (Ln = Y, Lu) by a dimeric rhenium polyhydride starting material yielded the reported complexes. Complex **1.2-Y** takes on an open triangular structure with the yttrium center coordinated to a single rhenium atom, while the unsolvated **1.2-Lu** instead binds symmetrically across both rhenium centers in a closed triangular geometry (Figure 1.2). ^1H NMR experiments revealed **1.2-Y** can be desolvated, upon which it converts to the closed triangular form found for **1.2-Lu**.

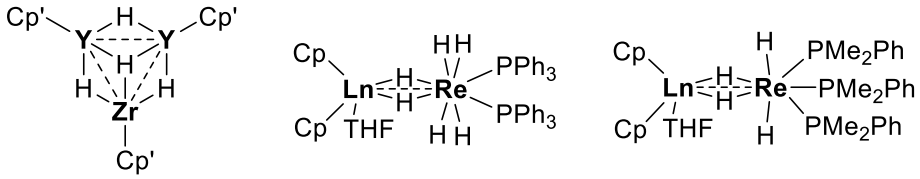

1.1 Cp' = C_5H_4Me | **1.3-Ln** (Ln = Y, Lu) | **1.4-Ln** (Ln = Y, Lu)

Figure 1.1 Initial RE–TM hydride species reported by Evans and coworkers.

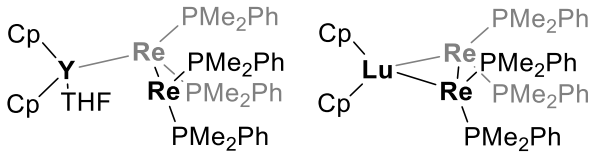

1.2-Y **1.2-Lu**

Figure 1.2 Geometry of complexes **1.2-Y** and **1.2-Lu**. Hydride geometry is not reported for these complexes and therefore is not shown; each trimetallic core contains 7 hydrides.

Subsequent studies replacing the rhenium dimer with monometallic rhenium polyhydrides led to heterobimetallic hydride complexes **1.3-Ln** and **1.4-Ln** (Ln = Y, Lu; Figure 1.1).[17] Bimetallic **1.3-Y** was found to be highly reactive toward olefin polymerization, but unreactive with CO or CO_2, while the opposite pattern was observed for the trimetallics **1.2-Y** and **1.2-Lu**. These initial studies demonstrated the effectiveness of hydrides in bringing f-block and transition metal centers together to form reactive complexes. These heterometallic species exhibit diverse reactivity that is highly dependent on the number of metal centers and their coordination environment, and reactivity diverging from that observed in their monometallic building blocks.

In the next decade, several synthetic approaches to RE–TM hydrides emerged. Green and coworkers prepared hydride-bridged tungsten– and niobium–ytterbium complexes **1.5** and **1.6** (Figure 1.3) *via* salt metathesis.[9,18] X-ray crystal structures and NMR data indicated the presence of three hydrides bridging each Yb–W interaction and two hydrides bridging each Yb–Nb interaction. Observation of ^{31}P–^{171}Yb coupling with the W-bound PMe_3 groups in **1.5** by $^{171}Yb\{^1H\}$ NMR provided strong evidence for covalency between the two metals, demonstrating the ability of bridging hydrides to support f-block–TM interactions.

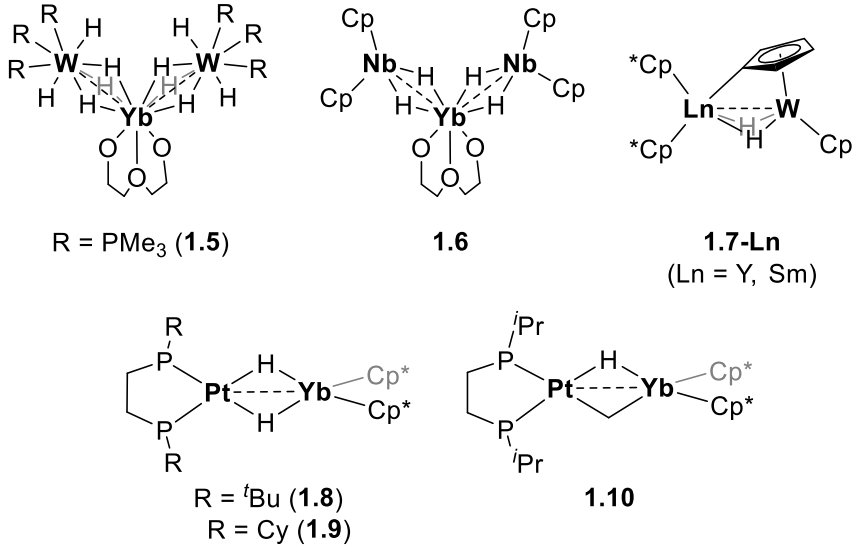

R = PMe_3 (**1.5**) **1.6** **1.7-Ln** (Ln = Y, Sm)

R = ^{t}Bu (**1.8**) R = Cy (**1.9**) **1.10**

Figure 1.3 RE–TM hydrides synthesized *via* salt metathesis, H_2 elimination, and direct coordination.

Tilley and coworkers reported that addition of Cp_2WH_2 to 0.5 equivalents of $[Cp^*_2SmH]_2$ (Cp* = pentamethylcyclopentadienyl) yielded the metallated cyclopentadienyl complex $[Cp^*_2Sm(\mu\text{-}\eta^1,\eta^5\text{-}C_5H_4)(\mu\text{-}H)_2WCp]$ (**1.7-Sm**, Figure 1.3). Rather than reacting with the tungsten hydride, the samarium hydride undergoes σ-bond metathesis with an aromatic C–H bond,

eliminating H_2. As no hydride signal was observed in the ^1H NMR spectrum of this complex, the yttrium analogue **1.7-Y** was synthesized for further analysis. NMR experiments on **1.7-Y** suggest that both hydrides bridge the metal centers, interacting more strongly with tungsten than the RE metals.

In another route to RE–TM hydrides, Andersen and coworkers reported direct coordination of *cis*-[$R_2P(CH_2)_2PR_2$]PtH_2 (R = Me, Cy) to Cp*$_2$Yb, yielding dihydride-bridged Yb–Pt complexes **1.8** and **1.9** (Figure 1.3).[11] These complexes were highly insoluble, but the mixed μ-CH_3, μ-H complex **1.10** proved more amenable to spectroscopic analysis. Similar to the complexes reported by Tilley, coupling in the NMR spectra for the monohydride species indicates communication between the Yb and Pt centers.

Tethered Heterobimetallic Complexes and their Reactivity

Following these reports, robust strategies for the synthesis of RE–TM hydrides had been established, yet their reaction chemistry remained largely unexplored. A series of studies by Hou and coworkers on tethered, heterobimetallic RE–Ru hydrides revealed the CO activation ability of these complexes. An initial study demonstrated that half-sandwich Lu alkyl complexes react with a series of (PMe_nPh_{3-n})RuH_3 complexes to yield phosphinomethyl- and phosphinophenyl-bridged Lu–Ru dihydrides **1.11**-**1.14** (Scheme 1.1).[14] The phosphinomethyl-bridged species was isolated for all complexes besides the triphenylphosphine derivative. These bimetallics feature short Lu–Ru distances (< 2.88 Å), demonstrating the effectiveness of these Ru phosphine hydrides as building blocks to RE–Ru species.

Scheme 1.1 Synthesis of tethered Lu–Ru dihydrides.

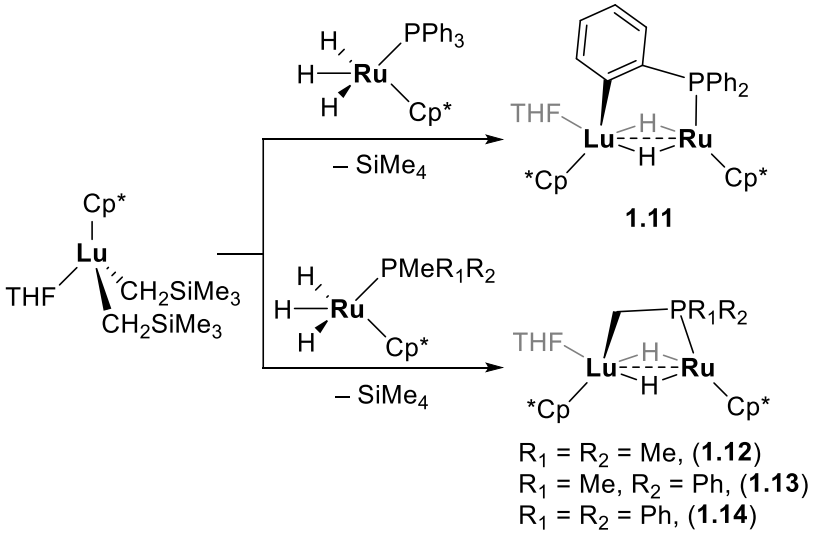

Further studies reported the tethered Y–Ru complex [^{TMS}CpY(DME)(μ-H)$_2$(μ-η^1,η^1-$C_6H_4PPh_2$)RuCp*] (**1.15**) and the Lu–Ru phosphinoethyl-bridged analogue [Cp*Lu(DME)(μ-H)$_2$(μ-η^1,η^1-$CH(CH_3)PEt_2$)RuCp*] (**1.16**).[16] Dimethyl-substituted complex **1.12** activates CO, providing tetranuclear trihydride oxo/vinyl-phosphine complex **1.17** (Scheme 1.2, top). ^{13}CO labeling studies indicate that the α-vinyl carbon in the final product originates from the activated CO. A mechanism was proposed involving CO insertion into the Lu–CH_2 bond, followed by reaction with another equivalent of the bimetallic and bond rearrangement to yield the final

product. The Y–Ru phosphinophenyl-bridged species **1.15** instead reacts with CO to form a phospha-benzyl carbonyl Ru complex (**1.18**), with no isolable yttrium-containing product (Scheme 1.2, middle). A third reaction occurs upon CO addition to the phosphinoethyl-bridged complex, resulting in a phospha-enolate bridged bimetallic, possibly through CO insertion into the Lu–CH_2 bond followed by phosphine migration (Scheme 1.2, bottom).

Scheme 1.2 Proposed mechanisms for the reactions of **1.12**, **1.15**, and **1.16** with CO.

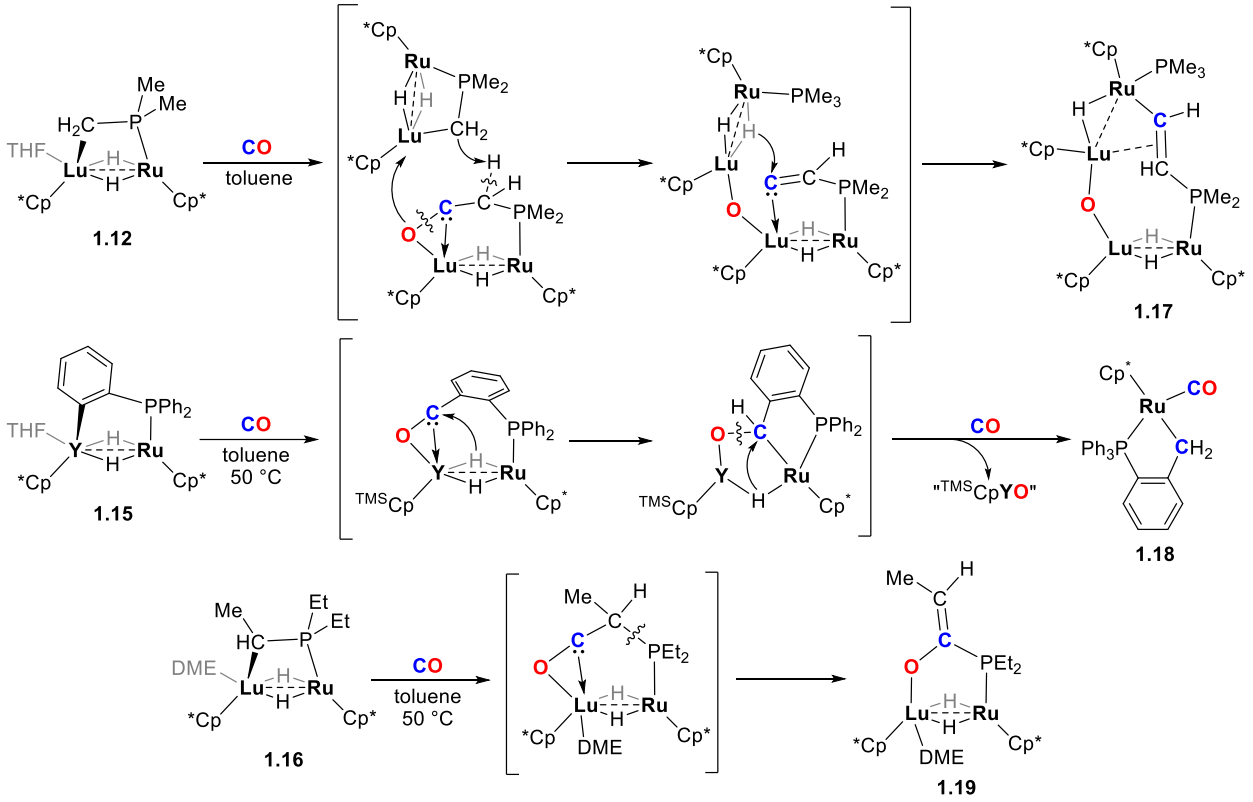

Replacement of the lanthanide half-sandwich scaffold with bis(phosphinophenyl)amido pincer (PNP) ligands yielded two series of tethered Ln–Ru (Ln = Y, Ho, Dy) dihydrides (**1.20-Ln** and **1.21-Ln**, Figure 1.4).[15] Yet another CO activation mechanism is observed for the Y phosphinophenyl species, with CO insertion into the Y–CH_2 bond followed by hydride migration to give pseudo(2-(diphenylphosphino)-phenyl)oxomethylene-bridged **1.22**. Taken as a whole, this series of tethered complexes highlights the unique reactivity of heterometallic RE–TM hydrides, and the significant effects that arise from subtle changes in the ligand environment.

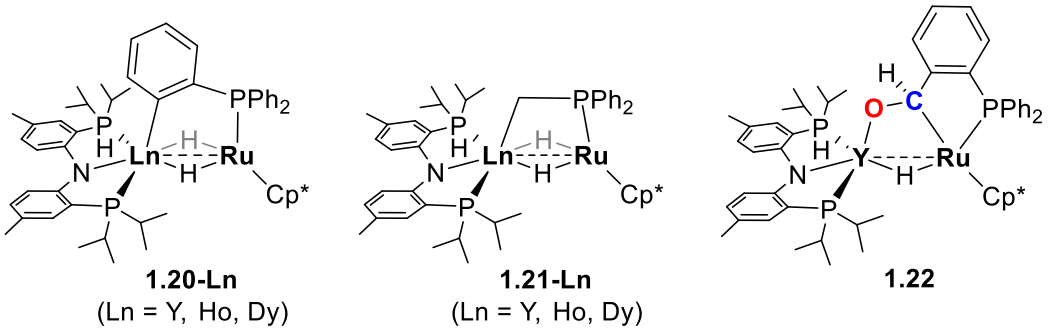

Figure 1.4 PNP-ligated, tethered Ln–Ru complexes and the CO reaction product **1.22-Y**.

Kempe and coworkers instead synthesized bridged RE–Ru hydrides from [HRu(dmpe)Cp] (dmpe = bis(dimethylphosphino)ethane) and the mono(alkyl) species [$Cp_2Ln(CH_2SiMe_3)(THF)$] (Ln = Y, Lu). C–H activation of the Ru-bound Cp followed by alkane elimination yielded complexes [$Cp_2Ln(\mu\text{-}\eta^1,\eta^5\text{-}C_5H_4)(\mu\text{-}H)Ru(dmpe)$] (**1.23-Ln**). Deuterium-labeling experiments confirmed that the hydride in **1.23-Ln** originates from the ruthenium-bound hydride rather than C–H activation of the Cp ring. Complex **1.23-Y** reacts with diphenylacetylene, inserting across the strained Y–C bond to form **1.24** (Scheme 1.3). Pairing the ruthenium hydride with bis(alkyl) complexes instead led to complexes **1.25-Ln** (Figure 1.5). These dimeric complexes feature two C–H activations, with the second occurring at one of the aliphatic methyl groups of the phosphine ligand.

Scheme 1.3 Insertion of diphenylacetylene into **1.23-Y**.

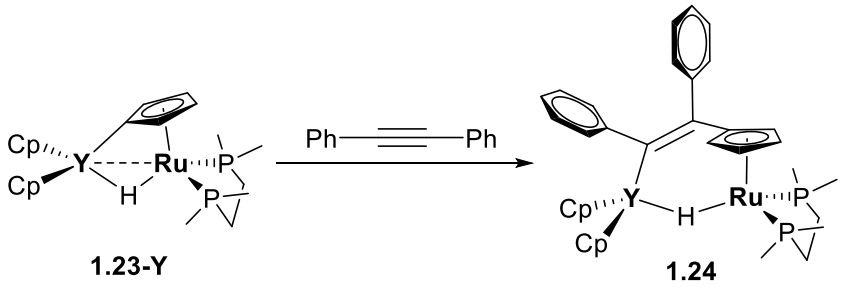

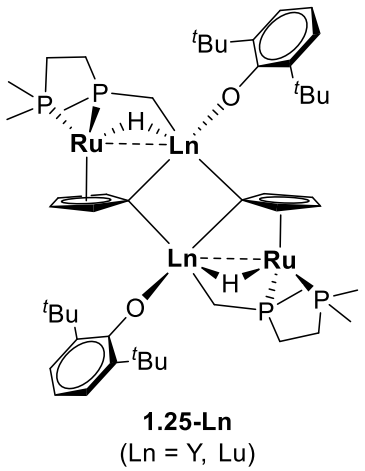

Figure 1.5 Tetrametallic complexes **1.25-Ln** (Ln = Y, Lu).

Cluster Chemistry – Hydrogen Capture and Release

Following the discovery that homometallic rare-earth polyhydride clusters exhibit different properties than their monohydride relatives, interest began to grow in heterometallic rare-earth polyhydride clusters as well.[19–25] Mixed-metal hydrides such as $LaNi_5H_n$ have outstanding hydrogen storage capabilities,[26] yet molecular models of these materials are rare. Therefore, study of such model compounds may deliver mechanistic insights to aid the development of more efficient H_2 storage systems.

Using ^{TMS}Cp-supported tetranuclear yttrium octahydrides, Hou and coworkers synthesized pentanuclear Y_4M (M = W, Mo) complexes which displayed hydrogen capture and release properties. Reaction of $^{TMS}Cp_4Y_4H_8(THF)$ with Cp*M(PMe$_3$)H$_5$ (M = Mo, W) led to the isolation of {[(^{TMS}CpY)$_4$(μ-H)$_7$](μ-H)$_4$MCp*(PMe$_3$)} (Ln = Mo, W; **1.26-M**).[12] These complexes were photolyzed to eliminate PMe$_3$, affording the hendecahydride clusters **1.27-Mo** and **1.27-W**. The molybdenum cluster oxidatively adds H_2 to form a species with 13 hydrides, which regenerates **1.27-Mo** upon irradiation with UV light (Scheme 1.4, top). In contrast, **1.27-W** reductively eliminates H_2 when subjected to heat and vacuum, yielding a product with 9 hydrides (Scheme 1.4, bottom). The starting complex regenerates upon exposure to H_2. Hydrides in these clusters were located in both X-ray (**1.26-M**, **1.27-M**, **1.28**, and **1.29**) and neutron (**1.26-W** and **1.27-W**) structures.

Scheme 1.4 H_2 uptake and release by Y_4M complexes.

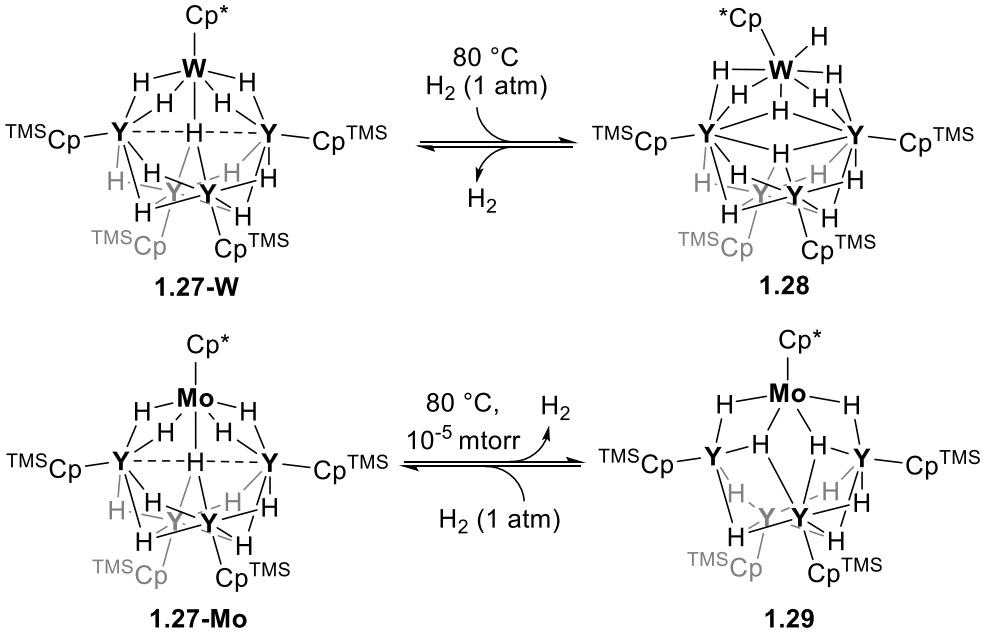

Additional clusters were synthesized from Cp'-ligated Y_4H_8 and Cp*-ligated Y_5H_{10} starting materials.[13] With the Cp'-ligated system, pentanuclear Y_4MH_{11} complexes **1.30-M** were isolated from reactions with Cp*M(PMe$_3$)H$_5$ (M = W, Mo) followed by UV irradiation to eliminate PMe$_3$. Reaction with a second equivalent of the transition metal starting material yielded $Y_4M_2H_{14}$ polyhydrides **1.31-M**, which once again could be photolyzed to yield complexes **1.32-M** (Scheme 1.5). Hexanuclear cluster **1.32-Mo** can release two equivalents of H_2 under vacuum at 120 °C; this process is again reversible upon exposure to H_2. Unlike **1.27-W**, tungsten species **1.32-W** does not

exhibit any H_2 uptake – the authors posit this is due to the additional steric hindrance around the metal centers in **1.32-W**. Reaction of the transition metal pentahydrides with {[Cp*Y(μ-H)$_2$]$_5$(THF)$_2$} instead yielded clusters of the form Y_5MH_{13}. For the Y_5MoH_{13} species, reversible loss of H_2 to a Y_5MoH_{11} species was observed; no isolable H_2 addition product was found for the tungsten analogue.

Scheme 1.5 Synthesis of $Y_4M_2H_{14}$ complexes **1.31-M** and **1.32-M** (M = W, Mo).

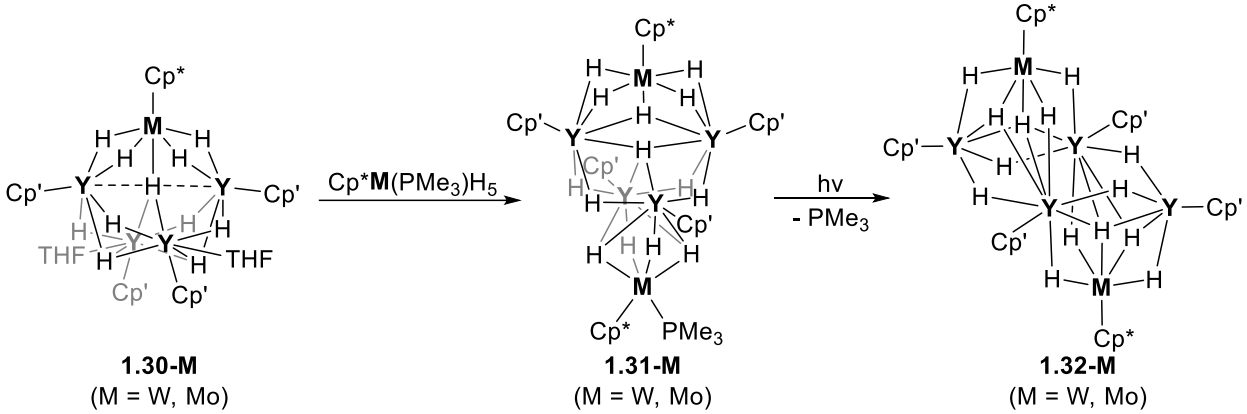

Other Multimetallic RE–TM Hydrides

Several other forays into RE–TM hydrides have been reported by the groups of Kempe and Hou. Dimeric transition metal hydrides have yielded many trimetallic species, though these tend to be less reactive than the compounds described previously. Kempe and coworkers described the synthesis of {[Cp*Ru(μ-H)]$_2$(μ-H)$_2$YCp$_2$} (**1.33**) *via* alkane elimination after reaction times of 7 days.[27] Hou reported multimetallic complexes upon reaction of Y- and Lu-alkyls with [Cp*WH$_4$]$_2$, [Cp*OsH$_2$]$_2$, and [Cp*RuH$_2$]$_2$; in each case a significantly different reaction product is obtained (Figure 1.6).[28] Complexes **1.35-Ln** and **1.36-Ln** feature the C–H activation and deprotonation of a Cp methyl group. Both **1.36-Y** and **1.36-Lu** react with H_2, cleaving the Ru–CH_2 bond and adding a fourth hydride across the terminal Ln–Ru interaction, but unlike the clusters described previously this reaction is not reversible. Heterobimetallic complexes [(C$_5$Me$_4$SiMe$_3$)$_2$Ln(μ-H)$_3$IrCp*] (Ln = Y, Dy, Lu; **1.37-Ln**) were also reported as the products of H_2 elimination from the reaction of [(C$_5$Me$_4$SiMe$_3$)$_2$LnH(THF)] and Cp*IrH$_4$.[29]

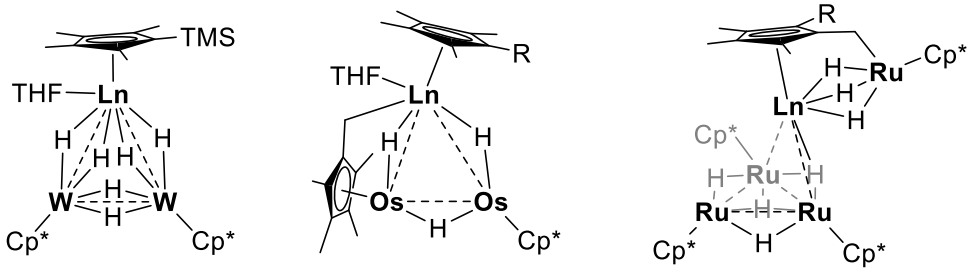

Figure 1.6 Multimetallic RE–TM hydrides synthesized from transition metal hydride dimers.

Actinide-transition metal hydrides

The body of actinide–transition metal hydride chemistry pales in comparison to that of the lanthanides. Ephritikhine and coworkers reported the first such examples, $Cp_3UH_6Re(PR_3)_2$ (R = *p*-F-C_6H_4, Ph) in 1986,[30] with several follow-up studies over the next decade.[31,32] The related species [K(18-crown-6)][Cp^*_2(Cl)U(μ-H)$_3$(H_3)Re(PPh_3)$_2$] (**1.37**), was structurally characterized, and remained the only such characterized An–TM hydride prior to this work. No reactivity toward unsaturated hydrocarbons, acetone, or CO_2 was observed, nor was H/D exchange upon refluxing or irradiation in d_8-THF.[32]

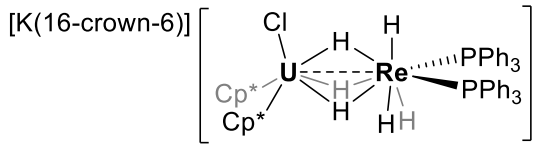

1.37

Figure 1.7 The structurally characterized U–Re complex **1.37**; hydrides were not located in the crystal structure, and are therefore placed in their predicted geometry according to NMR experiments.

Despite the dearth of literature on An–TM hydrides, these complexes hold strong potential in several areas of study. First, bridging hydride ligands are well-adapted to stabilize metal–metal interactions between actinides and transition metals, an area of fundamental interest for the actinides. Their small steric profile allows for close metal–metal contact, and direct bond formation *via* hydride elimination has strong precedent.[33] Second, the interaction of multiple metal centers can lead to novel reactivity, as we discovered while studying these fascinating compounds. Finally, much remains to be discovered about the physical properties of An–TM hydrides, which are predicted to have potential for hydrogen storage and superconductivity at high pressures.[34] The work presented in the following chapters seeks to establish the efficacy of bridging hydrides in supporting novel An–TM bonds, the unique reactivity engendered by placing these metal centers in proximity, and inspire further investigation to fully unlock the potential of these complexes.

References

(1) Esteruelas, M. A.; Oro, L. A. Dihydrogen Complexes as Homogeneous Reduction Catalysts. *Chem. Rev.* **1998**, *98* (2), 577–588. https://doi.org/10.1021/cr970322u.

(2) Jordan, A. J.; Lalic, G.; Sadighi, J. P. Coinage Metal Hydrides: Synthesis, Characterization, and Reactivity. *Chem. Rev.* **2016**, *116* (15), 8318–8372. https://doi.org/10.1021/acs.chemrev.6b00366.

(3) Crossley, S. W. M.; Obradors, C.; Martinez, R. M.; Shenvi, R. A. Mn-, Fe-, and Co-Catalyzed Radical Hydrofunctionalizations of Olefins. *Chem. Rev.* **2016**, *116* (15), 8912–9000. https://doi.org/10.1021/acs.chemrev.6b00334.

(4) Eberhardt, N. A.; Guan, H. Nickel Hydride Complexes. *Chem. Rev.* **2016**, *116* (15), 8373–8426. https://doi.org/10.1021/acs.chemrev.6b00259.

(5) Maity, A.; Teets, T. S. Main Group Lewis Acid-Mediated Transformations of Transition-Metal Hydride Complexes. *Chem. Rev.* **2016**, *116* (15), 8873–8911. https://doi.org/10.1021/acs.chemrev.6b00034.
(6) Albinati, A.; Venanzi, L. M. Transition Metal Hydrides as Ligands. *Coord. Chem. Rev.* **2000**, *200–202*, 687–715. https://doi.org/10.1016/S0010-8545(00)00257-5.
(7) Evans, W. J.; Meadows, J. H.; Hanusa, T. P. Organolanthanide and Organoyttrium Hydride Chemistry. 6. Direct Synthesis and Proton NMR Spectral Analysis of the Trimetallic Yttrium and Yttrium-Zirconium Tetrahydride Complexes, $\{[(C_5H_5)_2YH]_3H\}\{Li(THF)_4\}$ and $\{[(CH_3C_5H_4)_2YH]_2[(CH_3C_5H_4)_2ZrH]H\}$. *J. Am. Chem. Soc.* **1984**, *106* (16), 4454–4460. https://doi.org/10.1021/ja00328a027.
(8) Alvarez, D. Jr.; Caulton, K. G.; Evans, W. J.; Ziller, J. W. Reversible Opening and Closing of Hetero Trimetallic Units in $(C_5H_5)_2Y(THF)Re_2H_7(PMe_2Ph)_4$ and $(C_5H_5)_2LuRe_2H_7(PMe_2Ph)_4$. *J. Am. Chem. Soc.* **1990**, *112* (14), 5674–5676. https://doi.org/10.1021/ja00170a061.
(9) Green, M. L. H.; Hughes, A. K.; Michaelidou, D. M.; Mountford, P. New Lanthanide–Hydrogen–Transition Metal Compounds: $[\{(PMe_3)_3WH_5\}_2Yb\cdot L_3]$ and $[\{(\eta\text{-}C_5H_5)_2NbH_2\}_2Yb\cdot L_3]$ Where $L_3=(MeOCH_2CH_2)_2O$. *J. Chem. Soc., Chem. Commun.* **1993**, No. 7, 591–593. https://doi.org/10.1039/C39930000591.
(10) Radu, N. S.; Gantzel, P. K.; Tilley, T. D. Lanthanide–Tungsten Heterobimetallic Complexes *via* σ-Bond Metathesis. *J. Chem. Soc., Chem. Commun.* **1994**, No. 10, 1175–1176. https://doi.org/10.1039/C39940001175.
(11) Schwartz, D. J.; Ball, G. E.; Andersen, R. A. Interactions of cis-P_2PtX_2 Complexes (X = H, Me) with Bis(Pentamethylcyclopentadienyl)Ytterbium. *J. Am. Chem. Soc.* **1995**, *117* (22), 6027–6040. https://doi.org/10.1021/ja00127a016.
(12) Shima, T.; Luo, Y.; Stewart, T.; Bau, R.; McIntyre, G. J.; Mason, S. A.; Hou, Z. Molecular Heterometallic Hydride Clusters Composed of Rare-Earth and d-Transition Metals. *Nat. Chem.* **2011**, *3* (10), 814–820. https://doi.org/10.1038/nchem.1147.
(13) Shima, T.; Hou, Z. Heterometallic Polyhydride Complexes Containing Yttrium Hydrides with Different Cp Ligands: Synthesis, Structure, and Hydrogen-Uptake/Release Properties. *Chem.─Eur. J.* **2013**, *19* (10), 3458–3466. https://doi.org/10.1002/chem.201203495.
(14) Shima, T.; Hou, Z. Activation and Dehydrogenative Silylation of the C–H Bonds of Phosphine-Coordinated Ruthenium in Lu/Ru Heteromultimetallic Hydride Complexes. *Chem. Lett.* **2008**, *37* (3), 298–299. https://doi.org/10.1246/cl.2008.298.
(15) O, W. W. N.; Kang, X.; Luo, Y.; Hou, Z. PNP-Ligated Heterometallic Rare-Earth/Ruthenium Hydride Complexes Bearing Phosphinophenyl and Phosphinomethyl Bridging Ligands. *Organometallics* **2014**, *33* (4), 1030–1043. https://doi.org/10.1021/om401216v.
(16) Kawai, D.; Shima, T.; Nishiura, M.; Hou, Z. Cleavage of Carbon Monoxide and C-C Bond Formation Promoted by Rare-Earth/Ruthenium Heterobimetallic Hydride Complexes. *J. Organomet. Chem* **2017**, *847*, 74–81. https://doi.org/10.1016/j.jorganchem.2017.02.042.
(17) Alvarez, D. Jr.; Caulton, K. G.; Evans, W. J.; Ziller, J. W. Synthesis, Structure, and Reactivity of Heterometallic Polyhydride Complexes of Rhenium with Yttrium and Lutetium. *Inorg. Chem.* **1992**, *31* (26), 5500–5508. https://doi.org/10.1021/ic00052a028.
(18) Michaelidou, D. M.; Green, M. L. H.; Hughes, A. K.; Mountford, P.; Chernega, A. N. The Lanthanide-Hydrogen-Transition Metal Compounds: $[\{(PMe_3)_3WH_5\}_2Yb\cdot L_3]$ and $[\{(\eta\text{-}C_5H_5)_2NbH_2\}_2Yb\cdot L_3]$ Where $L_3 = (MeOCH_2CH_2)_2O$, and Related Studies. *Polyhedron* **1995**, *14* (19), 2663–2675. https://doi.org/10.1016/0277-5387(95)00183-S.

(19) Cheng, J.; Saliu, K.; Kiel, G. Y.; Ferguson, M. J.; McDonald, R.; Takats, J. Scorpionate-Supported Dialkyl and Dihydride Lanthanide Complexes: Ligand- and Solvent-Dependent Cluster Hydride Formation. *Angew. Chem., Int. Ed.* **2008**, *47* (26), 4910–4913. https://doi.org/10.1002/anie.200705977.

(20) Cheng, J.; Saliu, K.; Ferguson, M. J.; McDonald, R.; Takats, J. Variable Nuclearity Scorpionate-Supported Lanthanide Polyhydrides: $[(Tp^{R,R'})LnH_2]_n$ (n = 3, 4 and 6). *J. Organomet. Chem* **2010**, *695* (25), 2696–2702. https://doi.org/10.1016/j.jorganchem.2010.08.020.

(21) Cheng, J.; Ferguson, M. J.; Takats, J. Synthesis and Reaction of $[(Tp^{i}Pr_2)LnH_2]_3$ (Ln = Y, Lu) with CO: Trinuclear Cluster-Bound Propenolate En Route to Selective Formation of Propene. *J. Am. Chem. Soc.* **2010**, *132* (1), 2–3. https://doi.org/10.1021/ja905679k.

(22) Hultzsch, K. C.; Voth, P.; Spaniol, T. P.; Okuda, J. Synthesis and Characterization of a Tetranuclear Hydride Cluster of Yttrium $[(\eta^5\text{-}C_5Me_4SiMe_3)Y_4(\mu\text{-}H)_4(\mu_3\text{-}H)_4(THF)_2]$. *Z. Anorg. Allg. Chem.* **2003**, *629* (7–8), 1272–1276. https://doi.org/10.1002/zaac.200300063.

(23) Ohashi, M.; Konkol, M.; Del Rosal, I.; Poteau, R.; Maron, L.; Okuda, J. Rare-Earth Metal Alkyl and Hydride Complexes Stabilized by a Cyclen-Derived [NNNN] Macrocyclic Ancillary Ligand. *J. Am. Chem. Soc.* **2008**, *130* (22), 6920–6921. https://doi.org/10.1021/ja801771u.

(24) Lyubov, D. M.; Döring, C.; Fukin, G. K.; Cherkasov, A. V.; Shavyrin, A. S.; Kempe, R.; Trifonov, A. A. Selective Assembly of Trinuclear Rare-Earth Alkyl Hydrido Clusters Supported by Amidopyridinate Ligands. *Organometallics* **2008**, *27* (13), 2905–2907. https://doi.org/10.1021/om800364b.

(25) Lyubov, D. M.; Döring, C.; Ketkov, S. Yu.; Kempe, R.; Trifonov, A. A. Selective Protonation of the Y–C Bond in Trinuclear Yttrium Alkyl–Hydrido Clusters and Formation of the Cationic Polyhydrido Core. *Chem.─Eur. J.* **2011**, *17* (14), 3824–3826. https://doi.org/10.1002/chem.201003616.

(26) Schüth, F.; Bogdanović, B.; Felderhoff, M. Light Metal Hydrides and Complex Hydrides for Hydrogen Storage. *Chem. Commun.* **2004**, No. 20, 2249–2258. https://doi.org/10.1039/B406522K.

(27) Butovskii, M. V.; Tok, O. L.; Wagner, F. R.; Kempe, R. Bismetallocenes: Lanthanoid–Transition-Metal Bonds through Alkane Elimination. *Angew. Chem., Int. Ed.* **2008**, *47* (34), 6469–6472. https://doi.org/10.1002/anie.200800407.

(28) Shima, T.; Hou, Z. Rare Earth/d-Transition Metal Heteromultimetallic Polyhydride Complexes Based on Half-Sandwich Rare Earth Moieties. *Organometallics* **2009**, *28* (7), 2244–2252. https://doi.org/10.1021/om900024q.

(29) Takenaka, Y.; Hou, Z. Lanthanide Terminal Hydride Complexes Bearing Two Sterically Demanding $C_5Me_4SiMe_3$ Ligands. Synthesis, Structure, and Reactivity. *Organometallics* **2009**, *28* (17), 5196–5203. https://doi.org/10.1021/om900453j.

(30) Baudry, D.; Ephritikhine, M. Synthesis of a Hydride-Rich Uranium-Rhenium Dimer: $[(p\text{-}F\text{-}C_6H_4)_3P]_2ReH_6U(\eta\text{-}C_5H_5)_3$. *J. Organomet. Chem* **1986**, *311* (1), 189–192. https://doi.org/10.1016/0022-328X(86)80231-5.

(31) Cendrowski-Guillaume, S. M.; Lance, M.; Nierlich, M.; Vigner, J.; Ephritikhine, M. New Actinide Hydrogen Transition Metal Compounds. Synthesis of $[K(C_{12}H_{24}O_6)][(\eta\text{-}C_5Me_5)_2(Cl)UH_6Re(PPh_3)_2]$ and the Crystal Structure of Its Benzene Solvate. *J. Chem. Soc., Chem. Commun.* **1994**, No. 14, 1655–1656. https://doi.org/10.1039/C39940001655.

(32) Cendrowski-Guillaume, S. M.; Ephritikhine, M. Synthesis and Reactivity of Hydrogen-Rich Uranium–Rhenium Compounds; an Unsuspected Detrimental Effect of Alkali-Metal Halide on Chemical Metathesis. *J. Chem. Soc., Dalton Trans.* **1996**, No. 8, 1487–1491. https://doi.org/10.1039/DT9960001487.
(33) Perutz, R. N.; Procacci, B. Photochemistry of Transition Metal Hydrides. *Chem. Rev.* **2016**, *116* (15), 8506–8544. https://doi.org/10.1021/acs.chemrev.6b00204.
(34) Havela, L.; Legut, D.; Kolorenč, J. Hydrogen in Actinides: Electronic and Lattice Properties. *Rep. Prog. Phys.* **2023**, *86* (5), 056501. https://doi.org/10.1088/1361-6633/acbe50.

Chapter 2

A Versatile Strategy for the Formation of Hydride-Bridged Actinide–Iridium Multimetallics

Introduction

Despite the pioneering works of Marks[1] and Ryan,[2,3] who reported the first actinide–transition metal (An–TM) complexes nearly forty years ago, there is still a wide range of unexplored space in the field of An–TM multimetallic complexes.[4,5] The combination of their potential for *f*-orbital participation in bonding, access to unusual coordination environments, and diversity of accessible oxidation states set the actinides apart from the more comprehensively studied transition metals or the lanthanides, especially when considering multimetallic species with the potential for *d-f* intermetallic bonding. Incorporation of these elements, which have been demonstrated to facilitate unique activation of strong bonds[6–11] and small molecules,[12–18] in multimetallic systems could unlock modes of cooperative reactivity currently inaccessible to transition metal multimetallic species. Even in light of this potential, as recently as ten years ago, f-element–metal bonding chemistry was still described as "in its infancy."[4] While impressive progress has been made since that time, there remain numerous transition metals for which the correct combination of ligand scaffolds to support An–TM bonding has not been discovered.

The last decade has seen a proliferation of An–TM multimetallic species featuring bulky, multidentate N- or P-donor ligands, which allow for stabilization of both supported and unsupported An–TM multimetallic species.[19–23] These have been especially effective for the lighter group 9 metals, as numerous singly- and multiply-bonded complexes with uranium and cobalt/rhodium have been reported,[23–30] along with one example of a thorium–cobalt bond.[25] Noticeably absent from this chemistry, however, is their third row analogue, iridium. Iridium has demonstrated varied reactivity with other transition metals,[31–44] producing numerous catalytically active species, but current ligand scaffolds have been to date unable to stabilize iridium-actinide bonds. It was not until extremely recently that the first complexes to contain both iridium and an actinide were reported; however, these two uranium–iridium multimetallic nitrides feature bridging nitrides and azides between the metal centers along with fairly large U–Ir distances of 3.19 Å or greater.[29] Therefore, a different bonding motif was pursued for the synthesis of An–Ir interactions, one that ideally would be generalizable across numerous actinide starting materials, and potentially transferrable to other transition metal species.

Previous work with actinide-borohydrides has demonstrated the ability for multiple bridging hydrides to bring heteroatoms in relatively close proximity to actinide centers in high-coordinate complexes. The polymeric, 14-coordinate species $U(BH_4)_4$[45] and $Th(BH_4)_4$[46] have been known since the 1950s, and more recently a 15-coordinate thorium aminodiboranate has been described.[47] In addition, previous work in the Arnold group has demonstrated the effectiveness of bridging hydrides in stabilizing Th–Al and U–Al bonds.[48] The pentamethylcyclopentadienyl (Cp*) iridium polyhydride species Cp^*IrH_4 has demonstrated the ability to form highly reactive complexes when paired with other metal species (Scheme 2.1). For instance, Camp and coworkers showed that when reacted with several isobutylaluminum derivatives,[43,49] the resulting iridium aluminum complexes promote cooperative heteroallene cleavage, while reactions with group 4 and group 5 neopentylidene species[40,50] led to hafnium- and tantalum-iridium complexes that facilitate H/D exchange.[40,42] Promisingly, Hou and coworkers had also previously demonstrated the ability to form hydride-supported lanthanide–iridium bimetallic complexes of ytterbium, dysprosium, and lutetium in high yields.[51]

Scheme 2.1 Previously reported syntheses of reactive multimetallic complexes from Cp^*IrH_4.[40,43,49–51]

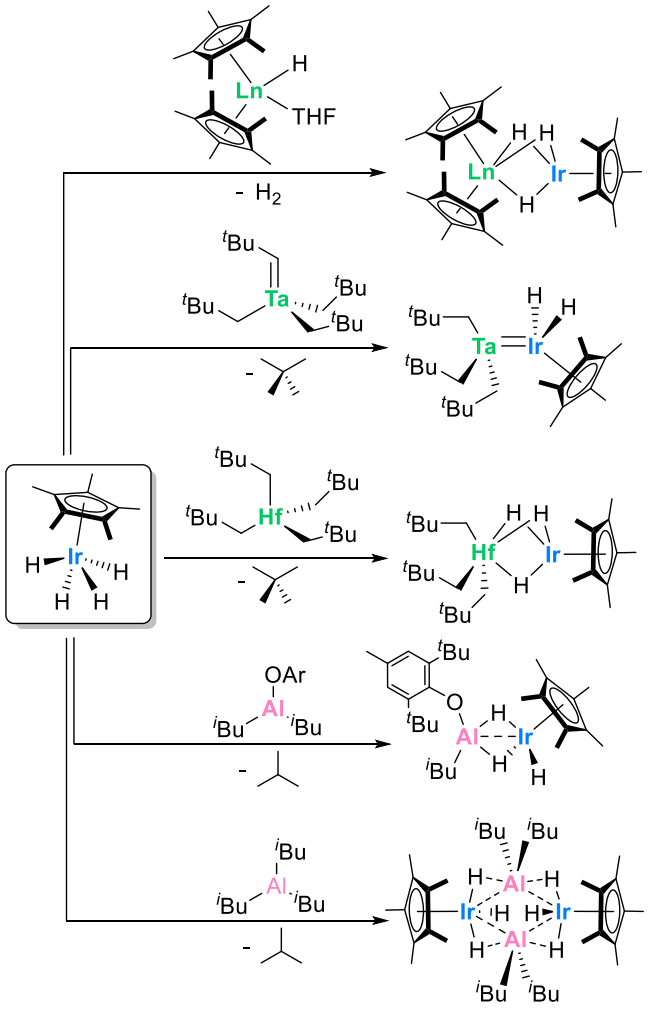

Previous efforts towards the formation of iridium–metal bonds with Cp^*IrH_4 have primarily focused on protonolysis pathways,[40,43,49,50] which are typically dependent on metal-alkyl or metal-aryl species as starting materials. Due to the greater prevalence and variety of actinide-halide starting materials, the previously reported, closely-related potassium iridate species $K[Cp^*IrH_3]$ was targeted for the formation of An–Ir multimetallic species *via* salt-elimination pathways.[49] Here, we report joint efforts from the Arnold and Camp groups to synthesize uranium- and thorium-iridium multimetallic species *via* salt-elimination reactions between U(IV)/Th(IV) halides and $K[Cp^*IrH_3]$ with unique actinide–iridium interactions. The synthesis of an octanuclear U_2Ir_6 complex featuring close metal-metal contacts from U(III) halide or aryl starting materials is also described. A host of computational studies were carried out to elucidate actinide oxidation states, frontier orbital compositions, and bond order information in order to better understand the bonding in these unusual complexes.

Results and Discussion

The potassium iridate species K[Cp*IrH$_3$] was formed *in situ* by the addition of benzylpotassium to Cp*IrH$_4$ in THF, resulting in a light-yellow solution.[49] Four equivalents of K[Cp*IrH$_3$] reacted rapidly with UCl$_4$ or ThCl$_4$(DME)$_2$ in THF to form the uranium(IV) and thorium(IV) complexes U{(μ-H)$_3$IrCp*}$_4$ (**2.1**) and Th{[(μ-H)$_2$(H)IrCp*]$_2$[(μ-H)$_3$IrCp*]$_2$} (**2.2**), as orange and colorless crystals, respectively (Scheme 2.2). Both complexes are soluble in hydrocarbon solvents and crystallize from *n*-hexane as thin plates at −40 °C. Only one resonance, a sharp peak at 4.98 ppm, attributed to the Cp* protons, was detected in the ^{1}H NMR spectrum of **2.1** in C$_6$D$_6$. No additional resonances were observed within a range of 200 to −200 ppm. The ^{1}H NMR spectrum of diamagnetic species **2.2**, however, contains two resonances, one at 2.08 ppm corresponding to the Cp* protons, and a hydride resonance at –11.30 ppm, which integrate in a 15:3 ratio. This suggests the presence of three hydrides *per* Cp*Ir fragment and twelve hydrides total in **2**. The solution state IR spectra of **2.1** and **2.2** in C$_6$D$_6$ are nearly identical, each exhibiting an intense, broad bridging hydride stretch at 1951 cm^{-1} and 1962 cm^{-1}, respectively. These values are in excellent agreement with values reported for systems featuring a Cp*Ir(μ-H)$_3$ bridging motif, such as [Hf(CH$_2$^{t}Bu)$_3$(μ-H)$_3$IrCp*] (ν_{M-H} = 1982 cm^{-1}) and [Cp*Ir(μ-H)$_3${Ln(η^5-C$_5$Me$_4$SiMe$_3$)$_2$}] (Ln = Y, Dy, Lu; ν_{M-H} = 1990, 1988 and 1994 cm^{-1}, respectively).[40,51] Given the similarities in both the synthesis and spectroscopic data of **2.1** and **2.2**, as well as considering chemically reasonable reaction pathways and structures, twelve hydrides are assigned to complex **2.1** as well.

Scheme 2.2 Synthesis of compounds **2.1** and **2.2**.

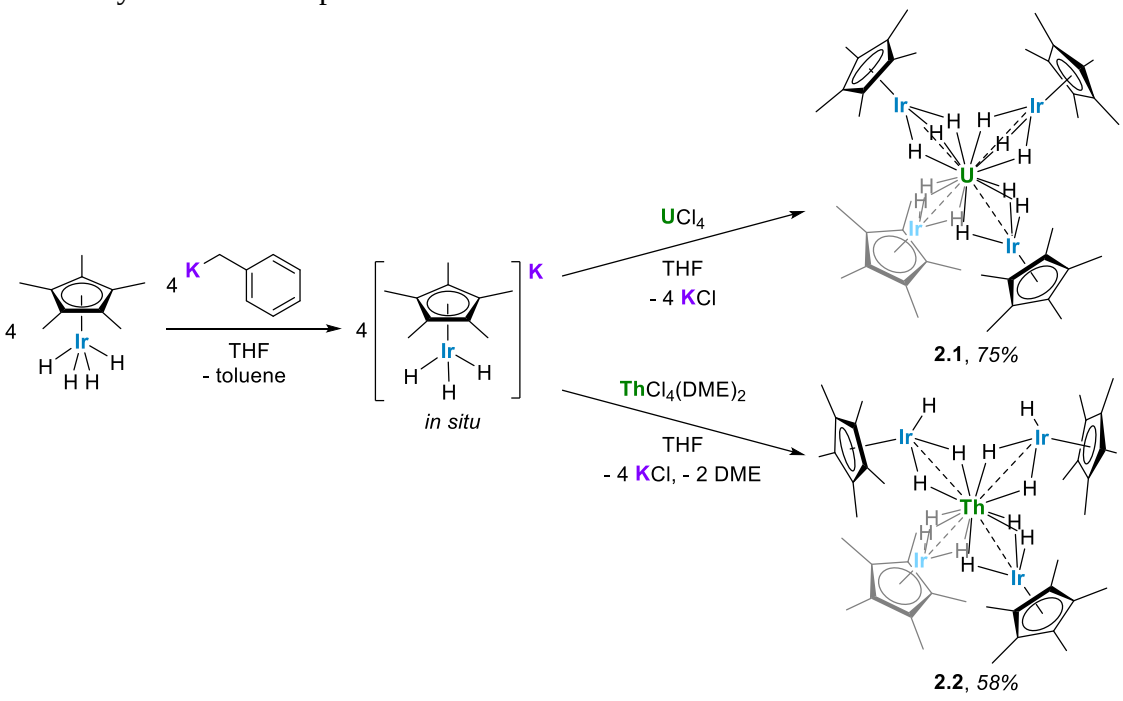

Single crystals of **2.1** and **2.2** suitable for X-ray diffraction were isolated from *n*-hexane at −40 °C, and their solid-state structures were determined accordingly (Figure 2.1). The uranium species **2.1** crystallizes in the space group *C*2/*c*, with two of the iridium centers generated through symmetry, and co-crystallizes with an equivalent of *n*-hexane. The thorium species **2.2** is also

monoclinic, crystallizing in the space group $P2_1/n$ with no solvent present in the lattice. Both species display a distorted tetrahedral geometry, albeit with greater distortion in the uranium species, as **2.1** has a τ_4 value of 0.87 (calculated with α, β = 118.94(1)°), while **2.2** has a significantly higher τ_4 value of 0.97 (calculated with α = 113.02(3)°, β = 109.77(4)°).[52] However, the most notable discrepancy in the solid-state structures of **2.1** and **2.2** involves the significant deviation from linearity in two of the Th–Ir–$Cp^*_{centroid}$ angles, a feature which is present in **2.2** but absent in **2.1**. The U–Ir–$Cp_{centroid}$ angles in **2.1** are all nearly linear at 174°. However, in **2.2** there are two nearly linear Th–Ir–$Cp_{centroid}$ angles of 172° and 173°, and two significantly bent angles of 126° and 129°. This suggests the presence of a terminal iridium-bound hydride in two iridate moieties in **2.2**, giving ten bridging and two terminal hydrides for this complex, as opposed to the twelve bridging hydrides in **2.1**. The discrepancy between the uranium and thorium species was unexpected and, to our knowledge, has not been reported in actinide polyhydride complexes, which are often isostructural between their uranium and thorium counterparts.[53–55] In addition, the close average An–Ir distances of 2.954(1) Å (**2.1**) and 2.993(1) Å (**2.2**) are well within the sum of covalent radii for U/Ir (3.37 Å) and Th/Ir (3.47 Å),[56] suggesting the possibility of An–Ir bonding interactions.

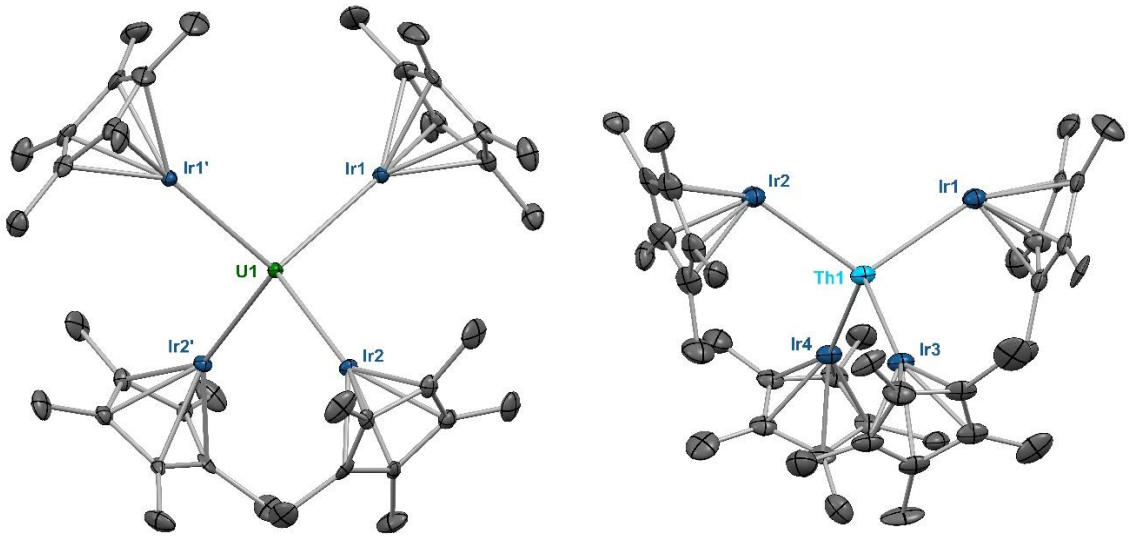

Figure 2.1 Solid-state molecular structures of **2.1** (left) and **2.2** (right). Ellipsoids are presented at the 50% probability level. Hydrogen atoms and co-crystallized solvent molecules have been omitted for clarity. Selected bond distances (Å) and angles (deg) for **2.1**: U1–Ir1 2.9508(5), U1–Ir2 2.9587(5), Ir1–U1–Ir2 106.40(1), Ir1–U1–Ir2 104.24(2), Ir1–U1–Ir2' 118.94(1). U1–Ir1–$Cp^*_{centroid}$ 173.61(1). Selected bond distances (Å) and angles (deg) for **2.2**: Th1–Ir1 2.9639(11), Th1–Ir2 2.9827(10), Th1–Ir3 3.0153(12), Th1–Ir4 3.0103(12), Ir1–Th1–Ir2 113.02(3), Ir3–Th1–Ir4 107.96(3), Ir1–Th1–Ir3 107.80(4), Ir1–Th1–$Cp^*_{centroid}$ 128.83(4), Ir3–Th1–$Cp^*_{centroid}$ 172.41(4).

The reactivity of the potassium iridate species was also investigated with a U(III) starting material. Three equivalents of $K[Cp^*IrH_3]$ reacted with $UI_3(1,4\text{-dioxane})_{1.5}$ in THF to form the octanuclear cluster $\{U[(\mu_2\text{-}H)_3IrCp^*]_2[(\mu_3\text{-}H)_2IrCp^*]\}_2$ (**2.3**), which was extracted into toluene before the removal of solvent *in vacuo* to afford a yellow-brown powder (Scheme 2.3). The solid-

state IR spectrum features a strong bridging hydride peak at 1951 cm^{-1}, identical to the peak found in **2.1**. This powder was sparingly soluble in benzene, allowing for the collection of ^{1}H and ^{13}C NMR spectra, but resisted all crystallization attempts from benzene or toluene. The limited solubility of **2.3** in aliphatic, aromatic, and ethereal solvents impeded attempts at recrystallization, and **2.3** reacted with halogenated solvents such as CCl_4, $CDCl_3$, and CD_2Cl_2 to form intractable mixtures, so an alternative synthetic route was explored. Layering of hexane solutions of $U(Terph)_3$ (Terph = 4,4″-di-*tert*-butyl-*m*-terphenyl-2′-yl)[57] and Cp^*IrH_4 at room temperature afforded yellow-black crystals of **2.3** after 18 h which were suitable for X-ray diffraction. These crystals were confirmed to match the powder afforded through the salt metathesis route, with increased purity, using NMR and IR spectroscopy in addition to elemental analysis (see experimental).

Scheme 2.3 Synthetic routes to **2.3**.

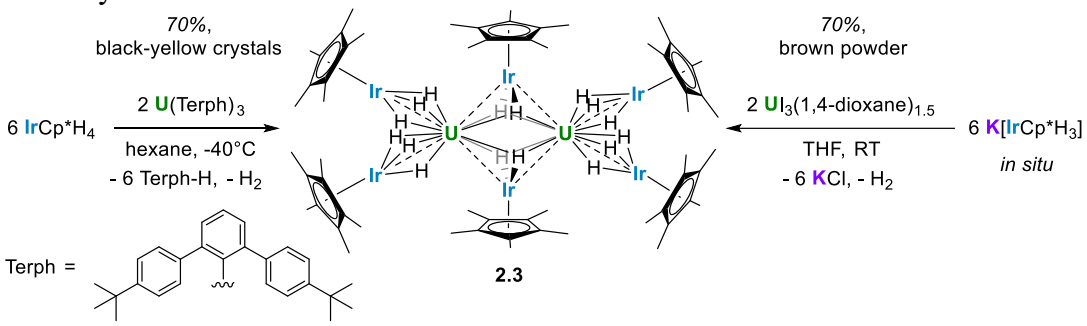

The X-ray crystal structure of **2.3** contains two molecules in the asymmetric unit, one in which the terminal IrCp* moieties are staggered, and one in which they are eclipsed, which will hereafter be referred to as **2.3s** and **2.3e** (Figure 2.2). For both conformations, half of the molecule is generated through symmetry. The terminal U–Ir distances in **2.3s** are slightly shorter, at 2.9653(3) Å and 2.9718(3) Å, than in **2.3e**, with distances of 2.9728(3) Å and 2.9899(3) Å. With a τ_4 value of 0.94 (α = 113.65(1)°, β = 113.47(1)°).), **3s** is also significantly more tetrahedral than **2.3e**, which has a τ_4 value of 0.89 (α = 120.85(1)°, β = 113.64(1)°).) These variations may be due to a slight reduction in steric stress between the Cp* rings in the eclipsed conformation, allowing both slightly closer U–Ir contacts and a more tetrahedral angle between the terminal IrCp* moieties. The central parallelogram formed by the U and bridging Ir centers features U–Ir distances of 2.8135(3) Å and 2.8406(3) Å in **2.3s** compared to 2.8266(3) Å and 2.8392(3) Å in **2.3e**. Compared to **2.1**, both **2.3s** and **2.3e** feature more tetrahedral coordination environments around their uranium centers, and have slightly elongated U–Ir distances, averaging 2.969 Å and 2.981 Å, respectively.

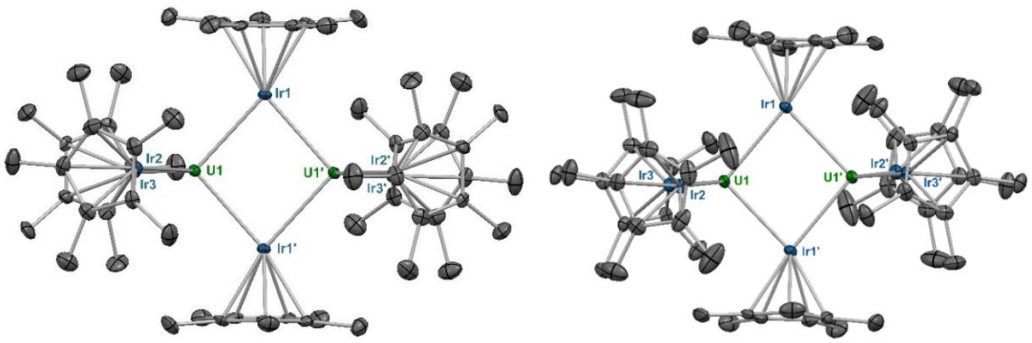

Figure 2.2 Solid-state molecular structures of **2.3s** (left) and **2.3e** (right). Ellipsoids are presented at the 50% probability level. Hydrogen atoms have been omitted for clarity. Selected distances (Å) and angles (deg) for **2.3s**: U1–Ir1 2.8135(3), U1–Ir2 2.9718(3), U1–Ir3 2.9653(3), U1–U1' 3.7945(4), Ir1–U1–Ir2 109.34(1), Ir1–U1–Ir1' 95.70(1), Ir2–U1–Ir3 113.47(1), U1–Ir2–Cp*$_{centroid}$ 175.55(1), Ir1'–Ir1–Cp*$_{centroid}$ 179.06(1). Selected bond distances (Å) and angles (deg) for **2.3e**: U1–Ir1 2.8392(3), U1–Ir2 2.9899(3), U1–Ir3 2.9728(3), U1–U1' 3.7819(4), Ir1–U1–Ir2 113.64(1), Ir1–U1–Ir1' 96.25(1), Ir2–U1–Ir3 120.85(1), U1–Ir2–Cp*$_{centroid}$ 177.89(1), Ir1'–Ir1–Cp*$_{centroid}$.

Although no hydrides could be located in the X-ray structure, it is proposed that each terminal U–Ir interaction features three μ_2-bridging hydrides, while each bridging U–Ir interaction features two μ_3-bridging hydrides centered around the iridium atoms Ir1 and Ir1'. This configuration balances the charge of two U(IV) cations with four $[Cp^*IrH_3]^-$ and two $[Cp^*IrH_2]^{2-}$ fragments. The formation of $[Cp^*IrH_2]^{2-}$ fragments bridging two metal centers has previous precedent with iridium–aluminum species.[49] A redox process involving the loss of one equivalent of H_2 for each molecule of **2.3** is required for this final product. Evidence of this formation of H_2 was confirmed by ^{1}H NMR monitoring of the protonolysis pathway.

In order to further probe the oxidation states of the actinide centers in **2.1** and **2.3**, variable temperature data on the magnetic moments of these compounds were obtained with a superconducting quantum interference device (SQUID). The tetrairidate complex **2.1** behaved as a typical monometallic U(IV) species (Figure 2.3, top),[58] with a room temperature magnetic moment (μ_{eff}) of 2.70μ_B which decreased to 0.47μ_B at 2 K. The behavior of the octametallic complex **2.3** is also consistent with U(IV) designations for the uranium oxidation state (Figure 2.3, bottom). These two metal centers contribute to its higher room temperature μ_{eff} of 3.61μ_B, but due to the singlet ground state at low temperature, the μ_{eff} still approaches zero with decreasing temperature, reaching 0.66μ_B at 2 K. UV-Vis spectra were collected for **2.1** and **2.3** as well, with increasing, featureless absorption from 550-300 nm. The broad bands characteristic of *f-d* transitions in U(III) are not observed, consistent with the assignment of **2.1** and **2.3** as U(IV) species.[59–61]

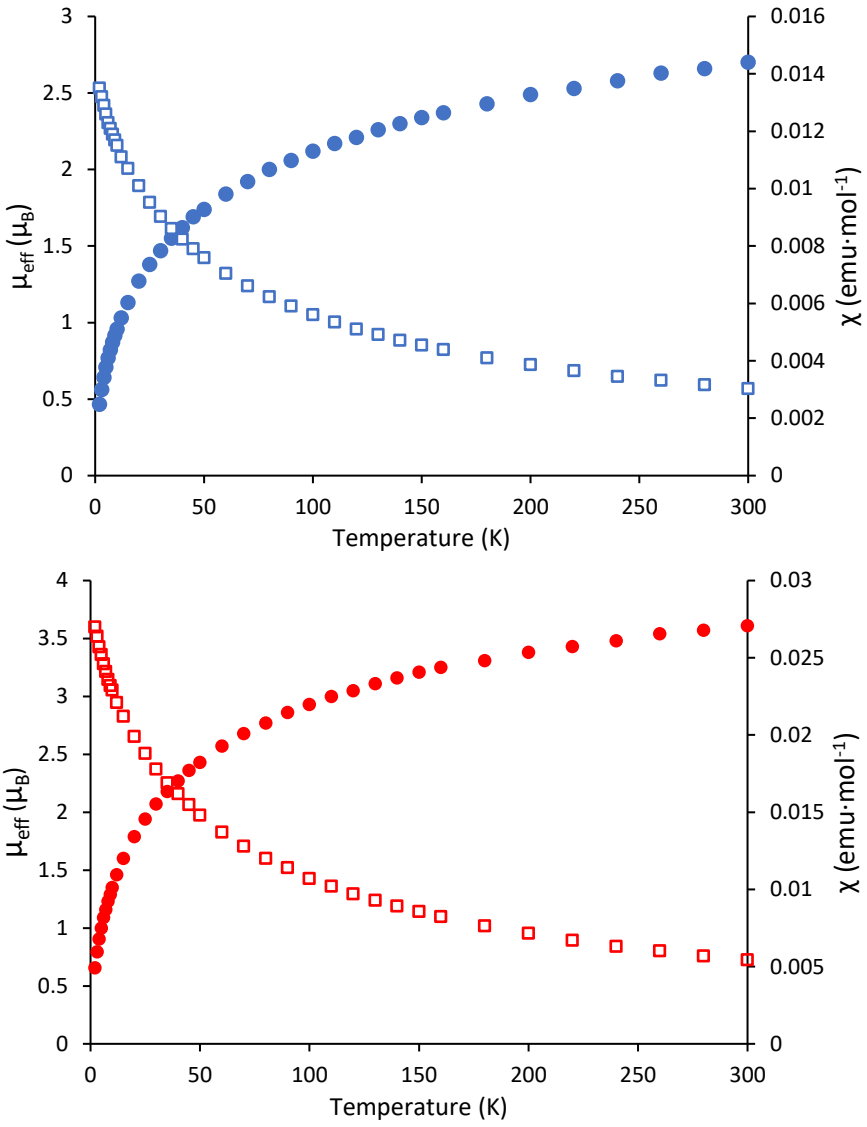

Figure 2.3 Temperature-dependent SQUID magnetization data (4 T) for **2.1** (blue) and **2.3** (red) plotted as μ_{eff} (filled circles) and χ (open squares) versus temperature. Data were corrected for diamagnetism.

Quantum chemical calculations were subsequently utilized to gain deeper insight into the structure and bonding of these systems, especially with regards to the level of metal–metal interactions, uranium oxidation state, and hydride quantity and geometry. All calculations were carried out at the B3PW91 level of theory, including dispersion corrections within the D3-BJ scheme (see experimental for details).

Given our interest in metal–metal bonding, the Natural Bonding Orbital (NBO) calculations of the Wiberg Bond Indices (WBIs) between U/Th and Ir in **2.1** and **2.2** are particularly intriguing. The WBI calculated between the U and Ir centers for **2.1** is 0.98, suggesting a high degree of covalency in the U–Ir interaction, and although the WBI found between Th and Ir in **2.2** is lower at 0.65, it is still quite significant and strongly implies a metal-metal bonding interaction. The WBI calculated for the U–Ir interaction in **2.1** is higher than the published WBIs of 0.8 for the U–Pt bonds in a U_2Pt_3 cluster,[22] as well as 0.720 and 0.625 for the U–TM bond in $IU^{IV}(\mu\text{-OAr}^{P}$-

$1\kappa^1O,2\kappa^1P)_3M^0$ (M = Ni, Pd).[19] The Ir–H WBIs are 0.53 in **2.1** and 0.57 in **2.2** while the An–H WBIs are 0.29 for U and 0.24 for Th. As expected, the Ir–H bond is more covalent than the An–H bond, but it is noteworthy that these M–H bonds are not affected by the nature of the actinide center. The bridging hydrides' interactions with the two metals are similar in complexes **2.1** and **2.2** and therefore do not explain the difference in An–Ir WBIs, but certainly account for the formation of such An–Ir bonds. These calculations suggest that these actinide iridate compounds contain hydride-supported actinide–iridium bonds. DFT analysis of the singly occupied molecular orbitals (SOMOs) of **2.1** revealed that these orbitals have contributions from uranium *f*-orbitals and iridium *d*-orbitals, with a 51:49 ratio between U and Ir, while the lowest unoccupied molecular orbital (LUMO) is an essentially non-bonding uranium f_{xyz} orbital (Figure 2.4). This contrasts with the f^0 species **2.2**, which has no signs of f-orbital participation in either the HOMO or LUMO.

These calculations also delivered greater insight into the oxidation states of the actinide centers in each compound, especially for the less-straightforward compound **2.3**. The computational results for compounds **2.1**-**2.3** suggest the +4 oxidation state is the most stable, and therefore plausible, configuration. For compound **2.1**, the triplet state (corresponding to U(IV)) is favorable over the singlet or quintet states by 30.3 and 41.0 kcal/mol, respectively. The dimer **2.3** favors the quintet state (corresponding to two U(IV) centers) over singlet and triplet states by 55.3 and 7.3 kcal/mol, respectively.

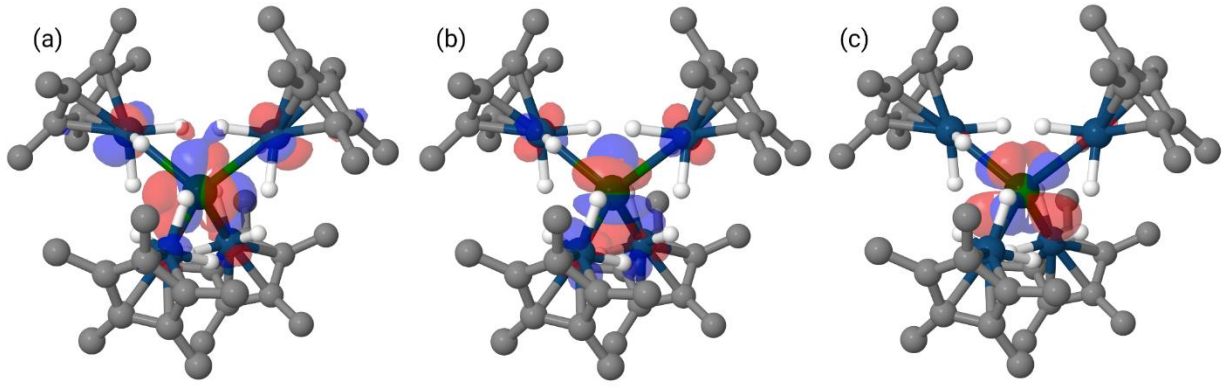

Figure 2.4 Renderings of the calculated SOMOs (a, b) and LUMO (c) of **2.1** (isovalue = 0.03).

Assuming an assignment of two U(IV) centers in **2.3**, charge-balancing would suggest the presence of four terminal $[Cp^*IrH_3]^-$ fragments and two bridging $[Cp^*IrH_2]^{2-}$ fragments. Given the linearity of the U–Ir–$Cp^*_{centroid}$ angle for the terminal fragments, it is most likely that the three hydrides bridge the U–Ir interaction. However, the location of the hydrides in the bridging fragments is far less clear, and was the subject of further computational study. An energy difference of 13.6 kcal/mol was calculated between the two found local minima, Geometries A and B, with Geometry A at the lower energy (Figure 2.5). In addition, accommodation of the U–Ir bridging hydrides in Geometry B requires a tilting of the Cp* moiety relative to the central U_2Ir_2 plane, a feature which is not observed in the X-ray crystal structure of **2.3**. However, the Cp* moieties in Geometry A are nearly perpendicular to the U_2Ir_2 plane, an excellent match to the experimentally determined structure.

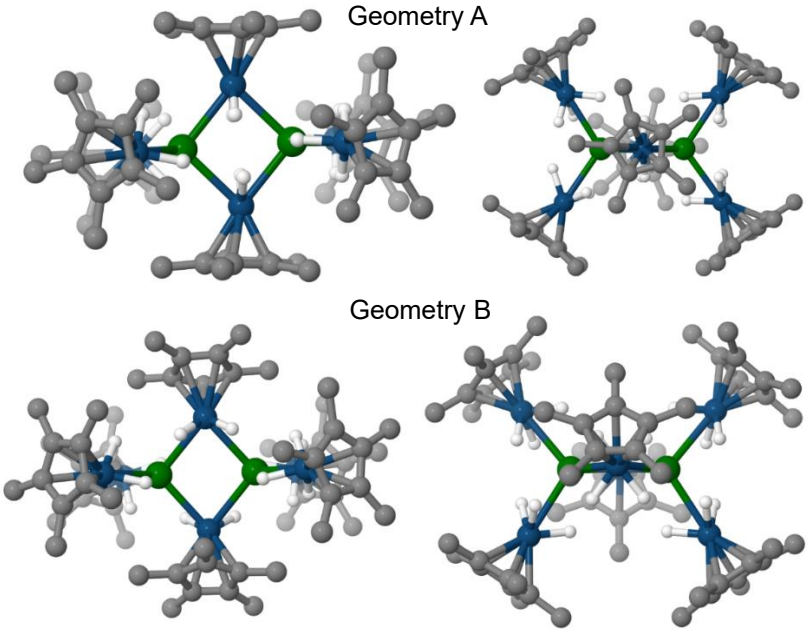

Figure 2.5 Calculated geometries for two local energy minima of **2.3**. The hydrides on the bridging $[Cp^*IrH_2]^{2-}$ fragments for Geometry A (top) are equidistant from the U atoms, and extend outward from the Ir atom so that the H–Ir–H bonds and Ir–U–Ir are nearly perpendicular. In Geometry B (bottom), the hydrides on the $[Cp^*IrH_2]^{2-}$ fragments bridge the Ir–U interactions on the same side of the U–Ir–U plane, resulting in significant deviation from planarity in the Ir–Cp* bond. Color key: green (uranium), blue (iridium), gray (carbon), white (hydrogen). Methyl hydrogens have been omitted for clarity.

Computations were also able to further elucidate the causes of the structural discrepancies between species **2.1** and **2.2**. Initial models without a dispersion correction found that the linear conformation was most stable for both **2.1** and **2.2**, with a difference of about 15-20 kcal/mol between the linear and bent conformations. After the inclusion of a dispersion correction (within the Grimme's correction scheme),[62] however, the linear conformation for **2.1** remained favorable by a small barrier of 4.0 kcal/mol, while the bent conformation for **2.2** was lower in energy than the linear conformation by 9.4 kcal/mol. This observation is in line with the in-depth study of the influence of London dispersion forces by Power.[63] Given the calculated energy difference for the two conformations of **2.2**, observation of the decoalescence of the terminal hydrides in the ^{1}H NMR spectrum at low temperatures was attempted, but no splitting of the NMR signal was observed down to a temperature of –80 °C. The difference in the preferred conformation for **2.1** and **2.2** can be partially explained by analysis of the WBIs, which suggest a greater loss in U–Ir bond order from bending in **2.1** (0.98 to 0.88) than to the Th–Ir bond order from bending in **2.2** (0.65 to 0.63). The bent conformation remains beneficial for **2.2** because of additional stability gained from dispersion interactions between the Cp* ligands, which are placed in closer proximity to one another. Compound **2.2** is therefore yet another example of a metal complex which is capable of isomerization in order to maximize dispersion interactions.[63] A similar stabilization is present in **2.1** but appears to be outweighed by the destabilization of bonding interactions between the U and Ir centers from bending.

Conclusions

In conclusion, a generalizable salt metathesis strategy involving a potassium iridate trihydride has been developed and utilized, resulting in a series of multimetallic uranium– and thorium–iridate complexes, all obtained in good yield. This strategy has utilized bridging hydrides to stabilize and enable the generation of the first reported actinide-iridium bonding interactions. These complexes display subtle differences in coordination number, which, based on computational analysis, arise from dispersion effects in the Cp* ligands. While both complexes gain stability from tilting of the Cp* ligands to increase dispersion interactions, only **2.1** experiences a significant decrease in An–TM interaction which makes this tilting unfavorable. Computational studies also indicate significant bonding character between U/Th and Ir in **2.1** and **2.2**, with *f*-orbital involvement in the SOMOs of **2.1** and no involvement, as expected, in the f^0 species **2.2**. Reactivity studies on H/D exchange and small molecule activation for these complexes are ongoing, as well as studies with other actinide halide starting materials and attempts to extend this synthetic strategy to other analogous metal polyhydrides.

Experimental Section

General considerations: Unless otherwise noted, all reactions were performed using standard Schlenk line techniques under an atmosphere of nitrogen or argon, or in an MBraun inert atmosphere glove box under an atmosphere of nitrogen. Glassware and Celite® were stored in an oven at ca. 150 °C for at least 3 h prior to use. Molecular sieves (4 Å) were activated by heating to 200 °C overnight under vacuum prior to storage in a glovebox. NMR spectra were recorded on Bruker AV-600 and AVB-400 spectrometers. ^{1}H chemical shifts are given relative to residual solvent peaks and are recorded in units of parts per million (ppm). FT-IR samples were prepared as Nujol mulls pressed between KBr plates or as solutions in C_6D_6 between KBr plates, with data collected with a Nicolet iS10 FT-IR spectrometer. Melting points were determined using sealed capillaries prepared under nitrogen on an OptiMelt automated melting point system. Elemental analyses were determined at the Microanalytical Facility at the College of Chemistry, University of California, Berkeley.

Materials: Toluene, *n*-hexane, and THF were purified by passage through columns of activated alumina and degassed by sparging with nitrogen. Deuterated solvents were degassed with three freeze-pump-thaw cycles and stored over molecular sieves. Benzylpotassium,[64] Cp*IrH$_4$,[65] UI$_3$(1,4-dioxane)$_{1.5}$,[66] UCl$_4$,[67] and ThCl$_4$(DME)$_2$[68] were synthesized according to literature procedures. All other chemicals were purchased from commercial sources and used as received.

Synthesis of U{(μ-H)$_3$IrCp*}$_4$ (2.1): Cp*IrH$_4$ (68.7 mg, 0.207 mmol, 4.0 equiv.) and benzyl potassium (28.5 mg, 0.219 mmol, 4.2 equiv.) were added to a 20 mL scintillation vial with THF (2 mL) to generate a solution of K[Cp*IrH$_3$]. UCl$_4$ (19.7 mg, 0.052 mmol, 1.0 equiv.) was dissolved in THF (2 mL) and added to the K[Cp*IrH$_3$] solution. The solution quickly turned orange and slightly opaque as KCl precipitated out of solution. After stirring at room temperature for 2.5 h, the solvent was removed *in vacuo*. The crude solid was then triturated with *n*-hexane and the product was extracted with *n*-hexane (5 mL), filtered through Celite, and concentrated (ca. 1.5 mL). The resulting orange solution was cooled to -40 °C overnight, affording thin orange plates (60.8 mg, 75% yield). X-ray quality crystals were grown by recrystallization of **1** in *n*-hexane at -

40 °C. Mp ca. 226 °C (decomp.); ^{1}H NMR (400 MHz, C_6D_6): δ 4.98 (s, 60H, CH_3), no hydride resonances were found within the range 200 ppm to -200 ppm; ^{13}C NMR (600 MHz, C_6D_6): δ 113.97 ($C_5(CH_3)_5$), 7.04 ($C_5(CH_3)_5$); IR (Nujol mull on KBr): 2144 (m), 2017 (m), 1951 (s), 1072 (m), 1029 (m), 856 (w), 802 (m), 615 (w), 585 (w), 561 (w), 530 (w); IR (solution in C_6D_6, solvent subtracted): 2979 (w), 2957 (w), 2902 (m), 2850 (w), 1955 (s), 1476 (w), 1381 (m), 1073 (w), 1033 (m) cm^{-1}. Anal. Calcd (%) for $UIr_4C_{40}H_{72}$: C, 30.80; H, 4.65. Found: C, 30.92; H, 4.67.

Th{[(μ-H)$_2$(H)IrCp*]$_2$[(μ-H)$_3$IrCp*]$_2$} (2.2). Cp*IrH$_4$ (71.1 mg, 0.214 mmol, 4.0 equiv.) and benzyl potassium (28.3 mg, 0.217 mmol, 4.0 equiv.) were added to a 20 mL scintillation vial with THF (2 mL) to generate a solution of K[Cp*IrH$_3$]. $ThCl_4(DME)_2$ (29.8 mg, 0.054 mmol, 1.0 equiv.) was dissolved in THF (2 mL) and added to the K[Cp*IrH$_3$] solution. The solution quickly turned pale yellow and slightly opaque as KCl precipitated out of solution. After stirring at room temperature for 2 h, the solvent was removed *in vacuo*. The crude solid was then triturated with *n*-hexane and the product was extracted with *n*-hexane (5 mL), filtered through Celite, and concentrated (ca. 1.5 mL). The resulting pale-yellow solution was cooled to -40 °C overnight, affording thin colorless plates (48.7 mg, 58% yield). X-ray quality crystals were grown by recrystallization of **2** in *n*-hexane at -40 °C. Mp ca. 171 °C (decomp.); ^{1}H NMR (600 MHz, C_6D_6): δ 2.08 (s, 60H, CH_3), -11.31 (s, 12H, Th–H–Ir); ^{13}C NMR (600 MHz, C_6D_6): δ 90.45 ($C_5(CH_3)_5$), 11.57 ($C_5(CH_3)_5$); IR (Nujol mull on KBr): 2138 (m), 2026 (m), 1962 (s), 1072 (m), 1029 (m), 860 (w), 810 (m), 616 (w), 565 (w), 531 (w), 501 (w); IR (solution in C_6D_6, solvent subtracted): 2979 (w), 2958 (w), 2902 (m), 2849 (w), 1962 (s), 1475 (w), 1381 (m), 1073 (w), 1033 (m) cm^{-1}. Anal. Calcd (%) for $ThIr_4C_{40}H_{72}$ (**2**): C, 30.92; H, 4.67. Found: C, 30.87; H, 4.59.

{U[(μ$_2$-H)$_3$IrCp*]$_2$[(μ$_3$-H)$_2$IrCp*]}$_2$ (2.3):
Method A: Cp*IrH$_4$ (48.0 mg, 0.145 mmol, 6.0 equiv.) and U(Terph)$_3$ (61.3 mg, 0.049 mmol, 2.0 equiv.) (Terph = C_6H_3-2,6-(C_6H_4-4-^{t}Bu)$_2$) were dissolved in separate 20 mL scintillation vials in *n*-hexane (2 mL and 6 mL, respectively). Both solutions were cooled to –40 °C, then the solution of Cp*IrH$_4$ was added to the solution of U(Terph)$_3$. The resulting black-yellow solution afforded black-yellow crystals of **2.3** (41.9 mg, 70% yield) after 18 h, which were rinsed with 2 × 2 mL *n*-hexane to remove any crystallized Terph–H. X-ray quality crystals were grown in a similar fashion at room temperature. Mp ca. 327 °C (decomp.); ^{1}H NMR (600 MHz, C_6D_6): δ 3.38 (s, 60H, CH_3 ($Cp^*Ir_{terminal}$)), –0.11 (s, 30H, CH_3 ($Cp^*Ir_{bridging}$)); ^{13}C NMR (600 MHz, C_6D_6): δ 112.63 ($U_2Ir(C_5(CH_3)_5)$), 105.44 ($Ir(C_5(CH_3)_5)$), 5.08 ($C_5(CH_3)_5$); IR (Nujol mull on KBr): 1951 (s), 1071 (w), 1031 (m), 793 (w), 628 (w), 585 (w) cm^{-1}. Anal. Calcd (%) for $U_2Ir_6C_{60}H_{106}$ (**3**): C, 29.33; H, 4.35. Found: C, 29.60; H, 4.39.

Method B: Cp*IrH$_4$ (19.9 mg, 0.060 mmol, 6.0 equiv.) and benzyl potassium (8.1 mg, 0.062 mmol, 6.2 equiv.) were added to a 20 mL scintillation vial with THF (2 mL) to generate a solution of K[Cp*IrH$_3$]. $UI_3(THF)_4$ (18.2 mg, 0.020 mmol, 2.0 equiv.) was dissolved in THF (2 mL) and added to the K[Cp*IrH$_3$] solution. The solution quickly turned cloudy yellow-brown and slightly opaque as KI precipitated out of solution. After stirring at room temperature for 1 h, the solvent was removed *in vacuo*. The crude solid was extracted in toluene, filtered through Celite, and dried *in vacuo*, affording **2.3** as a yellow-brown powder (17.1 mg, 70% yield). A slight impurity was detectible in the IR spectrum, corresponding to the peak at 2159 cm^{-1}; this peak is detectable but much smaller in the IR spectrum from Method A. ^{1}H NMR (400 MHz, C_6D_6): δ 3.35 (s, 60H, CH_3

($Cp^*Ir_{terminal}$)), –0.10 (s, 30H, CH_3 ($Cp^*Ir_{bridging}$)); IR (Nujol mull on KBr): 2159 (m), 1956 (s), 1071 (w), 1032 (m), 813 (m), 564 (w) cm^{-1}. Anal. Calcd (%) for $U_2Ir_6C_{60}H_{106}$ (**3**): C, 29.33; H, 4.35. Found: C, 29.49; H, 3.96.

H_2 Monitoring in the Synthesis of 2.3: Cp^*IrH_4 (13.7 mg) and $U(Terph)_3$ (17.3 mg) were each dissolved in 0.75 mL C_6D_6. The solution of Cp^*IrH_4 was added to a J. Young NMR tube, followed by a buffer layer of 0.5 mL C_6D_6, with the $U(Terph)_3$ solution layered on top of that. The remaining headspace of the tube was filled with C_6D_6, after which the tube was sealed, inverted 10 times, and then allowed to sit for 20 minutes before the ^1H NMR spectrum was measured.

SQUID magnetism measurements

Samples of **2.1** (7.1 mg) and **2.3** (5.4 mg) were loaded into 3 mm (O.D.) quartz tubes and sandwiched between two pieces of quartz wool (**2.1**, 4.1 mg; **2.3**, 6.3 mg) by a modified literature procedure.[69–71] Outside the glovebox, a pre-weighed amount of quartz wool, which had previously been leeched with oxalic and hydrochloric acid, was inserted and packed into a quartz tube with quartz rods. Afterwards, the tubes were oven-dried for 24 h at 150 ° C. Inside a glovebox, two 0.075" (O.D.) polyimide liners were placed inside both ends of the tube. A vacuum was applied to one end, such that no quartz wool was pushed out; the other end was used to vacuum sample into tube landing onto the quartz wool without touching the sidewalls. The polyimide liners were removed, and a second piece of quartz wool was inserted into the tube on top of the compound. The sample was compressed into a pellet with two quartz rods. The ends of the tube were capped with two 5 mm NMR tube rubber septa. The capped tubes were removed from the glovebox and surveyed for any contamination. The center of the tube was wrapped with a piece of open-cell foam, saturated with liquid nitrogen, and the ends were flame-sealed with a propane/oxygen torch. Variable temperature magnetization data were recorded from 2–300 K at 1, 2, and 4 T with a 7 T Quantum Design MPMS magnetometer utilizing a superconducting quantum interference device (SQUID) at Lawrence Berkeley National Lab. Molar susceptibility, χ_m, was calculated using the formula:

$$\chi_m = \frac{MW}{m}\left[\frac{M_{meas} - M_{imp}}{H} - \chi_{QW}\right] - \chi_d$$

Where MW is the molecular weight of the sample; m is the mass of the sample; M_{meas} is the measured magnetization; M_{imp} is the magnetization due to an assumed ferromagnetic impurity; H is the applied field; and χ_{QW} as well as χ_d are the diamagnetic corrections due to the quartz wool and the sample, respectively, calculated from Pascal's constants.[72] The different applied fields were chosen to saturate M_{imp} so that it's field dependence could be treated as a constant. The value of M_{imp} was allowed to vary to minimize the least squares difference of $\chi_m \cdot T$ between the measured fields from 100−300 K.

X-ray crystallographic details

In a dry nitrogen glovebox, samples of single crystals of **2.1**, **2.2**, and **2.3** were coated in Paratone-N oil prior to transport to diffraction facilities, where they were evaluated by polarized light microscopy and mounted on a Kaptan loop (for **2.1** and **2.3**) or on a MiTeGen 10 μm aperture DualThickness MicroMount (for **2.2**). X-ray diffraction data for **2.1** and **2.3** were collected at CheXray, Berkeley, CA, using a Rigaku XtaLAB P200 equipped with a MicroMax-007 HF

microfocus rotating anode and a Pilatus 200K hybrid pixel array; data for these samples were collected using Mo Kα radiation (λ = 0.71073 Å). X-ray diffraction data for **2.2** were collected at the Advanced Light Source (ALS), Lawrence Berkeley National Lab, Berkeley, CA, station 12.2.1 using a silicon monochromated beam of 17 keV (λ = 0.7288 Å) synchrotron radiation. All data collections were conducted at 100 K, with the crystals cooled by a stream of dry nitrogen. For **2.2**, Bruker APEX3 software was used for the data collections, Bruker SAINT V8.37A or V8.38A software was used to conduct the cell refinement and data reduction procedures, and absorption corrections were carried out by a multi-scan method utilizing the SADABS program. For, **2.1** and **2.3**, CrysAlisPro was used for the data collections and data processing, including a multiscan absorption correction applied using the SCALE3 ABSPACK scaling algorithm within CrysAlisPro. Initial structure solutions were found using direct methods (SHELXT), and refinements were carried out using SHELXL-2014. Thermal parameters for all non-hydrogen atoms were refined anisotropically. Thermal ellipsoid plots were made using Mercury. All structures have been deposited to the Cambridge Crystallographic Data Centre (CCDC), with deposition numbers 2204155 (**2.1**), 2204156 (**2.2**), and 2204157 (**2.3**).

Table 2.1 Crystallographic details for compounds **2.1**-**2.3**. *Hydrides are not observed, and are therefore not included in the empirical formulas.

Compound	**2.1**	**2.2**	**2.3**
Empirical formula*	$C_{46}H_{74}Ir_4U$	$C_{40}H_{60}Ir_4Th$	$C_{60}H_{90}Ir_6U_2$
Formula weight	1633.88	1541.72	2440.57
Temperature/K	100(2)	100(2)	100(2)
Crystal system	monoclinic	monoclinic	triclinic
Space group	C2/c	$P2_1/n$	P-1
a/Å	14.8239(6)	13.6424(17)	12.0833(2)
b/Å	21.1789(6)	19.070(2)	15.2848(2)
c/Å	17.2427(8)	17.520(2)	18.5723(3)
α/°	90	90	93.815(1)
β/°	107.318(5)	102.339(6)	98.607(1)
γ/°	90	90	93.365(1)
Volume/Å^3	5168.0(4)	4452.8(10)	3375.78(9)
Z	4	4	2
ρ_{calc}g/cm^3	2.100	2.300	2.401
μ/mm^{-1}	13.411	16.233	16.586
F(000)	3000.0	2792.0	2192.0
Crystal size/mm^3	0.3 × 0.08 × 0.08	0.12 × 0.12 × 0.005	0.20 × 0.10 × 0.08
Radiation	Mo Kα (λ = 0.71073)	synchrotron (λ = 0.7288)	Mo Kα (λ = 0.71073)
2Θ range for data collection/°	3.195 to 29.673	3.278 to 27.097	3.007 to 26.370
Index ranges	$-18 \le h \le 18$, $-26 \le k \le 26$, $-21 \le l \le 21$	$-17 \le h \le 16$, $0 \le k \le 23$, $0 \le l \le 21$	$-15 \le h \le 15$, $-19 \le k \le 18$, $-23 \le l \le 23$
Reflections collected	31322	9167	69850
Independent reflections	5280 [R_{int} = 0.0472]	9167 [R_{int} = 0.0518]	13763 [R_{int} = 0.0518]
Data/restraints/parameters	5280 / 48 / 290	9167 / 150 / 427	13763 / 0 / 643
Goodness-of-fit on F^2	1.389	1.037	1.015
Final R indexes [I>=2σ (I)]	R_1 = 0.0376, wR_2 = 0.0949	R_1 = 0.0625, wR_2 = 0.1430	R_1 = 0.0243, wR_2 = 0.0579
Final R indexes [all data]	R_1 = 0.0400, wR_2 = 0.0956	R_1 = 0.1052, wR_2 = 0.1750	R_1 = 0.0297, wR_2 = 0.596
Largest diff. peak/hole / e Å^{-3}	1.36/–2.04	3.44/–3.01	2.723/–1.262
CSD entry	2204155	2204155	2204155

Computational Details

All DFT calculations were carried out with the Gaussian 09 suite of programs.[73] Geometries were fully optimized in gas phase without symmetry constraints, employing the B3PW91 functional.[74,75] The nature of the extrema was verified by analytical frequency calculations. The calculation of electronic energies and enthalpies of the extrema of the potential energy surface (minima and transition states) were performed at the same level of theory as the geometry optimizations. IRC calculations were performed to confirm the connections of the optimized transition states. Uranium, thorium, and iridium atoms were treated with a small core effective core potential (60 MWB), associated with its adapted basis set[76–78] augmented for iridium atoms with a polarization function (ζf = 0.938).[79] For the other elements (H, C and N), Pople's double-ζ basis set 6-31G(d,p) was used.[80–82] Dispersion corrections were treated with the D3 version of Grimme's dispersion

with Becke-Johnson damping.[62] The electronic charges (at the DFT level) were computed using the natural population analysis (NPA) technique.[83]

Table 2.2 Calculated and experimental bond distances and angles for complex **2.1**.

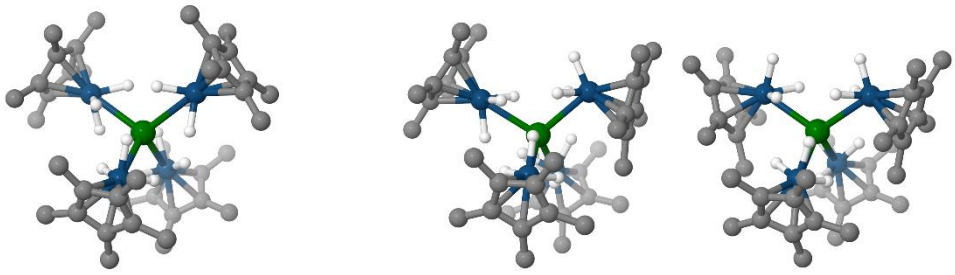

	Linear				1-Bent		2-Bent	
Multiplicity	singlet	triplet	triplet (disp)	quintet	triplet	triplet (disp)	triplet	triplet (disp)
$\Delta_r G$ (kcal/mol)	30.3	0.0	0.0	41.0	10.3	6.8	18.2	4.0
Ir–H dist. (Å)	[1.623–1.629]	[1.625–1.628]	[1.624–1.629]	[1.578–1.655]	1.583 [1.618–1.629]	1.584 [1.616–1.629]	[1.581–1.582] [1.615–1.627]	[1.582–1.583] [1.617–1.626]
U–H dist. (Å)	[2.339–2.365]	[2.353–2.467]	[2.326–2.350]	[2.387–2.735]	[2.342–2.398] 3.569	[2.319–2.406] 3.641	[2.352–2.390] [3.436–3.487]	[2.325–2.414] [3.607–3.617]
U–Ir dist. (Å)	2.941/2.941 2.940/2.942	2.954/2.956 2.951/2.952	2.905/2.907 2.912/2.913	3.032/3.033 3.056/3.175	2.921/2.934 2.961/2.964	2.849/2.891 2.920/2.922	2.901/2.903 2.973/2.973	2.828/2.831 2.930/2.932
Ir–U–Ir angle (°)	[108.0–111.5]	[108.8–110.4]	[106.8–111.4]	[109.6–116.7]	[108.6–110.7]	[106.9–112.8]	[107.1–110.8]	[107.6–113.5]

Table 2.3 Calculated NBO Wiberg Bond Indices for complex **2.1**.

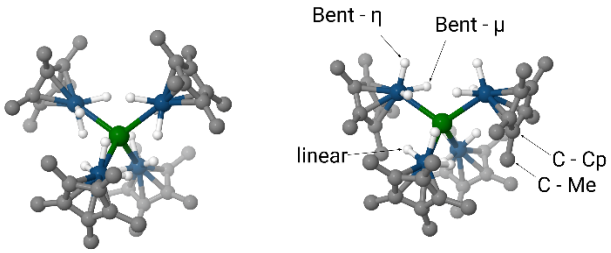

	Linear		2 - Bent	
	With disp	Without disp	With disp	Without disp
U – Ir	[0.96 - 0.98]	[0.94 - 0.95]	0.79 (linear) 0.88 (bent)	0.69 (linear) 0.78 (bent)
Ir – H	0.53	0.55	0.55 (linear) 0.56 (bent – μ) 0.70 (bent - η)	0.57 (linear) 0.56 (bent – μ) 0.70 (bent - η)
U – H	[0.28 – 0.30]	[0.27 - 0.29]	0.27 (linear) 0.25 (bent – μ) 0.04 (bent - η)	0.27 (linear) 0.26 (bent – μ) 0.051 (bent - η)
C(Cp*) – U	–	–	0.08 (C – Cp) 0.01 (C – Me)	0.07 (C – Cp) 0.00 (C – Me)

Table 2.4 Tabulated calculated bond distances/angles for complex **2.2**.

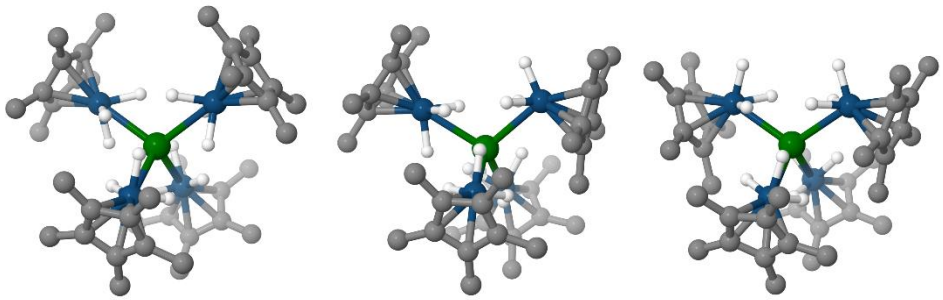

	Linear		1-Bent		2-Bent	
Multiplicity	singlet	singlet (disp)	singlet	singlet (disp)	singlet	singlet (disp)
$\Delta_r G$ (kcal/mol)	0.0	0.0	8.5	–4.3	16.4	–9.4
Ir–H dist. (Å)	[1.624–1.625]	[1.623–1.625]	1.583 [1.618–1.629]	1.584 [1.616–1.629]	[1.581–1.582] [1.615–1.627]	[1.582–1.583] [1.617–1.626]
Th–H dist. (Å)	[2.426–2.440]	[2.404–2.420]	[2.342–2.398] 3.569	[2.319–2.406] 3.641	[2.352–2.390] [3.436–3.487]	[2.325–2.414] [3.607–3.617]
Th–Ir dist. (Å)	3.022/3.022 3.022/3.022	2.978/2.978 2.979/2.979	2.984/3.005 3.024/3.036	2.916/2.964 2.985/2.988	2.964/2.970 3.036/3.047	2.899/2.902 2.995/2.999
Ir–Th–Ir angle (°)	[109.0–110.1]	[108.8–110.3]	[107.9–111.3]	[107.6–112.8]	[108.3–111.1]	[107.5–114.4]

Table 2.5 Calculated NBO Wiberg Bond Indexes for complex **2.2**.

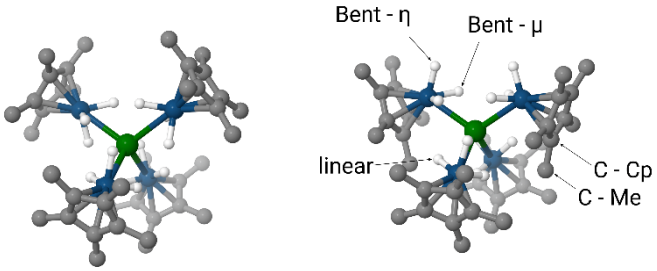

	Linear		2 - Bent	
	With disp	Without disp	With disp	Without disp
Th – Ir	0.65	0.63	0.63 (linear) 0.65 (Bent)	0.60 (linear) 0.69 (Bent)
Ir – H	0.56	0.57	0.57 (linear) 0.58 (Bent – μ) 0.70 (Bent - η)	0.59 (linear) 0.59 (Bent – μ) 0.70 (Bent - η)
Th – H	0.27	0.26	0.25 (linear) 0.24 (Bent – μ) 0.05 (Bent - η)	0.24 (linear) 0.24 (Bent – μ) 0.05 (Bent - η)
C(Cp*) – Th	–	–	0.10 (C – Cp) 0.04 (C – Me)	0.08 (C – Cp) 0.00 (C – Me)

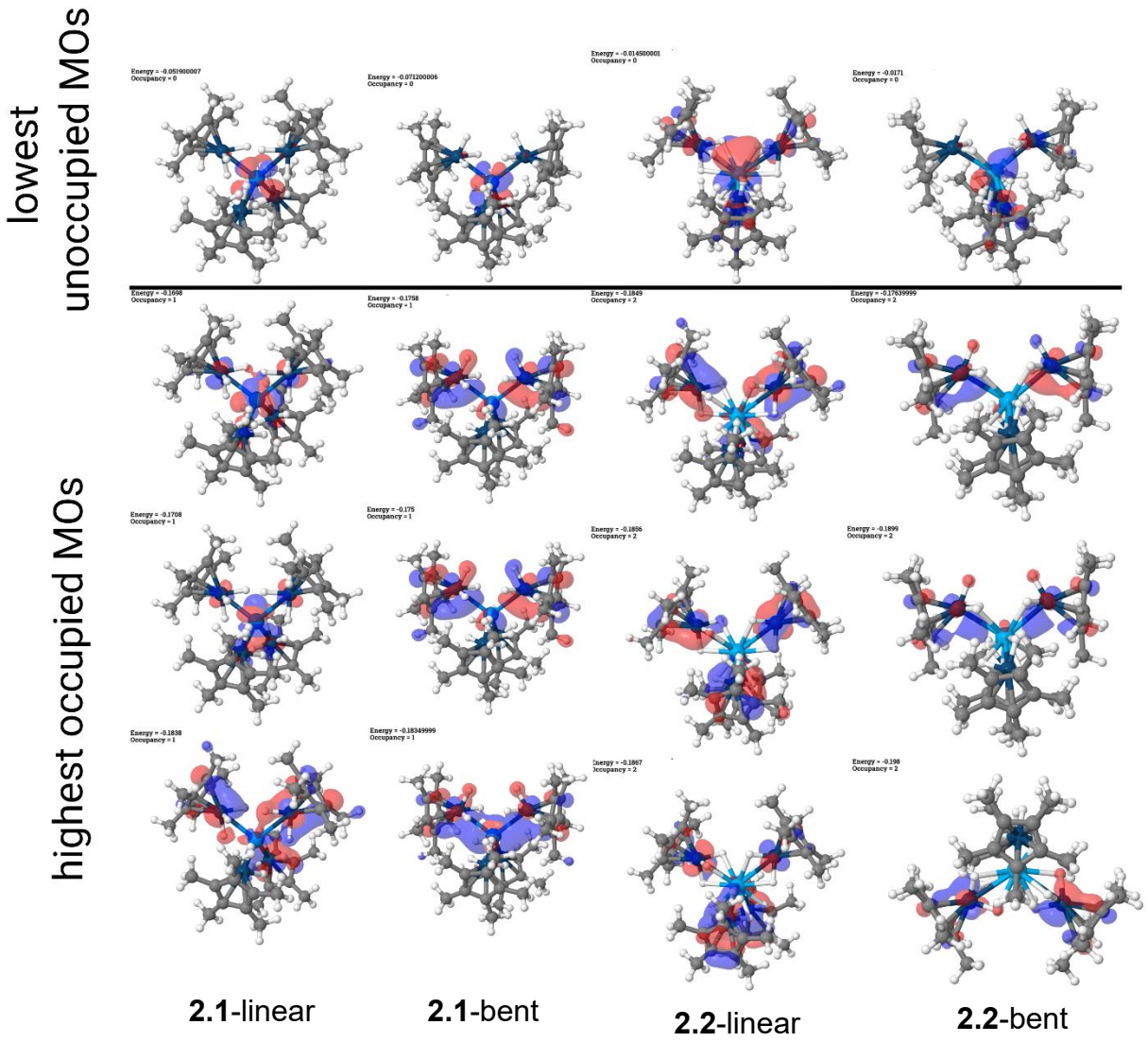

Figure 2.6 Renderings of the calculated HOMOs (**2.2**) or SOMOs (**2.1**), and LUMO of linear and bent structures of **2.1** and **2.2** (isovalue = 0.03).

Table 2.6 Calculated NBO Wiberg Bond Indexes for **2.3**.

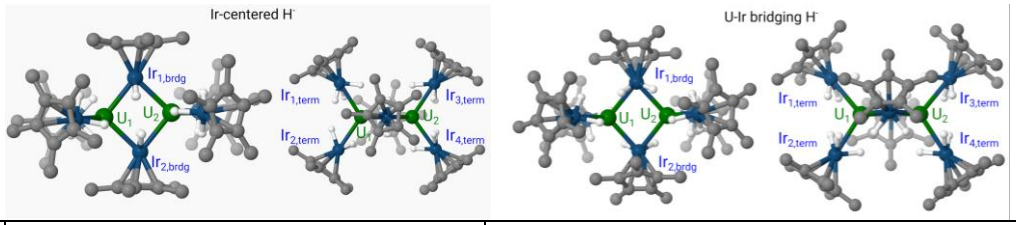

	Ir-centered H^-	U–Ir bridging H^-
Multiplicity	quintet	quintet
Ir_{brdg}–H_{brdg}	0.47	0.54
Ir_{brdg}–C(Cp)	[0.18-0.30]	[0.18-0.30]
Ir_{term}–H_{term}	0.58	[0.57-0.59]
Ir_{term}–C(Cp)	[0.32-0.35]	[0.32-0.35]
U_1–H_{brdg}	0.17 (H-$Ir_{1,brdg}$) / 0.20 (H-$Ir_{2,brdg}$)	0.24 / 0.04 (H-$Ir_{1,brdg}$) / 0.24 / 0.05 (H-$Ir_{2,brdg}$)
U_2–H_{brdg}	0.19 (H-$Ir_{1,brdg}$) / 0.22 (H-$Ir_{2,brdg}$)	0.22 / 0.04 (H-$Ir_{1,brdg}$) / 0.23 / 0.03 (H-$Ir_{2,brdg}$)
U_1–H_{term}	[0.23-0.25]	[0.23-0.25]
U_2–H_{term}	[0.24-0.26]	[0.24-0.25]
U–$Ir_{1,brdg}$	0.85 (U_1) / 0.83 (U_2)	0.88 (U_1) / 0.84 (U_2)
U–$Ir_{2,brdg}$	0.83 (U_1) / 0.85 (U_2)	0.84 (U_1) / 0.89 (U_2)
U_1–Ir_{term}	0.64 ($Ir_{1,term}$) / 0.66 ($Ir_{2,term}$)	0.X ($Ir_{1,term}$) / 0.X ($Ir_{2,term}$)
U_2–Ir_{term}	0.65 ($Ir_{3,term}$) / 0.65 ($Ir_{4,term}$)	0.X ($Ir_{3,term}$) / 0.X ($Ir_{4,term}$)
U_1–U_2	0.26	0.36
$Ir_{1,brdg}$–$Ir_{2,brdg}$	0.03	0.03

References

(1) Sternal, R. S.; Brock, C. P.; Marks, T. J. Metal-Metal Bonds Involving Actinides. Synthesis and Characterization of a Complex Having an Unsupported Actinide to Transition Metal Bond. *J. Am. Chem. Soc.* **1985**, *107* (26), 8270–8272. https://doi.org/10.1021/ja00312a081.

(2) Ritchey, J. M.; Zozulin, A. J.; Wrobleski, D. A.; Ryan, R. R.; Wasserman, H. J.; Moody, D. C.; Paine, R. T. An Organothorium-Nickel Phosphido Complex with a Short Thorium-Nickel Distance. The Structure of Th(η^5-C_5Me_5)$_2$(μ-PPh_2)$_2$Ni(CO)$_2$. *J. Am. Chem. Soc.* **1985**, *107* (2), 501–503. https://doi.org/10.1021/ja00288a039.

(3) Hay, P. J.; Ryan, R. R.; Salazar, K. V.; Wrobleski, D. A.; Sattelberger, A. P. Synthesis and X-Ray Structure of (C_5Me_5)$_2$Th(μ-PPh_2)$_2$Pt(PMe_3): A Complex with a Thorium-Platinum Bond. *J. Am. Chem. Soc.* **1986**, *108* (2), 313–315. https://doi.org/10.1021/ja00262a031.

(4) Oelkers, B.; Butovskii, M. V.; Kempe, R. F-Element–Metal Bonding and the Use of the Bond Polarity to Build Molecular Intermetalloids. *Chem.─Eur. J.* **2012**, *18* (43), 13566–13579. https://doi.org/10.1002/chem.201200783.

(5) Oelkers, B.; Kempe, R. Group 3, Lanthanide, and Actinide Metal–Metal Bonds. In *Molecular Metal-Metal Bonds*; John Wiley & Sons, Ltd, 2015; pp 47–71. https://doi.org/10.1002/9783527673353.ch3.

(6) Weydert, M.; Andersen, R. A.; Bergman, R. G. Reactions of Uranium Complex (MeC_5H_4)$_3$U(*t*-Bu): Intermolecular Fluorine Atom Abstraction from Fluorocarbons Including Saturated Perfluorocarbons. *J. Am. Chem. Soc.* **1993**, *115* (19), 8837–8838. https://doi.org/10.1021/ja00072a046.

(7) Clark, C. L.; Lockhart, J. J.; Fanwick, P. E.; Bart, S. C. Synthesis of Low-Valent Uranium Fluorides by C–F Bond Activation. *Chem. Commun.* **2015**, *51* (74), 14084–14087. https://doi.org/10.1039/C5CC05049A.
(8) Thomson, R. K.; Cantat, T.; Scott, B. L.; Morris, D. E.; Batista, E. R.; Kiplinger, J. L. Uranium Azide Photolysis Results in C–H Bond Activation and Provides Evidence for a Terminal Uranium Nitride. *Nat. Chem.* **2010**, *2* (9), 723–729. https://doi.org/10.1038/nchem.705.
(9) Palumbo, C. T.; Scopelliti, R.; Zivkovic, I.; Mazzanti, M. C–H Bond Activation by an Isolated Dinuclear U(III)/U(IV) Nitride. *J. Am. Chem. Soc.* **2020**, *142* (6), 3149–3157. https://doi.org/10.1021/jacs.9b12804.
(10) Boreen, M. A.; Ye, C. Z.; Kerridge, A.; McCabe, K. N.; Skeel, B. A.; Maron, L.; Arnold, J. Does Reduction-Induced Isomerization of a Uranium(III) Aryl Complex Proceed via C–H Oxidative Addition and Reductive Elimination across the Uranium(II/IV) Redox Couple? *Inorg. Chem.* **2022**, *61* (23), 8955–8965. https://doi.org/10.1021/acs.inorgchem.2c01563.
(11) Camp, C.; Kefalidis, C. E.; Pécaut, J.; Maron, L.; Mazzanti, M. Controlled Thermolysis of Uranium (Alkoxy)Siloxy Complexes: A Route to Polymetallic Complexes of Low-Valent Uranium. *Angew. Chem., Int. Ed.* **2013**, *52* (48), 12646–12650. https://doi.org/10.1002/anie.201307291.
(12) Mansell, S. M.; Kaltsoyannis, N.; Arnold, P. L. Small Molecule Activation by Uranium Tris(Aryloxides): Experimental and Computational Studies of Binding of N_2, Coupling of CO, and Deoxygenation Insertion of CO_2 under Ambient Conditions. *J. Am. Chem. Soc.* **2011**, *133* (23), 9036–9051. https://doi.org/10.1021/ja2019492.
(13) Mougel, V.; Camp, C.; Pécaut, J.; Copéret, C.; Maron, L.; Kefalidis, C. E.; Mazzanti, M. Siloxides as Supporting Ligands in Uranium(III)-Mediated Small-Molecule Activation. *Angew. Chem., Int. Ed.* **2012**, *51* (49), 12280–12284. https://doi.org/10.1002/anie.201206955.
(14) Camp, C.; Pécaut, J.; Mazzanti, M. Tuning Uranium–Nitrogen Multiple Bond Formation with Ancillary Siloxide Ligands. *J. Am. Chem. Soc.* **2013**, *135* (32), 12101–12111. https://doi.org/10.1021/ja405815b.
(15) Cooper, O.; Camp, C.; Pécaut, J.; Kefalidis, C. E.; Maron, L.; Gambarelli, S.; Mazzanti, M. Multimetallic Cooperativity in Uranium-Mediated CO_2 Activation. *J. Am. Chem. Soc.* **2014**, *136* (18), 6716–6723. https://doi.org/10.1021/ja5017624.
(16) Boreen, M. A.; Arnold, J. The Synthesis and Versatile Reducing Power of Low-Valent Uranium Complexes. *Dalton Trans.* **2020**, *49* (43), 15124–15138. https://doi.org/10.1039/D0DT03151H.
(17) Keener, M.; Fadaei-Tirani, F.; Scopelliti, R.; Zivkovic, I.; Mazzanti, M. Nitrogen Activation and Cleavage by a Multimetallic Uranium Complex. *Chem. Sci.* **2022**, *13* (27), 8025–8035. https://doi.org/10.1039/D2SC02997A.
(18) Camp, C.; Cooper, O.; Andrez, J.; Pécaut, J.; Mazzanti, M. CS2 Activation at Uranium(III) Siloxide Ate Complexes: The Effect of a Lewis Acidic Site. *Dalton Trans.* **2015**, *44* (6), 2650–2656. https://doi.org/10.1039/C4DT02585G.
(19) Hlina, J. A.; Pankhurst, J. R.; Kaltsoyannis, N.; Arnold, P. L. Metal–Metal Bonding in Uranium–Group 10 Complexes. *J. Am. Chem. Soc.* **2016**, *138* (10), 3333–3345. https://doi.org/10.1021/jacs.5b10698.

(20) Lu, E.; Wooles, A. J.; Gregson, M.; Cobb, P. J.; Liddle, S. T. A Very Short Uranium(IV)–Rhodium(I) Bond with Net Double-Dative Bonding Character. *Angew. Chem., Int. Ed.* **2018**, *57* (22), 6587–6591. https://doi.org/10.1002/anie.201803493.
(21) Feng, G.; Zhang, M.; Shao, D.; Wang, X.; Wang, S.; Maron, L.; Zhu, C. Transition-Metal-Bridged Bimetallic Clusters with Multiple Uranium–Metal Bonds. *Nat. Chem.* **2019**, *11* (3), 248–253. https://doi.org/10.1038/s41557-018-0195-4.
(22) Feng, G.; McCabe, K. N.; Wang, S.; Maron, L.; Zhu, C. Construction of Heterometallic Clusters with Multiple Uranium–Metal Bonds by Using Dianionic Nitrogen–Phosphorus Ligands. *Chem. Sci.* **2020**, *11* (29), 7585–7592. https://doi.org/10.1039/D0SC00389A.
(23) Patel, D.; Moro, F.; McMaster, J.; Lewis, W.; Blake, A. J.; Liddle, S. T. A Formal High Oxidation State Inverse-Sandwich Diuranium Complex: A New Route to f-Block-Metal Bonds. *Angew. Chem., Int. Ed.* **2011**, *50* (44), 10388–10392. https://doi.org/10.1002/anie.201104110.
(24) Napoline, J. W.; Kraft, S. J.; Matson, E. M.; Fanwick, P. E.; Bart, S. C.; Thomas, C. M. Tris(Phosphinoamide)-Supported Uranium–Cobalt Heterobimetallic Complexes Featuring Co → U Dative Interactions. *Inorg. Chem.* **2013**, *52* (20), 12170–12177. https://doi.org/10.1021/ic402343q.
(25) Ward, A. L.; Lukens, W. W.; Lu, C. C.; Arnold, J. Photochemical Route to Actinide-Transition Metal Bonds: Synthesis, Characterization and Reactivity of a Series of Thorium and Uranium Heterobimetallic Complexes. *J. Am. Chem. Soc.* **2014**, *136* (9), 3647–3654. https://doi.org/10.1021/ja413192m.
(26) Hlina, J. A.; Wells, J. a. L.; Pankhurst, J. R.; Love, J. B.; Arnold, P. L. Uranium Rhodium Bonding in Heterometallic Complexes. *Dalton Trans.* **2017**, *46* (17), 5540–5545. https://doi.org/10.1039/C6DT04570G.
(27) Feng, G.; Zhang, M.; Wang, P.; Wang, S.; Maron, L.; Zhu, C. Identification of a Uranium–Rhodium Triple Bond in a Heterometallic Cluster. *PNAS* **2019**, *116* (36), 17654–17658. https://doi.org/10.1073/pnas.1904895116.
(28) Xin, X.; Douair, I.; Zhao, Y.; Wang, S.; Maron, L.; Zhu, C. Dinitrogen Cleavage by a Heterometallic Cluster Featuring Multiple Uranium–Rhodium Bonds. *J. Am. Chem. Soc.* **2020**, *142* (35), 15004–15011. https://doi.org/10.1021/jacs.0c05788.
(29) Xin, X.; Douair, I.; Rajeshkumar, T.; Zhao, Y.; Wang, S.; Maron, L.; Zhu, C. Photochemical Synthesis of Transition Metal-Stabilized Uranium(VI) Nitride Complexes. *Nat Commun* **2022**, *13* (1), 3809. https://doi.org/10.1038/s41467-022-31582-z.
(30) Camp, C.; Toniolo, D.; Andrez, J.; Pécaut, J.; Mazzanti, M. A Versatile Route to Homo- and Hetero-Bimetallic 5f–5f and 3d–5f Complexes Supported by a Redox Active Ligand Framework. *Dalton Trans.* **2017**, *46* (34), 11145–11148. https://doi.org/10.1039/C7DT01993A.
(31) Hostetler, M. J.; Bergman, R. G. Synthesis and Reactivity of $Cp_2Ta(CH_2)_2Ir(CO)_2$: An Early-Late Heterobimetallic Complex That Catalytically Hydrogenates, Isomerizes and Hydrosilates Alkenes. *J. Am. Chem. Soc.* **1990**, *112* (23), 8621–8623. https://doi.org/10.1021/ja00179a078.
(32) Zhuang, J. M.; Batchelor, R. J.; Einstein, F. W. B.; Jones, R. H.; Hader, R.; Sutton, D. Heterometallic Analogs of $[(\eta^5\text{-}C_5Me_5)M(CO)_2]_2$ (M = Fe, Ru, Os). Synthesis and Structures of $(\eta^5\text{-}C_5Me_5)_2(CO)_4IrRe$, $(\eta^5\text{-}C_5Me_5)_2(CO)_4IrMn$, and $(\eta^5\text{-}C_5Me_5)(\eta_5\text{-}C_5H_5)(CO)_4IrRe$. *Organometallics* **1990**, *9* (10), 2723–2727. https://doi.org/10.1021/om00160a020.

(33) Baranger, A. M.; Bergman, R. G. Cooperative Reactivity in the Interactions of X-H Bonds with a Zirconium-Iridium Bridging Imido Complex. *J. Am. Chem. Soc.* **1994**, *116* (9), 3822–3835. https://doi.org/10.1021/ja00088a019.
(34) Baranger, A. M.; Hanna, T. A.; Bergman, R. G. Transfer of Oxygen and Sulfur from Organic Molecules to a Zr-Ir Bond. Evidence for an Unusually Rapid Atom Abstraction Reaction. *J. Am. Chem. Soc.* **1995**, *117* (40), 10041–10046. https://doi.org/10.1021/ja00145a015.
(35) Fulton, J. R.; Hanna, T. A.; Bergman, R. G. Insertion of Nitriles into a Zirconium−Iridium Heterobimetallic Complex: A Mechanistic Study. *Organometallics* **2000**, *19* (4), 602–614. https://doi.org/10.1021/om9907851.
(36) Shima, T.; Suzuki, H. P−C Bond Cleavage by a Heterobimetallic Polyhydrido Complex, $(C_5Me_5)Ru(\mu\text{-}H)_3Ir(C_5Me_5)$. Structure Determination and Fluxional Behavior of a Bridging Phosphido Complex, $(C_5Me_5)Ru(\mu\text{-}PPh_2)(\mu\text{-}H)(\mu\text{-}\eta^1{:}\eta^2\text{-}C_6H_5)Ir(C_5Me_5)$. *Organometallics* **2005**, *24* (7), 1703–1708. https://doi.org/10.1021/om049162k.
(37) Shima, T.; Namura, K.; Kameo, H.; Kakuta, S.; Suzuki, H. Synthesis and Structure of a Novel Ruthenium Hydrido Bis(Dihydrogen) Complex with 1,4,7-Trimethyl-1,4,7-Triazacyclononane Ligand: A Useful Precursor for Synthesis of Heterometallic Complexes. *Organometallics* **2010**, *29* (2), 337–346. https://doi.org/10.1021/om900692j.
(38) Curley, J. J.; Bergman, R. G.; Tilley, T. D. Preparation and Physical Properties of Early-Late Heterobimetallic Compounds Featuring Ir–M Bonds (M = Ti, Zr, Hf). *Dalton Trans.* **2011**, *41* (1), 192–200. https://doi.org/10.1039/C1DT11753J.
(39) Yamamoto, K.; Higashida, K.; Nagae, H.; Tsurugi, H.; Mashima, K. Synthesis and Characterization of Heterobimetallic Tantalum–Rhodium and Tantalum–Iridium Complexes Connected by a Tantalacyclopentadiene Fragment. *Helv. Chim. Acta* **2016**, *99* (11), 848–858. https://doi.org/10.1002/hlca.201600180.
(40) Lassalle, S.; Jabbour, R.; Schiltz, P.; Berruyer, P.; Todorova, T. K.; Veyre, L.; Gajan, D.; Lesage, A.; Thieuleux, C.; Camp, C. Metal–Metal Synergy in Well-Defined Surface Tantalum–Iridium Heterobimetallic Catalysts for H/D Exchange Reactions. *J. Am. Chem. Soc.* **2019**, *141* (49), 19321–19335. https://doi.org/10.1021/jacs.9b08311.
(41) Lassalle, S.; Jabbour, R.; Del Rosal, I.; Maron, L.; Fonda, E.; Veyre, L.; Gajan, D.; Lesage, A.; Thieuleux, C.; Camp, C. Stepwise Construction of Silica-Supported Tantalum/Iridium Heteropolymetallic Catalysts Using Surface Organometallic Chemistry. *J. Catal.* **2020**, *392*, 287–301. https://doi.org/10.1016/j.jcat.2020.10.016.
(42) Rosal, I. D.; Lassalle, S.; Dinoi, C.; Thieuleux, C.; Maron, L.; Camp, C. Mechanistic Investigations via DFT Support the Cooperative Heterobimetallic C–H and O–H Bond Activation across TaIr Multiple Bonds. *Dalton Trans.* **2021**, *50* (2), 504–510. https://doi.org/10.1039/D0DT03818K.
(43) Escomel, L.; Del Rosal, I.; Maron, L.; Jeanneau, E.; Veyre, L.; Thieuleux, C.; Camp, C. Strongly Polarized $Iridium^{\delta-}$–$Aluminum^{\delta+}$ Pairs: Unconventional Reactivity Patterns Including CO_2 Cooperative Reductive Cleavage. *J. Am. Chem. Soc.* **2021**, *143* (12), 4844–4856. https://doi.org/10.1021/jacs.1c01725.
(44) Escomel, L.; Abbott, D. F.; Mougel, V.; Veyre, L.; Thieuleux, C.; Camp, C. Highly Dispersed Silica-Supported Iridium and Iridium–Aluminium Catalysts for Methane Activation Prepared via Surface Organometallic Chemistry. *Chem. Commun.* **2022**, *58* (59), 8214–8217. https://doi.org/10.1039/D2CC02139K.
(45) Schlesinger, H. I.; Brown, H. C. Uranium(IV) Borohydride. *J. Am. Chem. Soc.* **1953**, *75* (1), 219–221. https://doi.org/10.1021/ja01097a058.

(46) Hoekstra, H. R.; Katz, J. J. The Preparation and Properties of the Group IV-B Metal Borohydrides. *J. Am. Chem. Soc.* **1949**, *71* (7), 2488–2492. https://doi.org/10.1021/ja01175a073.
(47) Daly, S. R.; Piccoli, P. M. B.; Schultz, A. J.; Todorova, T. K.; Gagliardi, L.; Girolami, G. S. Synthesis and Properties of a Fifteen-Coordinate Complex: The Thorium Aminodiboranate $[Th(H_3BNMe_2BH_3)_4]$. *Angew. Chem., Int. Ed.* **2010**, *49* (19), 3379–3381. https://doi.org/10.1002/anie.200905797.
(48) Altman, A. B.; Brown, A. C.; Rao, G.; Lohrey, T. D.; Britt, R. D.; Maron, L.; Minasian, S. G.; Shuh, D. K.; Arnold, J. Chemical Structure and Bonding in a Thorium(III)–Aluminum Heterobimetallic Complex. *Chem. Sci.* **2018**, *9* (18), 4317–4324. https://doi.org/10.1039/C8SC01260A.
(49) Escomel, L.; Soulé, N.; Robin, E.; Del Rosal, I.; Maron, L.; Jeanneau, E.; Thieuleux, C.; Camp, C. Rational Preparation of Well-Defined Multinuclear Iridium–Aluminum Polyhydride Clusters and Comparative Reactivity. *Inorg. Chem.* **2022**, *61* (15), 5715–5730. https://doi.org/10.1021/acs.inorgchem.1c03120.
(50) Lassalle, S.; Petit, J.; Falconer, R. L.; Hérault, V.; Jeanneau, E.; Thieuleux, C.; Camp, C. Reactivity of Tantalum/Iridium and Hafnium/Iridium Alkyl Hydrides with Alkyl Lithium Reagents: Nucleophilic Addition, Alpha-H Abstraction, or Hydride Deprotonation? *Organometallics* **2022**, *41* (13), 1675–1687. https://doi.org/10.1021/acs.organomet.2c00158.
(51) Takenaka, Y.; Hou, Z. Lanthanide Terminal Hydride Complexes Bearing Two Sterically Demanding $C_5Me_4SiMe_3$ Ligands. Synthesis, Structure, and Reactivity. *Organometallics* **2009**, *28* (17), 5196–5203. https://doi.org/10.1021/om900453j.
(52) Yang, L.; Powell, D. R.; Houser, R. P. Structural Variation in Copper(I) Complexes with Pyridylmethylamide Ligands: Structural Analysis with a New Four-Coordinate Geometry Index, τ_4. *Dalton Trans.* **2007**, No. 9, 955–964. https://doi.org/10.1039/B617136B.
(53) Dunbar, A. C.; Wright, J. C.; Grant, D. J.; Girolami, G. S. X-Ray Crystal Structure of Thorium Tetrahydroborate, $Th(BH_4)_4$, and Computational Studies of $An(BH_4)_4$ (An = Th, U). *Inorg. Chem.* **2021**, *60* (16), 12489–12497. https://doi.org/10.1021/acs.inorgchem.1c01710.
(54) Broach, R. W.; Schultz, A. J.; Williams, J. M.; Brown, G. M.; Manriquez, J. M.; Fagan, P. J.; Marks, T. J. Molecular Structure of an Unusual Organoactinide Hydride Complex Determined Solely by Neutron Diffraction. *Science* **1979**, *203* (4376), 172–174. https://doi.org/10.1126/science.203.4376.172.
(55) Evans, W. J.; Miller, K. A.; Kozimor, S. A.; Ziller, J. W.; DiPasquale, A. G.; Rheingold, A. L. Actinide Hydride Complexes as Multielectron Reductants: Analogous Reduction Chemistry from $[(C_5Me_5)_2UH]_2$, $[(C_5Me_5)_2UH_2]_2$, and $[(C_5Me_5)_2ThH_2]_2$. *Organometallics* **2007**, *26* (14), 3568–3576. https://doi.org/10.1021/om7003139.
(56) Cordero, B.; Gómez, V.; Platero-Prats, A. E.; Revés, M.; Echeverría, J.; Cremades, E.; Barragán, F.; Alvarez, S. Covalent Radii Revisited. *Dalton Trans.* **2008**, No. 21, 2832–2838. https://doi.org/10.1039/B801115J.
(57) Boreen, M. A.; Parker, B. F.; Lohrey, T. D.; Arnold, J. A Homoleptic Uranium(III) Tris(Aryl) Complex. *J. Am. Chem. Soc.* **2016**, *138* (49), 15865–15868. https://doi.org/10.1021/jacs.6b11182.
(58) Kindra, D. R.; Evans, W. J. Magnetic Susceptibility of Uranium Complexes. *Chem. Rev.* **2014**, *114* (18), 8865–8882. https://doi.org/10.1021/cr500242w.

(59) Wooles, A. J.; Lewis, W.; Blake, A. J.; Liddle, S. T. β-Diketiminate Derivatives of Alkali Metals and Uranium. *Organometallics* **2013**, *32* (18), 5058–5070. https://doi.org/10.1021/om400435b.
(60) La Pierre, H. S.; Kameo, H.; Halter, D. P.; Heinemann, F. W.; Meyer, K. Coordination and Redox Isomerization in the Reduction of a Uranium(III) Monoarene Complex. *Angew. Chem., Int. Ed.* **2014**, *53* (28), 7154–7157. https://doi.org/10.1002/anie.201402048.
(61) Riedhammer, J.; Aguilar-Calderón, J. R.; Miehlich, M.; Halter, D. P.; Munz, D.; Heinemann, F. W.; Fortier, S.; Meyer, K.; Mindiola, D. J. Werner-Type Complexes of Uranium(III) and (IV). *Inorg. Chem.* **2020**, *59* (4), 2443–2449. https://doi.org/10.1021/acs.inorgchem.9b03229.
(62) Grimme, S.; Ehrlich, S.; Goerigk, L. Effect of the Damping Function in Dispersion Corrected Density Functional Theory. *Journal of Computational Chemistry* **2011**, *32* (7), 1456–1465. https://doi.org/10.1002/jcc.21759.
(63) Liptrot, D. J.; Power, P. P. London Dispersion Forces in Sterically Crowded Inorganic and Organometallic Molecules. *Nat Rev Chem* **2017**, *1* (1), 1–12. https://doi.org/10.1038/s41570-016-0004.
(64) Bailey, P. J.; Coxall, R. A.; Dick, C. M.; Fabre, S.; Henderson, L. C.; Herber, C.; Liddle, S. T.; Loroño-González, D.; Parkin, A.; Parsons, S. The First Structural Characterisation of a Group 2 Metal Alkylperoxide Complex: Comments on the Cleavage of Dioxygen by Magnesium Alkyl Complexes. *Chem.─Eur. J.* **2003**, *9* (19), 4820–4828. https://doi.org/10.1002/chem.200305053.
(65) Gilbert, T. M.; Hollander, F. J.; Bergman, R. G. (Pentamethylcyclopentadienyl)Iridium Polyhydride Complexes: Synthesis of Intermediates in the Mechanism of Formation of (Pentamethylcyclopentadienyl)Iridium Tetrahydride and the Preparation of Several Iridium(V) Compounds. *J. Am. Chem. Soc.* **1985**, *107* (12), 3508–3516. https://doi.org/10.1021/ja00298a018.
(66) Monreal, M. J.; Thomson, R. K.; Cantat, T.; Travia, N. E.; Scott, B. L.; Kiplinger, J. L. $UI_4(1,4\text{-Dioxane})_2$, $[UCl_4(1,4\text{-Dioxane})]_2$, and $UI_3(1,4\text{-Dioxane})_{1.5}$: Stable and Versatile Starting Materials for Low- and High-Valent Uranium Chemistry. *Organometallics* **2011**, *30* (7), 2031–2038. https://doi.org/10.1021/om200093q.
(67) Kiplinger, J. L.; Morris, D. E.; Scott, B. L.; Burns, C. J. Convenient Synthesis, Structure, and Reactivity of $(C_5Me_5)U(CH_2C_6H_5)_3$: A Simple Strategy for the Preparation of Monopentamethylcyclopentadienyl Uranium(IV) Complexes. *Organometallics* **2002**, *21* (26), 5978–5982. https://doi.org/10.1021/om0206610.
(68) Cantat, T.; Scott, B. L.; Kiplinger, J. L. Convenient Access to the Anhydrous Thorium Tetrachloride Complexes $ThCl_4(DME)_2$, $ThCl_4(1,4\text{-Dioxane})_2$ and $ThCl_4(THF)_{3.5}$ Using Commercially Available and Inexpensive Starting Materials. *Chem. Commun.* **2010**, *46* (6), 919–921. https://doi.org/10.1039/B923558B.
(69) Walter, M. D.; Booth, C. H.; Lukens, W. W.; Andersen, R. A. Cerocene Revisited: The Electronic Structure of and Interconversion Between $Ce_2(C_8H_8)_3$ and $Ce(C_8H_8)_2$. *Organometallics* **2009**, *28* (3), 698–707. https://doi.org/10.1021/om7012327.
(70) Booth, C. H.; Walter, M. D.; Kazhdan, D.; Hu, Y.-J.; Lukens, W. W.; Bauer, E. D.; Maron, L.; Eisenstein, O.; Andersen, R. A. Decamethylytterbocene Complexes of Bipyridines and Diazabutadienes: Multiconfigurational Ground States and Open-Shell Singlet Formation. *J. Am. Chem. Soc.* **2009**, *131* (18), 6480–6491. https://doi.org/10.1021/ja809624w.

(71) Booth, C. H.; Kazhdan, D.; Werkema, E. L.; Walter, M. D.; Lukens, W. W.; Bauer, E. D.; Hu, Y.-J.; Maron, L.; Eisenstein, O.; Head-Gordon, M.; Andersen, R. A. Intermediate-Valence Tautomerism in Decamethylytterbocene Complexes of Methyl-Substituted Bipyridines. *J. Am. Chem. Soc.* **2010**, *132* (49), 17537–17549. https://doi.org/10.1021/ja106902s.
(72) Bain, G. A.; Berry, J. F. Diamagnetic Corrections and Pascal's Constants. *J. Chem. Educ.* **2008**, *85* (4), 532. https://doi.org/10.1021/ed085p532.
(73) Frisch, M. J.; Trucks, G. W.; Schlegel, H. B.; Scuseria, G. E.; Robb, M. A.; Cheeseman, J. R.; Scalmani, G.; Barone, V.; Petersson, G. A.; Nakatsuji, H.; Li, X.; Caricato, M.; Marenich, A.; Bloino, J.; Janesko, B. G.; Gomperts, R.; Mennucci, B.; Hratchian, H. P.; Ortiz, J. V.; Izmaylov, A. F.; Sonnenberg, J. L.; Williams-Young, D.; Ding, F.; Lipparini, F.; Egidi, F.; Goings, J.; Peng, B.; Petrone, A.; Henderson, T.; Ranasinghe, D.; Zakrzewski, V. G.; Gao, J.; Rega, N.; Zheng, G.; Liang, W.; Hada, M.; Ehara, M.; Toyota, K.; Fukuda, R.; Hasegawa, J.; Ishida, M.; Nakajima, T.; Honda, Y.; Kitao, O.; Nakai, H.; Vreven, T.; Throssell, K.; Montgomery, Jr., J. A.; Peralta, J. E.; Ogliaro, F.; Bearpark, M.; Heyd, J. J.; Brothers, E.; Kudin, K. N.; Staroverov, V. N.; Keith, T.; Kobayashi, R.; Normand, J.; Raghavachari, K.; Rendell, A.; Burant, J. C.; Iyengar, S. S.; Tomasi, J.; Cossi, M.; Millam, J. M.; Klene, M.; Adamo, C.; Cammi, R.; Ochterski, J. W.; Martin, R. L.; Morokuma, K.; Farkas, O.; Foresman, J. B.; Fox, D. J. Gaussian 09.
(74) Perdew, J. P.; Chevary, J. A.; Vosko, S. H.; Jackson, K. A.; Pederson, M. R.; Singh, D. J.; Fiolhais, C. Atoms, Molecules, Solids, and Surfaces: Applications of the Generalized Gradient Approximation for Exchange and Correlation. *Phys. Rev. B* **1992**, *46* (11), 6671–6687. https://doi.org/10.1103/PhysRevB.46.6671.
(75) Becke, A. D. Density-functional Thermochemistry. III. The Role of Exact Exchange. *J. Chem. Phys.* **1993**, *98* (7), 5648–5652. https://doi.org/10.1063/1.464913.
(76) Cao, X.; Dolg, M. Segmented Contraction Scheme for Small-Core Actinide Pseudopotential Basis Sets. *Journal of Molecular Structure: THEOCHEM* **2004**, *673* (1), 203–209. https://doi.org/10.1016/j.theochem.2003.12.015.
(77) Cao, X.; Dolg, M.; Stoll, H. Valence Basis Sets for Relativistic Energy-Consistent Small-Core Actinide Pseudopotentials. *J. Chem. Phys.* **2003**, *118* (2), 487–496. https://doi.org/10.1063/1.1521431.
(78) Andrae, D.; Häußermann, U.; Dolg, M.; Stoll, H.; Preuß, H. Energy-Adjustedab Initio Pseudopotentials for the Second and Third Row Transition Elements. *Theoret. Chim. Acta* **1990**, *77* (2), 123–141. https://doi.org/10.1007/BF01114537.
(79) Ehlers, A. W.; Böhme, M.; Dapprich, S.; Gobbi, A.; Höllwarth, A.; Jonas, V.; Köhler, K. F.; Stegmann, R.; Veldkamp, A.; Frenking, G. A Set of F-Polarization Functions for Pseudo-Potential Basis Sets of the Transition Metals Sc–Cu, Y–Ag and La–Au. *Chemical Physics Letters* **1993**, *208* (1), 111–114. https://doi.org/10.1016/0009-2614(93)80086-5.
(80) Hariharan, P. C.; Pople, J. A. The Influence of Polarization Functions on Molecular Orbital Hydrogenation Energies. *Theoret. Chim. Acta* **1973**, *28* (3), 213–222. https://doi.org/10.1007/BF00533485.
(81) Ditchfield, R.; Hehre, W. J.; Pople, J. A. Self-Consistent Molecular-Orbital Methods. IX. An Extended Gaussian-Type Basis for Molecular-Orbital Studies of Organic Molecules. *J. Chem. Phys.* **1971**, *54* (2), 724–728. https://doi.org/10.1063/1.1674902.
(82) Hehre, W. J.; Ditchfield, R.; Pople, J. A. Self—Consistent Molecular Orbital Methods. XII. Further Extensions of Gaussian—Type Basis Sets for Use in Molecular Orbital Studies of

Organic Molecules. *J. Chem. Phys.* **1972**, *56* (5), 2257–2261. https://doi.org/10.1063/1.1677527.
(83) Reed, A. E.; Curtiss, L. A.; Weinhold, F. Intermolecular Interactions from a Natural Bond Orbital, Donor-Acceptor Viewpoint. *Chem. Rev.* **1988**, *88* (6), 899–926. https://doi.org/10.1021/cr00088a005.

Chapter 3

Photolysis-Driven Bond Activation by Thorium and Uranium Tetraosmate Polyhydride Complexes

Introduction

Metal hydrides have seen extensive interest due to their importance in processes such as catalytic hydrofunctionalization of olefins,[1] reduction of organic substrates and small molecules,[2,3] and electrocatalytic redox reactions.[4] While d-block metal hydrides have been the focus of the majority of these investigations, it was soon discovered that f-block hydrides exhibit unique reactivity that, in some cases (particularly the hydrogenation and polymerization of unsaturated organic substrates), render them even better catalysts than their transition metal (TM) counterparts.[5] For example, $Cp^*_2AnMe_2$ (An = U, Th) supported on dehydroxylated alumina and activated by H_2 exhibited 10 times the catalytic activity for propene hydrogenation than typical Pt/SiO_2 catalysts under the same conditions.[6,7] Furthermore, heterometallic hydride complexes—derived from the combination of f-block and transition metals—have exciting potential for cooperative reactivity utilizing the unique properties of each metal center; they also offer the possibility of providing fundamental insight into f-block–TM bonding. Bridging hydrides are well suited to support these interactions, as their minimal steric profile allows for close metal–metal contact. In addition, hydride elimination to form metal–metal bonds is well-precedented in the transition metal literature, offering a potential route to unsupported metal–metal bonds.[8] Lastly, heterometallic actinide hydrides are of wider interest due to their potential for hydrogen storage and possible superconductive properties at high pressures.[9]

Significant strides have been made in the synthesis of rare earth/transition metal polyhydrides since the first example, a trimetallic Y_2Zn tetrahydride, was synthesized by Evans in 1984.[10] In subsequent years, several groups have reported the successful syntheses of such complexes using alkane elimination, H_2 elimination, and salt metathesis.[11–17] Hou has reported extensive studies on Y– and Lu–TM complexes, synthesizing polyhydride clusters with all of the 2nd and 3rd row transition metals between groups 6 and 9 (excluding Tc), several of which display hydrogen addition and release properties.[18–24]

In contrast, multimetallic hydride chemistry of the actinides (An) is underdeveloped. Ephritikhine reported a series of U/Re complexes supported by three bridging hydrides, utilizing potassium rhenate salts to install the rhenium center on uranium pentamethylcyclopentadienyl (Cp*) halide complexes.[25–27] The U–Re distance in $[K(18\text{-crown-6}][(Cp^*)_2(Cl)U(\mu\text{-}H)_3Re(H)_3(PPh_3)_2]$ was long (3.255(8) Å), leading the authors to conclude there was no direct U–Re interaction;[26] limited reactivity was observed with all U–Re species described.

Following our report of hydride-supported An–Al bonds (An = Th, U),[28] we have recently focused on applying this strategy to stabilize new An–TM interactions. Our efforts have resulted in the syntheses of several multimetallic actinide tetrairidate dodecahydride complexes, $Th\{[(\mu\text{-}H)_2(H)IrCp^*]_2[(\mu\text{-}H)_3IrCp^*]_2\}$ (**3.A**) and $U\{(\mu\text{-}H)_3IrCp^*\}_4$ (**3.B**), from the iridium polyhydride starting material $K[Cp^*IrH_3]$ and actinide halides (Scheme 3.1). These complexes featured the first reported computational evidence for An–Ir interaction.[29] Given the efficacy of eliminating a bridging ligand to form An–Co bonds,[30] we sought to engender An–TM bonds *via* dihydrogen elimination, but both **3.A** and **3.B** proved resistant to this process, either by thermolysis up to 80 °C, or *via* photolysis with 254 nm light.

We turned to the osmium counterpart, Cp^*OsH_5, reported by Girolami, to pursue the synthesis of An–Os multimetallic complexes. This species is known to be photoactive, losing multiple hydrides to form the $[Cp^*OsH_2]_2$ dimer.[31] We reasoned that synthesis of actinide tetraosmate complexes analogous to tetrairidate complexes **3.A** and **3.B** might lead to more productive photolysis, ideally with the loss of hydrides and formation of An–Os bonds. Here, we

report the syntheses, calculated bonding character, and photolytic chemistry of these uranium and thorium tetraosmate species.

Scheme 3.1 Previously reported syntheses of An–Ir multimetallic complexes **3.A** and **3.B**.

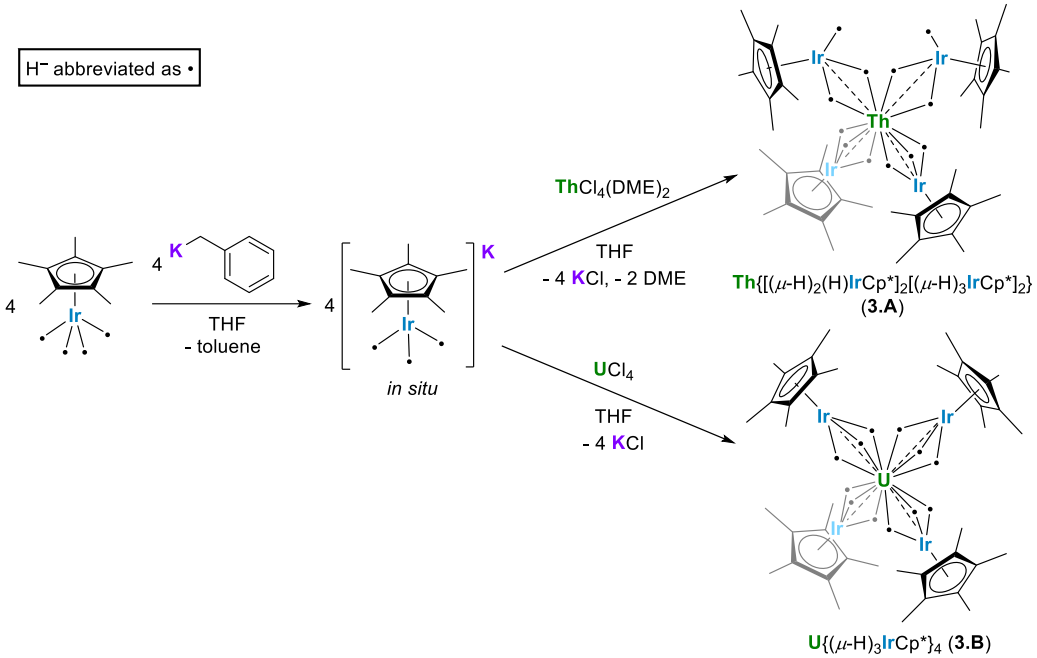

Results and discussion

In order to install the osmium centers around the actinide center, Cp^*OsH_5 was converted *in situ* to the potassium osmate species $K[Cp^*OsH_4]$ (**3.1**) with the addition of benzylpotassium in THF, forming a pale-yellow solution. ^1H NMR confirms the stoichiometric deprotonation of Cp^*OsH_5, resulting in formation of **3.1** and toluene. Compared to Cp^*OsH_5, the hydride resonance of **1** shifts upfield from –11.00 ppm to –17.15 ppm, with a concomitant reduction in integration from five protons to four (relative to the Cp* resonance). The ^1H NMR spectrum closely resembles that of the $Li[Cp^*OsH_4]$ species reported by Suzuki, which contains a hydride resonance at –17.52 ppm.[32]

Reaction of four equivalents of **3.1** with $ThCl_4(DME)_2$ or UCl_4 in THF led to the formation of $Th\{(\mu\text{-}H)_4OsCp^*\}_4$ (**3.3.2-Th**) and $U\{(\mu\text{-}H)_4OsCp^*\}_4$ (**3.2-U**), which can be isolated as colorless and yellow crystals from *n*-hexane in 66% and 68% yield, respectively (Scheme 3.2).

The ^1H NMR spectrum of diamagnetic **3.2-Th** features two resonances for the Cp* methyl protons and hydrides at 2.13 ppm and –11.01 ppm, respectively. These integrate in a 15:4 ratio, indicating that all hydrides in the potassium metalate starting material are preserved. The ^1H NMR spectrum of **3.2-U** contains a sharp resonance at 3.65 ppm for the Cp* methyl protons, as well as a hydride resonance at 89.8 ppm, shifted significantly downfield due to the paramagnetic influence of the formally uranium(IV) center. Once again, the two peaks integrate in a 15:4 ratio.

The solid-state IR spectra of **3.2-Th** and **3.2-U** each feature a single metal-hydride stretching signal at 1993 cm^{-1} and 1990 cm^{-1}, respectively, shifted by about 100 cm^{-1} compared to the reported hydride stretch for Cp^*OsH_5 of 2083 cm^{-1}.[31] These values are significantly higher than the bridging hydride stretch of 1762 cm^{-1} found in $[Cp^*OsH_2]_2$.[33] Several other examples of bridging hydrides in Cp*-substituted osmium multimetallic complexes have been reported, but

lack reported hydride stretches for comparison.[32,34] However, our values are in good agreement with the bridging hydride stretches of 1962 and 1951 cm^{-1} for the iridate complexes **3.A** and **3.B** ,[29] which exhibit a similar decrease in frequency by approximately 100 cm^{-1} from the value for Cp*IrH_4 of 2150 cm^{-1}.[35]

Scheme 3.2 Synthetic route to compounds **3.1** and **3.2-An**.

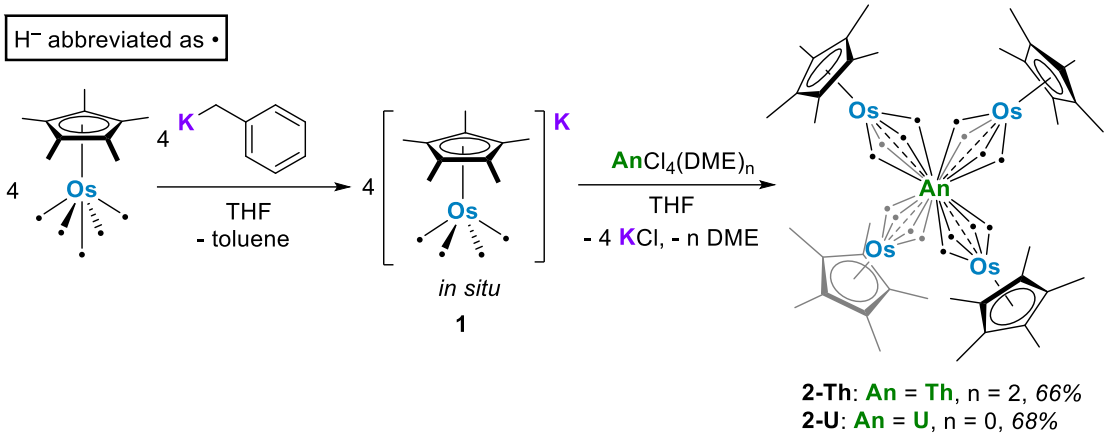

Single crystals of **3.2-Th** and **3.2-U** suitable for X-ray diffraction were grown from saturated solutions of cold *n*-pentane, and the solid-state structures of both were crystallographically characterized, confirming that four osmium centers are coordinated around the actinide centers. No hydrides could be located in the difference maps, most likely due to the close proximity of numerous heavy atoms, a phenomenon that we observed previously with the related actinide-iridium complexes.[29] Complex **3.2-Th** crystallizes in the space group $P2_1/c$ with Th–Os distances ranging from 3.0183(6) Å to 3.0379(6) Å, well within the sum of covalent radii for Th and Os (3.50 Å).[36] The Os centers are slightly distorted from an ideal tetrahedral geometry around Th, with a τ_4 value[37] of 0.93 (calculated with α = 115.80(2)°, β = 112.32(2)°), slightly less than that of A (0.97).[29] The Os–Os distances range from 4.7446(7) Å to 5.1395(7) Å, which precludes any Os–Os interactions considering osmium's covalent radius of 1.44 Å.[36] Unlike **3.A**, complex **3.2-Th** has one consistent hydride binding mode across all osmate moieties. All osmate fragments feature fairly linear Th–Os–$Cp^*_{centroid}$ angles (171.10(15)° to 176.92(14)°). These values are sufficiently close to linearity to indicate that all four hydrides in each $[Cp^*OsH_4]^-$ fragment bridge the Th and Os centers. Therefore, **3.2-Th** is formally 16-coordinate, with 16 bridging hydrides around the thorium center, matching the highest observed coordination number around an atom.[38,39] This is reminiscent of the 15-coordinate aminodiboranate thorium complex reported by Girolami, which also features thorium with an extraordinarily large number of bridging hydrides, in this case provided by borohydride-based ligands rather than transition metal polyhydrides.[40]

Complex **3.2-U** crystallizes in the cubic space group $Pa\bar{3}$, with a single osmate moiety centered on the 3-fold symmetry axis and another which generates the remaining three osmate fragments through symmetry. The on-axis U–Os distance is 2.9490(6) Å, while the off-axis U–Os distances are each 2.9501(4) Å, far shorter than the sum of covalent radii for U and Os (3.40 Å)[36] and on average shorter than those of **3.2-Th** by approximately 0.08 Å (3.027(6) Å vs. 2.950(6) Å). The Os centers are arranged in an essentially tetrahedral manner around uranium, with a τ_4 value of 0.98 (calculated with α = 111.00(2)°, β = 111.00(2)°), significantly more tetrahedral than **3.B**,

which has a τ_4 value of 0.87.[29] As in **3.2-Th**, the Os–Os distances are long enough to rule out any possible interaction, varying from 4.7703(8) Å to 4.8615(7) Å. The U–Os–Cp*$_{centroid}$ angles are quite linear, at 175.30(11)° for the on-axis fragment and 176.4(5)° for the off-axis fragments, indicating that as in **3.2-Th**, all 16 hydrides of **3.2-U** bridge the osmium centers and uranium. This is the first report of such a high coordination number for uranium, which previously had been limited to 14-coordinate complexes,[41,42] and a second example of a formally 16-coordinate actinide complex.

To further support our conclusions about the hydride binding modes in **3.2-Th** and **3.2-U** as well as investigate potential metal-metal interactions, we turned to density functional theory (DFT) calculations for further insight. All DFT computations employed the B3PW91 functional (full details in the experimental section). Computational modeling of **3.2-Th** and **3.2-U** predicts near-tetrahedral configurations for the osmium fragments around the actinide centers, as observed in the solid-state structures, as well as sixteen bridging hydrides for each species (Figure 3.1). The calculated An–Os distances are consistently ~0.04 Å shorter than the experimentally determined distances, but this and all other observed disparities between computational and experimental metrics are quite minor (Table 3.1). In addition, the two highest experimentally observed stretching frequencies for **3.2-Th** and **3.2-U** fall within the predicted ranges according to calculations, further evidence that these calculations are accurately modeling the hydrides within these compounds.

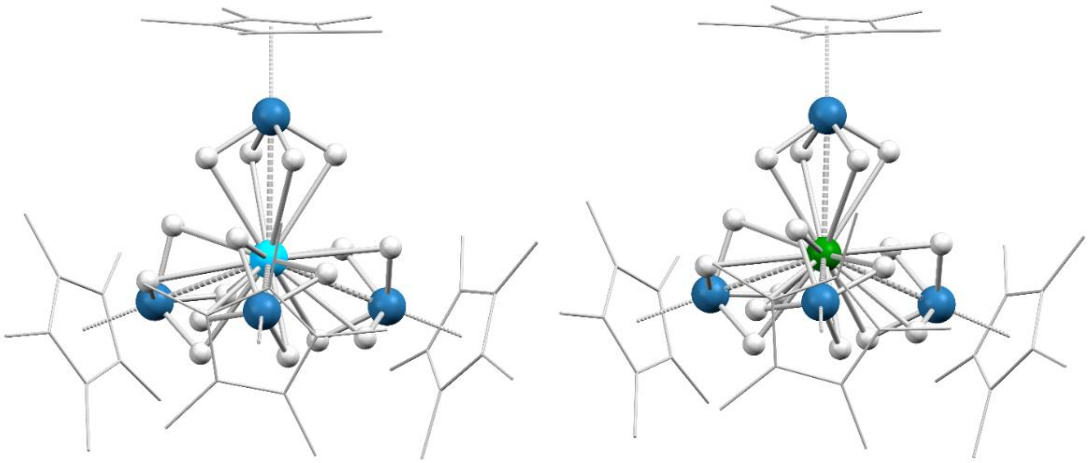

Figure 3.1 Computed structures for **3.2-Th** and **3.2-U** (ORTEP diagrams can be found in Figures S32-S33). Color key: Light blue (thorium), green (uranium), blue (osmium), white (hydrogen). Hydrogen atoms on the Cp* rings are omitted and Cp* ligands are wireframed for clarity.

Natural Bond Order (NBO) analyses were carried out on **3.2-Th** and **3.2-U** as well, to analyze the degree of metal-metal interaction between the actinide and osmium centers. Wiberg Bond Indices (WBIs) of 0.72-0.73 were calculated for the Th–Os interactions in **3.2-Th**, while values of 0.81-0.83 were found for the U–Os interactions in **3.2-U**. These values suggest significant bonding interactions between the actinide and osmium centers, and are comparable to previously reported An–TM bonds as well as our An–Ir systems.[43,44,29] Complexes **3.2-Th** and **3.2-U** are, to the best of our knowledge, the first reported compounds to evidence An–Os covalency. Analysis of the M–H bonds reveals a more covalent hydride interaction with Os than U or Th, with Os–H WBIs of 0.57-0.60 compared to An–H WBIs of 0.18-0.24. Similar to **3.A** and **3.B**, the identity of the actinide does not appear to affect hydride covalency in **2-An**.

Table 3.1 Experimentally and computationally derived bond distances, angles, and Os–H stretches for **3.2-Th** and **3.2-U**.

	3.2-Th		**3.2-U**	
	Expt.	Comp.	Expt.	Comp.
An–Os dist. (Å)	3.0183(6)–3.0379(6)	2.977–2.978	2.9490(6)–2.9501(4)	2.911–2.913
Os–C_{Cp*} dist. (Å)	2.173(11)–2.320(10)	2.187–2.306	2.18(3)–2.29(3)	2.187–2.300
∠An–Os–$Cp^*_{centroid}$ (°)	171.10(15)–176.92(14)	178.9–179.3	175.30(11)–176.4(5)	177.1–179.2
Os–H (cm^{-1})	1990 862	2051–1963 947– 838	1993 863	2056–1947 939–818

With these actinide-osmium polyhydrides in hand, we investigated the potential for thermolytic and photolytic H_2 elimination in **3.2-U** and **3.2-Th**. Both complexes were stable in C_6D_6 when heated at 60 °C for 8 hours, as monitored by ^{1}H NMR spectroscopy. However, upon irradiation by 254 nm light in C_6H_6, complex **3.2-U** undergoes a color change from yellow to dark brown, forming complex **3.3-U** (Scheme 3.3) *via* the C–H activation of a Cp* methyl group and the loss of hydrides as H_2, as detected by ^{1}H NMR spectroscopy.

Scheme 3.3 Photolysis of **3.2-U** and **3.2-Th** with 254 nm light in C_6H_6 to produce **3.3-U**, **3.3-Th**, and **3.4-Th**.

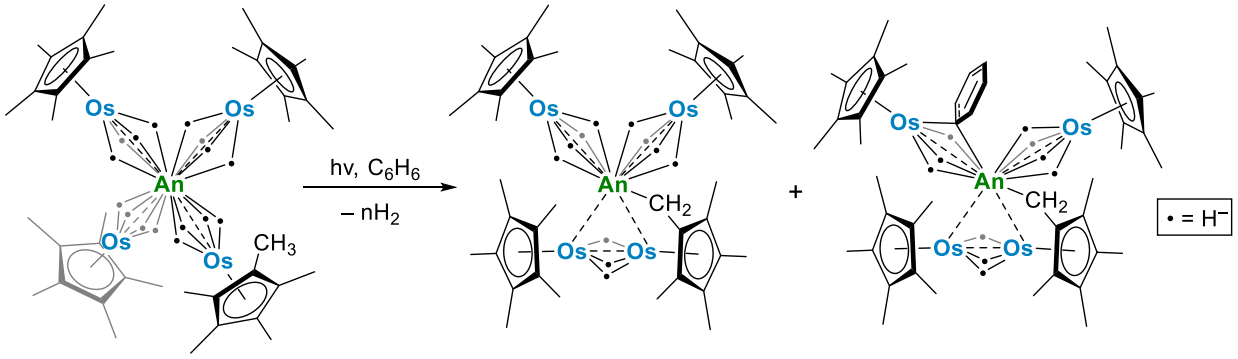

Complex **3.3-U** shows significantly reduced solubility compared to **3.2-U**. It exhibits minimal solubility in *n*-hexane, requiring several drops of benzene to facilitate dissolution of the crude material. Upon workup in this manner, **3.3-U** crystallizes at –40 °C as tiny brown crystals in 43% yield. Larger, X-ray quality crystals were grown from dilute solutions in *n*-hexane without benzene, from which the solid-state structure was determined (Figure 3.2, left). As a result of photolysis, two of the Cp*Os moieties in **3.3-U** feature a significantly reduced Os–Os distance of 2.4639(4) Å and a U–C bond forms between uranium and the activated Cp* methylene. The U–Os distances of the remaining two fragments are slightly lengthened compared to **3.2-U**, ranging from 2.9571(7) Å to 3.0264(7) Å. The actinide center is disordered across two positions, asymmetrically bridging the diosmium fragment towards either osmium atom with near-50%

occupancy. There is some variation in the U–C bond length depending on which direction the asymmetric U atom favors, at 2.603(7) Å and 2.657(9) Å. These values are similar to the U–C bond lengths found for other uranium "tuck-over" complexes, such as Cp*U[μ-η^5:η^1:η^1-$C_5Me_3(CH_2)_2$](μ-H)$_2$UCp*$_2$.[45,46] In addition, the two unreacted $[Cp^*OsH_4]^-$ fragments in complex **3.3-U** splay further outward from the tetrahedral geometry of **3.2-U**, with an Os–U–Os angle of 118.15(3)° or 120.75(3)° depending on the uranium position. As with the previous complexes, no hydrides could be resolved in the solid-state structure.

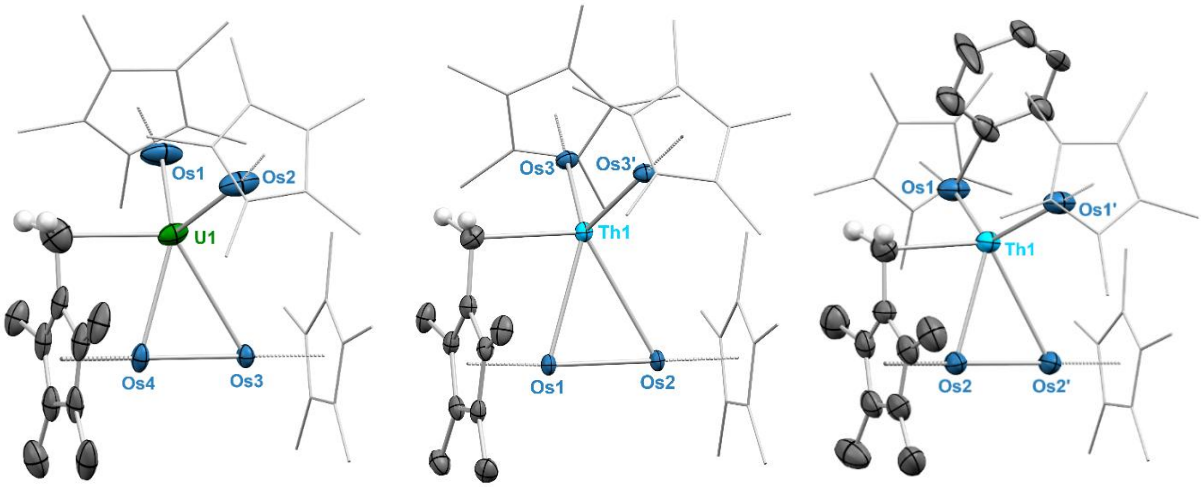

Figure 3.2 ORTEP diagrams for **3.3-U** (left), **3.3-Th** (middle), and **3.4-Th** (right), with ellipsoids drawn at the 50% probability level. Non-methylene hydrogen atoms have been omitted and non-cyclometallated Cp* ligands have been wireframed for clarity. Only the major component of the disordered actinide center is shown in **3.3-U** and **3.3-Th**. Hydrides were not resolved in the crystal structures due to the numerous heavy metal centers in proximity. Selected bond distances (Å) and angles (°) for **3.3-U**: U1–Os1 2.9870(12), U1–Os2 3.0267(11), U1–Os3 3.2205(8), U1–Os4 2.7974(8), U1–C6 2.657(9), Os3–Os4, 2.4640(5), Os1–U1–Os2 118.15(3), Os3–Os4–Cp*$_{centroid}$ 179.49(15), Os4–Os3–Cp*$_{centroid}$ 179.45(10). Selected bond distances (Å) and angles (°) for **3.3-Th**: Th1–Os3 3.0260(3), Th1–Os2 3.2567(5), Th1–Os1 2.9539(4), Th1–C1 2.534(10), Os1–Os2, 2.4689(4), Os3–Th1–Os3' 121.133(14), Os1–Os2–Cp*$_{centroid}$ 179.86(2), Os4–Os3–Cp*$_{centroid}$ 177.133(17). Selected bond distances (Å) and angles (°) for **3.4-Th**: Th1–Os1 3.0593(9), Th1–Os2' 3.2965(11), Th1–Os2 2.9403(12), Th1–C12 2.703(12), Os2–Os2', 2.4536(9), Os1–Th1–Os1' 135.06(4), Os2–Os2'–Cp*$_{centroid}$ 179.89(16).

As discussed previously, photolytic loss of hydrides has precedence with Cp^*OsH_5, which is known to photolyze with the loss of 3 equivalents of H_2 to form the dimer $[Cp^*OsH_2]_2$. This species has an essentially identical Os–Os distance of 2.4568(6) Å to that of **3.3-U**.[33] The newly formed $[(CH_2)Me_4C_5Os(\mu\text{-}H)_3OsCp^*]^{2-}$ fragment closely resembles the doubly deprotonated dimer, with one deprotonation occurring at a Cp* methyl group and the other occurring from the bridging hydrides, coordinated side-on to the actinide center. Hou previously reported the reaction and side-on coordination of $[Cp^*OsH_2]_2$ with rare earth dialkyl complexes of the form $(C_5Me_4SiMe_3)Ln(CH_2SiMe_3)_2(THF)$ (Ln = Y, Lu) resulting in trinuclear, C–H activated complexes.[19] However, in these species, the geometry of the $[Cp^*OsH_2]_2$ fragment was not preserved due to the migration of several hydrides to bridge the lanthanide and osmium atoms, and reactivity was promoted *via* thermolysis rather than photolysis.

The ^{1}H NMR spectrum of C_s symmetric **3.3-U** contains six observable resonances, allowing all protons to be assigned besides the hydrides of the diosmium fragment. The mirror plane passes through the Os–Os and U–CH_2 bonds, resulting in the observation of two Cp* resonances (in a 2:1 ratio) and two methyl resonances from the activated Cp* (in a 1:1 ratio). The activated methylene resonance is shifted far upfield to –89.1 ppm. The hydrides of **3.3-U** are observed at 55.5 ppm, significantly more shielded than the hydrides of **3.2-U**, which are shifted to 89.8 ppm. This downfield signal integrates to about eight protons, and is therefore assigned to the hydrides of the two unactivated $[Cp^*OsH_4]^-$ fragments. However, the hydrides associated with the diosmium fragment were not observed between –100 to 100 ppm in the ^{1}H NMR spectrum, perhaps due to the paramagnetic nature of **3.3-U**. We therefore hypothesized that a diamagnetic thorium photolysis product could serve as a useful analogue to **3.3-U**.

Complex **3.2-Th** displays slightly divergent reactivity from **3.2-U**, photolyzing over four hours with a color change from colorless to orange to produce both **3.3-Th** and **3.4-Th** (Scheme 3.3). As with the photolysis of **3.2-U**, H_2 formation can be detected by ^{1}H NMR spectroscopy. However, complex **3.3-Th**, the analogous species to **3.3-U**, is the minor product in this reaction. The major product, **3.4-Th**, results from the additional activation of one equivalent of the benzene solvent, replacing one bridging hydride from one $[Cp^*OsH_4]^-$ fragment with an asymmetrical bridging μ-η^1,η^1-phenyl ligand. This benzene activation appears to lend stability to the photolysis product, as reactions in *n*-hexane instead result in dark brown intractable mixtures and yield no crystalline product. In contrast, the photolysis product **3.3-U** can be prepared and isolated from *n*-hexane in satisfactory yields.

Compounds **3.3-Th** and **3.4-Th** consistently co-crystallize from the crude photolysis mixture, typically in a 22:78 **3.3-Th** to **3.4-Th** ratio (mol/mol%) as measured by ^{1}H NMR. Complex **3.4-Th** could be isolated in sparing (<20%) yield with photolysis times in excess of two days. Tracking of the reaction by ^{1}H NMR shows that **3.4-Th** forms in significant quantities with **3.3-Th** upon photolysis of **3.2-Th** and gradually increases in concentration over time, such that **3.3-Th** cannot be isolated with short reaction times. Addition of H_2 gas to a sample of **3.4-Th** did not lead to protonation of the bridging phenyl ligand to form **3.3-Th**. Separation of **3.3-Th** from **3.4-Th** was achieved a single time by recrystallization of a particularly high-percentage **3.3-Th**-containing photolysis crop (47% **3.3-Th** by ^{1}H NMR) from a 1:1 hexane/benzene solution at –40 °C, yielding crystals containing 88% **3.3-Th**. As a result, the ^{1}H NMR signals of each compound can be distinctly identified, although quantities sufficient for high-quality 2D NMR spectra were not obtained. Spectroscopic analyses were instead carried out on the crystalline mixture of **3.3-Th** and **3.4-Th**. As confirmation that two species are present in this material, Diffusion Ordered Spectroscopy (DOSY) experiments on a nearly 1:1 solution of **3.3-Th**/**3.4-Th** demonstrate that the ^{1}H NMR peaks associated with **3.3-Th** and **3.4-Th** have slightly different diffusion coefficients (Figure 3.5). This slight difference in diffusion rate is unsurprising given the relatively small difference in molecular weight and steric bulk between the two complexes, and is well outside the margin of error in these experiments.

The ^{1}H NMR spectrum of **3.3-Th** contains one more resonance than the spectrum of **3.3-U**. Analogous to **3.3-U**, there are four resonances in the methyl region, in addition to a singlet methylene resonance at 1.34 ppm. In contrast to the uranium species, there are two hydride signals, one integrating to eight hydrides and the other integrating to three hydrides, found at –9.74 ppm and –11.06 ppm, respectively. These signals are in turn assigned to the hydrides of the two $[Cp^*OsH_4]^-$ fragments and the hydrides of the diosmium fragment, $[(CH_2)Me_4C_5Os(\mu$-

$H)_3OsCp^*]^{2-}$. Therefore, we assign three hydrides to the diosmium fragment of **3.3-U** as well, resulting in 11 total hydrides for both **3.3-U** and **3.3-Th**.

The ^1H NMR spectrum of **3.4-Th** is significantly more complex, as the bridging phenyl ligand renders each osmate fragment distinct. The phenyl signals of **3.4-Th** are observed between 7.07 and 7.98 ppm. The three unactivated Cp* moieties and four methyl groups of the activated Cp* each appear as separate signals, and the methylene resonances arising from the Cp* cyclometallation are split as an AX system centered at 1.08 and 1.37 ppm.^1H,^{13}C HSQC experiments confirm that the protons giving rise to these signals are bonded to the same carbon, which appears at 61.07 ppm in the ^{13}C NMR spectrum. In the hydride region, the three hydrides of the $[Cp^*OsH_3(C_6H_5)]^-$ fragment are distinct in solution, and splitting can be observed between the three signals. The hydride distal to the activated benzene appears furthest downfield, at –8.16 ppm, and is split into a triplet by the two proximal hydrides, which appear as doublets at –10.54 and –10.84 ppm. The bridging hydrides of the $[(CH_2)Me_4C_5Os(\mu\text{-}H)_3OsCp^*]^{2-}$ and $[Cp^*OsH_4]^-$ fragments are observed as two singlets at –9.80 and –11.59 ppm, respectively.

Both **3.3-Th** and **3.4-Th** are highly soluble in benzene and toluene while only sparingly so in *n*-hexane. Recrystallization of the aforementioned singular **3.3-Th** sample from *n*-hexane and minimal benzene afforded single crystals of **3.3-Th** suitable for diffraction experiments. X-ray quality crystals of **3.4-Th** were grown from *n*-hexane by recrystallizing the primarily **3.4-Th** crystalline material isolated from long photolysis times (>1 day).

Complex **3.3-Th** crystallizes with one equivalent of *n*-hexane in the space group $Pmn2_1$, with half of the molecule generated by a mirror plane (Figure 3.2, middle). It is isostructural to **3.3-U**, but unlike **3.3-U**, the disorder of the central actinide atom strongly favors one orientation, at over 90% occupancy, indicating a preference for the molecules to align in the same orientation. Further discussion of the structure of **3.3-Th** will primarily refer to this major component. The diosmium fragment in **3.3-Th** is nearly identical to that of **3.3-U**, with a similar Os–Os distance of 2.4689(4) Å, but a shorter Th–C bond measuring 2.534(10) Å (2.729(10) Å in the minor component). The monoosmate fragments feature slightly longer Th–Os bond lengths than the U–Os distances in **3.3-U** at 3.0260(3) Å, with a similar Os–Th–Os angle of 121.133(14)°.

In comparison, the primary notable feature in the structure of **3.4-Th** is the presence of an asymmetric bridging phenyl ligand across one Th–Os interaction (Figure 3.2, right). The structure is completely asymmetric, but due to disorder **3.4-Th** crystallizes in the space group $P4_2/ncm$, with the thorium center and the bridging phenyl ligand disordered equivalently across two sites, resulting in four possible conformations for the molecule. The diosmium fragment is isostructural to that of **3.3-Th**, with an Os–Os distance of 2.4536(9) Å and a Th–C bond length of 2.703(12) Å between Th and the activated Cp* methylene.

In the remaining portion of **3.4-Th**, the two monoosmate fragments splay further outward to accommodate the activated phenyl ring, with an expanded Os–Th–Os angle of 135.06(4)°, compared to 121.133(14)° in **3.3-Th**. Within this expanded pocket, one equivalent of activated benzene is present as a bridging $\mu\text{-}\eta^1,\eta^1$-phenyl across one Th–Os interaction, replacing one of the bridging hydrides. This phenyl ring is coordinated asymmetrically, angled at 67.0(14)° relative to the Th–Os bond. It is heavily skewed toward the osmium center, with an Os–C distance of 2.12(5) Å compared to a Th–C distance of 2.96(4) Å. Examples of bridging $\mu\text{-}\eta^1,\eta^1$-aryl ligands involving osmium are limited to triosmium carbonyl clusters and feature symmetric coordination modes.[47–49] Several late transition metal multimetallic species feature similar $\mu\text{-}\eta^1,\eta^1$-aryls, including two related Au-Ag and Au-Cu polymeric chains,[50] as well as Pt-Ag and Pt-Cu complexes.[51,52] The polymeric complex $[Au_2Ag_2(C_6F_5)_4(N{\equiv}CCH_3)_2]_n$ most closely resembles the highly asymmetric

phenyl coordination mode of **3.4-Th**, with Ag–C_{phenyl} distances of 2.508(6) and 2.687(6) Å, Au–C_{phenyl} distances of 2.055(6) and 2.088(6) Å, and a C_{phenyl}–Au–Ag angle of 66.00(15)°. In all these cases, however, the bridging aryl ligand is coordinated to a metal center in the starting material, whereas in **3.4-Th** it arises from the C–H activation of benzene. In the rare earths, a symmetric η^1-phenyl bridging two scandium centers has been proposed as an intermediate in the activation of benzene by (1,1′-fc(NSi^{t}BuMe$_2$)$_2$)ScI(THF)$_2$ and KC_8, though no bridging aryl species were isolated.[53]

Photolysis reactions of **3.2-Th** in substituted aryl solvents such as toluene, mesitylene, and fluorobenzene were attempted as well. Photolysis in toluene led to a color change to orange, similar to the reaction in benzene. ^{1}H NMR analysis reveals a mixture of numerous products, presumably from the activation of the aryl ring at the *ortho*, *meta*, and *para* positions, as well as the formation of **3.3-Th**, further evidence that **3.3-Th** is formed without the activation of benzene (or any solvent). There does not appear to be a strong preference for activation at any position, making isolation of a single product untenable. Photolysis was less fruitful in mesitylene, with detection of **3.3-Th** as the major product, but less evidence of aryl activation products in the ^{1}H NMR spectrum. In contrast, reactions in fluorobenzene rapidly became brown, but the major identifiable products were Cp*OsH$_5$ and Cp*Os(μ-H)$_4$OsCp*, with no isolable C–H or C–F activation products of fluorobenzene.

In order to investigate potential metal-metal bonding interactions in compounds **3.3-U**, **3.3-Th**, and **3.4-Th**, better elucidate the positions of the hydrides in these photolysis products, and gain insight into the benzene activation by **3.4-Th**, we undertook a similar computational investigation as for complexes **3.2-U** and **3.2-Th**, at the same level of theory. Complexes with different numbers of hydrides were computed, considering different spin states for each (see Figures 3.8-3.9 and Tables 3.7-3.8). For **3.3-U** and **3.3-Th**, the most stable structures are found with eleven hydrides in a triplet and singlet spin state, respectively, which is in line with the presence of a U(IV) and Th(IV) actinide center (Figure 3.3, left and Figure 3.8). In **3.4-Th**, a singlet spin state is once again most stable, indicating a Th(IV) center, while only ten hydrides are found due to the substitution of the bridging phenyl ligand with one hydride (Figure 3.3, right). It is worth noting that the three optimized structures are the only structures with linear Os–Os–Cp*$_{centroid}$ angles in line with the experimental structures; simulations with greater or fewer hydrides converged to structures with bent Os–Os–Cp*$_{centroid}$ geometries. As with complexes **3.2-An**, the optimized geometries compare well with the experimental data (Table 3.9). Among others, the Os–Os distance is well reproduced computationally at 2.47 Å, versus about 2.46 Å experimentally.

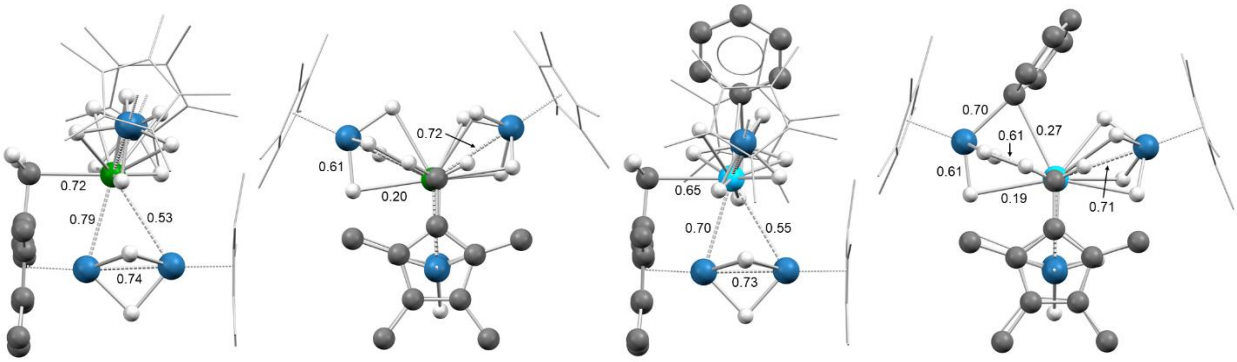

Figure 3.3 Calculated structures for **3.3-U** (left) and **3.4-Th** (right), with WBIs labeled for select bonds. Color key: green (uranium), light blue (thorium), blue (osmium), gray (carbon), white

(hydrogen). Methyl hydrogen atoms have been omitted and non-cyclometallated Cp* ligands have been wireframed for clarity.

NBO analyses were carried out on the most stable optimized structures for the three complexes. WBIs of 0.53-0.79 were found for the U–Os interactions in **3.3-U**, while WBIs of 0.55-0.70 were found for the Th–Os interactions in **3.3-Th**, with comparable values of 0.55-0.71 in **3.4-Th**. These values are lower than that found in the parent complexes **3.2-An** but indicates that a substantial covalent bonding An–Os interaction remains in these complexes. As in complexes **3.2-U** and **3.2-Th**, the M–H bonds are more covalent with Os than U or Th, with Os–H WBIs of 0.30-0.60 compared to An–H WBIs of 0.02-0.21 for 3-An and 4-An.

Interestingly, in the three complexes an Os–Os WBI of 0.73-0.74 is found in the diosmium fragment. This result is in line with a substantial bonding interaction between the two Os centers. The interaction is further corroborated at the NBO level where a single covalent Os–Os bond is found in **3.3-U** and **3.3-Th** (only a second order perturbation was found for **3.4-Th**). This bond implies a 5d-5d overlap between the two Os centers in an almost non-polarized covalent bond (Table 3.11); the hydride-mediated metal–metal interaction can also be observed in the HOMO-3 orbital of **3.3-Th** and **3.4-Th** (Figure 3.4, left). As previously mentioned, the diosmium fragment in complexes **3-An** and **3.4-Th** is similar to $[Cp^*OsH_2]_2$, which Girolami and coworkers concluded to contain no Os–Os bond, citing the results of Morokuma on the analogous diruthenium complex.[32,33,54,55] There are several key differences between the compounds and computational methods used which may contribute to the discrepancy. First, the calculations in the 1993 paper were done using the *ab initio*, restricted Hartree-Fock method, in contrast to the semi-empirical method employed in this study. The geometry of the antibonding osmium, $5d_z2$ orbitals is different between the thorium compounds and $[Cp^*RuH_2]_2$ as well. In the HOMO-4 orbital of **3.3-Th** and **3.4-Th**, the osmium $5d_z2$ orbitals are oriented such that they overlap with a thorium 6d orbital (Figure 3.4, right), resulting in δ-antibonding interactions between the osmium orbitals rather than the σ-antibonding overlap predicted for $[Cp^*RuH_2]_2$. This should decrease the repulsive interaction experienced between the osmium centers, and may account for the difference in the calculated Os–Os bonding.

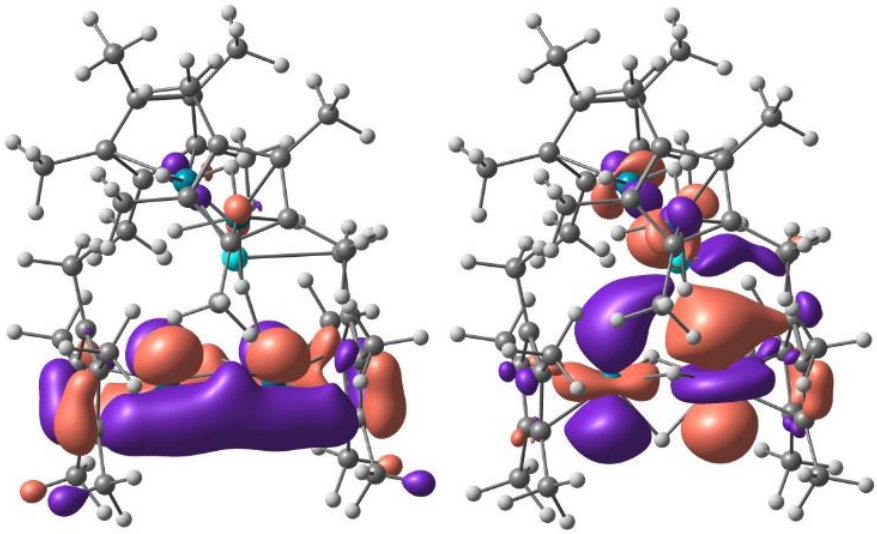

Figure 3.4 Kohn-Sham Os–Os bonding orbitals for **3.3-Th** derived from DFT (isovalue = 0.03). The orbitals for **3.4-Th** are nearly identical and may be found in Figure 3.10.

Conclusions

Complexes **3.3-U**, **3.3-Th**, and **3.4-Th** are notable as products of photolysis-driven C–H activation by both actinide and transition metal centers. All feature the intramolecular activation of sp^3 C–H bonds, while **3.4-Th** also features the uncommon intermolecular activation of a benzene sp^2 C–H bond by an actinide complex, resulting in a bridging Th–C–Os bond. Actinide-promoted benzene activation has been documented in uranium inverse sandwich complexes, resulting in the direct borylation of benzene and naphthalene, but in this instance did not result in the formation of a new An–C bond following activation.[56] Despite the report of thermolytic benzene C–H activation by thorium neopentyl species in 1981, subsequent examples of benzene activation by f-block metal centers remain few and far between. These reports have been limited to the rare-earth elements and involve thermolysis at high temperatures[57,58] or strong reductants such as a potassium mirror or KC_8.[59,53] In contrast, the formation of **3.4-Th** is photolytically driven, occurring at ambient conditions. The osmium polyhydride $OsH_6(P^iPr_3)_2$ has been known to activate a variety of polycyclic, *N*-substituted aromatic species upon thermolysis,[60–64] but no reactivity with smaller, less substituted aromatics such as toluene or benzene has been reported. In addition, the photolytic reactivity of **3.2-U** and **3.2-Th** is not solely dependent on the osmium centers, as both Cp^*OsH_5 and $[Cp^*OsH_2]_2$ do not form stable Os–C bonds upon photolysis in benzene, although H/D exchange is observed when Cp^*OsH_5 is photolyzed to form $[Cp^*OsH_2]_2$ in C_6D_6. This is particularly exciting, as heterobimetallic cooperative C–H activation is a field of growing interest, yet systems featuring An–TM cooperativity are rare.[65]

In the context of actinide photolysis reactivity, the reactions of **3.2-U** and **3.2-Th** are also unique. In contrast to previously reported photolytic actinide C–H activations, which were driven by irradiation of stable or transient terminal uranium nitrides[66,67] or Th–C bond cleavage,[68] here the chemistry is driven by the loss of hydrides as H_2. This contributes to the minimal record of photolytic elimination of hydrides in the actinides,[25] as well as photolysis-driven actinide–metal bond formation.[30] It is, to the best of our knowledge, the first documented example of the formation of new actinide bonds *via* photolytic hydride elimination. Future work will focus on the synthesis of heterobimetallic hydride-supported An–TM systems, hydride elimination to drive unsupported metal-metal bonding in those systems, and potential cooperative reactivity with small molecules.

Experimental

General considerations: Unless otherwise noted, all reactions were performed using standard Schlenk line techniques under an atmosphere of nitrogen, or in an MBraun inert atmosphere glove box under an atmosphere of nitrogen. Glassware and Celite® were stored in an oven at ca. 150 °C for at least 3 h prior to use. Molecular sieves (4 Å) were activated by heating to 200 °C overnight under vacuum prior to storage in a glovebox. NMR spectra were recorded on Bruker AV-600, AV-700, and AV-500 spectrometers. ^{1}H chemical shifts are given relative to residual solvent peaks and are recorded in units of parts per million (ppm). FT-IR samples were prepared as Nujol mulls pressed between KBr plates, with data collected with a Nicolet iS10 FT-IR spectrometer. Melting points were determined using sealed capillaries prepared under nitrogen on an OptiMelt automated

melting point system. Elemental analyses were determined at the Microanalytical Facility at the College of Chemistry, University of California, Berkeley.

Materials: Tetrahydrofuran (THF), toluene, benzene, *n*-hexane, and *n*-pentane were purified by passage through columns of activated alumina and degassed by sparging with dinitrogen. Deuterated solvents were degassed with three freeze-pump-thaw cycles and stored over molecular sieves. Benzylpotassium,[69] Cp^*OsH_5,[33,70] UCl_4,[71] and $ThCl_4(DME)_2$[72] were synthesized according to literature procedures. Mesitylene and fluorobenzene were purchased from commercial sources and stored on molecular sieves. All other chemicals were purchased from commercial sources and used as received.

***In-situ* generation of K[Cp*OsH$_5$] (3.1):**
Cp^*OsH_5 (5.0 mg, 0.015 mmol, 1.0 equiv.) and benzyl potassium (2.0 mg, 0.015 mmol, 1.0 equiv.) were dissolved in 0.4 mL d_8-THF each, then added together in a J. Young NMR tube and sealed. The colorless and orange solutions immediately become very pale yellow (nearly colorless). Analysis of the solution revealed the quantitative formation of **3.1** along with toluene. ^{1}H NMR (500 MHz, THF-d_8): δ 2.16 (s, 15H, CH_{3Cp^*}), –17.15 (s, 4H, Os–H).

Synthesis of Th{(μ-H$_4$)OsCp*}$_4$ (3.2-Th):
Cp^*OsH_5 (160.4 mg, 0.485 mmol, 4.0 equiv.) and benzyl potassium (63.1 mg, 0.485 mmol, 4.0 equiv.) were added to a 20 mL scintillation vial with THF (4 mL) to generate a solution of $K[Cp^*OsH_4]$. $ThCl_4(DME)_2$ (67.2 mg, 0.121 mmol, 1.0 equiv.) was dissolved in THF (4 mL) and added to the $K[Cp^*OsH_4]$ solution. The colorless solution immediately turned pale yellow and opaque as KCl precipitated out of solution. After stirring at room temperature for 2 h, the solvent was removed *in vacuo*. The crude solid was then triturated with *n*-hexane and the product was extracted with *n*-hexane (8 mL), filtered through Celite, and concentrated (2 mL). This solution was cooled to –40 °C, affording cubic colorless crystals (104.4 mg). A second crop of crystals were grown after concentration of the mother liquor to 1 mL (124.3 mg total, 66% total yield). Mp ca. 190 °C (slow decomp. starting from 110 °C); ^{1}H NMR (600 MHz, C_6D_6): δ 2.13 (s, 60H, CH_{3Cp^*}), –11.01 (s, 16H, Th–H–Os); ^{13}C NMR (600 MHz, C_6D_6): δ 92.5 ($C_5(CH_3)_5$), 12.5 ($C_5(CH_3)_5$); IR (Nujol mull on KBr): 1993 (s), 1073 (w), 1034 (m), 863 (m), 560 (m); Anal. Calcd (%) for $ThOs_4C_{40}H_{76}$: C, 31.00; H, 4.94. Found: C, 31.16; H, 4.93.

Synthesis of U{(μ-H$_4$)OsCp*}$_4$ (3.2-U):
Cp^*OsH_5 (146.8 mg, 0.444 mmol, 4.0 equiv.) and benzyl potassium (59.8 mg, 0.459 mmol, 4.1 equiv.) were added to a 20 mL scintillation vial with THF (4 mL) to generate a solution of $K[Cp^*OsH_4]$. UCl_4 (42.1 mg, 0.111 mmol, 1.0 equiv.) was dissolved in THF (4 mL) and added to the $K[Cp^*OsH_4]$ solution. The colorless solution immediately turned bright yellow and opaque as KCl precipitated out of solution. After stirring at room temperature for 2 h, the solvent was removed *in vacuo*. The crude solid was then triturated with *n*-hexane and the product was extracted with *n*-hexane (8 mL), filtered through Celite, and concentrated (2 mL). This solution was cooled to –40 °C, affording cubic yellow crystals (87.6 mg). A second crop of crystals were grown after concentration of the mother liquor to 1 mL (110.7 mg total, 64% total yield). Mp ca. 240 °C (decomp.); ^{1}H NMR (600 MHz, C_6D_6): δ 89.8 (s, 16H, U–H–Os), 3.65 (s, 60H, CH_{3Cp^*}); ^{13}C NMR (600 MHz, C_6D_6): δ 114.2 ($C_5(CH_3)_5$), 12.4 ($C_5(CH_3)_5$); IR (Nujol mull on KBr): 2091 (w), 1990

(s), 1072 (w), 1034 (m), 862 (m), 559 (m); Anal. Calcd (%) for $UOs_4C_{40}H_{76}$: C, 30.88; H, 4.92. Found: C, 31.21; H, 4.75.

Synthesis of 3.3-U *via* photolysis of 3.2-U:
Complex **3.2-U** (38.5 mg, 0.025 mmol) was dissolved in 3 mL benzene and transferred to a Teflon-tap sealed quartz cuvette. The yellow solution was photolyzed for 6 hours, yielding a dark brown solution. After removing the solvent *in vacuo*, the crude solid was extracted with *n*-hexane, filtered, and concentrated to 0.5 mL. This solution was allowed to stand at RT overnight, yielding dark brown crystals (16.7 mg, 43% yield). Mp. 235 °C (slow decomp. starting from 208 °C); ^{1}H NMR (600 MHz, C_6D_6): δ 55.46 (s, 8H, Cp*Os_a(μ-*H*)$_4$), 9.84 (s, 6H, [(CH_2)*Me*$_4C_5$]Os_c), 1.43 (s, 30H, *Cp**Os_a), –2.44 (s, 15H, *Cp**Os_b), –4.82 (s, 6H, [(CH_2)*Me*$_4C_5$]Os_c), –89.11 (s, 2H, [(C*H*$_2$)Me$_4C_5$]Os_c); ^{13}C NMR (600 MHz, C_6D_6): δ 106.43, 74.34 (*C*H_2), 29.97, 12.75, 7.52, –4.46; IR (Nujol mull on KBr): 1990 (s), 1152 (w), 1072 (w), 1032 (m), 947 (w), 890 (w), 625 (w), 585 (w); Anal. Calcd (%) for $UOs_4C_{40}H_{73}$•C_6H_{14}: C, 33.71; H, 5.35. Found: Sample 1: C, 33.81; H, 4.97. Sample 2: C, 33.78; H, 5.04.

Synthesis of 3.3-Th and 3.4-Th *via* photolysis of 3.2-Th:
Complex **3.2-Th** (29.4 mg, 0.019 mmol) was dissolved in 3 mL benzene and transferred to a Teflon-tap sealed quartz cuvette. The colorless solution was photolyzed for 6 hours, yielding an orange solution. After removing the solvent *in vacuo*, the crude solid was extracted with *n*-hexane and minimal benzene, filtered, and concentrated to 0.5 mL. This solution was allowed to stand at RT overnight, yielding orange crystals composed of 22% **3.3-Th** and 78% **3.4-Th** (mol/mol %) by ^{1}H NMR (20.4 mg, 66% total yield by Th). Both products consistently co-crystallize in similar ratios across multiple syntheses, and show no evident differences in color. Mp. 215 °C (slow decomp. starting from 182 °C); IR (Nujol mull on KBr): 2009 (s), 1566 (w), 1549 (w), 1152 (w), 1071 (w), 1033 (m), 901 (w), 710 (w), 585 (w); Anal. Calcd (%) for 0.22 $ThOs_4C_{40}H_{70}$·C_6H_{14}/0.78 $ThOs_4C_{46}H_{74}$: C, 34.06; H, 4.73. Found: C, 34.29; H, 4.85.

Isolation of **3.3-Th**: A sample of **3.2-Th** (9.6 mg, 0.006 mmol) was dissolved in 0.75 mL benzene and photolyzed in a sealed J.Young NMR tube for 66.5 hours, then dried *in vacuo*, extracted with *n*-hexane, filtered, and concentrated to 0.5 mL. This solution was allowed to stand at –40 °C overnight, yielding orange crystals of **3.3-Th** (1.7 mg, 17% yield).

3.3-Th: ^{1}H NMR (700 MHz, C_6D_6): δ 7.98 (d, 1H, H_d), 7.76 (d, 1H, H_c), 7.20 (td, 1H, H_e), 7.07 (m, 2H, H_f/$H_{f'}$), 2.87 (s, 3H, Cp*$_{activ}$), 2.79 (s, 3H, Cp*$_{activ}$), 2.15 (s, 15H, Cp*), 2.13 (s, 15H, Cp*), 1.87 (s, 15H, Cp*), 1.82 (s, 3H, Cp*$_{activ}$), 1.77 (s, 3H, Cp*$_{activ}$), 1.37 (d, 1H, H_a), 1.08 (d, 1H, H_b), –8.16 (t, 1H, H_h), –9.80 (s, 3H, $H_{hydride}$), –10.54 (d, 1H, H_g), –10.84 (s, 1H, H_i), –11.59 (s, 4H, Cp*Os(μ-*H*)$_4$Th); ^{13}C NMR (600 MHz, C_6D_6): δ 155.0 (C_d), 150.9 (C_c), 136.0 (C_c–*C*–C_d), 130.1 (C_e), 127.0 (C_f, $C_{f'}$), 100.4, 93.9, 92.0, 80.3, 79.7, 78.8, 77.4, 77.4, 61.0 (CH_aH_b), 14.0, 13.7, 12.6, 11.8, 11.4, 11.1, 11.1.

Isolation of **3.4-Th**: A single sample containing 16.1 mg **3.3-Th** and 13.7 mg **3.4-Th** was recrystallized from a 1:1 *n*-hexane/benzene solution at –40 °C, yielding 8.2 mg of crystals containing 88% **3.4-Th** (mol%).

3.4-Th: ^{1}H NMR (600 MHz, C_6D_6) δ 2.89 (s, 6H, Cp*$_{activ.}$), 2.16 (s, 15H, *Cp**Os(μ-H)$_3$OsCp*$_{activ.}$), 2.13 (s, 30H, [*Cp**Os(μ-H)$_4$]$_2$Th), 1.77 (s, 6H, Cp*$_{activ.}$), 1.34 (s, 2H, C*H*$_2$–Th), –9.76 (s, 3H, Cp*Os(μ-*H*)$_3$OsCp*$_{activ}$), –11.07 (s, 8H, [Cp*Os(μ-*H*)$_4$]$_2$Th); ^{13}C NMR (600 MHz, C_6D_6): δ 103.6 (Cp*$_{activ.}$, ring C), 92.9 ([*C*$_5$Me$_5$Os(μ-H)$_4$]$_2$Th), 80.9 (*C*$_5$Me$_5$Os(μ-H)$_3$OsCp*$_{active}$), 79.7 (Cp*$_{activ.}$, ring C), 77.2 (Cp*$_{activ.}$, ring C), 65.6 (Th–*C*H$_2$), 13.8 (Cp*$_{activ.}$, CH$_3$), 12.4 ([C$_5$*Me*$_5$Os(μ-H)$_4$]$_2$Th), 11.7 (C$_5$*Me*$_5$Os(μ-H)$_3$OsCp*$_{active}$), 10.9 (Cp*$_{activ.}$, CH$_3$).

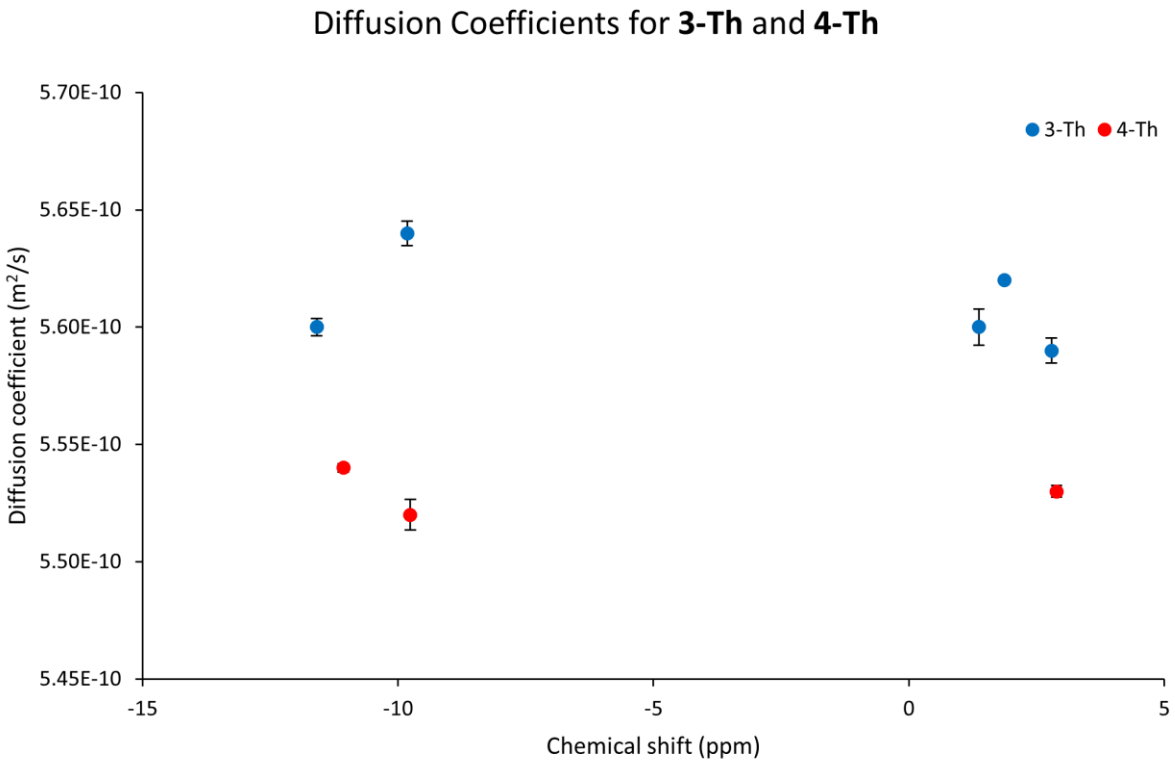

Figure 3.5 Diffusion coefficients calculated for ^{1}H NMR resonances from DOSY of a ~1:1 sample of **3.3-Th**/**3.4-Th**. Experiments were run at 298 K with a sample of 3.5·10^{-5} M **3.3-Th**/**3.4-Th** in C_6D_6 on a NEO-400 instrument.

X-ray crystallography details

In a dry nitrogen glovebox, samples of single crystals of were coated in Paratone-N oil for transport to the Advanced Light Source (ALS) or CheXray. Crystals were mounted on a MiTeGen 10 μm aperture Dual-Thickness MicroMount loop (ALS) or Kaptan loop (CheXray). X-ray diffraction data for **3.2-Th**, **3.2-U**, **3.3-U**, and **3.4-Th** were collected at the ALS, Lawrence Berkeley National Lab, Berkeley, CA, station 12.2.1 using a silicon monochromated beam of 17 keV (λ = 0.7288 Å) synchrotron radiation. Data was collected at 100 K, with the crystals cooled by a stream of dry nitrogen. Bruker APEX3 software was used for the data collections, Bruker SAINT v8.37A or V8.38A software was used to conduct the cell refinement and data reduction procedures,[73] and absorption corrections were carried out by a multi-scan method utilizing the SADABS program.[73] X-ray diffraction data for **3.3-Th** were collected at CheXray, Berkeley, CA, using a Rigaku XtaLAB P200 equipped with a MicroMax-007 HF microfocus rotating anode and a Pilatus 200K hybrid pixel array detector. Data was collected using Mo Kα radiation (λ =

0.71073 Å). All data collections were conducted at 100 K, with the crystals cooled by a stream of dry nitrogen. CrysAlis Pro was used for the data collections and data processing, including a multi-scan absorption correction applied using the SCALE3 ABSPACK scaling algorithm within CrysAlis Pro. Initial structure solutions were found using direct methods (SHELXT),[74] and refinements were carried out using SHELXL-2014,[75] as implemented by Olex2.[76] Thermal parameters for all non-hydrogen atoms were refined anisotropically. Hydrogen atoms were placed in calculated positions and refined isotropically. Thermal ellipsoid plots were made using Mercury.[77] The structures have been deposited to the Cambridge Crystallographic Data Centre (CCDC) with deposition numbers 2346841 (**3.2-Th**), 2346842 (**3.2-U**), 2346843 (**3.3-U**), 2346844 (**3.3-Th**), and 2346845 (**3.4-Th**).

Table 3.2 Crystal data for complexes **3.2-Th**, **3.2-U**, **3.3-U**, **3.3-Th**, and **3.4-Th**. *Hydrides are not observed, and are therefore not included in the empirical formulas.

Compound	**3.2-Th**	**3.2-U**	**3.3-U**	**3.3-Th**	**3.4-Th**
Empirical formula*	$C_{40}H_{60}Os_4Th$	$C_{40}H_{60}Os_4U$	$C_{40}H_{59}Os_4U$	$C_{40}H_{59}Os_4Th \cdot C_6H_{14}$	$C_{46}H_{64}Os_4Th$
Formula weight	1533.72	1539.71	1538.70	1618.88	1609.81
Temperature/K	100	100	100	100.00	100
Crystal system	monoclinic	cubic	monoclinic	orthorhombic	tetragonal
Space group	$P2_1/c$	Pa-3	C2/c	$Pmn2_1$	$P4_2/ncm$
a/Å	23.163(2)	21.395(2)	40.875(4)	18.6052(5)	13.7391(15)
b/Å	12.6413(11)	21.395(2)	10.0269(10)	9.9998(3)	13.7391(15)
c/Å	15.7810(13)	21.395(2)	23.315(2)	13.3830(4)	25.158(3)
α/°	90	90	90	90	90
β/°	91.796(3)	90	113.731(4)	90	90
γ/°	90	90	90	90	90
Volume/Å^3	4618.6(7)	9793(3)	8747.7(15)	2489.88(12)	4748.8(12)
Z	4	8	8	2	4
ρ_{calc}g/cm^3	2.206	2.089	2.337	2.159	2.252
μ/mm^{-1}	15.063	12.483	13.975	13.171	14.656
F(000)	2776.0	5568.0	5560.0	1486.0	2936.0
Crystal size/mm^3	0.05 × 0.05 × 0.01	0.1 × 0.1 × 0.05	0.03 × 0.02 × 0.02	0.2 × 0.1 × 0.05	0.3 × 0.02 × 0.02
Radiation	synchrotron (λ = 0.7288)	synchrotron (λ = 0.7288)	synchrotron (λ = 0.7288)	Mo Kα (λ = 0.71073)	synchrotron (λ = 0.7288)
2Θ range for data collection/°	1.882 to 29.119	3.904 to 55.608	3.642 to 52.084	5.982 to 61.012	4.608 to 52.084
Index ranges	$-30 \le h \le 30$, $0 \le k \le 16$, $0 \le l \le 21$	$-27 \le h \le 27$, $-27 \le k \le 27$, $-27 \le l \le 27$	$-49 \le h \le 49$, $-12 \le k \le 11$, $-28 \le l \le 28$	$-25 \le h \le 26$, $-14 \le k \le 13$, $-19 \le l \le 18$	$-16 \le h \le 16$, $-16 \le k \le 16$, $-30 \le l \le 30$
Reflections collected	11258	125415	52702	27906	53451
Independent reflections	11258	3605 [R_{int} = 0.1087, R_{sigma} = 0.0356]	7991 [R_{int} = 0.0502, R_{sigma} = 0.0335]	7260 [R_{int} = 0.0340, R_{sigma} = 0.0322]	2317 [R_{int} = 0.1416, R_{sigma} = 0.0530]
Data/restraints/parameters	11258/206/427	3605/75/206	7991/186/532	7260/31/279	2317/51/177
Goodness-of-fit on F^2	1.041	1.109	1.069	1.045	1.214
Final R indexes [I>=2σ (I)]	R1 = 0.0387, wR2 = 0.0801	R_1 = 0.0342, wR_2 = 0.0965	R_1 = 0.0314, wR_2 = 0.0670	R_1 = 0.0216, wR_2 = 0.0463	R_1 = 0.0445, wR_2 = 0.1071
Final R indexes [all data]	R1 = 0.0521, wR2 = 0.0862	R_1 = 0.0372, wR_2 = 0.0986	R_1 = 0.0397, wR_2 = 0.0701	R_1 = 0.0247, wR_2 = 0.0470	R_1 = 0.0510, wR_2 = 0.1101
Largest diff. peak/hole / e Å^{-3}	2.77/-2.36	1.35/-1.91	1.90/-2.54	2.13/-1.14	1.08/-1.37
CSD entry	2346841	2346842	2346843	2346844	2346845

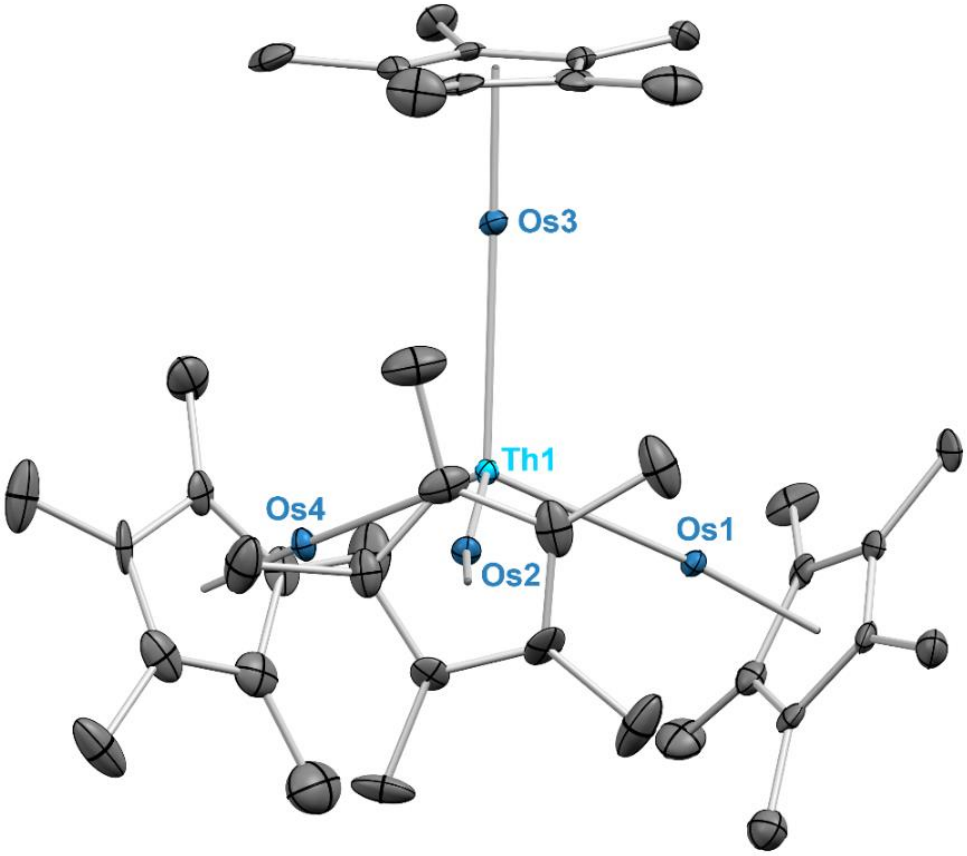

Figure 3.6 ORTEP diagram for **3.2-Th**, with ellipsoids drawn at the 50% probability level. Hydrogen atoms have been omitted for clarity. Selected bond distances (Å) and angles (°): Th1–Os1 3.0215(7), Th1–Os2 3.0379(6), Th1–Os3 3.0183(6), Th1–Os4 3.0288(7), Th1–Os1–Cp*$_{centroid}$ 175.81(2), Th1–Os2–Cp*$_{centroid}$ 171.10(2), Th1–Os3–Cp*$_{centroid}$ 176.92(3), Th1–Os4–Cp*$_{centroid}$ 171.88(3), Os1–Th1–Os4 103.291(17), Os2–Th1–Os4 115.805(16).

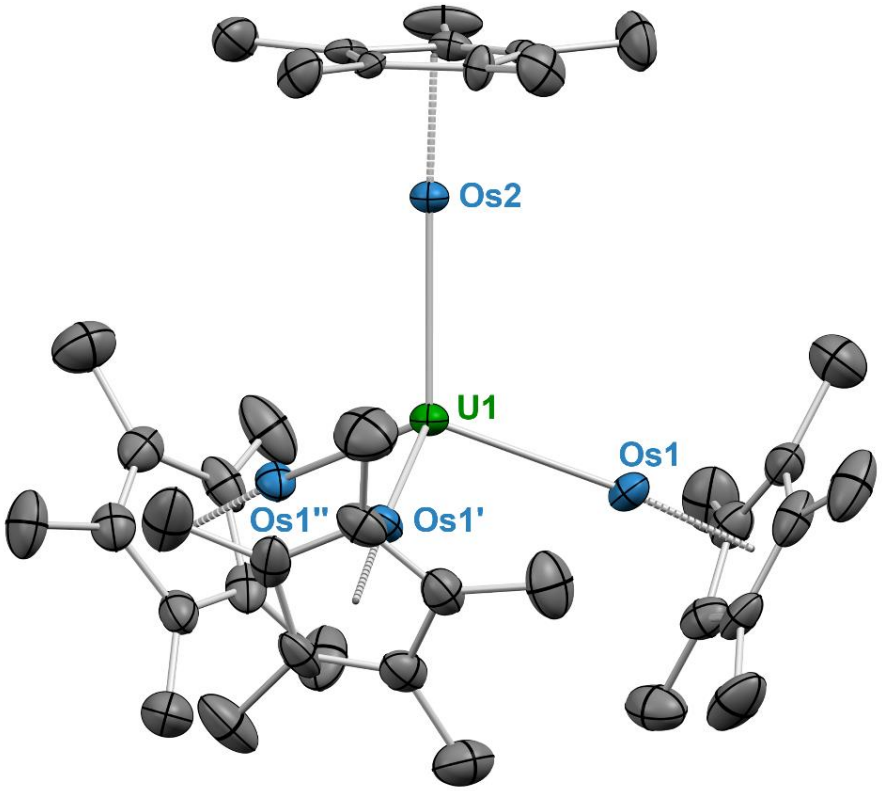

Figure 3.7 ORTEP diagram for **3.2-U**, with ellipsoids drawn at the 50% probability level. Hydrogen atoms have been omitted for clarity. Selected bond distances (Å) and angles (°): U1–Os1 2.9501(7), U1–Os2 2.9490(6), U1–Os1–Cp*$_{centroid}$ 175.30(2), U1–Os2–Cp*$_{centroid}$ 176.40(2), Os1–U1–Os1' 107.900(9), Os1–U1–Os2 110.998(9).

Computational details

All DFT calculations were carried out with the Gaussian 09 suite of programs.[78] Geometries were fully optimized in gas phase without symmetry constraints, employing the B3PW91 functional.[79,80] The nature of the extrema was verified by analytical frequency calculations. The calculation of electronic energies and enthalpies of the extrema of the potential energy surface (minima and transition states) were performed at the same level of theory as the geometry optimizations. IRC calculations were performed to confirm the connections of the optimized transition states. Uranium, thorium and osmium atoms were treated with a small core effective core potential (60 MWB), associated with its adapted basis set[81–83] augmented, for osmium atoms, with a polarization function (ζ_f = 0.886).[84] For the other elements (H and C), Pople's double-ζ basis set 6-31G(d,p) was used.[85–87] Dispersion corrections were treated with the D3 version of Grimme's dispersion with Becke-Johnson damping.[88] The electronic charges (at the DFT level) were computed using the natural population analysis (NPA) technique.[89]

Table 3.3 Relative energies for **3.2-U** as a function of the number of bent Cp^* groups and spin multiplicity.

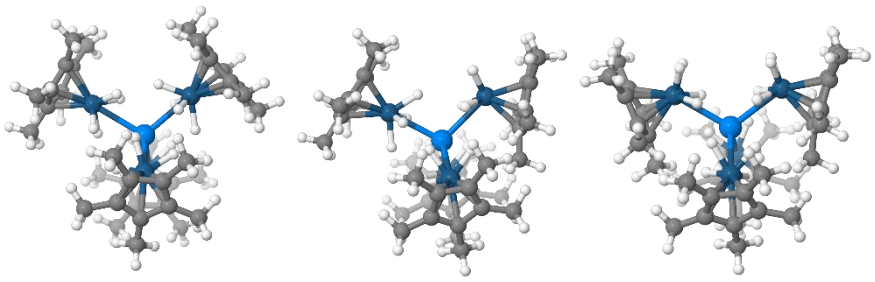

3.2-U	Linear			1 - Bent			2 - Bent		
Spin Multiplicity	singlet	triplet	quintet	singlet	triplet	quintet	singlet	triplet	quintet
ΔrH (kcal/mol)	25.0	0.0	–	26.1	1.5	35.7	30.7	4.1	39.0
ΔrG (kcal/mol)	26.7	0.0	–	32.5	5.9	40.4	39.7	12.7	44.5

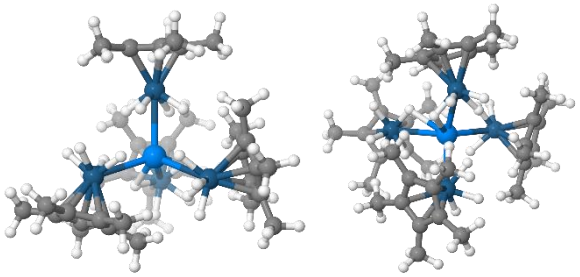

3.2-U	3 - Bent			4 - Bent		
Spin Multiplicity	singlet	triplet	quintet	singlet	triplet	quintet
ΔrH (kcal/mol)	–	9.9	–	58.6	17.5	–
ΔrG (kcal/mol)	–	17.9	–	66.8	27.3	–

Table 3.4 Relative energies for **3.2-Th** as a function of the number of bent Cp^* groups and spin multiplicity.

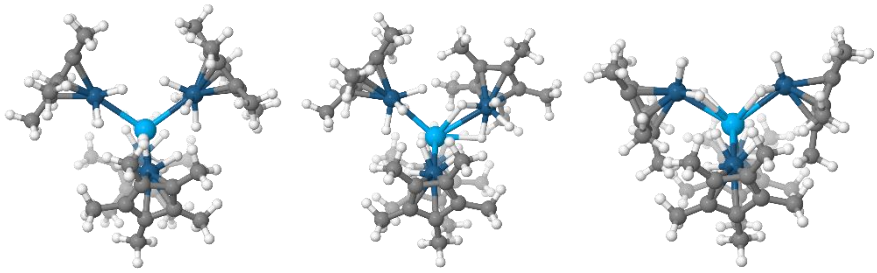

3.2-Th	Linear		1 - Bent		2 - Bent	
Spin Multiplicity	singlet	triplet	singlet	triplet	singlet	triplet
ΔrH (kcal/mol)	0.0	269.7	1.4	57.7	5.8	58.4
ΔrG (kcal/mol)	0.0	273.7	6.3	61.0	15.5	65.9

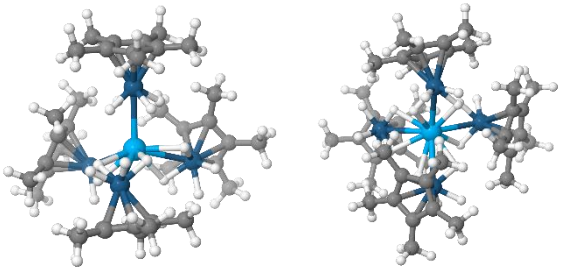

3.2-Th	3 - Bent		4 - Bent	
Spin Multiplicity	singlet	triplet	singlet	triplet
ΔrH (kcal/mol)	11.7	63.6	18.7	–
ΔrG (kcal/mol)	20.5	73.43	30.5	–

Table 3.5 Tabulated calculated bond distances/angles and Os-H frequencies for **3.2-U** and **3.2-Th**.

	3.2-U	**3.2-Th**
	Linear (triplet)	Linear (singlet)
Os – H distance (Å)	[1.628 – 1.652] (μ-H)	[1.630 – 1.648] (μ-H)
U/Th – H distance (Å)	[2.444 – 2.595]	[2.536 – 2.601]
U/Th – Os distance (Å)	2.911, 2.912, 2.913, 2.913	2.977, 2.977, 2.977, 2.978
U/Th – C (Cp*) distance (Å)	[4.858 – 5.037]	[4.945 – 5.089]
U/Th – C (Me-Cp*) distance (Å)	[5.476 – 5.708]	[5.564 – 5.749]
Os – C (Cp*) distance (Å)	[2.187 – 2.300]	[2.187 – 2.306]
Os – U/Th – Re angle (º)	[107.1 – 111.3]	[108.3 – 110.1]
Os – U/Th – Cp(centroid) angle (º)	177.1 ; 177.8 ; 179.1 ; 179.2	178.9 ; 179.8 ; 179.2, 179.3
Os – H (cm^{-1})	[2056 – 1947], [939 – 818], [675 – 653]	[2051 – 1963], [947 – 838], [678 – 667]

Table 3.6 Wiberg Bond Indexes and Natural Charges for **3.2-U** and **3.2-Th**.

	3.2-U (triplet)	**3.2–Th (singlet)**
	Wiberg Bond Indexes (WBI)	
Os – H	[0.57 – 0.60]	[0.60]
U/Th – (μ-H)	[0.18 – 0.24]	[0.19 – 0.21]
U/Th – Os	[0.81 - 0.83]	[0.72 - 0.73]
U/Th – C (Cp*)	[0.02 - 0.03]	[0.02 - 0.03]
2nd Order NBO Analysis	LP C (Cp*) → LP* U: [4 – 5] kcal/mol	BD C (Cp*) – C (Cp*) → LP*: 3 kcal/mol BD C (Me-Cp*) – H → LP* U: [8 - 12] kcal/mol LP C (Cp*) → LP* U: [42 – 48] kcal/mol
	Natural Charges	
Os Natural Charges	-0.95 - -0.96	-0.98
U/Th Natural Charges	-0.36	0.04

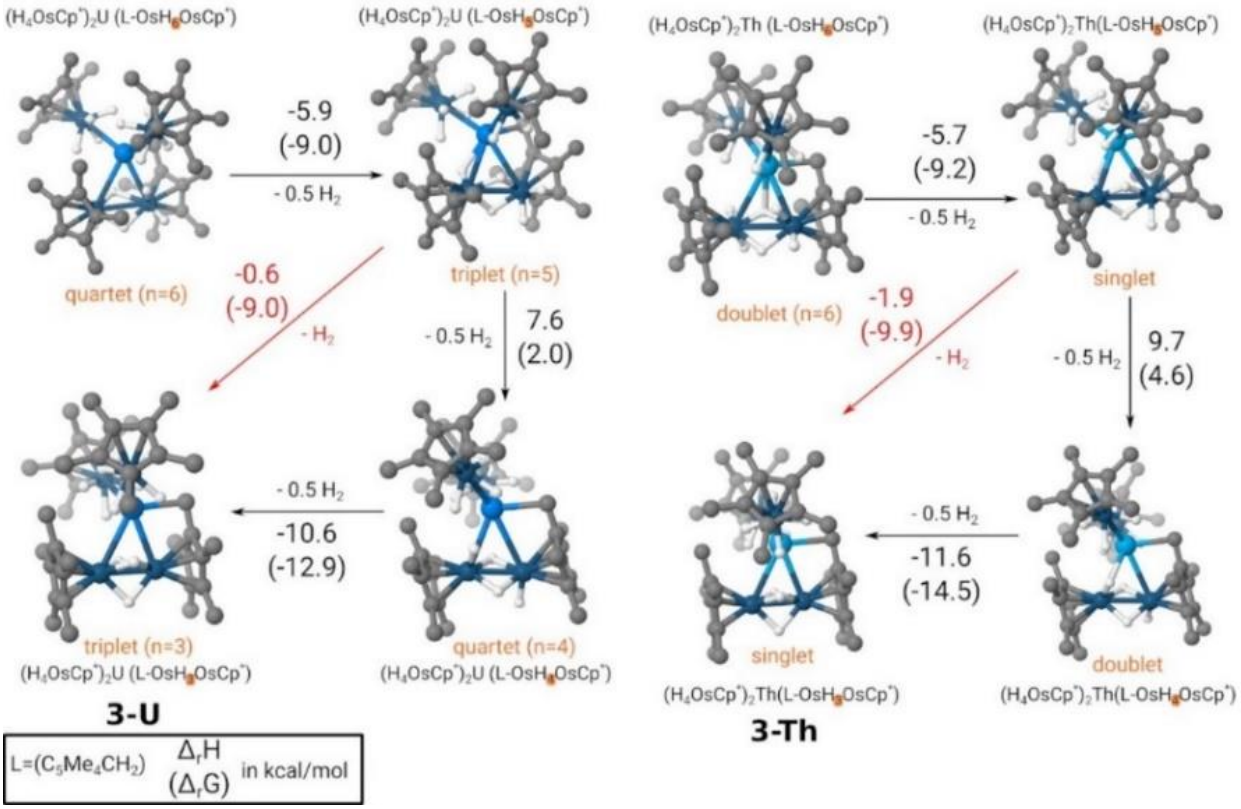

Figure 3.8 Determination of the number of hydrogen atoms on complexes **3.3-U** and **3.3-Th**.

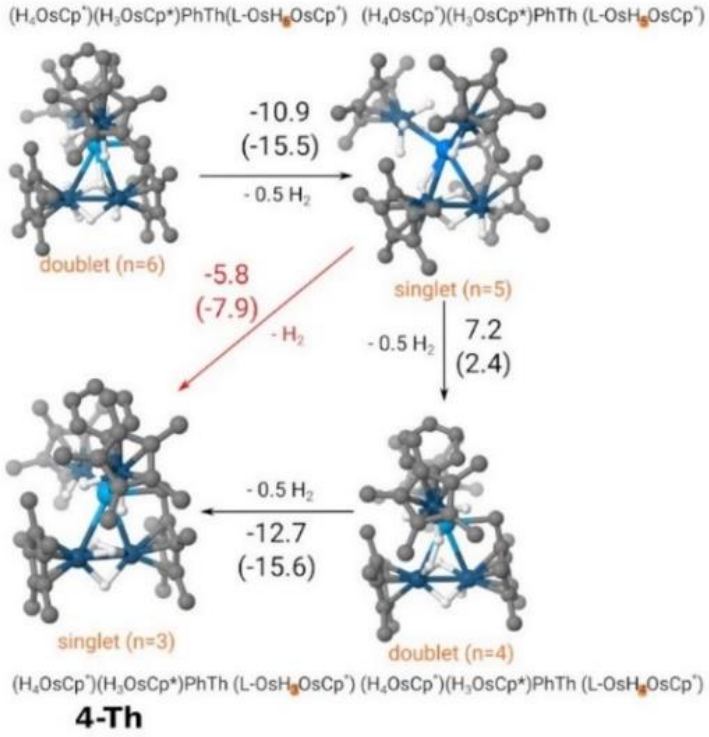

Figure 3.9 Determination of the number of hydrogen atoms on complex **3.4-Th**.

Table 3.7 Relative energies for **3.3-U** as a function of the number of hydrogens atoms and of the spin multiplicity.

$(H_4OsCp^*)_2U((C_5Me_4CH_2)OsH_nOsCp^*)$	n=2			n = 3			n = 4		
Spin Multiplicity	doublet	quartet	sextet	singlet	triplet	quintet	doublet	quartet	sextet
ΔrH (kcal/mol)	1.1	0.0	34.3	25.6	0.0	23.3	2.7	0.0	29.3
ΔrG (kcal/mol)	0.6	0.0	32.6	26.8	0.0	22.9	3.6	0.0	27.8

$(H_4OsCp^*)_2U((C_5Me_4CH_2)OsH_nOsCp^*)$	n = 5			n = 6		
Spin Multiplicity	singlet	triplet	quintet	doublet	quartet	sextet
ΔrH (kcal/mol)	32.6	0.0	11.1	1.2	0.0	30.3
ΔrG (kcal/mol)	32.0	0.0	9.6	1.6	0.0	26.8

Table 3.8 Relative energies for **3.4-Th** as a function of the number of hydrogens atoms and of the spin multiplicity.

$(PhH_3OsCp^*)(H_4OsCp^*)Th((C_5Me_4CH_2)OsH_nOsCp^*)$	n = 0		n = 1		n = 2		n = 3	
Spin Multiplicity	doublet	quartet	singlet	triplet	doublet	quartet	singlet	triplet
ΔrH (kcal/mol)	0.0	44.4	0.0	36.5	0.0	46.8	0.0	42.4
ΔrG (kcal/mol)	0.0	40.8	0.0	34.6	0.0	45.2	0.0	36.6

$(PhH_3OsCp^*)(H_4OsCp^*)Th((C_5Me_4CH_2)OsH_nOsCp^*)$	n = 4		n = 5		n = 6	
Spin Multiplicity	doublet	quartet	singlet	triplet	doublet	quartet
ΔrH (kcal/mol)	0.0	-	0.0	-	0.0	-
ΔrG (kcal/mol)	0.0	-	0.0	-	0.0	-

Table 3.9 Tabulated calculated bond distances/angles and Os–H frequencies for **3.3-U, 3.3-Th**, and **3.4-Th**.

	3.3–U (triplet)	**3.3–Th (singlet)**	**3.4–Th (singlet)**
Os – H distance (Å)	[1.630 – 1.649] $(H_4OsCp^*)_2$ [1.794 – 1.838] $((C_5Me_4CH_2)OsH_3OsCp^*)$	[1.632 – 1.647] $(H_4OsCp^*)_2$ [1.798 – 1.834] $((C_5Me_4CH_2)OsH_3OsCp^*)$	[1.625 – 1.642] $(H_4OsCp^*)_2$ [1.797 – 1.834] $((C_5Me_4CH_2)OsH_3OsCp^*)$
Os – C (Ph) distance (Å)	-	-	2.113
U/Th – H (distance (Å)	[2.464 – 2.543] $(H_4OsCp^*)_2$ [2.662, 2.667, 4.065] $((C_5Me_4CH_2)OsH_3OsCp^*)$	[2.542 – 2.630] $(H_4OsCp^*)_2$ [2.738, 2.734, 4.127] $((C_5Me_4CH_2)OsH_3OsCp^*)$	[2.518 – 2.644] $(H_4OsCp^*)_2$ [2.737, 2.742, 4.132] $((C_5Me_4CH_2)OsH_3OsCp^*)$
U/Th – C (Ph) distance (Å)	-	-	2.856
U/Th – Os distance (Å)	[2.918, 2.922] $(H_4OsCp^*)_2$ [2.856, 3.150] $((C_5Me_4CH_2)OsH_3OsCp^*)$	[2.984, 2.987] $(H_4OsCp^*)_2$ [2.941, 3.178] $((C_5Me_4CH_2)OsH_3OsCp^*)$	[3.040, 2.988] $(H_4OsCp^*)_2$ [2.948, 3.179] $((C_5Me_4CH_2)OsH_3OsCp^*)$
Os – Os distance (Å) $((C_5Me_4CH_2)OsH_3OsCp^*)$	2.474	2.475	2.472
Os – C (Cp*) distance (Å)	[2.188 – 2.301] $(H_4OsCp^*)_2$ [2.175 – 2.241] $((C_5Me_4CH_2)OsH_3OsCp^*)$	[2.193 – 2.309] $(H_4OsCp^*)_2$ [2.175 – 2.248] $((C_5Me_4CH_2)OsH_3OsCp^*)$	[2.183 – 2.318] $(H_4OsCp^*)_2$ [2.178 – 2.243] $((C_5Me_4CH_2)OsH_3OsCp^*)$
Os – C (Me-Cp*) distance (Å)	[3.306 – 3.412] $(H_4OsCp^*)_2$ [3.280 – 3.446] $((C_5Me_4CH_2)OsH_3OsCp^*)$	[3.313 – 3.421] $(H_4OsCp^*)_2$ [3.281 – 3.437] $((C_5Me_4CH_2)OsH_3OsCp^*)$	[3.305 – 3.431] $(H_4OsCp^*)_2$ [3.284 – 3.405] $((C_5Me_4CH_2)OsH_3OsCp^*)$
U/Th – C (CH2) distance (Å)	2.438	2.504	2.518
Os – U/Th – Os angle (º) (H_4OsCp^*)	116.3	120.7	135.6
Os – U/Th – Os angle (º) $((C_5Me_4CH_2)OsH_3OsCp^*)$	48.3	47.5	47.4
U/Th – Os – Os angle (º) $((C_5Me_4CH_2)OsH_3OsCp^*)$	72.0, 59.6	71.3, 61.2	71.2, 61.4
U/Th – Os – Cp (centroid) angle (º)	179.1, 179.1 $(H_4OsCp^*)_2$ 103.0, 121.7 $((C_5Me_4CH_2)OsH_3OsCp^*)$	178.1, 179.6 $(H_4OsCp^*)_2$ 103.6, 120.0 $((C_5Me_4CH_2)OsH_3OsCp^*)$	177.9, 177.6 $(H_4OsCp^*)_2$ 104.2, 119.3 $((C_5Me_4CH_2)OsH_3OsCp^*)$
Os – Os – Cp (centroid) angle (º)	175.0, 178.5	174.8, 178.7	175.3, 179.3
Os – H (cm^{-1})	[2050 – 1953] $(H_4OsCp^*)_2$ [1619 – 1561] $((C_5Me_4CH_2)OsH_3OsCp^*)$ [1061 – 1057, 1036, 947, 900, 776, 644] $((C_5Me_4CH_2)OsH_3OsCp^*)$ [930 – 918, 856 – 837, 644 – 642, 585 – 564] $(H_4OsCp^*)_2$	[2037 – 1964] $(H_4OsCp^*)_2$ [1608 – 1561] $((C_5Me_4CH_2)OsH_3OsCp^*)$ [1032 – 1019, 958, 907, 788, 648] $((C_5Me_4CH_2)OsH_3OsCp^*)$ [949 – 916, 887 – 846, 667 – 660, 588 – 570] $(H_4OsCp^*)_2$	[2072 – 1999] $(H_4OsCp^*)_2$ [1620 – 1565] $((C_5Me_4CH_2)OsH_3OsCp^*)$ [1061 – 1060, 1034, 958, 908, 790 – 787, 651] $((C_5Me_4CH_2)OsH_3OsCp^*)$ [955 – 923, 902, 875 – 825, 759, 674, 576 – 569] $(H_4OsCp^*)_2$

Table 3.10 Wiberg Bond Indexes and Natural Charges for **3.3-U, 3.3-Th**, and **3.4-Th**.

	3.3–U (triplet)	**3.3–Th (singlet)**	**3.4–Th (singlet)**
	Wiberg Bond Indexes (WBI)		
Os – H	[0.60 – 0.62] $(H_4OsCp^*)_2$ [0.32 – 0.41] $((C_5Me_4CH_2)OsH_3OsCp^*)$	[0.61 – 0.63] $(H_4OsCp^*)_2$ [0.32 – 0.41] $((C_5Me_4CH_2)OsH_3OsCp^*)$	[0.60 – 0.61] (PhH_3OsCp^*) [0.60 – 0.62] (H_4OsCp^*) [0.31 – 0.40] $((C_5Me_4CH_2)OsH_3OsCp^*)$
Os – Os $((C_5Me_4CH_2)OsH_3OsCp^*)$	0.74	0.73	0.73
U/Th – H	[0.18 – 0.21] $H_4OsCp^*)_2$ [0.14, 0.15, 0.01] $((C_5Me_4CH_2)OsH_3OsCp^*)$	[0.18 – 0.21] $H_4OsCp^*)_2$ [0.15, 0.16, 0.02] ((C5Me4CH2)OsH3OsCp*)	[0.16 – 0.21] (PhH_3OsCp^*) [0.18 – 0.20] (H_4OsCp^*) [0.16, 0.16, 0.03] ((C5Me4CH2)OsH3OsCp*)
U/Th – Os	[0.72, 0.72] $H_4OsCp^*)_2$ [0.79, 0.53] $((C_5Me_4CH_2)OsH_3OsCp^*)$	[0.69, 0.70] $H_4OsCp^*)_2$ [0.68, 0.53] $((C_5Me_4CH_2)OsH_3OsCp^*)$	[0.61 (Ph), 0.71] $(H_4OsCp^*)_2$ [0.70, 0.55] $((C_5Me_4CH_2)OsH_3OsCp^*)$
U/Th – CH_2	0.72	0.64	0.65
C (Cp*)–Os, C (Cp*)–Th	-	-	0.70, 0.27
Os – C (Cp*)	[0.31 – 0.42] $H_4OsCp^*)_2$ [0.35 – 0.43] $((C_5Me_4CH_2)OsH_3OsCp^*)$	[0.30 – 0.41] $H_4OsCp^*)_2$ [0.36 – 0.43] $((C_5Me_4CH_2)OsH_3OsCp^*)$	[0.30 – 0.41] (PhH_3OsCp^*) [0.29 – 0.41] (H_4OsCp^*) [0.36 – 0.42] $((C_5Me_4CH_2)OsH_3OsCp^*)$
	Natural Charges		
Os Natural Charges $(H_4OsCp^*)_2$	[-1.02, -1.03]	[-1.02, -1.03]	[-0.82 (Ph), -1.00]
Os Natural Charges $((C_5Me_4CH_2)OsH_3OsCp^*)$	[-0.57, -0.60]	[-0.60, -0.61]	[-0.58, -0.58]
U/Th Natural Charges	0.52	0.68	0.44

Table 3.11 NBO Analysis of the Os–Os bonding in **3.3-U**, **3.3-Th**, and **3.4-Th**.

3.3-U	**3.3-Th**	**3.4-Th**
Alpha Spin Orbitals (0.75325) BD (1)Os 15 -Os 16 (50.26%) Os 15 s(0.08%)p48.18(3.80%)d99.99(96.10%) (49.74%) Os 16 s(0.06%)p81.37(4.50%)d99.99(95.41%) (0.72128) BD (2)Os 15 -Os 16 (48.78%) Os 15 s(0.00%)p 1.00(3.14%)d30.83(96.84%) (51.22%) Os 16 s(0.00%)p1.00(3.44%)d28.04(96.54%) **Beta Spin Orbitals** (0.75552) BD (1)Os 15 -Os 16 (50.54%) Os 15 s(0.09%)p42.07(3.66%)d99.99(96.23%) (49.46%) Os 16 s(0.07%)p63.21(4.31%)d99.99(95.59%) (0.72156) BD (2)Os 15 -Os 16 (48.87%) Os 15 s(0.00%)p 1.00(3.12%)d31.01(96.86%) (51.13%) Os 16 s(0.00%)p 1.00(3.44%)d28.09(96.55%)	(1.83739) BD (1)Os 25 -Os 36 (55.70%) Os 25 s(0.24%)p 7.41(1.81%)d99.99(97.94%) (44.30%) Os 36 s(0.20%)p 8.17(1.65%)d99.99(98.14%) (1.59753) BD*(1)Os 25 -Os 36 (44.30%) Os 25 s(0.24%)p 7.41(1.81%)d99.99(97.94%) (55.70%) Os 36 s(0.20%)p 8.17(1.65%)d99.99(98.14%)	
Alpha Spin Orbitals CR Os 15 → LP* Os 16 ~190 LP Os 15 → LP* Os 16 ~140 CR Os 16 → LP* Os 15 ~150 LP Os 16 → LP*Os 15 ~70 **Beta Spin Orbitals** CR Os 15 → LP* Os 16 ~210 LP Os 15 → LP* Os 16 ~140 CR Os 16 → LP* Os 15 ~140 LP Os 16 → LP*Os 15 ~70	CR Os 25 → LP* Os 36 ~430 LP Os 25 → LP* Os 36 ~205 CR Os 36 → LP* Os 25 ~303 LP Os 36 → LP*Os 25 ~130	CR Os 30 → LP* Os 41 ~440 LP Os 30 → LP* Os 41 ~320 CR Os 41 → LP* Os 30 ~370 LP Os 41 → LP* Os 30 ~240

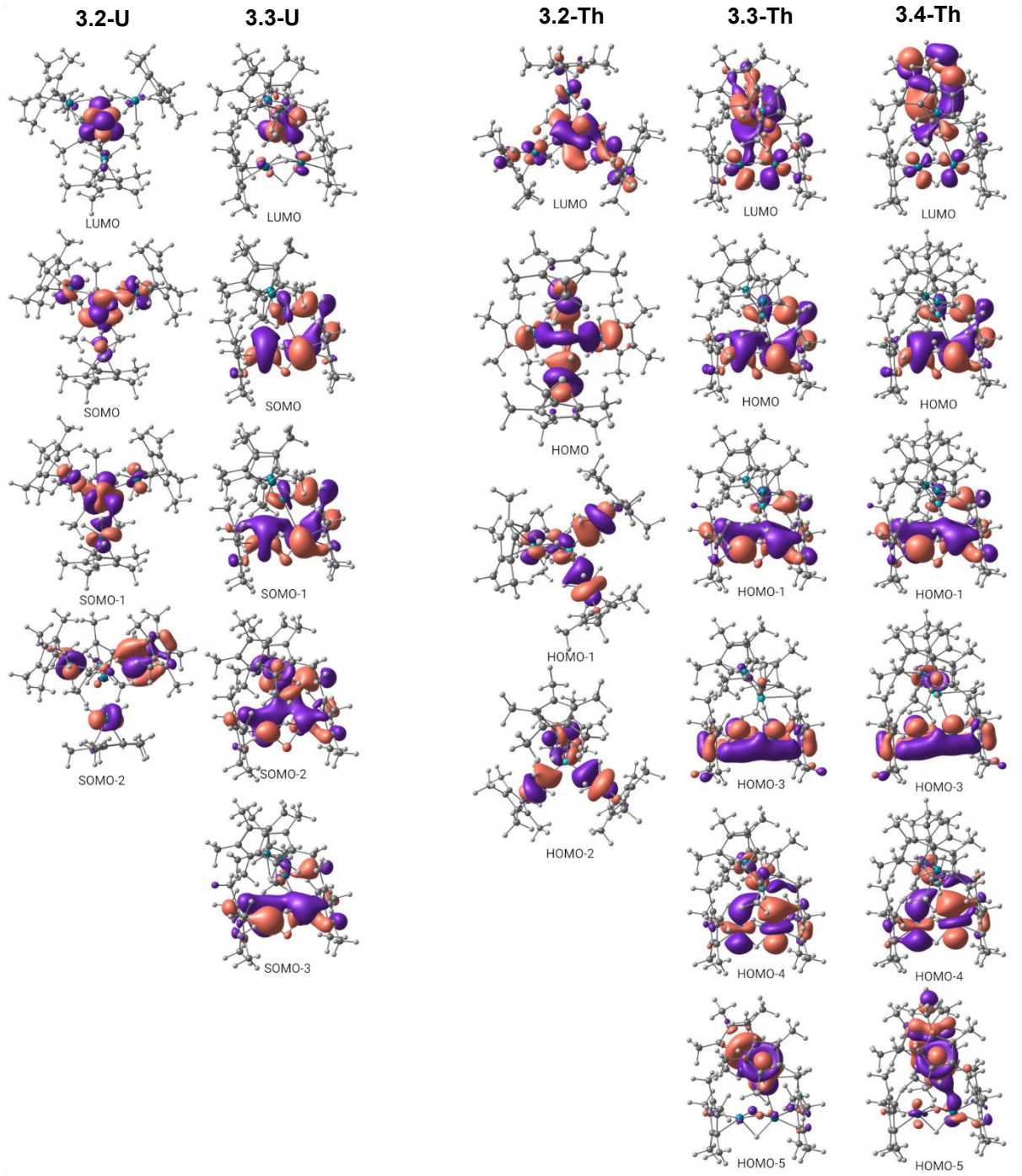

Figure 3.10 Lowest unoccupied molecular orbital and highest occupied molecular orbitals of complexes **3.2-U, 3.3-U, 3.2-Th, 3.3-Th**, and **3.4-Th**.

References

(1) Crossley, S. W. M.; Obradors, C.; Martinez, R. M.; Shenvi, R. A. Mn-, Fe-, and Co-Catalyzed Radical Hydrofunctionalizations of Olefins. *Chem. Rev.* **2016**, *116* (15), 8912–9000. https://doi.org/10.1021/acs.chemrev.6b00334.

(2) Esteruelas, M. A.; Oro, L. A. Dihydrogen Complexes as Homogeneous Reduction Catalysts. *Chem. Rev.* **1998**, *98* (2), 577–588. https://doi.org/10.1021/cr970322u.
(3) Jordan, A. J.; Lalic, G.; Sadighi, J. P. Coinage Metal Hydrides: Synthesis, Characterization, and Reactivity. *Chem. Rev.* **2016**, *116* (15), 8318–8372. https://doi.org/10.1021/acs.chemrev.6b00366.
(4) Eberhardt, N. A.; Guan, H. Nickel Hydride Complexes. *Chem. Rev.* **2016**, *116* (15), 8373–8426. https://doi.org/10.1021/acs.chemrev.6b00259.
(5) Ephritikhine, M. Synthesis, Structure, and Reactions of Hydride, Borohydride, and Aluminohydride Compounds of the f-Elements. *Chem. Rev.* **1997**, *97* (6), 2193–2242. https://doi.org/10.1021/cr960366n.
(6) Bowman, R. G.; Nakamura, R.; Fagan, P. J.; Burwell, R. L.; Marks, T. J. Catalystic Activity of Supported f-Element Organometallic Complexes. *J. Chem. Soc., Chem. Commun.* **1981**, No. 6, 257–258. https://doi.org/10.1039/C39810000257.
(7) He, M. Y.; Xiong, G.; Toscano, P. J.; Burwell, R. L. Jr.; Marks, T. J. Supported Organoactinides. Surface Chemistry and Catalytic Properties of Alumina-Bound Cyclopentadienyl and Pentamethylcyclopentadienyl Thorium and Uranium Hydrocarbyls and Hydrides. *J. Am. Chem. Soc.* **1985**, *107* (3), 641–652. https://doi.org/10.1021/ja00289a016.
(8) Perutz, R. N.; Procacci, B. Photochemistry of Transition Metal Hydrides. *Chem. Rev.* **2016**, *116* (15), 8506–8544. https://doi.org/10.1021/acs.chemrev.6b00204.
(9) Havela, L.; Legut, D.; Kolorenč, J. Hydrogen in Actinides: Electronic and Lattice Properties. *Rep. Prog. Phys.* **2023**, *86* (5), 056501. https://doi.org/10.1088/1361-6633/acbe50.
(10) Evans, W. J.; Meadows, J. H.; Hanusa, T. P. Organolanthanide and Organoyttrium Hydride Chemistry. 6. Direct Synthesis and Proton NMR Spectral Analysis of the Trimetallic Yttrium and Yttrium-Zirconium Tetrahydride Complexes, $\{[(C_5H_5)_2YH]_3H\}\{Li(THF)_4\}$ and $\{[(CH_3C_5H_4)_2YH]_2[(CH_3C_5H_4)_2ZrH]H\}$. *J. Am. Chem. Soc.* **1984**, *106* (16), 4454–4460. https://doi.org/10.1021/ja00328a027.
(11) Alvarez, D. Jr.; Caulton, K. G.; Evans, W. J.; Ziller, J. W. Reversible Opening and Closing of Hetero Trimetallic Units in $(C_5H_5)_2Y(THF)Re_2H_7(PMe_2Ph)_4$ and $(C_5H_5)_2LuRe_2H_7(PMe_2Ph)_4$. *J. Am. Chem. Soc.* **1990**, *112* (14), 5674–5676. https://doi.org/10.1021/ja00170a061.
(12) Alvarez, D. Jr.; Caulton, K. G.; Evans, W. J.; Ziller, J. W. Synthesis, Structure, and Reactivity of Heterometallic Polyhydride Complexes of Rhenium with Yttrium and Lutetium. *Inorg. Chem.* **1992**, *31* (26), 5500–5508. https://doi.org/10.1021/ic00052a028.
(13) Green, M. L. H.; Hughes, A. K.; Michaelidou, D. M.; Mountford, P. New Lanthanide–Hydrogen–Transition Metal Compounds: $[\{(PMe_3)_3WH_5\}_2Yb\cdot L_3]$ and $[\{(\eta\text{-}C_5H_5)_2NbH_2\}_2Yb\cdot L_3]$ Where $L_3=(MeOCH_2CH_2)_2O$. *J. Chem. Soc., Chem. Commun.* **1993**, No. 7, 591–593. https://doi.org/10.1039/C39930000591.
(14) Radu, N. S.; Gantzel, P. K.; Tilley, T. D. Lanthanide–Tungsten Heterobimetallic Complexes Viaσ-Bond Metathesis. *J. Chem. Soc., Chem. Commun.* **1994**, No. 10, 1175–1176. https://doi.org/10.1039/C39940001175.
(15) Schwartz, D. J.; Ball, G. E.; Andersen, R. A. Interactions of Cis-P_2PtX_2 Complexes (X = H, Me) with Bis(Pentamethylcyclopentadienyl)Ytterbium. *J. Am. Chem. Soc.* **1995**, *117* (22), 6027–6040. https://doi.org/10.1021/ja00127a016.

(16) Butovskii, M. V.; Tok, O. L.; Wagner, F. R.; Kempe, R. Bismetallocenes: Lanthanoid–Transition-Metal Bonds through Alkane Elimination. *Angewandte Chemie International Edition* **2008**, *47* (34), 6469–6472. https://doi.org/10.1002/anie.200800407.
(17) Sobaczynski, A. P.; Bauer, T.; Kempe, R. Heterometallic Hydride Complexes of Rare-Earth Metals and Ruthenium through C–H Bond Activation. *Organometallics* **2013**, *32* (5), 1363–1369. https://doi.org/10.1021/om301039g.
(18) Shima, T.; Hou, Z. Activation and Dehydrogenative Silylation of the C–H Bonds of Phosphine-Coordinated Ruthenium in Lu/Ru Heteromultimetallic Hydride Complexes. *Chemistry Letters* **2008**, *37* (3), 298–299. https://doi.org/10.1246/cl.2008.298.
(19) Shima, T.; Hou, Z. Rare Earth/d-Transition Metal Heteromultimetallic Polyhydride Complexes Based on Half-Sandwich Rare Earth Moieties. *Organometallics* **2009**, *28* (7), 2244–2252. https://doi.org/10.1021/om900024q.
(20) Takenaka, Y.; Shima, T.; Baldamus, J.; Hou, Z. Reduction of Transition-Metal-Coordinated Carbon Monoxide by a Rare-Earth Hydride Cluster: Isolation of Well-Defined Heteromultimetallic Oxycarbene, Oxymethyl, Carbene, and Methyl Complexes. *Angewandte Chemie International Edition* **2009**, *48* (42), 7888–7891. https://doi.org/10.1002/anie.200903660.
(21) Takenaka, Y.; Hou, Z. Lanthanide Terminal Hydride Complexes Bearing Two Sterically Demanding $C_5Me_4SiMe_3$ Ligands. Synthesis, Structure, and Reactivity. *Organometallics* **2009**, *28* (17), 5196–5203. https://doi.org/10.1021/om900453j.
(22) Shima, T.; Luo, Y.; Stewart, T.; Bau, R.; McIntyre, G. J.; Mason, S. A.; Hou, Z. Molecular Heterometallic Hydride Clusters Composed of Rare-Earth and d-Transition Metals. *Nature Chem* **2011**, *3* (10), 814–820. https://doi.org/10.1038/nchem.1147.
(23) Shima, T.; Hou, Z. Heterometallic Polyhydride Complexes Containing Yttrium Hydrides with Different Cp Ligands: Synthesis, Structure, and Hydrogen-Uptake/Release Properties. *Chemistry – A European Journal* **2013**, *19* (10), 3458–3466. https://doi.org/10.1002/chem.201203495.
(24) O, W. W. N.; Kang, X.; Luo, Y.; Hou, Z. PNP-Ligated Heterometallic Rare-Earth/Ruthenium Hydride Complexes Bearing Phosphinophenyl and Phosphinomethyl Bridging Ligands. *Organometallics* **2014**, *33* (4), 1030–1043. https://doi.org/10.1021/om401216v.
(25) Baudry, D.; Ephritikhine, M. Synthesis of a Hydride-Rich Uranium-Rhenium Dimer: $[(p\text{-}FC_6H_4)_3P]_2ReH_6U(\eta\text{-}C_5H_5)_3$. *J. Organomet. Chem.* **1986**, *311* (1), 189–192. https://doi.org/10.1016/0022-328X(86)80231-5.
(26) Cendrowski-Guillaume, S. M.; Lance, M.; Nierlich, M.; Vigner, J.; Ephritikhine, M. New Actinide Hydrogen Transition Metal Compounds. Synthesis of $[K(C_{12}H_{24}O_6)][(\eta\text{-}C_5Me_5)_2(Cl)UH_6Re(PPh_3)_2]$ and the Crystal Structure of Its Benzene Solvate. *J. Chem. Soc., Chem. Commun.* **1994**, No. 14, 1655–1656. https://doi.org/10.1039/C39940001655.
(27) Cendrowski-Guillaume, S. M.; Ephritikhine, M. Synthesis and Reactivity of Hydrogen-Rich Uranium–Rhenium Compounds; an Unsuspected Detrimental Effect of Alkali-Metal Halide on Chemical Metathesis. *J. Chem. Soc., Dalton Trans.* **1996**, No. 8, 1487–1491. https://doi.org/10.1039/DT9960001487.
(28) Altman, A. B.; Brown, A. C.; Rao, G.; Lohrey, T. D.; Britt, R. D.; Maron, L.; Minasian, S. G.; Shuh, D. K.; Arnold, J. Chemical Structure and Bonding in a Thorium(III)–Aluminum Heterobimetallic Complex. *Chem. Sci.* **2018**, *9* (18), 4317–4324. https://doi.org/10.1039/C8SC01260A.

(29) Ye, C. Z.; Rosal, I. D.; Boreen, M. A.; Ouellette, E. T.; Russo, D. R.; Maron, L.; Arnold, J.; Camp, C. A Versatile Strategy for the Formation of Hydride-Bridged Actinide–Iridium Multimetallics. *Chem. Sci.* **2023**, *14* (4), 861–868. https://doi.org/10.1039/D2SC04903A.
(30) Ward, A. L.; Lukens, W. W.; Lu, C. C.; Arnold, J. Photochemical Route to Actinide-Transition Metal Bonds: Synthesis, Characterization and Reactivity of a Series of Thorium and Uranium Heterobimetallic Complexes. *J. Am. Chem. Soc.* **2014**, *136* (9), 3647–3654. https://doi.org/10.1021/ja413192m.
(31) Gross, C. L.; Wilson, S. R.; Girolami, G. S. Synthesis and Characterization of $(C_5Me_5)_2Os_2Br_4$ and the Osmium Polyhydride $(C_5Me_5)OsH_5$: A New Synthetic Entry into Mono(Pentamethylcyclopentadienyl)Osmium Chemistry. *J. Am. Chem. Soc.* **1994**, *116* (22), 10294–10295. https://doi.org/10.1021/ja00101a057.
(32) Shima, T.; Suzuki, H. Heterobimetallic Polyhydride Complex, Cp*Ru(μ-H)$_4$OsCp* (Cp* = η^5-C_5Me_5). Synthesis and Reaction with Ethylene. *Organometallics* **2005**, *24* (16), 3939–3945. https://doi.org/10.1021/om0503996.
(33) Gross, C. L.; Girolami, G. S. Synthesis and Characterization of Osmium Polyhydrides. X-Ray Crystal Structures of $(C_5Me_5)OsH_5$ and $(C_5Me_5)_2Os_2H_4$. *Organometallics* **2007**, *26* (1), 160–166. https://doi.org/10.1021/om060920b.
(34) Shima, T.; Ichikawa, T.; Suzuki, H. Reaction of a Heterobimetallic Polyhydrido Cluster, [Cp*Ru(μ-H)$_4$OsCp*] (Cp* = η^5-C_5Me_5), with Diphenylacetylene. Regioselective C−H Bond Activation at the Osmium Center. *Organometallics* **2007**, *26* (25), 6329–6337. https://doi.org/10.1021/om700606q.
(35) Gilbert, T. M.; Bergman, R. G. Preparation and Reactions of Tetrahydrido(Pentamethylcyclopentadienyl)Iridium: A Novel Iridium(V) Polyhydride. *Organometallics* **1983**, *2* (10), 1458–1460. https://doi.org/10.1021/om50004a037.
(36) Cordero, B.; Gómez, V.; Platero-Prats, A. E.; Revés, M.; Echeverría, J.; Cremades, E.; Barragán, F.; Alvarez, S. Covalent Radii Revisited. *Dalton Trans.* **2008**, No. 21, 2832–2838. https://doi.org/10.1039/B801115J.
(37) Yang, L.; Powell, D. R.; Houser, R. P. Structural Variation in Copper(I) Complexes with Pyridylmethylamide Ligands: Structural Analysis with a New Four-Coordinate Geometry Index, T4. *Dalton Trans.* **2007**, No. 9, 955–964. https://doi.org/10.1039/B617136B.
(38) Popov, I. A.; Jian, T.; Lopez, G. V.; Boldyrev, A. I.; Wang, L.-S. Cobalt-Centred Boron Molecular Drums with the Highest Coordination Number in the CoB16− Cluster. *Nat Commun* **2015**, *6* (1), 8654. https://doi.org/10.1038/ncomms9654.
(39) Pollak, D.; Goddard, R.; Pörschke, K.-R. $Cs[H_2NB_2(C_6F_5)_6]$ Featuring an Unequivocal 16-Coordinate Cation. *J. Am. Chem. Soc.* **2016**, *138* (30), 9444–9451. https://doi.org/10.1021/jacs.6b02590.
(40) Daly, S. R.; Piccoli, P. M. B.; Schultz, A. J.; Todorova, T. K.; Gagliardi, L.; Girolami, G. S. Synthesis and Properties of a Fifteen-Coordinate Complex: The Thorium Aminodiboranate $[Th(H_3BNMe_2BH_3)_4]$. *Angewandte Chemie International Edition* **2010**, *49* (19), 3379–3381. https://doi.org/10.1002/anie.200905797.
(41) Bernstein, E. R.; Hamilton, W. C.; Keiderling, T. A.; La Placa, S. J.; Lippard, S. J.; Mayerle, J. J. 14-Coordinate Uranium(IV). Structure of Uranium Borohydride by Single-Crystal Neutron Diffraction. *Inorg. Chem.* **1972**, *11* (12), 3009–3016. https://doi.org/10.1021/ic50118a027.

(42) Blake, A. V.; Fetrow, T. V.; Theiler, Z. J.; Vlaisavljevich, B.; Daly, S. R. Homoleptic Uranium and Lanthanide Phosphinodiboranates. *Chem. Commun.* **2018**, *54* (44), 5602–5605. https://doi.org/10.1039/C8CC02862A.
(43) Hlina, J. A.; Pankhurst, J. R.; Kaltsoyannis, N.; Arnold, P. L. Metal–Metal Bonding in Uranium–Group 10 Complexes. *J. Am. Chem. Soc.* **2016**, *138* (10), 3333–3345. https://doi.org/10.1021/jacs.5b10698.
(44) Feng, G.; McCabe, K. N.; Wang, S.; Maron, L.; Zhu, C. Construction of Heterometallic Clusters with Multiple Uranium–Metal Bonds by Using Dianionic Nitrogen–Phosphorus Ligands. *Chem. Sci.* **2020**, *11* (29), 7585–7592. https://doi.org/10.1039/D0SC00389A.
(45) Evans, W. J.; Miller, K. A.; DiPasquale, A. G.; Rheingold, A. L.; Stewart, T. J.; Bau, R. A Crystallizable F-Element Tuck-In Complex: The Tuck-in Tuck-over Uranium Metallocene $[(C_5Me_5)U\{\mu\text{-}\eta^5\text{:}\eta^1\text{:}\eta^1\text{-}C_5Me_3(CH_2)_2\}(\mu\text{-}H)_2U(C_5Me_5)_2]$. *Angewandte Chemie International Edition* **2008**, *47* (27), 5075–5078. https://doi.org/10.1002/anie.200801062.
(46) Gardner, B. M.; McMaster, J.; Lewis, W.; Blake, A. J.; Liddle, S. T. A Crystallizable Dinuclear Tuck-In-Tuck-Over Tuck-Over Dialkyl Tren Uranium Complex and Double Dearylation of BPh_4^- To Give the BPh_2-Functionalized Metallocycle $[U\{N(CH_2CH_2NSiMe_3)_2(CH_2CH_2NSiMe_2CHBPh_2)\}(THF)]$. *J. Am. Chem. Soc.* **2009**, *131* (30), 10388–10389. https://doi.org/10.1021/ja904459q.
(47) Adams, R. D.; Rassolov, V.; Zhang, Q. Synthesis and Transformations of Triosmium Carbonyl Cluster Complexes Containing Bridging Aryl Ligands. *Organometallics* **2012**, *31* (8), 2961–2964. https://doi.org/10.1021/om300235n.
(48) Adams, R. D.; Rassolov, V.; Zhang, Q. Unsaturated Triosmium Carbonyl Cluster Complexes with Bridging Aryl Ligands: Structures, Bonding, and Transformations. *Organometallics* **2013**, *32* (21), 6368–6378. https://doi.org/10.1021/om4007399.
(49) Adams, R. D.; Luo, Z.; Wong, Y. O. Bridging Phenyl Ligands. Unsaturated Mercury-Triosmium Carbonyl Cluster Complexes Containing Bridging Phenyl Ligands. *J. Organomet. Chem.* **2015**, *784*, 46–51. https://doi.org/10.1016/j.jorganchem.2014.08.009.
(50) Fernández, E. J.; Laguna, A.; López-de-Luzuriaga, J. M.; Monge, M.; Montiel, M.; Olmos, M. E.; Rodríguez-Castillo, M. Photophysical and Theoretical Studies on Luminescent Tetranuclear Coinage Metal Building Blocks. *Organometallics* **2006**, *25* (15), 3639–3646. https://doi.org/10.1021/om060181z.
(51) Moret, M.-E.; Chen, P. Mononuclear Organometallic Platinum(II) Complexes and Platinum(II)−Copper(I) Mixed Complexes from Symmetrical 3,5-Bis(Iminoacetyl)Pyrazolate Ligands. *Organometallics* **2008**, *27* (19), 4903–4916. https://doi.org/10.1021/om800403y.
(52) Moret, M.-E.; Chen, P. Interaction of Organoplatinum(II) Complexes with Monovalent Coinage Metal Triflates. *J. Am. Chem. Soc.* **2009**, *131* (15), 5675–5690. https://doi.org/10.1021/ja900449y.
(53) Huang, W.; Dulong, F.; Khan, S. I.; Cantat, T.; Diaconescu, P. L. Bimetallic Cleavage of Aromatic C–H Bonds by Rare-Earth-Metal Complexes. *J. Am. Chem. Soc.* **2014**, *136* (50), 17410–17413. https://doi.org/10.1021/ja510761j.
(54) Suzuki, H.; Omori, H.; Lee, D. H.; Yoshida, Y.; Morooka, Y. A Novel Dinuclear Tetrahydride Bridged Ruthenium Complex, $(\eta^5\text{-}C_5Me_5)Ru(\mu\text{-}H)_4Ru(\eta^5\text{-}C_5Me_5)$. *Organometallics* **1988**, *7* (10), 2243–2245. https://doi.org/10.1021/om00100a032.

(55) Koga, N.; Morokuma, K. Ab Initio Study on the Structure and H_2 Dissociation Reaction of a Tetrahydride-Bridged Dinuclear Ru Complex, $(C_5H_5)Ru(\mu\text{-}H)_4Ru(C_5H_5)$. *Journal of Molecular Structure* **1993**, *300*, 181–189. https://doi.org/10.1016/0022-2860(93)87016-3.
(56) Arnold, P. L.; Mansell, S. M.; Maron, L.; McKay, D. Spontaneous Reduction and C–H Borylation of Arenes Mediated by Uranium(III) Disproportionation. *Nature Chem* **2012**, *4* (8), 668–674. https://doi.org/10.1038/nchem.1392.
(57) Thompson, M. E.; Baxter, S. M.; Bulls, A. R.; Burger, B. J.; Nolan, M. C.; Santarsiero, B. D.; Schaefer, W. P.; Bercaw, J. E. σ-Bond Metathesis for Carbon-Hydrogen Bonds of Hydrocarbons and Sc-R (R = H, Alkyl, Aryl) Bonds of Permethylscandocene Derivatives. Evidence for Noninvolvement of the π System in Electrophilic Activation of Aromatic and Vinylic C-H Bonds. *J. Am. Chem. Soc.* **1987**, *109* (1), 203–219. https://doi.org/10.1021/ja00235a031.
(58) Maron, L.; Werkema, E. L.; Perrin, L.; Eisenstein, O.; Andersen, R. A. Hydrogen for Fluorine Exchange in C_6F_6 and C_6F_5H by Monomeric $[1,3,4\text{-}(Me_3C)_3C_5H_2]_2CeH$: Experimental and Computational Studies. *J. Am. Chem. Soc.* **2005**, *127* (1), 279–292. https://doi.org/10.1021/ja0451012.
(59) Coles, M. P.; Hitchcock, P. B.; Lappert, M. F.; Protchenko, A. V. Syntheses and Structures of the Crystalline, Highly Crowded 1,3-Bis(Trimethylsilyl)Cyclopentadienyls $[MCp''_3]$ (M = Y, Er, Yb), $[PbCp''_2]$, $[\{YCp''_2(\mu\text{-}OH)\}_2]$, $[(ScCp''_2)_2(\mu\text{-}\eta^2\text{:}\eta^2\text{-}C_2H_4)]$, $[YbCp''_2Cl(\mu\text{-}Cl)K(18\text{-}Crown\text{-}6)]$, and $[\{KCp''\}_\infty]$. *Organometallics* **2012**, *31* (7), 2682–2690. https://doi.org/10.1021/om2009364.
(60) Esteruelas, M. A.; Masamunt, A. B.; Oliván, M.; Oñate, E.; Valencia, M. Aromatic Diosmatricyclic Nitrogen-Containing Compounds. *J. Am. Chem. Soc.* **2008**, *130* (35), 11612–11613. https://doi.org/10.1021/ja8048892.
(61) Esteruelas, M. A.; Fernández, I.; Herrera, A.; Martín-Ortiz, M.; Martínez-Álvarez, R.; Oliván, M.; Oñate, E.; Sierra, M. A.; Valencia, M. Multiple C−H Bond Activation of Phenyl-Substituted Pyrimidines and Triazines Promoted by an Osmium Polyhydride: Formation of Osmapolycycles with Three, Five, and Eight Fused Rings. *Organometallics* **2010**, *29* (4), 976–986. https://doi.org/10.1021/om901030q.
(62) Eguillor, B.; Esteruelas, M. A.; Fernández, I.; Gómez-Gallego, M.; Lledós, A.; Martín-Ortiz, M.; Oliván, M.; Oñate, E.; Sierra, M. A. Azole Assisted C–H Bond Activation Promoted by an Osmium-Polyhydride: Discerning between N and NH. *Organometallics* **2015**, *34* (10), 1898–1910. https://doi.org/10.1021/acs.organomet.5b00174.
(63) Esteruelas, M. A.; Larramona, C.; Oñate, E. Osmium-Mediated Direct C–H Bond Activation at the 8-Position of Quinolines. *Organometallics* **2016**, *35* (11), 1597–1600. https://doi.org/10.1021/acs.organomet.6b00264.
(64) Cancela, L.; Esteruelas, M. A.; López, A. M.; Oliván, M.; Oñate, E.; San-Torcuato, A.; Vélez, A. Osmium- and Iridium-Promoted C–H Bond Activation of 2,2′-Bipyridines and Related Heterocycles: Kinetic and Thermodynamic Preferences. *Organometallics* **2020**, *39* (11), 2102–2115. https://doi.org/10.1021/acs.organomet.0c00156.
(65) Lachguar, A.; Pichugov, A. V.; Neumann, T.; Dubrawski, Z.; Camp, C. Cooperative Activation of Carbon–Hydrogen Bonds by Heterobimetallic Systems. *Dalton Trans.* **2024**, *53* (4), 1393–1409. https://doi.org/10.1039/D3DT03571A.
(66) Thomson, R. K.; Cantat, T.; Scott, B. L.; Morris, D. E.; Batista, E. R.; Kiplinger, J. L. Uranium Azide Photolysis Results in C–H Bond Activation and Provides Evidence for a

Terminal Uranium Nitride. *Nature Chem* **2010**, *2* (9), 723–729. https://doi.org/10.1038/nchem.705.
(67) King, D. M.; Tuna, F.; McInnes, E. J. L.; McMaster, J.; Lewis, W.; Blake, A. J.; Liddle, S. T. Isolation and Characterization of a Uranium(VI)–Nitride Triple Bond. *Nature Chem* **2013**, *5* (6), 482–488. https://doi.org/10.1038/nchem.1642.
(68) Settineri, N. S.; Arnold, J. Insertion, Protonolysis and Photolysis Reactivity of a Thorium Monoalkyl Amidinate Complex. *Chem. Sci.* **2018**, *9* (10), 2831–2841. https://doi.org/10.1039/C7SC05328B.
(69) Bailey, P. J.; Coxall, R. A.; Dick, C. M.; Fabre, S.; Henderson, L. C.; Herber, C.; Liddle, S. T.; Loroño-González, D.; Parkin, A.; Parsons, S. The First Structural Characterisation of a Group 2 Metal Alkylperoxide Complex: Comments on the Cleavage of Dioxygen by Magnesium Alkyl Complexes. *Chemistry – A European Journal* **2003**, *9* (19), 4820–4828. https://doi.org/10.1002/chem.200305053.
(70) Shima, T.; Suzuki, H. Heterobimetallic Polyhydride Complex, Cp*Ru(μ-H)$_4$OsCp* (Cp* = η^5-C_5Me_5). Synthesis and Reaction with Ethylene. *Organometallics* **2005**, *24* (16), 3939–3945. https://doi.org/10.1021/om0503996.
(71) Kiplinger, J. L.; Morris, D. E.; Scott, B. L.; Burns, C. J. Convenient Synthesis, Structure, and Reactivity of $(C_5Me_5)U(CH_2C_6H_5)_3$: A Simple Strategy for the Preparation of Monopentamethylcyclopentadienyl Uranium(IV) Complexes. *Organometallics* **2002**, *21* (26), 5978–5982. https://doi.org/10.1021/om0206610.
(72) Cantat, T.; Scott, B. L.; Kiplinger, J. L. Convenient Access to the Anhydrous Thorium Tetrachloride Complexes $ThCl_4(DME)_2$, $ThCl_4$(1,4-Dioxane)$_2$ and $ThCl_4(THF)_{3.5}$ Using Commercially Available and Inexpensive Starting Materials. *Chem. Commun.* **2010**, *46* (6), 919–921. https://doi.org/10.1039/B923558B.
(73) APEX2, APEX3, SADABS, TWINABS and SAINT. Bruker AXS. Madison, WI, USA.
(74) Sheldrick, G. M. *SHELXT* – Integrated Space-Group and Crystal-Structure Determination. *Acta Crystallogr A Found Adv* **2015**, *71* (1), 3–8. https://doi.org/10.1107/S2053273314026370.
(75) Sheldrick, G. M. Crystal Structure Refinement with *SHELXL*. *Acta Crystallogr C Struct Chem* **2015**, *71* (1), 3–8. https://doi.org/10.1107/S2053229614024218.
(76) Dolomanov, O. V.; Bourhis, L. J.; Gildea, R. J.; Howard, J. A. K.; Puschmann, H. *OLEX2* : A Complete Structure Solution, Refinement and Analysis Program. *J Appl Crystallogr* **2009**, *42* (2), 339–341. https://doi.org/10.1107/S0021889808042726.
(77) Macrae, C. F.; Bruno, I. J.; Chisholm, J. A.; Edgington, P. R.; McCabe, P.; Pidcock, E.; Rodriguez-Monge, L.; Taylor, R.; van de Streek, J.; Wood, P. A. Mercury CSD 2.0– New Features for the Visualization and Investigation of Crystal Structures. *Journal of Applied Crystallography* **2008**, *41*, 466–470.
(78) Frisch, M. J.; Trucks, G. W.; Schlegel, H. B.; Scuseria, G. E.; Robb, M. A.; Cheeseman, J. R.; Scalmani, G.; Barone, V.; Petersson, G. A.; Nakatsuji, H.; Li, X.; Caricato, M.; Marenich, A.; Bloino, J.; Janesko, B. G.; Gomperts, R.; Mennucci, B.; Hratchian, H. P.; Ortiz, J. V.; Izmaylov, A. F.; Sonnenberg, J. L.; Williams-Young, D.; Ding, F.; Lipparini, F.; Egidi, F.; Goings, J.; Peng, B.; Petrone, A.; Henderson, T.; Ranasinghe, D.; Zakrzewski, V. G.; Gao, J.; Rega, N.; Zheng, G.; Liang, W.; Hada, M.; Ehara, M.; Toyota, K.; Fukuda, R.; Hasegawa, J.; Ishida, M.; Nakajima, T.; Honda, Y.; Kitao, O.; Nakai, H.; Vreven, T.; Throssell, K.; Montgomery, Jr., J. A.; Peralta, J. E.; Ogliaro, F.; Bearpark, M.; Heyd, J. J.; Brothers, E.; Kudin, K. N.; Staroverov, V. N.; Keith, T.; Kobayashi, R.; Normand, J.; Raghavachari, K.;

Rendell, A.; Burant, J. C.; Iyengar, S. S.; Tomasi, J.; Cossi, M.; Millam, J. M.; Klene, M.; Adamo, C.; Cammi, R.; Ochterski, J. W.; Martin, R. L.; Morokuma, K.; Farkas, O.; Foresman, J. B.; Fox, D. J. Gaussian 09.

(79) Perdew, J. P.; Chevary, J. A.; Vosko, S. H.; Jackson, K. A.; Pederson, M. R.; Singh, D. J.; Fiolhais, C. Atoms, Molecules, Solids, and Surfaces: Applications of the Generalized Gradient Approximation for Exchange and Correlation. *Phys. Rev. B* **1992**, *46* (11), 6671–6687. https://doi.org/10.1103/PhysRevB.46.6671.

(80) Becke, A. D. Density-functional Thermochemistry. III. The Role of Exact Exchange. *J. Chem. Phys.* **1993**, *98* (7), 5648–5652. https://doi.org/10.1063/1.464913.

(81) Cao, X.; Dolg, M. Segmented Contraction Scheme for Small-Core Actinide Pseudopotential Basis Sets. *Journal of Molecular Structure: THEOCHEM* **2004**, *673* (1), 203–209. https://doi.org/10.1016/j.theochem.2003.12.015.

(82) Cao, X.; Dolg, M.; Stoll, H. Valence Basis Sets for Relativistic Energy-Consistent Small-Core Actinide Pseudopotentials. *J. Chem. Phys.* **2003**, *118* (2), 487–496. https://doi.org/10.1063/1.1521431.

(83) Andrae, D.; Häußermann, U.; Dolg, M.; Stoll, H.; Preuß, H. Energy-Adjustedab Initio Pseudopotentials for the Second and Third Row Transition Elements. *Theoret. Chim. Acta* **1990**, *77* (2), 123–141. https://doi.org/10.1007/BF01114537.

(84) Ehlers, A. W.; Böhme, M.; Dapprich, S.; Gobbi, A.; Höllwarth, A.; Jonas, V.; Köhler, K. F.; Stegmann, R.; Veldkamp, A.; Frenking, G. A Set of F-Polarization Functions for Pseudo-Potential Basis Sets of the Transition Metals Sc–Cu, Y–Ag and La–Au. *Chemical Physics Letters* **1993**, *208* (1), 111–114. https://doi.org/10.1016/0009-2614(93)80086-5.

(85) Hariharan, P. C.; Pople, J. A. The Influence of Polarization Functions on Molecular Orbital Hydrogenation Energies. *Theoret. Chim. Acta* **1973**, *28* (3), 213–222. https://doi.org/10.1007/BF00533485.

(86) Ditchfield, R.; Hehre, W. J.; Pople, J. A. Self-Consistent Molecular-Orbital Methods. IX. An Extended Gaussian-Type Basis for Molecular-Orbital Studies of Organic Molecules. *J. Chem. Phys.* **1971**, *54* (2), 724–728. https://doi.org/10.1063/1.1674902.

(87) Hehre, W. J.; Ditchfield, R.; Pople, J. A. Self—Consistent Molecular Orbital Methods. XII. Further Extensions of Gaussian—Type Basis Sets for Use in Molecular Orbital Studies of Organic Molecules. *J. Chem. Phys.* **1972**, *56* (5), 2257–2261. https://doi.org/10.1063/1.1677527.

(88) Grimme, S.; Ehrlich, S.; Goerigk, L. Effect of the Damping Function in Dispersion Corrected Density Functional Theory. *Journal of Computational Chemistry* **2011**, *32* (7), 1456–1465. https://doi.org/10.1002/jcc.21759.

(89) Reed, A. E.; Curtiss, L. A.; Weinhold, F. Intermolecular Interactions from a Natural Bond Orbital, Donor-Acceptor Viewpoint. *Chem. Rev.* **1988**, *88* (6), 899–926. https://doi.org/10.1021/cr00088a005.

Chapter 4

Synthesis, Structure, and Bonding of Actinide–Rhenium Polyhydrides

Introduction

The study of main group[1–4] and transition metal (TM) hydrides[5–8] has seen interest since the advent of organometallic chemistry, contributing to fields such as catalytic hydrofunctionalization of olefins,[9] reduction of organic substrates and small molecules,[10,11] and electrocatalytic redox reactions,[12] among others. More recently, heterometallic hydride species have been studied for their fundamental bonding properties, cooperative reactivity,[13–16] and hydrogen storage capabilites.[17] Looking past the d-block, the rare earths, particularly yttrium, have been incorporated into heterometallic polyhydrides, beginning with the trimetallic Y_2Zr tetrahydride reported by Evans in 1984.[18] Hou has reported Y– and Lu–TM polyhydride complexes incorporating nearly all of the later transition metals (excluding technetium), allowing for study of the influence of transition metal identity on the structure and reactivity of these heterometallic complexes.[19–25] Several of these complexes also enabled hydrogen storage and release, properties that were not observed in monometallic species.[23]

Actinide–transition metal polyhydrides have not been studied to the same extent; for decades the field consisted of several U–Re hydrides synthesized by Ephritikhine.[26–28] Due to the long (>3.25 Å) U–Re distances in these complexes, no computational bonding studies were carried out. Additionally, no reactivity with unsaturated hydrocarbons, acetone, CO_2, or H/D exchange was observed.[28] However, recently we have developed a versatile salt metathesis strategy for the synthesis of a variety of An–TM polyhydrides. By converting mono-pentamethylcyclopentadienyl-substituted (Cp*) transition metal polyhydrides to potassium metalate salts of the form $K[Cp^*MH_n]$ (M = Ir, Os; n = 3, 4), we were able to synthesize actinide tetrametallate complexes **4.1-An** and **4.2-An** (An = Th, U) from actinide(IV) halides (Figure 4.1).[29] Both the iridate and osmate complexes were calculated to contain significant bonding interactions between the transition metal and actinide centers, and the osmium complexes were found to promote C–H activation upon photolysis. Protonolysis and aryl elimination upon reaction of the U(III) starting material $U(Terph)_3$ (Terph = C_6H_3-2,6-(C_6H_4-4-^{t}Bu)$_2$) with Cp^*IrH_4 led to an octametallic U_2Ir_6 polyhydride as well.[29]

The effectiveness of these strategies led us to pursue analogous actinide tetrarhenate species using the other known monomeric Cp* transition metal polyhydride, Cp^*ReH_5, reported by Herrmann.[30] We report the synthesis of thorium and uranium tetrarhenate polyhydrides, as well as octametallic polyhydrides of osmium and rhenium, completing the three series of heterometallic, An–TM polyhydride species (ThM_4, UM_4, and U_2M_6, M = Re, Os, Ir). Structural and computational analyses were carried out on the novel compounds, and the effects of varying transition metal identity and number of hydrides are described below.

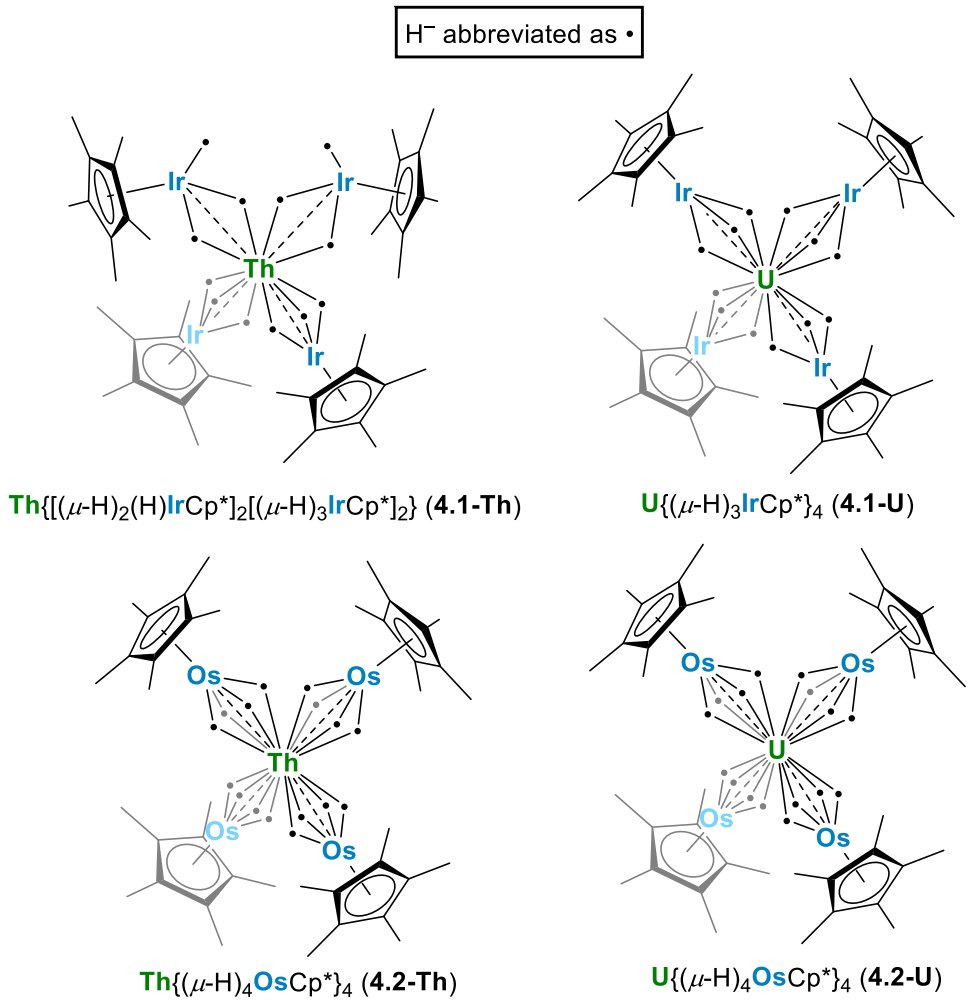

Figure 4.1 Previously reported An–Ir and An–Os multimetallic complexes.

Results and discussion

Cp*ReH$_6$ was converted to the potassium rhenate species K[Cp*ReH$_5$] (**4.3**) with the addition of benzylpotassium in THF. The rhenate species **4.3** precipitated as a colorless solid and exhibited minimal solubility in hydrocarbon and ethereal solvents. Reaction of four equivalents of the THF slurry of **4.3** with solutions of UCl$_4$ or ThCl$_4$(DME)$_2$ yielded the actinide–rhenate species Th{(μ-H)$_3$(H)$_2$ReCp*}$_4$ (**4.4-Th**) and U{(μ-H)$_3$(H)$_2$ReCp*}$_4$ (**4.4-U**), respectively (Scheme 4.1). Crystallizations from *n*-hexane at –40 °C produced light-yellow crystals of **4.4-Th** in 49% yield and dark-red crystals of **4.4-U** in 46% yield.

Scheme 4.1 Synthetic route to compounds **4.3**, **4.4-Th**, and **4.4-U**.

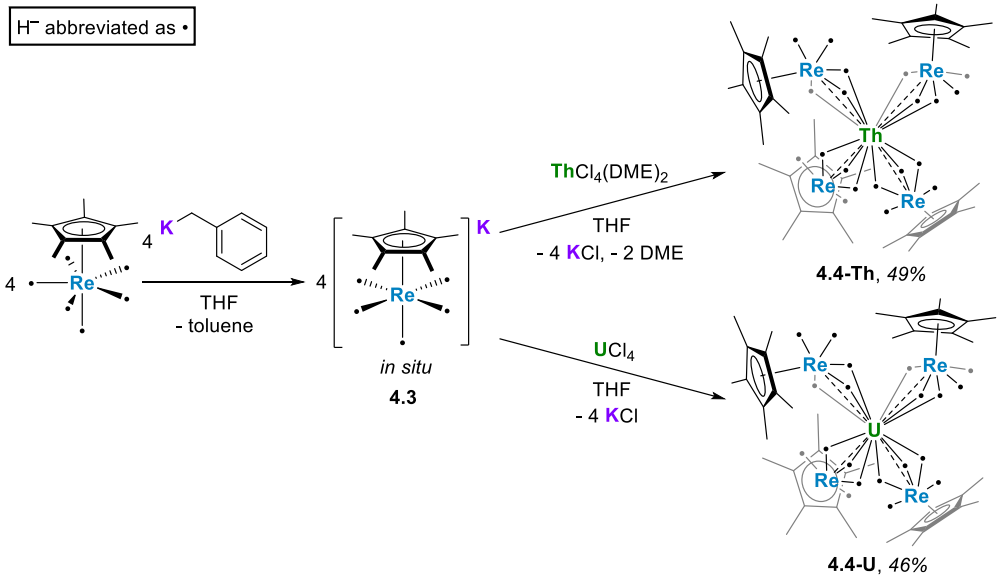

The ^{1}H NMR spectrum of **4.4-Th** contains two resonances, with the Cp* signal appearing at 2.36 ppm and the hydride resonance shifted upfield at –3.10 ppm. The Cp* protons and hydrides integrate in a 15:5 ratio in **4.4-Th**, indicating that all hydrides in the potassium rhenate species have been preserved. The ^{1}H NMR spectrum of complex **4.4-U** features a similar chemical shift for the Cp* ligands at 2.27 ppm, but contains an extreme downfield signal of 86.10 ppm corresponding to the hydrides, demonstrating the influence of the paramagnetic uranium center on the hydride signal.

Complex **4.4-Th** features IR stretching frequencies of 1970, 1919, and 1805 cm^{-1} for the hydrides, compared to 1979, 1908, and 1801 cm^{-1} for **4.4-U**. Both species have lower hydride vibrational frequencies than Cp*ReH$_6$ (2068, 2018 and 2008 cm^{-1}).[30] We observe a decrease of ~100 cm^{-1} in the hydride stretch upon complexation with an actinide center, a finding in line with the An–Ir species Th{[(μ-H)$_2$(H)IrCp*]$_2$[(μ-H)$_3$IrCp*]$_2$ (**4.1-Th**) and U{(μ-H)$_3$IrCp*}$_4$ (**4.1-U**), as well as the An–Os species Th{(μ-H)$_4$OsCp*}$_4$ (**4.2-Th**) and U{(μ-H)$_4$OsCp*}$_4$ (**4.2-U**).[29]

Complexes **4.4-Th** and **4.4-U** were characterized by single crystal X-ray diffraction (Figure 4.2). In contrast to the previously reported iridium and osmium species, all four Cp* ligands of the rhenate moieties in compounds **4.4-U** and **4.4-Th** are significantly bent relative to the An–Re axis, possibly due to the steric pressure from the five hydrides present in each rhenate fragment.

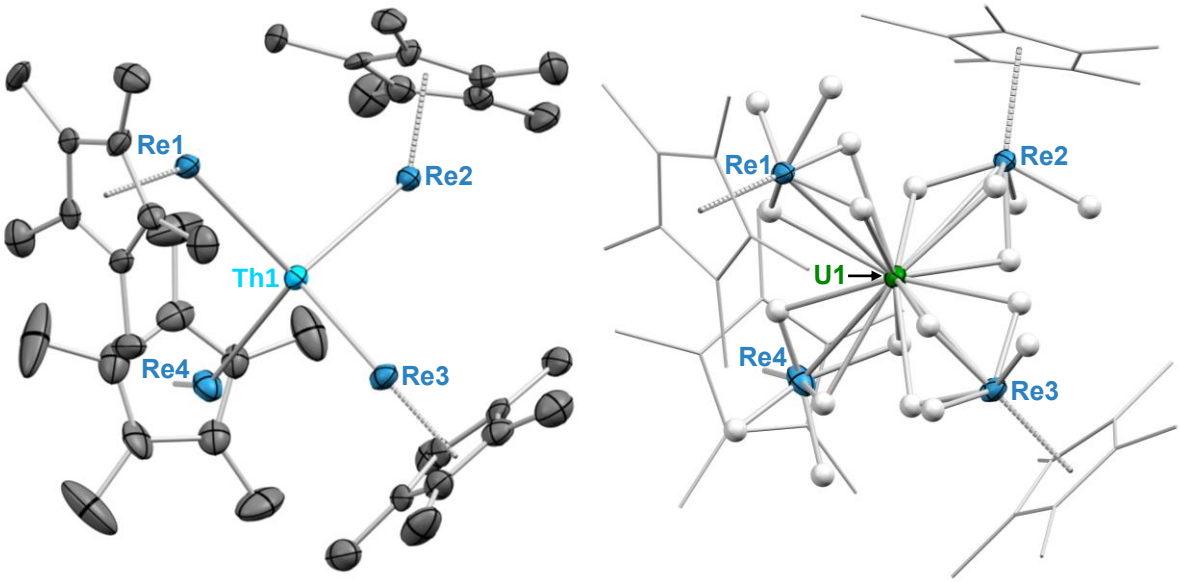

Figure 4.2 Solid-state structures of **4.4-Th** and **4.4-U**, with ellipsoids drawn at the 50% probability level. Methyl hydrogen atoms have been omitted and carbon atoms in **4.4-U** have been wireframed for clarity. Selected bond distances (Å) and angles (°) for **4.4-Th**: Th1–Re1 3.0929(6), Th1–Re2 3.1968(7), Th1–Re3 3.1372(5), Th1–Re4 3.1843(6), Re1–Th1–Re2 106.873(12), Re1–Th1–Re3 111.700(15), Re1–Th1–Re4 110.971(13), Re2–Th1–Re3 111.469(15), Re2–Th1–Re4 106.980(13), Re3–Th1–Re4 108.751(16), Th1–Re1–Cp*$_{centroid}$ 125.11(12), Th1–Re2–Cp*$_{centroid}$ 139.31(12), Th1–Re3–Cp*$_{centroid}$ 129.35(11), Th1–Re4–Cp*$_{centroid}$ 137.08(15). Selected bond distances (Å) and angles (°) for **4.4-U**: U1–Re1 3.0275(4), U1–Re2 3.1255(4), U1–Re3 3.0693(3), U1–Re4 3.1147(4), Re1–U1–Re2 106.847(8), Re1–U1–Re3 111.845(10), Re1–U1–Re4 110.928(9), Re2–U1–Re3 111.817(10), Re2–U1–Re4 107.057(9), Re3–U1–Re4 108.261(10), U1–Re1–Cp*$_{centroid}$ 126.03(8), U1–Re2–Cp*$_{centroid}$ 140.24(7), U1–Re3–Cp*$_{centroid}$ 130.41(7), U1–Re4–Cp*$_{centroid}$ 137.27(10).

Complex **4.4-Th** crystallizes in the space group *C*2/*c* with one equivalent of *n*-pentane and contains four crystallographically distinct rhenium centers. The Cp*Re moieties are significantly bent with regards to the Th–Re interactions, with Th–Re–Cp*$_{centroid}$ angles ranging between 125.11(12)° and 139.31(12)°. The Th–Re distances vary from 3.0929(6) Å to 3.1968(7) Å, falling within the sum of covalent radii for the two metals (3.57 Å).[31] The rhenium atoms are arranged in an essentially tetrahedral manner around thorium, with a τ_4 value[32] of 0.97 (calculated with α = 111.700(15)°, β = 111.469(15)°).

Complex **4.4-U** is isomorphous and isostructural to **4.4-Th**, featuring An–Re–Cp*$_{centroid}$ angles and Re–An–Re angles within 1° of the values for **4.4-Th**. Due to the presence of *n*-hexane on a special position in the crystal structure, a solvent mask was applied to that molecule of *n*-hexane. The U–Re distances fall between 3.0275(4) Å to 3.1255(4) Å, once again within the sum of covalent radii for the two metals (3.47 Å).[31] Setting this structure apart is the fact that the hydrides were resolved in the difference map and crystallographically modeled in the final structure, a first for these hydride-bridged actinide tetrametallate complexes. Each rhenium is bonded to three bridging hydrides and two terminal hydrides, which cause the Cp* moieties to be bent relative to the U–Re axis. These can also be visualized as pseudo-square pyramidal Cp*ReH$_5$ fragments which are bound at an angle through one axial and two equatorial hydrides. The hydride

distances vary rather significantly from one another, with the eight terminal Re–H distances ranging from 1.47(6) to 1.77(6) Å, while the twelve bridging Re–H–U hydrides feature Re–H distances of 1.47(5) to 1.78(6) Å and U–H distances of 2.24(5) to 2.48(6) Å. The H–Re–$Cp^*_{centroid}$ angles for the axial hydrides are fairly linear, ranging from 169(2) to 179(2)°.

The DFT-optimized structure for **4.4-U** (Figure 4.7) matches the geometry of the experimentally derived structure well, particularly with respect to the hydride geometry around the rhenium center (Figure 4.3 and Table 4.1). Natural Bonding Orbital (NBO) analyses on these optimized structures provided insight into the bonding interactions between the metals and hydrides in **4.4-U** and **4.4-Th**. In **4.4-U**, Wiberg Bond Indices (WBIs) of 0.57 and 0.75 were found for the bridging and terminal Re–H interactions, respectively. The bridging U–H interaction is significantly less covalent, with a calculated WBI of 0.25. The hydride bonding in **4.4-Th** is quite similar, with WBIs of 0.60 and 0.74 for the bridging and terminal Re–H interactions, respectively, and 0.22 for the Th–H interactions.

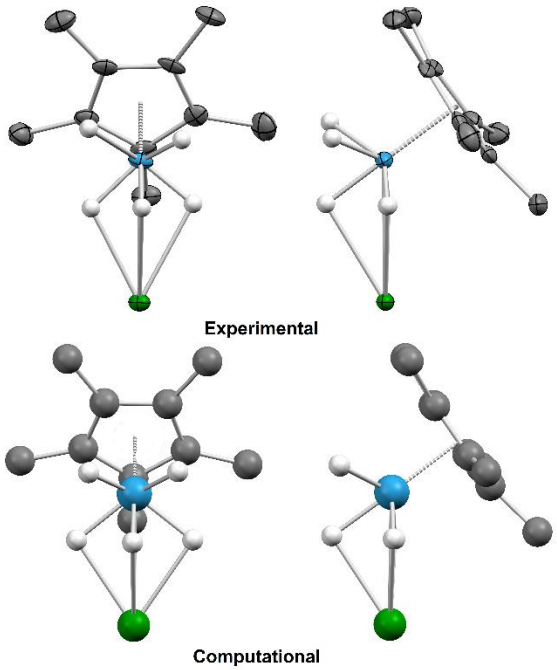

Figure 4.3 Front and side-on views of experimentally determined (top) and computationally modeled (bottom) structures for a single rhenate fragment (Re1) in **4.4-U**, with ellipsoids drawn at the 50% probability level in the experimental structure. Methyl hydrogen atoms have been omitted in both structures for clarity. Color key: green = uranium, blue = rhenium, gray = carbon, white = hydrogen.

Table 4.1 Selected metrics for the experimentally determined and computationally modeled structures of **4.4-U**.

	Experimental	Computational
U–Re (Å)	3.0276(6)	2.998
Re–$Cp^*_{centroid}$ (Å)	1.9207(6)	1.916
U–Re–$Cp^*_{centroid}$ (°)	126.12(2)	127.93
U–Re–$H_{terminal}$ (°)	111(2), 114(2)	109.94, 111.23
$Cp^*_{centroid}$–Re–H_{axial} (°)	179(2)	178.38

The calculated An–Re distances matched experimental values well, with an average U–Re distance of 3.023 Å for **4.4-U** and an average Th–Re distance of 3.080 Å for **4.4-Th**. WBIs of 0.71-0.80 were calculated for the U–Re interactions in **4.4-U**, compared to 0.68-0.70 for the Th–Re interactions in **4.4-Th**. Although there are no other reported WBIs for U–Re bonds to serve as a comparison, Liddle and coworkers reported the related Mayer Bond Order for an unsupported U–Re bond, with a value of 0.896.[33] The WBIs for **4.4-U** and **4.4-Th** are comparable to this value, indicative of significant covalent interaction between the actinide center and rhenium centers despite the presence of bridging hydrides.

With the synthesis of **4.4-Th** and **4.4-U**, we have access to a series of An–TM multimetallic complexes with varying metal identities, formal oxidation states, and number of hydride ligands. Examining the WBIs between the actinide and transition metal centers, separate patterns emerge for uranium versus thorium (Table 4.2). The uranium trend in the WBIs may be attributed to the electronics of the transition metal species. In moving from Re(V) to Os(IV) to Ir(III), the transition metal becomes more electron-rich and there is greater potential for covalent interaction with the electron-poor uranium center, resulting in a higher calculated bond index. However, the same electronic influence is not operative in the thorium complexes, where the Th–Ir bond index of **4.1-Th** is the lowest of the three complexes. This can be rationalized by considering the Cp* tilt observed in two iridate moieties of **4.1-Th**; the molecule gains stability from dispersion forces between Cp* moieties upon tilting, at the cost of covalent bonding between thorium and iridium.[29] This phenomenon is not observed in the other thorium species (in **4.4-Th**, the ring tilt is driven by the high coordination number), and accounts for the unusually low Th–Ir WBI.

The average An–TM distance (Table 4.3) does not appear to correlate to the degree of bonding between the two metals. Despite the clear trend in WBIs for the uranium complexes, **4.2-U** has a slightly shorter average U–TM distance than iridium complex **4.1-U**. This is most likely due to the additional bridging hydride in each U–Os interaction, which provides increased impetus for close U–TM metal contact despite the lower amount of covalent interaction. In the thorium complexes, the An–TM distances shorten with transition metal covalent radius.[31] For the rhenium and osmium species, the average An–TM distance is about 0.07 Å longer in the thorium complexes than the uranium complexes, consistent with the larger size of thorium compared to uranium. In **4.1-U**, the trend is only observed in the linear moieties (3.0128(12) Å), while the two bent moieties feature significantly shorter average Th–Ir distances (2.9548(5) Å), once again attributed to the effects of dispersion forces.

Table 4.2 Average WBIs calculated for An–TM interactions in compounds **4.1-An**, **4.2-An**, and **4.4-An**.

An	Ir(III) (**4.1-An**)	Os(IV) (**4.2-An**)	Re(V) (**4.4-An**)
Th	0.65	0.73	0.69
U	0.97	0.83	0.80

Table 4.3 Crystallographically obtained average An–TM distances in compounds **4.1-An**, **4.2-An**, and **4.4-An**.

An	Ir (**4.1-An**)	Os (**4.2-An**)	Re (**4.4-An**)
Th	2.993 Å	3.027 Å	3.153 Å
U	2.954 Å	2.950 Å	3.084 Å

We were also interested in the reactivity of Cp^*OsH_5 and Cp^*ReH_6 with $U(Terph)_3$[34] and their potential to produce octametallic species such as **4.5-Ir** (Scheme 4.2).[29] Upon addition of *n*-hexane solutions of Cp^*OsH_5 and Cp^*ReH_6 to *n*-hexane solutions of $U(Terph)_3$ and subsequent cooling to –40 °C, octametallic species $\{U[(\mu_2\text{-H})_4OsCp^*]_2[(\mu_3\text{-H})_2(\mu_2\text{-H})OsCp^*]\}_2$ (**4.5-Os**) and $\{U[(\mu_2\text{-H})_3(H)_2ReCp^*]_2[(\mu_3\text{-H})(\mu_2\text{-H})_3ReCp^*]\}_2$ (**4.5-Re**) were isolated as black crystals in 71% and 45% yield, respectively (Scheme 4.2). As with the iridium octametallic species, they were highly insoluble in aliphatic and aromatic solvents. Complex **4.5-Os** demonstrated sparing solubility in benzene, allowing for characterization by ^1H NMR, but **4.5-Re** proved insoluble in hydrocarbon and ethereal NMR solvents. Two signals are observable at 10.43 ppm and –16.31 ppm in the ^1H NMR spectrum of **4.5-Os**, corresponding to the Cp* ligands of the terminal osmate moieties and the Cp* ligands of the bridging osmate moieties, respectively. The IR spectrum of **4.5-Os** contains two primary hydride vibrations at 1985 cm^{-1} and 1875 cm^{-1}, while that of **4.5-Re** features a large, broad hydride stretch centered at 1855 cm^{-1}.

Scheme 4.2 Synthetic route to compounds **4.5-Ir** (previously reported), **4.5-Os**, and **4.5-Re**.

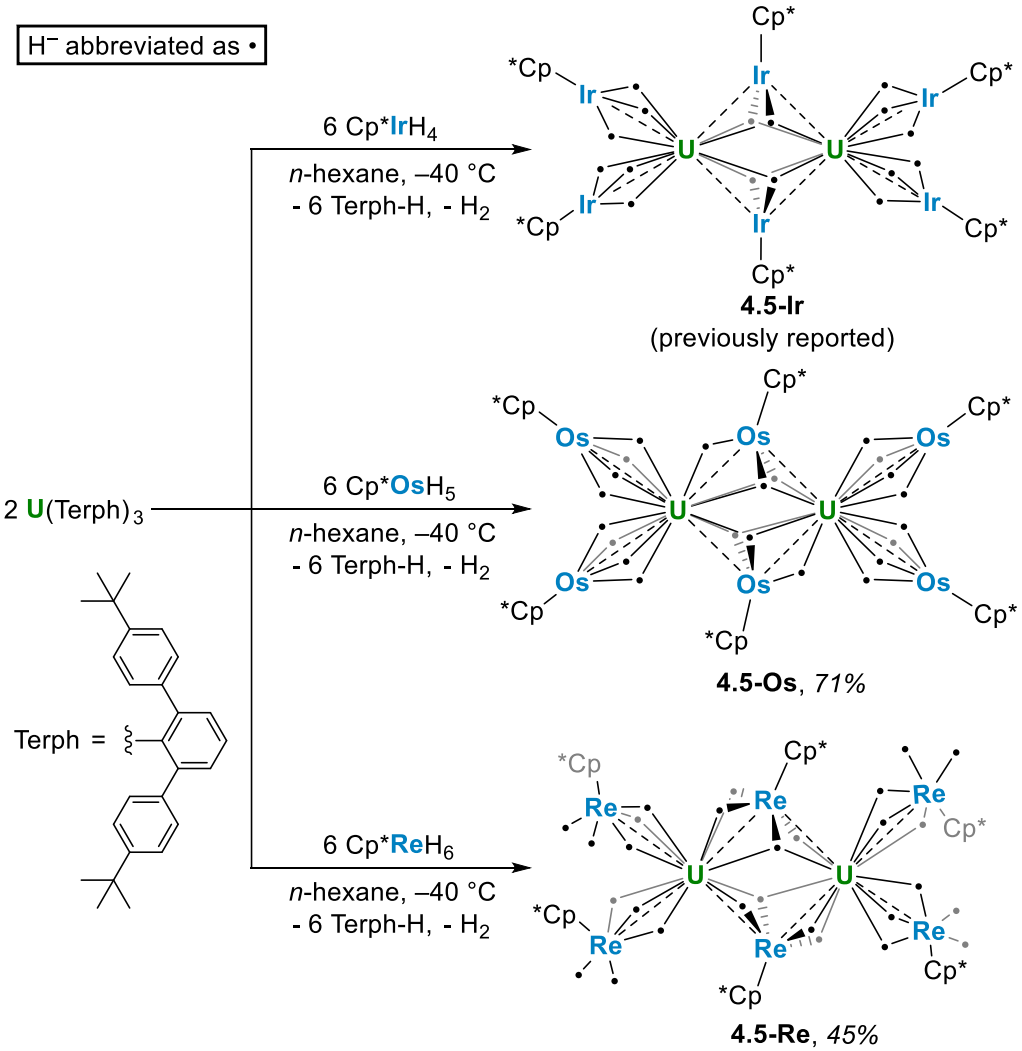

Complex **4.5-Os** crystallizes in the space group $P\bar{1}$ with two equivalents of *n*-hexane (Figure 4.4, top). Half of the molecule is generated by symmetry, with an inversion center located

between the two uranium centers. The U–Os lengths are nearly identical, with the terminal U–Os distances measuring 2.9655(4) Å and 2.9546(3) Å, while the bridging distances measure 2.9724(4) Å and 2.9625(4) Å. The U–U separation is quite long, at 3.7115(5) Å, shorter than that found for **4.5-Ir** (3.7945(4) Å). As typical with these An–TM polyhydrides, no hydrides were observed in the solid-state structures, but the Cp*Os tilt angles give some insight into the hydride bonding modes present in the molecule. The Cp* ligands of the terminal osmate moieties are nearly linear with respect to the U–Os bonds, with $Cp^*_{cent.}$–Os–U angles of 172.28(8)° and 174.22(9)°, suggesting that all four hydrides bridge the interaction, as with the previously reported complex $U\{(\mu\text{-}H)_4OsCp^*\}_4$. In contrast, the Cp* ligands of the bridging osmate moieties are angled about 20° relative to the U–U axis, as evidenced by the $Cp^*_{cent.}$–Os1–Os1′ angle of 159.86(8)°. This suggests the presence of one asymmetrically bound hydride in the bridging fragments, which we predict to contain three hydrides after the loss of one equivalent of H_2, as in the formation of the iridium analogue. This would result in four Os(IV) centers and two Os(II) centers in the complex, with twenty-two total hydrides.

The rhenium complex **4.5-Re** crystallizes in the same space group as **4.5-Os** and also contains an inversion center between the two uranium atoms which generates half of the molecule (Figure 4.4, bottom). The U–Re distances of the terminal fragments are slightly longer at 3.1020(6) Å and 3.1199(5) Å compared to 2.9823(6) Å and 3.0708(6) Å for the bridging moieties. Compared to **4.5-Os**, the U–U distance is longer by about 0.1 Å, at 3.8230(7) Å. No hydrides were refinable in the structure, but the significant tilting of the Cp* ligands in each fragment reflects the presence of terminal hydrides for all rhenate moieties. In the terminal moieties, the Cp*–Re–U angles measure 130.40(18)° and 135.39(11)°, matching those of tetrarhenate compound **4.4-U**. This suggests that as in **4.4-U**, the terminal $[Cp^*ReH_5]^-$ fragments consist of three bridging and two terminal hydrides. The Cp* ligands of the bridging fragments are also tilted, with a $Cp^*_{cent.}$–Re1–Re1′ angle of 157.43(11)°. Given an analogous mechanism for the formation of **4.5-Re** to the other octametallic species, the bridging rhenate fragments are expected to contain four hydrides, which are not distributed symmetrically between rhenium and the two uranium centers. These bridging fragments would contain Re(III) centers, while the terminal fragments would contain Re(V) centers, with twenty-eight predicted hydrides (four terminal fragments with five hydrides each, and two bridging fragments with four hydrides each).

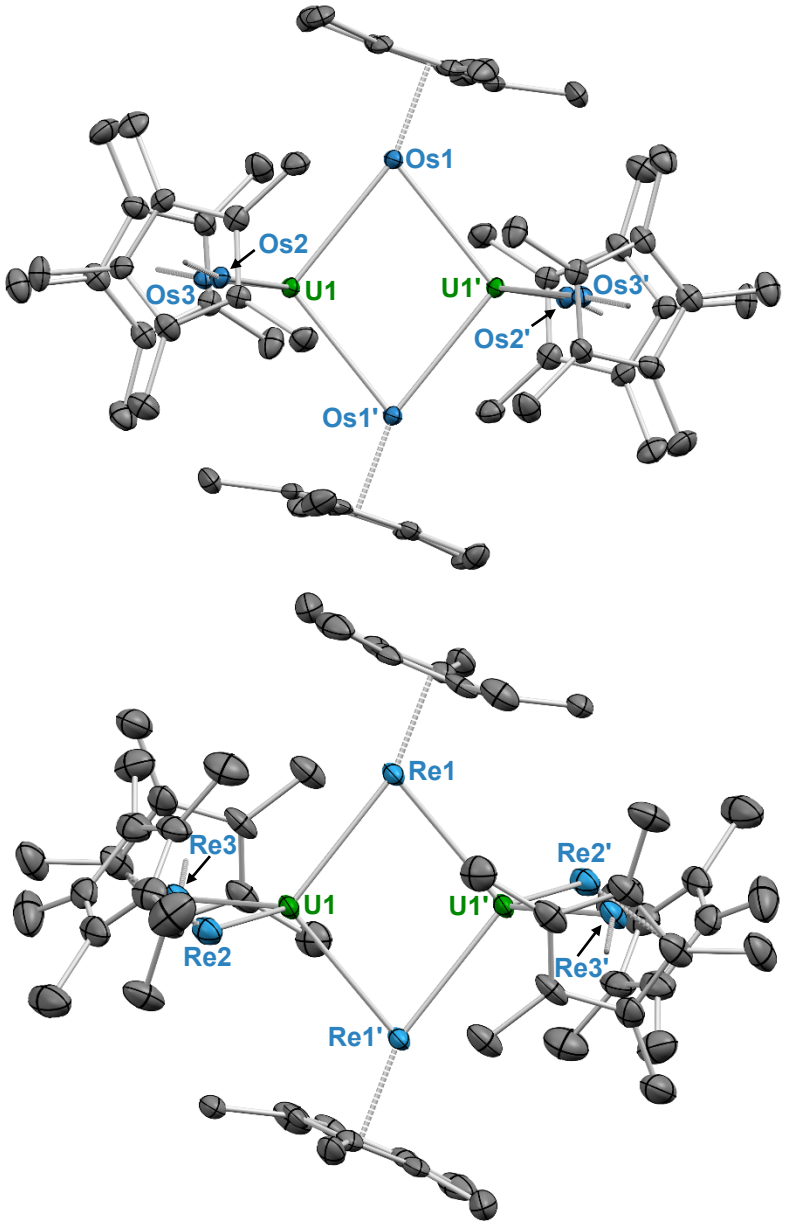

Figure 4.4 Solid-state structures of **4.5-Os** (top) and **4.5-Re** (bottom), with ellipsoids drawn at the 50% probability level. Hydrogen atoms and co-crystallized solvent molecules have been omitted for clarity. Hydrides were not located in the structures due to the proximity of numerous metal centers – calculated hydride positions can be found in Figure 4.5. Selected bond distances (Å) and angles (°) for **4.5-Os**: U1–Os1 2.9724(4), U1–Os2 2.9654(4), U1–Os3 2.9546(5), U1–Os1' 2.9625(4), U1–U1' 3.7116(6), U1–Os2–Cp*$_{centroid}$ 174.223(14), U1–Os2–Cp*$_{centroid}$ 172.282(12), Os1'–Os1–Cp*$_{centroid}$ 159.861(13). Selected bond distances (Å) and angles (°) for **4.5-Re**: U1–Re1 2.9823(7), U1–Re2 3.1021(6), U1–Re3 3.1199(6), U1–Re1' 3.0707(6), U1–U1' 3.8229(7), U1–Re2–Cp*$_{centroid}$ 130.40(2), U1–Re2–Cp*$_{centroid}$ 135.39(2), Re1'–Re1–Cp*$_{centroid}$ 157.428(14).

For **4.5-Os**, the most stable DFT-computed structure contains four bridging hydrides per terminal osmate fragment, while each bridging osmate fragment features one coplanar μ_2-hydride with respect to the U_2Os_2 plane and two out-of-plane μ_3-hydrides (Figure 4.5, left). This closely

matches the structural parameters of the solid-state structure, particularly with regards to the geometry of the metal centers and Cp* ligands (Table 4.11). The metal-metal distances are also quite similar, albeit systematically shorter in the calculated structure. In the optimized structure, the Os–H distances range between 1.627 Å and 1.683 Å, while the U–H distances fall between 2.456 Å and 2.534 Å, with the exception of the μ_2-hydrides of the bridging fragments, which have a U–H length of 2.164 Å. The Os–H and U–H distances in the terminal osmate fragments are comparable to those of **4.2-U**. The extent of U–TM bonding in **4.5-Os** is also comparable, if slightly lower, to that of **4.2-U**, with WBIs of 0.77-0.79 for the terminal fragments and 0.74-0.77 for the bridging fragments. As with the tetraosmate complex, the Os–H interactions are stronger than U–H interactions, though the coplanar μ_2-hydride has a particularly high U–H WBI of 0.34 (Table 4.13). Predicted M–H stretches of 1952-2040 cm^{-1} and 1849-1883 cm^{-1}, match observed hydride stretches in the IR spectrum (1986 cm^{-1} and 1875 cm^{-1}).

The optimized computed structure of complex **4.5-Re** (Figure 4.5, right) reveals an analogous hydride geometry for the terminal rhenate fragments as that found in **4.4-U**, with three bridging and two terminal hydrides. The bridging rhenate fragments contain three μ_2-hydrides and one μ_3-hydride. Similar to **4.5-Os**, all geometric parameters of the experimental structure are well-replicated, with slight underestimation of the metal–metal distances (Table 4.12). The U–TM interactions in **4.5-Re** are similar to those of the osmium analogue, with U–Re WBIs of 0.69-0.76 for the terminal fragments and 0.73-0.80 for the bridging fragments, and are only slightly lower than the calculated values for **4.4-U**. The two terminal hydrides per terminal rhenium pentahydride fragment are predicted to have negligible interaction with the nearest uranium centers (Table 4.13). Finally, the calculated hydride stretches of **4.5-Re** match well with experiment, ranging from 1923-1992 cm^{-1} and 1904-1917 cm^{-1}.

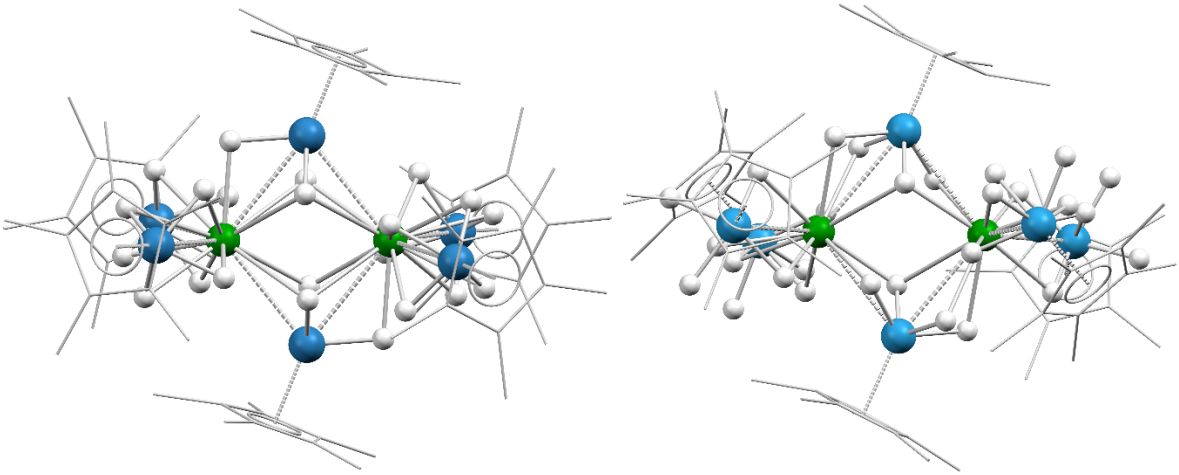

Figure 4.5 Computed structures of **4.5-Os** (left) and **4.5-Re** (right). Methyl hydrogen atoms have been omitted and Cp* ligands have been wireframed for clarity. Color key: green = uranium, blue = osmium, light blue = rhenium, gray = carbon, white = hydrogen.

Along with the iridium octametallic **4.5-Ir**, we can observe the effects of the steric pressure from increasing the number of hydrides in the molecule from 16 (**4.5-Ir**) to 22 (**4.5-Os**) to 28 (**4.5-Re**). There are no bent Cp* ligands relative to the U–M axis in **4.5-Ir**, followed by two in the bridging osmate moieties of **4.5-Os**, and finally all six in **4.5-Re**, which must accommodate 12 more hydrides than the original iridium complex. Despite the large variance in the number of hydrides, the extent of U–TM interaction does not vary greatly between the complexes, with WBIs ranging from 0.64-0.79 for the terminal U–TM fragments and 0.73-0.85 for the bridging U–TM

fragments. Unfortunately, in all cases the complexes are highly insoluble and unreactive, demonstrating no hydrogenation capabilities with alkenes or alkynes.

Conclusions

We have synthesized thorium and uranium tetrarhenate polyhydrides of the form $An(H_5ReCp^*)_4$ (An = Th, U), adding to our library of actinide tetraosmate and tetrairidate complexes $An(H_4OsCp^*)_4$ and $An(H_3IrCp^*)_4$. Octametallic uranium osmate and uranium rhenate complexes were also prepared, completing the series of three octametallic complexes of the form $[U(H_nMCp^*)_2(H_{n-1}MCp^*)]_2$ (M = Re, Os, Ir; n = 5, 4, 3). In the tetrametallate complexes, we see that An–TM bond distance does not correlate with the calculated WBI, though in all complexes a significant bonding interaction is predicted. Sterically, the An–TM interactions are able to support up to four bridging hydrides; for the pentahydride rhenate fragments of **4.4-Th** and **4.4-U**, only three hydrides bridge the metal–metal interaction. The octametallic species experience even greater steric crowding from bridging hydrides as the transition metal identity changes, with less variation in An–TM WBI. These complexes feature slightly lower levels of An–TM interaction than the tetrametallate complexes, with WBIs decreased by 0.05-0.10 compared to the tetrametallate species.

Experimental Procedures

General considerations: Unless otherwise noted, all reactions were performed using standard Schlenk line techniques under an atmosphere of nitrogen or argon, or in an MBraun inert atmosphere glove box under an atmosphere of nitrogen. Glassware and Celite® were stored in an oven at ca. 150 °C for at least 3 h prior to use. Molecular sieves (4 Å) were activated by heating to 200 °C overnight under vacuum prior to storage in a glovebox. NMR spectra were recorded on Bruker AV-600, AV-500, and AVB-400 spectrometers. ^{1}H chemical shifts are given relative to residual solvent peaks and are recorded in units of parts per million (ppm). FT-IR samples were prepared as Nujol mulls pressed between KBr plates, with data collected with a Nicolet iS10 FT-IR spectrometer. Melting points were determined using sealed capillaries prepared under nitrogen on an OptiMelt automated melting point system. Elemental analyses were determined at the Microanalytical Facility at the College of Chemistry, University of California, Berkeley.

Materials: Toluene, *n*-hexane, *n*-pentane, and THF were purified by passage through columns of activated alumina and degassed by sparging with nitrogen. Deuterated solvents were degassed with three freeze-pump-thaw cycles and stored over molecular sieves. Benzylpotassium,[35] Cp^*OsH_5,[36] Cp^*ReH_6,[30] $U(Terph)_3$,[34] UCl_4,[37] and $ThCl_4(DME)_2$[38] were synthesized according to literature procedures. All other chemicals were purchased from commercial sources and used as received.

Synthesis of $K[Cp^*ReH_5]$ (4.3):
Cp^*ReH_6 (16.1 mg, 0.049 mmol, 1.0 equiv.) and benzylpotassium (6.4 mg, 0.049 mmol, 1.0 equiv.) were measured out in separate 20 mL scintillation vials and each dissolved in 1 mL THF. The benzylpotassium was added to Cp^*ReH_6 with stirring, rapidly forming a colorless slurry of $K[Cp^*ReH_5]$. After 1 hr, the THF was decanted and the $K[Cp^*ReH_5]$ was rinsed with *n*-hexane and dried *in vacuo*, yielding a colorless powder (15.5 mg, 86% yield). IR (Nujol mull on KBr): 1937 (w), 1870 (s), 1072 (w), 1043 (m), 939 (w), 829 (w), 636 (w).

Synthesis of Th{(μ-H)$_3$(H)$_2$ReCp*}$_4$ (4.4-Th):
Cp*ReH$_6$ (18.5 mg, 0.056 mmol, 4.0 equiv.) and benzyl potassium (7.4 mg, 0.057 mmol, 4.0 equiv.) were added to a 20 mL scintillation vial with THF (3 mL) to generate K[Cp*ReH$_5$]. ThCl$_4$(DME)$_2$ (7.8 mg, 0.015 mmol, 1.0 equiv.) was dissolved in THF (1 mL) and added to the K[Cp*ReH$_5$] slurry. The pale-yellow suspension quickly became a transparent yellow solution. After stirring at room temperature for 16 h, the solvent was removed *in vacuo*. The crude solid was then triturated with *n*-hexane and the product was extracted with *n*-hexane (4 mL), filtered through Celite, and concentrated (1 mL). This solution was cooled to –40 °C, affording pale yellow crystals in multiple crops (13.7 mg, 63% yield). X-ray quality crystals were grown from *n*-pentane. Mp ca. 210 °C (slow decomp. starting from 180 °C); ^{1}H NMR (600 MHz, C$_6$D$_6$): δ 2.36 (s, 60H, CH$_{3Cp*}$), –3.10 (s, 20H, Re–H/Re–H–Th); ^{13}C NMR (600 MHz, C$_6$D$_6$): δ 92.2 (*C*$_5$Me$_5$), 13.3 (C$_5$*Me*$_5$); IR (Nujol mull on KBr): 1970 (m), 1921 (s), 1808 (s), 1073 (w), 1033 (m), 901 (w), 831 (w), 787 (s), 580 (w). Anal. Calcd (%) for ThRe$_4$C$_{40}$H$_{80}$: C, 31.24; H, 5.24. Found: C, 31.14; H, 5.24.

Synthesis of U{(μ-H)$_3$(H)$_2$ReCp*}$_4$ (4.4-U):
Cp*ReH$_6$ (27.9 mg, 0.085 mmol, 4.0 equiv.) and benzyl potassium (11.2 mg, 0.086 mmol, 4.0 equiv.) were added to a 20 mL scintillation vial with THF (2 mL) to generate a slurry of K[Cp*ReH$_5$]. UCl$_4$ (8.2 mg, 0.022 mmol, 1.0 equiv.) was dissolved in THF (1 mL) and added to the K[Cp*ReH$_5$]. The pale-yellow suspension immediately turned dark purple, and over the course of 2 hours the solid K[Cp*ReH$_5$] disappeared as it reacted. After stirring at room temperature for 1 h, the solvent was removed *in vacuo*. The solid was triturated with *n*-hexane and the product was extracted with toluene (2 mL), filtered through Celite, and dried. This material was further extracted with *n*-hexane (4 mL), filtered, and concentrated to 1 mL. This solution was cooled to –40 °C, affording multiple crops of dark red crystals (24.0 mg, 73% yield). Mp ca. 225 °C; ^{1}H NMR (600 MHz, C$_6$D$_6$): δ 86.1 (s, 20H, Re–H/Re–H–U), 2.27 (s, 60H, C$_5$*Me*$_5$); ^{13}C NMR (600 MHz, C$_6$D$_6$): δ 90.6 (*C*$_5$Me$_5$), 10.2 (C$_5$*Me*$_5$); IR (Nujol mull on KBr): 1980 (s), 1909 (s), 1804 (s), 1073 (w), 1034 (m), 909 (w), 831 (w), 786 (s), 589 (w). Anal. Calcd (%) for URe$_4$C$_{40}$H$_{80}$: C, 31.12; H, 5.22. Found: C, 31.31; H, 5.26.

Synthesis of 4.5-Os:
Cp*OsH$_5$ (21.0 mg, 0.064 mmol, 6.0 equiv.) and U(Terph)$_3$ (26.4 mg, 0.021 mmol, 2.0 equiv.) (Terph = C$_6$H$_3$-2,6-(C$_6$H$_4$-4-^{t}Bu)$_2$) were dissolved in separate vials in *n*-hexane (1.5 mL and 1.5 mL, respectively). Cp*OsH$_5$ was added to U(Terph)$_3$, then the mixture was stirred overnight. A black solid precipitated out of solution after 18 h, from which the mother liquor was decanted. After rinsing with 2 × 2 mL *n*-hexane to remove any Terph–H, **4.5-Os** was isolated and dried as a black powder (18.4 mg, 71% yield). X-ray quality crystals were grown from an analogous procedure without stirring at –40 C. Mp ca. 280 °C (decomp.); ^{1}H NMR (500 MHz, C$_6$D$_6$): δ 10.43 (s, 60H, CH$_3$ (Cp*Os$_{terminal}$)), –16.31 (s, 30H, CH$_3$ (Cp*Os$_{bridging}$)); IR (Nujol mull on KBr): 1986 (s), 1875 (s), 1072 (m), 1033 (s), 948 (w), 562 (w). Anal. Calcd (%) for U$_2$Os$_6$C$_{60}$H$_{112}$: C, 29.40; H, 4.61. Found: C, 29.57; H, 4.52.

Synthesis of 4.5-Re:
Cp*ReH$_6$ (20.7 mg, 0.063 mmol, 6.0 equiv.) and U(Terph)$_3$ (27.1 mg, 0.021 mmol, 2.0 equiv.) (Terph = C$_6$H$_3$-2,6-(C$_6$H$_4$-4-^{t}Bu)$_2$) were dissolved in separate vials in *n*-hexane (1 mL each). The solution of Cp*ReH$_6$ was added to the solution of U(Terph)$_3$, then the mixture was cooled to –40 °C to crystallize. The resulting black solution afforded black crystals of **4.5-Re** (11.4 mg, 45%

yield) after 18 h, which were rinsed with 2 × 2 mL *n*-hexane to remove any Terph–H. Mp ca. 163 °C (slow decomp.); IR (Nujol mull on KBr): 1998 (w), 1970 (m), 1917 (s), 1855 (s), 1270 (w), 1114 (w), 1072 (w), 1033 (m), 898 (w), 835 (m), 792 (m), 570 (w). Anal. Calcd (%) for $U_2Re_6C_{60}H_{118}$: C, 29.62; H, 4.89. Found: C, 29.75; H, 4.79.

X-ray crystallography details

In a dry nitrogen glovebox, samples of single crystals were coated in Paratone-N oil for transport to the Advanced Light Source (ALS). Crystals were mounted on a MiTeGen 10 μm aperture Dual-Thickness MicroMount loop. X-ray diffraction data for **4-Th**, **4-U**, **5-Os**, and **5-Re** were collected at the ALS, Lawrence Berkeley National Lab, Berkeley, CA, station 12.2.1 using a silicon monochromated beam of 17 keV (λ = 0.7288 Å) synchrotron radiation. Data was collected at 100 K, with the crystals cooled by a stream of dry nitrogen. Bruker APEX3 software was used for the data collections, Bruker SAINT v8.37A or V8.38A software was used to conduct the cell refinement and data reduction procedures,[39] and absorption corrections were carried out by a multi-scan method utilizing the SADABS program.[39] Initial structure solutions were found using direct methods (SHELXT),[40] and refinements were carried out using SHELXL-2014,[41] as implemented by Olex2.[42] Thermal parameters for all non-hydrogen atoms were refined anisotropically. Hydrogen atoms were placed in calculated positions and refined isotropically. Thermal ellipsoid plots were made using Mercury.[43] The structures have been deposited to the Cambridge Crystallographic Data Centre (CCDC) with deposition numbers 2349729 (**4-Th**), 2349730 (**4-U**), 2349731 (**5-Os**), and 2349732 (**5-Re**).

Table 4.4 Crystal data for complexes **4.4-Th**, **4.4-U**, **4.5-Os**, and **4.5-Re**. *Hydrides are not observed, and are therefore not included in the empirical formulas. †0.5 equivalents of C_6H_{14} were located on a special position in the structure and masked from the final structure.

Compound	**4.4-Th**	**4.4-U**	**4.5-Os**	**4.5-Re**
Empirical formula	$C_{40}H_{60}Re_4Th^* \cdot C_5H_{12}$	$C_{40}H_{80}Re_4U \cdot 0.5\ C_6H_{14}$†	$C_{72}H_{118}Os_6U_2^* \cdot 2\ C_6H_{14}$	$C_{60}H_{90}Re_6U_2$*
Formula weight	1589.86	1586.95	2600.92	2404.57
Temperature/K	100.0	100.00	100	100
Crystal system	monoclinic	monoclinic	triclinic	triclinic
Space group	C2/c	C2/c	P-1	P-1
a/Å	29.273(5)	29.186(3)	12.7115(12)	12.3116(17)
b/Å	17.583(3)	17.5154(15)	12.7334(12)	12.3935(17)
c/Å	22.024(3)	21.8237(19)	12.8769(12)	13.6757(18)
α/°	90	90	76.378(4)	76.035(5)
β/°	103.212(6)	102.775(3)	82.101(4)	84.814(5)
γ/°	90	90	79.268(4)	71.297(5)
Volume/Å^3	11036(3)	10880.1(16)	1980.6(3)	1917.9(5)
Z	8	8	1	1
ρ_{calc}g/cm^3	1.914	1.938	2.181	2.082
μ/mm^{-1}	12.145	10.767	12.075	11.926
F(000)	5856.0	5896.0	1190.0	1084.0
Crystal size/mm^3	0.3 × 0.25 × 0.2	0.1 × 0.05 × 0.05	0.5 × 0.15 × 0.15	0.12 × 0.1 × 0.015
Radiation	synchrotron (λ = 0.7288)	synchrotron (λ = 0.7288)	synchrotron (λ = 0.7288)	synchrotron (λ = 0.7288)
2Θ range for data collection/°	3.206 to 58.306	4.55 to 55.182	3.418 to 62.398	3.582 to 54.19
Index ranges	-39 ≤ h ≤ 39, -23 ≤ k ≤ 23, -29 ≤ l ≤ 29	-37 ≤ h ≤ 37, -22 ≤ k ≤ 22, -27 ≤ l ≤ 27	-18 ≤ h ≤ 18, -17 ≤ k ≤ 18, -18 ≤ l ≤ 18	-15 ≤ h ≤ 15, -15 ≤ k ≤ 15, -17 ≤ l ≤ 17
Reflections collected	79060	73384	33131	25485
Independent reflections	13745 [R_{int} = 0.0901, R_{sigma} = 0.0661]	11649 [R_{int} = 0.0593, R_{sigma} = 0.0433]	11835 [R_{int} = 0.0479, R_{sigma} = 0.0623]	7830 [R_{int} = 0.0418, R_{sigma} = 0.0444]
Data/restraints/parameters	13745/89/517	11649/82/562	11835/12/378	7830/0/322
Goodness-of-fit on F^2	1.102	1.083	1.049	1.069
Final R indexes [I>=2σ (I)]	R_1 = 0.0483, wR_2 = 0.1211	R_1 = 0.0280, wR_2 = 0.0609	R_1 = 0.0361, wR_2 = 0.0735	R_1 = 0.0377, wR_2 = 0.1012
Final R indexes [all data]	R_1 = 0.0655, wR_2 = 0.1298	R_1 = 0.0391, wR_2 = 0.0642	R_1 = 0.0501, wR_2 = 0.0780	R_1 = 0.0439, wR_2 = 0.1041
Largest diff. peak/hole / e Å^{-3}	1.55/-1.94	0.99/-1.53	1.77/-1.55	6.52/-2.75
CSD entry	2349729	2349730	2349731	2349732

Computational details

All DFT calculations were carried out with the Gaussian 09 suite of programs.[44] Geometries were fully optimized in gas phase without symmetry constraints, employing the B3PW91 functional.[45,46] The nature of the extrema was verified by analytical frequency calculations. The calculation of electronic energies and enthalpies of the extrema of the potential energy surface (minima and transition states) were performed at the same level of theory as the geometry optimizations. IRC

calculations were performed to confirm the connections of the optimized transition states. Uranium, thorium, rhenium, and osmium atoms were treated with a small core effective core potential (60 MWB), associated with its adapted basis set[47–49] augmented, for osmium atoms, with a polarization function ($\zeta_f = 0.886$).[50] For the other elements (H and C), Pople's double-ζ basis set 6-31G(d,p) was used.[51–53] Dispersion corrections were treated with the D3 version of Grimme's dispersion with Becke-Johnson damping.[54] The electronic charges (at the DFT level) were computed using the natural population analysis (NPA) technique.[55]

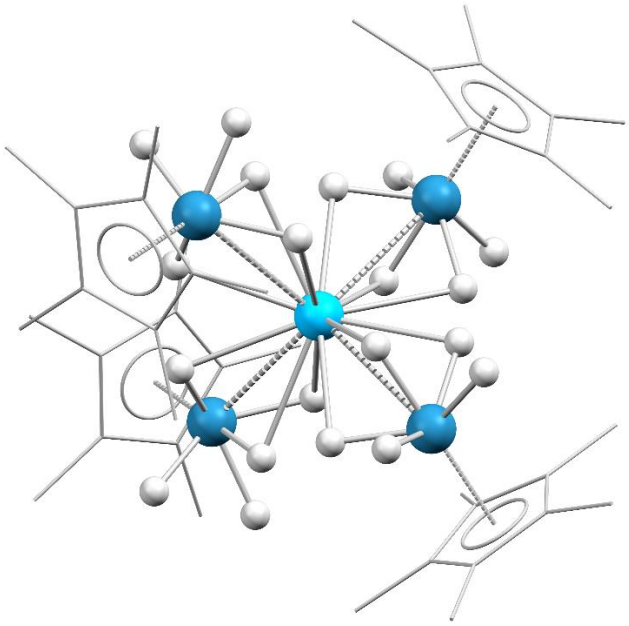

Figure 4.6. DFT-optimized structure of **4.4-Th**, with carbon atoms wireframed and methyl hydrogens omitted for clarity. Color key: light blue = thorium, blue = rhenium, gray = carbon, white = hydrogen.

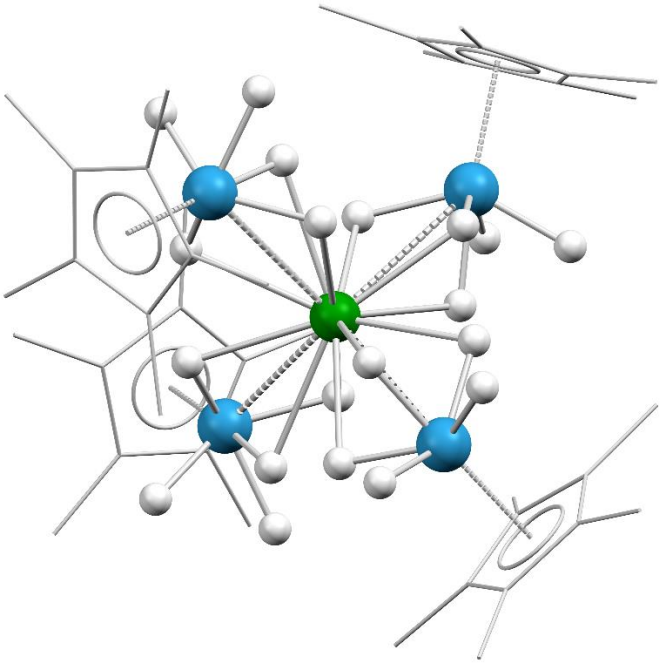

Figure 4.7. DFT-optimized structure of **4.4-U**, with carbon atoms wireframed and methyl hydrogens omitted for clarity. Color key: green = uranium, blue = rhenium, gray = carbon, white = hydrogen.

Table 4.5 Relative energies for **4.4-Th** as a function of the number of bent Cp^* groups and spin multiplicity.

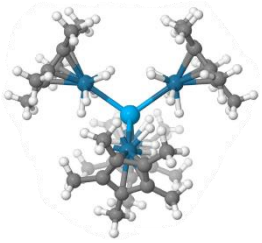
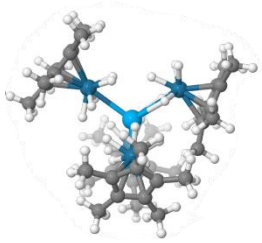
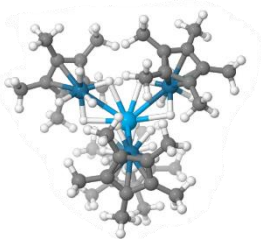

4.4-Th	Linear		1 - Bent		2 - Bent	
Spin Multiplicity	singlet	triplet	singlet	triplet	singlet	triplet
ΔrH (kcal/mol)	0.0	269.7	1.4	57.7	5.8	58.4
ΔrG (kcal/mol)	0.0	273.7	6.3	61.0	15.5	65.9

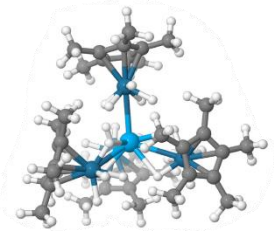
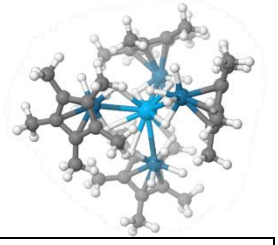

4.4-Th	3 - Bent		4 - Bent	
Spin Multiplicity	singlet	triplet	singlet	triplet
ΔrH (kcal/mol)	11.7	63.6	18.7	–
ΔrG (kcal/mol)	20.5	73.43	30.5	–

Table 4.6. Relative energies for **4.4-U** as a function of the number of bent Cp^* groups and spin multiplicity.

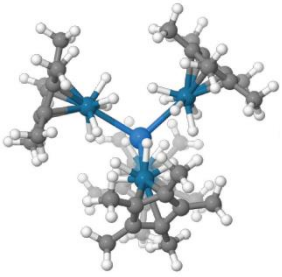
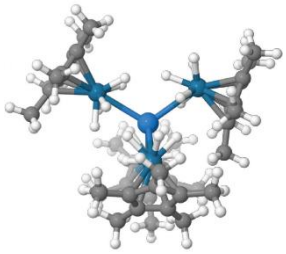
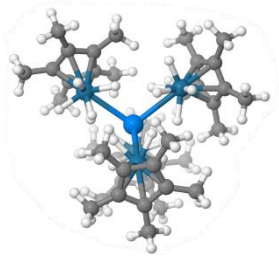

4.4-U	Linear			1 - Bent			2 - Bent		
Spin Multiplicity	singlet	triplet	quintet	singlet	triplet	quintet	singlet	triplet	quintet
ΔrH (kcal/mol)	–	38.1	–	54.0	21.6	62.9	47.5	–	–
ΔrG (kcal/mol)	–	25.9	–	48.5	27.2	54.3	44.5	–	–

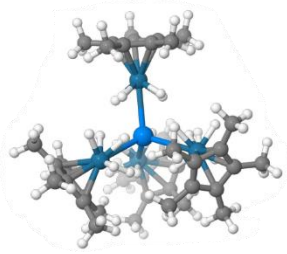
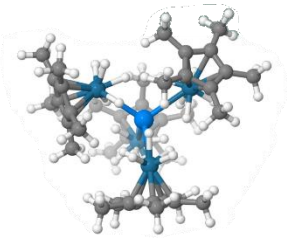

4.4-U	3 - Bent			4 - Bent		
Spin Multiplicity	singlet	triplet	quintet	singlet	triplet	quintet
ΔrH (kcal/mol)	48.9	12.2	41.4	28.2	0.0	27.0
ΔrG (kcal/mol)	45.3	9.7	36.9	30.6	0.0	27.5

Table 4.7 Tabulated experimentally determined and computationally derived bond distances/angles and Re–H frequencies for **4.4-Th**.

4.4-Th	Experimental	Computational
Re–H distance (Å)	–	[1.678 – 1.687] (μ-H) [1.671 – 1.672] (η-H)
Th–H distance (Å)	–	[2.414 – 2.510]
Th–Re distance (Å)	3.093 / 3.137 3.184 / 3.197	3.073 / 3.078 3.081 / 3.086
Th–C(Cp*) distance (Å)	[3.895 – 4.047]; [4.407 – 4.609]; [4.947 – 5.404]	[3.876 – 3.928]; [4.368 – 4.500]; [5.134 – 5.216]
Th–C(Me-Cp*) distance (Å)	[3.884 – 4.083]; [4.495 – 5.156]; [5.683 – 6.475]	[3.889 – 3.945]; [4.772 – 5.066]; [6.226 – 6.362]
Re–C(Cp*) distance (Å)	[2.217 – 2.323]	[2.240 – 2.316]
Re–Th–Re angle (º)	[106.9 – 111.7]	[106.5 – 111.2]
Th–Re–Cp(centroid) angle (º)	125.1, 129.4, 137.1, 139.3	125.3, 126.0, 126.3, 126.7
Re–H (cm^{-1})	1979, 1908, 1801	[1984 – 1896] [1037 – 773] [665 – 646]

Table 4.8 Tabulated experimentally determined and computationally derived bond distances/angles and Re–H frequencies for **4.4-U**.

4.4-U	Experimental	Computational
Re–H distance (Å)	[1.47 – 1.77] (μ-H) [1.47 – 1.78] (η-H)	[1.679 – 1.710] (μ-H) [1.657 – 1.672] (η-H)
U–H distance (Å)	[2.24 – 2.48]	[2.281 – 2.450]
U–Re distance (Å)	3.028 / 3.069 3.115 / 3.126	2.983 / 2.998 3.045 / 3.066
U–C(Cp*) distance (Å)	[3.861 – 4.034]; [4.372 – 4.888]; [5.021 – 5.304]	[3.795 – 4.040]; [4.282 – 4.614]; [4.942 – 5.257]
U–C(Me-Cp*) distance (Å)	[3.894 – 4.930]; [5.152 – 5.986]; [6.231 – 6.403]	[3.816 – 4.093]; [4.676 – 5.265]; [5.747 – 6.355]
Re–C(Cp*) distance (Å)	[2.207 – 2.29]	[2.240 – 2.332]
Re–U–Re angle (º)	[106.8 – 111.8]	[106.2 – 112.6]
U–Re–Cp(centroid) angle (º)	126.0, 130.4, 137.3, 140.2	124.8, 127.9, 130.5, 138.0
Re–H (cm^{-1})	1979, 1908, 1801	[2023 – 1820] [1071 – 651]

Table 4.9 Wiberg Bond Indexes and Natural Charges for **4.4-Th** and **4.4-U**.

	4.4-Th	**4.4-U**
	4-Bent (singlet)	4-Bent (triplet)
Re–H	[0.60] (μ-H) [0.74] (η-H)	[0.57] (μ-H) [0.75] (η-H)
An–(μ-H)	[0.22]	[0.25]
An–Re	[0.68 - 0.70]	[0.71 - 0.80]
An–C(Cp*)	[0.02 - 0.07]	[0.03 - 0.08]
An–C(Me-Cp*)	[0.00 - 0.04]	[0.00 - 0.01]
2nd Order Analysis	BD C(Cp*)–C(Cp*)→LP* U 3 kcal/mol BD C(Me-Cp*)–H→LP* U [8-12] kcal/mol LP C(Cp*)→LP* U [42–48] kcal/mol	BD Re–C(83)(Cp*)→LP* U 220 kcal/mol LP C(Cp*)→LP* U [8–30] kcal/mol
Re Natural Charges	[–1.15 - –1.16]	[–1.03 - –1.14]
An Natural Charges	0.33	0.09

Table 4.10 Relative energies for **4.5-Os** and **4.5-Re** as a function of spin multiplicity.

	4.5-Os			**4.5-Re**		
Spin Multiplicity	triplet	quintet	septet	triplet	quintet	septet
ΔrH (kcal/mol)	7.2	0.0	30.5	8.7	0.0	24.7
ΔrG (kcal/mol)	7.5	0.0	26.3	9.1	0.0	21.5

Table 4.11 Tabulated experimentally determined and computationally derived bond distances/angles and Os–H frequencies for **4.5-Os**.

4.5-Os	Experimental	Computational
μ-Os–H distance (Å)	–	1.664 (μ-H); [1.680 – 1.683] (η-H)
η-Os–H distance (Å)	–	[1.627 – 1.651]
U–H-(μ-Os) distance (Å)	–	2.164 (μ-H); [2.458 – 2.468] (η-H)
U–H-(η-Os) distance (Å)	–	[2.456 – 2.534]
U–μ-Os distance (Å)	2.962; 2.972; 2.962; 2.972	2.912; 2.912; 2.909; 2.914
U–η-Os distance (Å)	2.955; 2.965; 2.955; 2.965	2.907; 2.911; 2.917; 2.917
U–U distance (Å)	3.712	3.623
Os–Os distance (Å)	4.631	4.559
μ-Os–C(Cp*) distance (Å)	[2.218 – 2.275]	[2.209 – 2.274]
η-Os–C(Cp*) distance (Å)	[2.189 – 2.295]	[2.187 – 2.317]
η-Os–U–η-Os angle (º)	122.3	120.5
μ-Os–U–μ-Os angle (º)	102.6	[103.0 – 103.1]
U–μ-Os–U angle (º)	77.4	[76.9 – 77.0]
U–η-Os–Cp(centroid) angle (º)	[121.0 – 121.1]; [161.5 – 161.6]	[119.4 – 119.5]; [163.3 – 163.6]
U–μ-Os–Cp(centroid) angle (º)	[172.3 – 174.2]	[176.4 – 177.3]
Os–H (cm^{-1})	1985, 1875	η-Os: [1952 – 2040] μ-Os: [1849 – 1883]

Table 4.12 Tabulated experimentally determined and computationally derived bond distances/angles and Os–H frequencies for **4.5-Re**.

4.5-Re	Experimental	Computational
μ-Re–H distance (Å)	–	[1.683 – 1.713]
η-Re–H distance (Å)	–	[1.663 – 1.706]
U–H-(μ-Re) distance (Å)	–	[2.286 – 2.449]; [2.582 – 3.055]
U–H-(η-Re) distance (Å)	–	[2.285 – 2.389] (μ-H); [2.426 – 2.462] (H trans Cp*); [3.888 – 3.960] (η-H)
U–μ-Re distance (Å)	2.982; 3.071; 2.982; 3.071	2.979; 3.001; 2.983; 3.012
U–η-Re distance (Å)	3.102; 3.120; 3.102; 3.120	3.002; 3.072; 3.006; 3.061
U–U distance (Å)	3.823	3.772
Re–Re distance (Å)	4.694	4.650
μ-Re–C(Cp*) distance (Å)	[2.268 – 2.326]	[2.259 – 2.342]
η-Re–C(Cp*) distance (Å)	[2.218 – 2.322]	[2.203 – 2.348]
η-Re–U–η-Re angle (º)	113.8	[114.7 – 115.2]
μ-Re–U–μ-Re angle (º)	101.7	[101.8 – 102.0]
U–μ-Re–U angle (º)	78.3	[78.0 – 78.2]
U–η-Re–Cp(centroid) angle (º)	[118.9 – 119.0]; [162.3 – 162.7]	[117.5 – 118.8]; [162.3 – 164.1]
U–μ-Re–Cp(centroid) angle (º)	[130.4 - 130.5]	[123.8 - 132.1]
Re–H (cm^{-1})	1855	η-Re: [1923 – 1992] μ-Re: [1904 – 1917]

Table 4.13 Wiberg Bond Indexes for **4.5-Os** and **4.5-Re**.

	4.5-Os	**4.5-Re**
	quintet	quintet
U–U	0.40	0.28
U–μ-TM	[0.74 – 0.77]	[0.73 – 0.80]
U–η-TM	[0.77 – 0.79]	[0.69 – 0.76]
U–H(μ-TM)	0.34 (μ-H); [0.19 – 0.22] (η-H)	[0.01 – 0.02]*2; [0.07 – 0.15]*2; [0.22 – 0.26]*4
U–H(η-TM)	[0.19 – 0.23]	[0.21 – 0.25] (μ-H); [0.02 – 0.03] (η-H); [0.18 – 0.19] (H trans Cp*)
μ-TM–μ-TM	0.02	0.02
μ-TM–C(Cp*)	[0.34 – 0.38]	[0.29 – 0.39]
η-TM–C(Cp*)	[0.29 – 0.42]	[0.32 – 0.45]
μ-TM–H	[0.49 – 0.50] (μ-H); [0.43 – 0.44] (η-H)	[0.46 – 0.59]
η-TM–H	[0.58 – 0.60]	[0.74 – 0.75] (η-H); [0.57 – 0.59] (μ-H and H trans Cp*)

Table 4.14 Natural charges for **4.5-Os** and **4.5-Re**.

	4.5-Os	**4.5-Re**
	quintet	quintet
U	–0.09; –0.11	0.18; 0.20
μ-TM	–0.76; –0.76	–0.96; –0.97
η-TM	[–0.96 - –0.98]	[–1.08 - –1.15]
H(μ-TM)	0.13 (μ-H) ; 0.21 (η-H)	[0.13 – 0.18]
H(η-TM)	[0.16 – 0.24]	[0.11 – 0.17] ; [0.19 – 0.20] (H trans Cp*)

References

(1) Aldridge, S.; Downs, A. J. Hydrides of the Main-Group Metals: New Variations on an Old Theme. *Chem. Rev.* **2001**, *101* (11), 3305–3366. https://doi.org/10.1021/cr960151d.

(2) Hill, M. S.; Liptrot, D. J.; Weetman, C. Alkaline Earths as Main Group Reagents in Molecular Catalysis. *Chem. Soc. Rev.* **2016**, *45* (4), 972–988. https://doi.org/10.1039/C5CS00880H.

(3) Hadlington, T. J.; Driess, M.; Jones, C. Low-Valent Group 14 Element Hydride Chemistry: Towards Catalysis. *Chem. Soc. Rev.* **2018**, *47* (11), 4176–4197. https://doi.org/10.1039/C7CS00649G.

(4) Roy, M. M. D.; Omaña, A. A.; Wilson, A. S. S.; Hill, M. S.; Aldridge, S.; Rivard, E. Molecular Main Group Metal Hydrides. *Chem. Rev.* **2021**, *121* (20), 12784–12965. https://doi.org/10.1021/acs.chemrev.1c00278.

(5) McCue, J. P. Transition Metal Hydrides. *Coord. Chem. Rev.* **1973**, *10* (3), 265–333. https://doi.org/10.1016/S0010-8545(00)80237-4.

(6) Moore, D. S.; Robinson, S. D. Hydrido Complexes of the Transition Metals. *Chem. Soc. Rev.* **1983**, *12* (4), 415–452. https://doi.org/10.1039/CS9831200415.

(7) McGrady, G. S.; Guilera, G. The Multifarious World of Transition Metal Hydrides. *Chem. Soc. Rev.* **2003**, *32* (6), 383–392. https://doi.org/10.1039/B207999M.

(8) Hoskin, A. J.; Stephan, D. W. Early Transition Metal Hydride Complexes: Synthesis and Reactivity. *Coord. Chem. Rev.* **2002**, *233–234*, 107–129. https://doi.org/10.1016/S0010-8545(02)00030-9.

(9) Crossley, S. W. M.; Obradors, C.; Martinez, R. M.; Shenvi, R. A. Mn-, Fe-, and Co-Catalyzed Radical Hydrofunctionalizations of Olefins. *Chem. Rev.* **2016**, *116* (15), 8912–9000. https://doi.org/10.1021/acs.chemrev.6b00334.
(10) Esteruelas, M. A.; Oro, L. A. Dihydrogen Complexes as Homogeneous Reduction Catalysts. *Chem. Rev.* **1998**, *98* (2), 577–588. https://doi.org/10.1021/cr970322u.
(11) Jordan, A. J.; Lalic, G.; Sadighi, J. P. Coinage Metal Hydrides: Synthesis, Characterization, and Reactivity. *Chem. Rev.* **2016**, *116* (15), 8318–8372. https://doi.org/10.1021/acs.chemrev.6b00366.
(12) Eberhardt, N. A.; Guan, H. Nickel Hydride Complexes. *Chem. Rev.* **2016**, *116* (15), 8373–8426. https://doi.org/10.1021/acs.chemrev.6b00259.
(13) Maity, A.; Teets, T. S. Main Group Lewis Acid-Mediated Transformations of Transition-Metal Hydride Complexes. *Chem. Rev.* **2016**, *116* (15), 8873–8911. https://doi.org/10.1021/acs.chemrev.6b00034.
(14) Batuecas, M.; Gorgas, N.; Crimmin, M. R. Catalytic C–H to C–M (M = Al, Mg) Bond Transformations with Heterometallic Complexes. *Chem. Sci.* **2021**, *12* (6), 1993–2000. https://doi.org/10.1039/D0SC03695A.
(15) Lau, S.; White, A. J. P.; Casely, I. J.; Crimmin, M. R. Tunable Binding of Dinitrogen to a Series of Heterobimetallic Hydride Complexes. *Organometallics* **2018**, *37* (23), 4521–4526. https://doi.org/10.1021/acs.organomet.8b00340.
(16) De Leon, E.; Gonzalez, F.; Bauskar, P.; Gonzalez-Eymard, S.; De Los Santos, D.; Shoshani, M. M. Amplifying Reactivity of Metal Hydrides: A Heterotrimetallic $NiAl_2(\mu_2\text{-}H)_2$ Catalyst for the Dearomatization of N-Heterocycles. *Organometallics* **2023**, *42* (6), 435–440. https://doi.org/10.1021/acs.organomet.2c00668.
(17) Klopčič, N.; Grimmer, I.; Winkler, F.; Sartory, M.; Trattner, A. A Review on Metal Hydride Materials for Hydrogen Storage. *J. Energy Storage* **2023**, *72*, 108456. https://doi.org/10.1016/j.est.2023.108456.
(18) Evans, W. J.; Meadows, J. H.; Hanusa, T. P. Organolanthanide and Organoyttrium Hydride Chemistry. 6. Direct Synthesis and Proton NMR Spectral Analysis of the Trimetallic Yttrium and Yttrium-Zirconium Tetrahydride Complexes, $\{[(C_5H_5)_2YH]_3H\}\{Li(THF)_4\}$ and $\{[(CH_3C_5H_4)_2YH]_2[(CH_3C_5H_4)_2ZrH]H\}$. *J. Am. Chem. Soc.* **1984**, *106* (16), 4454–4460. https://doi.org/10.1021/ja00328a027.
(19) Shima, T.; Hou, Z. Activation and Dehydrogenative Silylation of the C–H Bonds of Phosphine-Coordinated Ruthenium in Lu/Ru Heteromultimetallic Hydride Complexes. *Chem. Lett.* **2008**, *37* (3), 298–299. https://doi.org/10.1246/cl.2008.298.
(20) Shima, T.; Hou, Z. Rare Earth/d-Transition Metal Heteromultimetallic Polyhydride Complexes Based on Half-Sandwich Rare Earth Moieties. *Organometallics* **2009**, *28* (7), 2244–2252. https://doi.org/10.1021/om900024q.
(21) Takenaka, Y.; Shima, T.; Baldamus, J.; Hou, Z. Reduction of Transition-Metal-Coordinated Carbon Monoxide by a Rare-Earth Hydride Cluster: Isolation of Well-Defined Heteromultimetallic Oxycarbene, Oxymethyl, Carbene, and Methyl Complexes. *Angew. Chem., Int. Ed.* **2009**, *48* (42), 7888–7891. https://doi.org/10.1002/anie.200903660.
(22) Takenaka, Y.; Hou, Z. Lanthanide Terminal Hydride Complexes Bearing Two Sterically Demanding $C_5Me_4SiMe_3$ Ligands. Synthesis, Structure, and Reactivity. *Organometallics* **2009**, *28* (17), 5196–5203. https://doi.org/10.1021/om900453j.

(23) Shima, T.; Luo, Y.; Stewart, T.; Bau, R.; McIntyre, G. J.; Mason, S. A.; Hou, Z. Molecular Heterometallic Hydride Clusters Composed of Rare-Earth and d-Transition Metals. *Nat. Chem.* **2011**, *3* (10), 814–820. https://doi.org/10.1038/nchem.1147.
(24) Shima, T.; Hou, Z. Heterometallic Polyhydride Complexes Containing Yttrium Hydrides with Different Cp Ligands: Synthesis, Structure, and Hydrogen-Uptake/Release Properties. *Chem.─Eur. J.* **2013**, *19* (10), 3458–3466. https://doi.org/10.1002/chem.201203495.
(25) O, W. W. N.; Kang, X.; Luo, Y.; Hou, Z. PNP-Ligated Heterometallic Rare-Earth/Ruthenium Hydride Complexes Bearing Phosphinophenyl and Phosphinomethyl Bridging Ligands. *Organometallics* **2014**, *33* (4), 1030–1043. https://doi.org/10.1021/om401216v.
(26) Baudry, D.; Ephritikhine, M. Synthesis of a Hydride-Rich Uranium-Rhenium Dimer: [(*p*-F-$C_6H_4)_3P]_2ReH_6U(\eta$-$C_5H_5)_3$. *J. Organomet. Chem* **1986**, *311* (1), 189–192. https://doi.org/10.1016/0022-328X(86)80231-5.
(27) Cendrowski-Guillaume, S. M.; Lance, M.; Nierlich, M.; Vigner, J.; Ephritikhine, M. New Actinide Hydrogen Transition Metal Compounds. Synthesis of $[K(C_{12}H_{24}O_6)][(\eta$-$C_5Me_5)_2(Cl)UH_6Re(PPh_3)_2]$ and the Crystal Structure of Its Benzene Solvate. *J. Chem. Soc., Chem. Commun.* **1994**, No. 14, 1655–1656. https://doi.org/10.1039/C39940001655.
(28) Cendrowski-Guillaume, S. M.; Ephritikhine, M. Synthesis and Reactivity of Hydrogen-Rich Uranium–Rhenium Compounds; an Unsuspected Detrimental Effect of Alkali-Metal Halide on Chemical Metathesis. *J. Chem. Soc., Dalton Trans.* **1996**, No. 8, 1487–1491. https://doi.org/10.1039/DT9960001487.
(29) Ye, C. Z.; Rosal, I. D.; Boreen, M. A.; Ouellette, E. T.; Russo, D. R.; Maron, L.; Arnold, J.; Camp, C. A Versatile Strategy for the Formation of Hydride-Bridged Actinide–Iridium Multimetallics. *Chem. Sci.* **2023**, *14* (4), 861–868. https://doi.org/10.1039/D2SC04903A.
(30) Herrmann, W. A.; Okuda, J. Hexahydrido(Pentamethylcyclopentadienyl)Rhenium, $[(C_5Me_5)ReH_6]$. *Angew. Chem., Int. Ed.* **1986**, *25* (12), 1092–1093. https://doi.org/10.1002/anie.198610921.
(31) Cordero, B.; Gómez, V.; Platero-Prats, A. E.; Revés, M.; Echeverría, J.; Cremades, E.; Barragán, F.; Alvarez, S. Covalent Radii Revisited. *Dalton Trans.* **2008**, No. 21, 2832–2838. https://doi.org/10.1039/B801115J.
(32) Yang, L.; Powell, D. R.; Houser, R. P. Structural Variation in Copper(I) Complexes with Pyridylmethylamide Ligands: Structural Analysis with a New Four-Coordinate Geometry Index, τ_4. *Dalton Trans.* **2007**, No. 9, 955–964. https://doi.org/10.1039/B617136B.
(33) Gardner, B. M.; McMaster, J.; Lewis, W.; Liddle, S. T. Synthesis and Structure of $[\{N(CH_2CH_2NSiMe_3)_3\}URe(\eta^5$-$C_5H_5)_2]$: A Heterobimetallic Complex with an Unsupported Uranium–Rhenium Bond. *Chem. Commun.* **2009**, No. 20, 2851–2853. https://doi.org/10.1039/B906554G.
(34) Boreen, M. A.; Parker, B. F.; Lohrey, T. D.; Arnold, J. A Homoleptic Uranium(III) Tris(Aryl) Complex. *J. Am. Chem. Soc.* **2016**, *138* (49), 15865–15868. https://doi.org/10.1021/jacs.6b11182.
(35) Bailey, P. J.; Coxall, R. A.; Dick, C. M.; Fabre, S.; Henderson, L. C.; Herber, C.; Liddle, S. T.; Loroño-González, D.; Parkin, A.; Parsons, S. The First Structural Characterisation of a Group 2 Metal Alkylperoxide Complex: Comments on the Cleavage of Dioxygen by Magnesium Alkyl Complexes. *Chem.─Eur. J.* **2003**, *9* (19), 4820–4828. https://doi.org/10.1002/chem.200305053.

(36) Shima, T.; Suzuki, H. Heterobimetallic Polyhydride Complex, Cp*Ru(μ-H)$_4$OsCp* (Cp* = η^5-C$_5$Me$_5$). Synthesis and Reaction with Ethylene. *Organometallics* **2005**, *24* (16), 3939–3945. https://doi.org/10.1021/om0503996.
(37) Kiplinger, J. L.; Morris, D. E.; Scott, B. L.; Burns, C. J. Convenient Synthesis, Structure, and Reactivity of (C$_5$Me$_5$)U(CH$_2$C$_6$H$_5$)$_3$: A Simple Strategy for the Preparation of Monopentamethylcyclopentadienyl Uranium(IV) Complexes. *Organometallics* **2002**, *21* (26), 5978–5982. https://doi.org/10.1021/om0206610.
(38) Cantat, T.; Scott, B. L.; Kiplinger, J. L. Convenient Access to the Anhydrous Thorium Tetrachloride Complexes ThCl$_4$(DME)$_2$, ThCl$_4$(1,4-Dioxane)$_2$ and ThCl$_4$(THF)$_{3.5}$ Using Commercially Available and Inexpensive Starting Materials. *Chem. Commun.* **2010**, *46* (6), 919–921. https://doi.org/10.1039/B923558B.
(39) APEX2, APEX3, SADABS, TWINABS and SAINT. Bruker AXS. Madison, WI, USA.
(40) Sheldrick, G. M. *SHELXT* – Integrated Space-Group and Crystal-Structure Determination. *Acta Crystallogr A Found Adv* **2015**, *71* (1), 3–8. https://doi.org/10.1107/S2053273314026370.
(41) Sheldrick, G. M. Crystal Structure Refinement with *SHELXL*. *Acta Crystallogr C Struct Chem* **2015**, *71* (1), 3–8. https://doi.org/10.1107/S2053229614024218.
(42) Dolomanov, O. V.; Bourhis, L. J.; Gildea, R. J.; Howard, J. A. K.; Puschmann, H. *OLEX2* : A Complete Structure Solution, Refinement and Analysis Program. *J Appl Crystallogr* **2009**, *42* (2), 339–341. https://doi.org/10.1107/S0021889808042726.
(43) Macrae, C. F.; Bruno, I. J.; Chisholm, J. A.; Edgington, P. R.; McCabe, P.; Pidcock, E.; Rodriguez-Monge, L.; Taylor, R.; van de Streek, J.; Wood, P. A. Mercury CSD 2.0– New Features for the Visualization and Investigation of Crystal Structures. *Journal of Applied Crystallography* **2008**, *41*, 466–470.
(44) Frisch, M. J.; Trucks, G. W.; Schlegel, H. B.; Scuseria, G. E.; Robb, M. A.; Cheeseman, J. R.; Scalmani, G.; Barone, V.; Petersson, G. A.; Nakatsuji, H.; Li, X.; Caricato, M.; Marenich, A.; Bloino, J.; Janesko, B. G.; Gomperts, R.; Mennucci, B.; Hratchian, H. P.; Ortiz, J. V.; Izmaylov, A. F.; Sonnenberg, J. L.; Williams-Young, D.; Ding, F.; Lipparini, F.; Egidi, F.; Goings, J.; Peng, B.; Petrone, A.; Henderson, T.; Ranasinghe, D.; Zakrzewski, V. G.; Gao, J.; Rega, N.; Zheng, G.; Liang, W.; Hada, M.; Ehara, M.; Toyota, K.; Fukuda, R.; Hasegawa, J.; Ishida, M.; Nakajima, T.; Honda, Y.; Kitao, O.; Nakai, H.; Vreven, T.; Throssell, K.; Montgomery, Jr., J. A.; Peralta, J. E.; Ogliaro, F.; Bearpark, M.; Heyd, J. J.; Brothers, E.; Kudin, K. N.; Staroverov, V. N.; Keith, T.; Kobayashi, R.; Normand, J.; Raghavachari, K.; Rendell, A.; Burant, J. C.; Iyengar, S. S.; Tomasi, J.; Cossi, M.; Millam, J. M.; Klene, M.; Adamo, C.; Cammi, R.; Ochterski, J. W.; Martin, R. L.; Morokuma, K.; Farkas, O.; Foresman, J. B.; Fox, D. J. Gaussian 09.
(45) Perdew, J. P.; Chevary, J. A.; Vosko, S. H.; Jackson, K. A.; Pederson, M. R.; Singh, D. J.; Fiolhais, C. Atoms, Molecules, Solids, and Surfaces: Applications of the Generalized Gradient Approximation for Exchange and Correlation. *Phys. Rev. B* **1992**, *46* (11), 6671–6687. https://doi.org/10.1103/PhysRevB.46.6671.
(46) Becke, A. D. Density-functional Thermochemistry. III. The Role of Exact Exchange. *J. Chem. Phys.* **1993**, *98* (7), 5648–5652. https://doi.org/10.1063/1.464913.
(47) Cao, X.; Dolg, M. Segmented Contraction Scheme for Small-Core Actinide Pseudopotential Basis Sets. *Journal of Molecular Structure: THEOCHEM* **2004**, *673* (1), 203–209. https://doi.org/10.1016/j.theochem.2003.12.015.

(48) Cao, X.; Dolg, M.; Stoll, H. Valence Basis Sets for Relativistic Energy-Consistent Small-Core Actinide Pseudopotentials. *J. Chem. Phys.* **2003**, *118* (2), 487–496. https://doi.org/10.1063/1.1521431.
(49) Andrae, D.; Häußermann, U.; Dolg, M.; Stoll, H.; Preuß, H. Energy-Adjustedab Initio Pseudopotentials for the Second and Third Row Transition Elements. *Theoret. Chim. Acta* **1990**, *77* (2), 123–141. https://doi.org/10.1007/BF01114537.
(50) Ehlers, A. W.; Böhme, M.; Dapprich, S.; Gobbi, A.; Höllwarth, A.; Jonas, V.; Köhler, K. F.; Stegmann, R.; Veldkamp, A.; Frenking, G. A Set of F-Polarization Functions for Pseudo-Potential Basis Sets of the Transition Metals Sc–Cu, Y–Ag and La–Au. *Chemical Physics Letters* **1993**, *208* (1), 111–114. https://doi.org/10.1016/0009-2614(93)80086-5.
(51) Hariharan, P. C.; Pople, J. A. The Influence of Polarization Functions on Molecular Orbital Hydrogenation Energies. *Theoret. Chim. Acta* **1973**, *28* (3), 213–222. https://doi.org/10.1007/BF00533485.
(52) Ditchfield, R.; Hehre, W. J.; Pople, J. A. Self-Consistent Molecular-Orbital Methods. IX. An Extended Gaussian-Type Basis for Molecular-Orbital Studies of Organic Molecules. *J. Chem. Phys.* **1971**, *54* (2), 724–728. https://doi.org/10.1063/1.1674902.
(53) Hehre, W. J.; Ditchfield, R.; Pople, J. A. Self—Consistent Molecular Orbital Methods. XII. Further Extensions of Gaussian—Type Basis Sets for Use in Molecular Orbital Studies of Organic Molecules. *J. Chem. Phys.* **1972**, *56* (5), 2257–2261. https://doi.org/10.1063/1.1677527.
(54) Grimme, S.; Ehrlich, S.; Goerigk, L. Effect of the Damping Function in Dispersion Corrected Density Functional Theory. *Journal of Computational Chemistry* **2011**, *32* (7), 1456–1465. https://doi.org/10.1002/jcc.21759.
(55) Reed, A. E.; Curtiss, L. A.; Weinhold, F. Intermolecular Interactions from a Natural Bond Orbital, Donor-Acceptor Viewpoint. *Chem. Rev.* **1988**, *88* (6), 899–926. https://doi.org/10.1021/cr00088a005.

Chapter 5

Reduction of CS_2 to an Ethanetetrathiolate by a Hydride-Bridged Uranium–Iridium Heterobimetallic

Introduction

Transition metal (TM) hydrides have carved out a substantial role in organometallic chemistry in the nearly 100 years since their discovery. They have been implicated as intermediates in numerous catalytic reactions, such as olefin hydrofunctionalization,[1] redox electrocatalysis,[2] and small molecule reduction/activation,[3,4] while also finding application in fields such as renewable fuel production and solar energy storage.[5,6] These species are also well-suited to forming heterobimetallic complexes, typically consisting of an electron-rich transition metal hydride in concert with an electron-deficient Lewis acid, that are capable of novel reactivity that diverges from that of single-metal systems. Main-group Lewis acids and cationic coinage metals have been shown to be competent partners for electron-rich transition metal hydrides, enabling transformations including carbonyl reduction, H_2 activation, and olefin polymerization.[7,8]

Despite the well-established Lewis acidity of the actinides (An),[9] relatively few efforts to pair them with transition metal hydrides have been reported. Ephritikhine synthesized the first hydride-bridged An–TM complexes over thirty years ago with a series of U–Re species; no reactivity with small molecules was reported,[10–12] and the field has laid dormant in the subsequent years. We recently demonstrated that salt metathesis reactions with K[Cp*IrH$_3$] and actinide halide starting materials led to hydride-supported An(IV)–Ir species.[13] These species contained multiple anionic, iridium-containing (iridate) fragments, and also showed no evidence of small-molecule reactivity. Nevertheless, given the documented ability of Lewis acid-coupled iridium hydrides to promote reactions such as ketone hydrogenation,[14] H/D exchange,[15–19] cleavage of heteroallenes,[20] and alkene dehydrogenation,[21] we devoted further study to the discovery of more reactive, hydride-supported An–Ir complexes.

To increase the reactivity of An–Ir polyhydride species, we targeted two particular changes. First, we aimed to synthesize a heterobimetallic system with only one metal–metal interaction, which would allow for a more accessible actinide center, with the added benefit of more controlled reactivity. Second, we aimed to install a U(III) center rather than the U(IV) center in our previous An–Ir compounds, given the well-catalogued reducing power of low-valent uranium species.[22] With these aims in mind, the bulky U(III) metallocene $(Cp^{iPr4})_2UI$ (Cp^{iPr4} = tetra(isopropyl)cyclopentadienyl) appeared to be an ideal system to support a reactive U(III)–Ir complex *via* salt metathesis.[23]

Results and Discussion

Equimolar amounts of K[Cp*IrH$_3$] and $(Cp^{iPr4})_2UI$ were combined as THF solutions to yield the U(III) iridate trihydride $(Cp^{iPr4})_2U(\mu\text{-H})_3IrCp^*$ (**5.1**) (Scheme 5.1). Compound **5.1** is highly soluble in nonpolar solvents, requiring the cooling of concentrated solutions in hexamethyldisiloxane (HMDSO) to –40 °C to isolate solid product as dark green crystals in 51% yield. The influence of the paramagnetic U(III) center is clear in the ^{1}H NMR spectrum; it contains only two sharp resonances, corresponding to the iridium-bound Cp* ligand at 4.39 ppm, and 0.5 equivalents of co-crystallized HMDSO at 0.12 ppm. Two of the remaining broad resonances, at 6.25 ppm and –6.55 ppm, each integrate to 12 protons and are tentatively assigned to isopropyl methyl groups of the Cp^{iPr4} ligands. A third, less intense resonance is located at –31.0 ppm, but cannot be assigned with confidence to either the bridging hydrides or the Cp^{iPr4} ligands. The IR spectrum of **1** contains a strong hydride stretch at 1955 cm^{-1} with a shoulder at 2033 cm^{-1}, comparable to the hydride stretch of 1951 cm^{-1} found in $U\{(\mu\text{-H})_3IrCp^*\}_4$ (**5.A**).[13]

Scheme 5.1 Synthesis of $(Cp^{iPr4})_2U(\mu\text{-}H)_3IrCp^*$ (**5.1**).

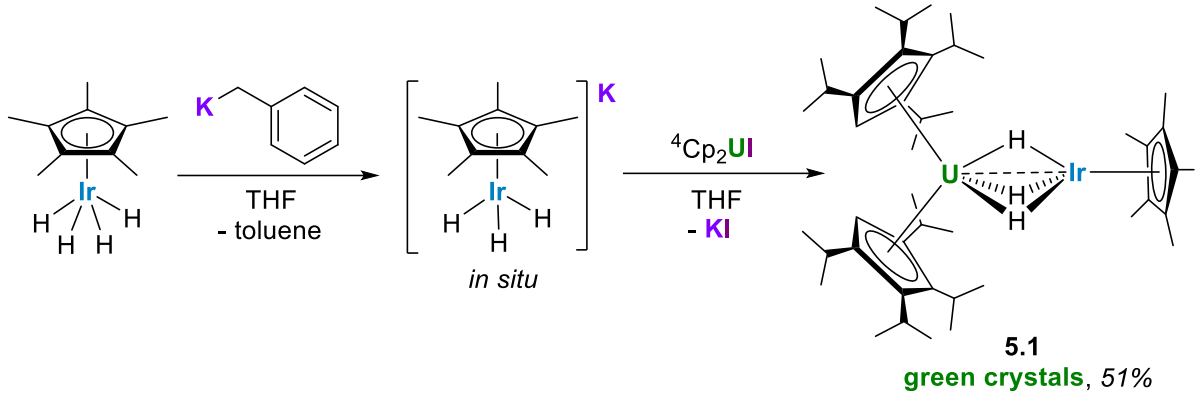

Complex **5.1** crystallizes in the space group $P\bar{1}$ with 0.5 equivalents of HMDSO. Unlike many previously isolated hydride-supported An–TM complexes,[13] the hydrides in **5.1** were located and refined. Given the monoanionic nature of $Cp^*IrH_3^-$,[13,20,16,24] the structure is consistent with a U(III) product with two anionic Cp^{iPr4-} ligands in addition to the $Cp^*IrH_3^-$ moiety. The U–Ir distance of 3.0308(3) Å is longer than the average U–Ir distance of 2.954(1) Å in **5.A**, which is unsurprising given the larger size of the U(III) ion in comparison to U(IV). The Ir–H and U–H bond lengths average 1.52(5) Å and 2.44(5) Å, respectively. These metrics agree well with computationally predicted M–H bond lengths in the uranium tetrairidate species.[13] The highly linear U–Ir–$Cp^*_{centroid}$ angle of 176.56(6)° is consistent with three bridging hydrides, as observed in numerous multimetallic complexes with $Cp^*IrH_3^-$ moieties.[13,25–27]

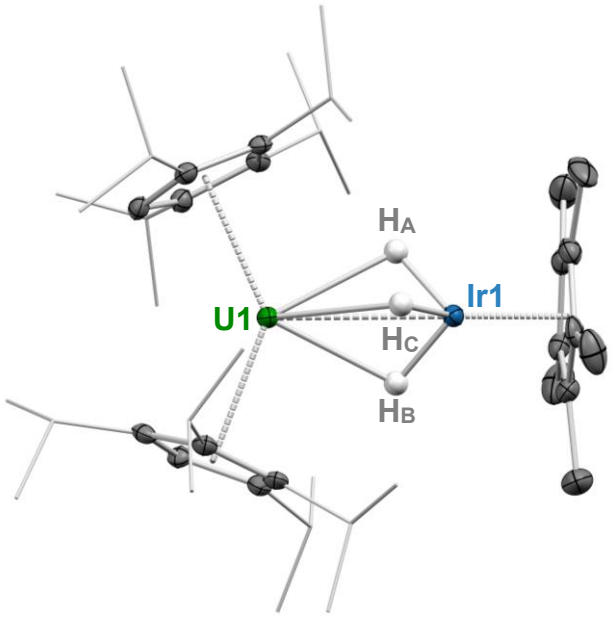

Figure 5.1 Solid-state molecular structure of **5.1**. Ellipsoids are presented at the 50% probability level. Non-hydride hydrogen atoms have been omitted and isopropyl groups have been wireframed for clarity. Selected bond distances (Å) and angles (°): U1–Ir1 3.0308(3), U1–Cp^{iPr4}(cent) 2.5233(3)/2.5387(3), U1–H_A 2.42(5), U1–H_B 2.43(4), U1–H_C 2.46(4), Ir1–H_A 1.47(5), Ir1–H_B 1.54(5), Ir1–H_C 1.51(4), U1–Ir1–$Cp^*_{cent.}$ 176.56(6).

With this heterobimetallic U(III)–Ir species in hand, we began to probe whether it was more reactive to small molecules than the U(IV) complex **5.A**. Upon addition of 1 equivalent of CS_2 to a hexane solution of **5.1**, there was a rapid color change from dark green to red. Cooling the red solution to –40 °C yielded red crystals of the ethanetetrathiolate dimeric complex **5.2** (Scheme 5.2). These red crystals exhibited poor solubility in benzene and THF, which in conjunction with the paramagnetism of the compound made assignment of the ^{1}H NMR spectrum unfeasible. IR spectroscopy reveals several hydride stretches at 2040, 1958, and 1915 cm^{-1} for **5.2**, shifted slightly higher in frequency relative to those of **5.1**.

Scheme 2 Activation of CS_2 and C–C bond formation by complex **5.1** to form the ethanetetrathiolate-bridged dimer **5.2**.

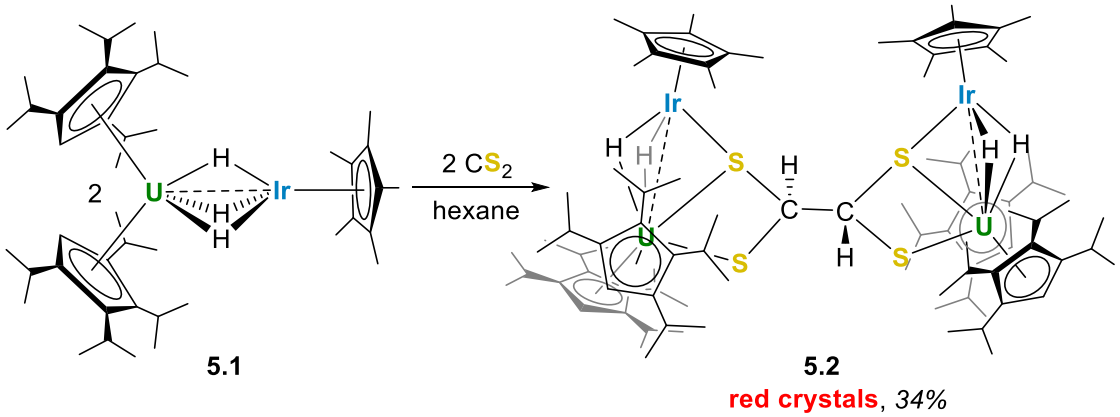

Complex **5.2** crystallizes with one equivalent of *n*-hexane in the space group *C*2/*c*, with half of the molecule generated around a C_2 axis perpendicular to the central C–C bond (Figure 5.2). The U–Ir distance is significantly lengthened in **5.2** compared to **5.1**, at 3.1382(6) Å. The average metal hydride distances are within error of those found for **5.2**, at 2.47(7) Å (U–H) and 1.56(6) Å (Os–H). The U–S bond is significantly shorter for the non-bridging sulfur atom compared to the U–S–Ir bridging atom, at 2.6618(13) Å and 2.8204(13) Å, respectively, with a shorter Ir–S bond length of 2.3585(14) Å. The carbon atoms in the $C_2S_4H_2^{4-}$ moiety have near-tetrahedral geometries (τ_4 = 0.96, with α = 113.38(15)°, β = 112(3)°), and the C–C bond length (1.543(8) Å) is that of a C–C single bond.

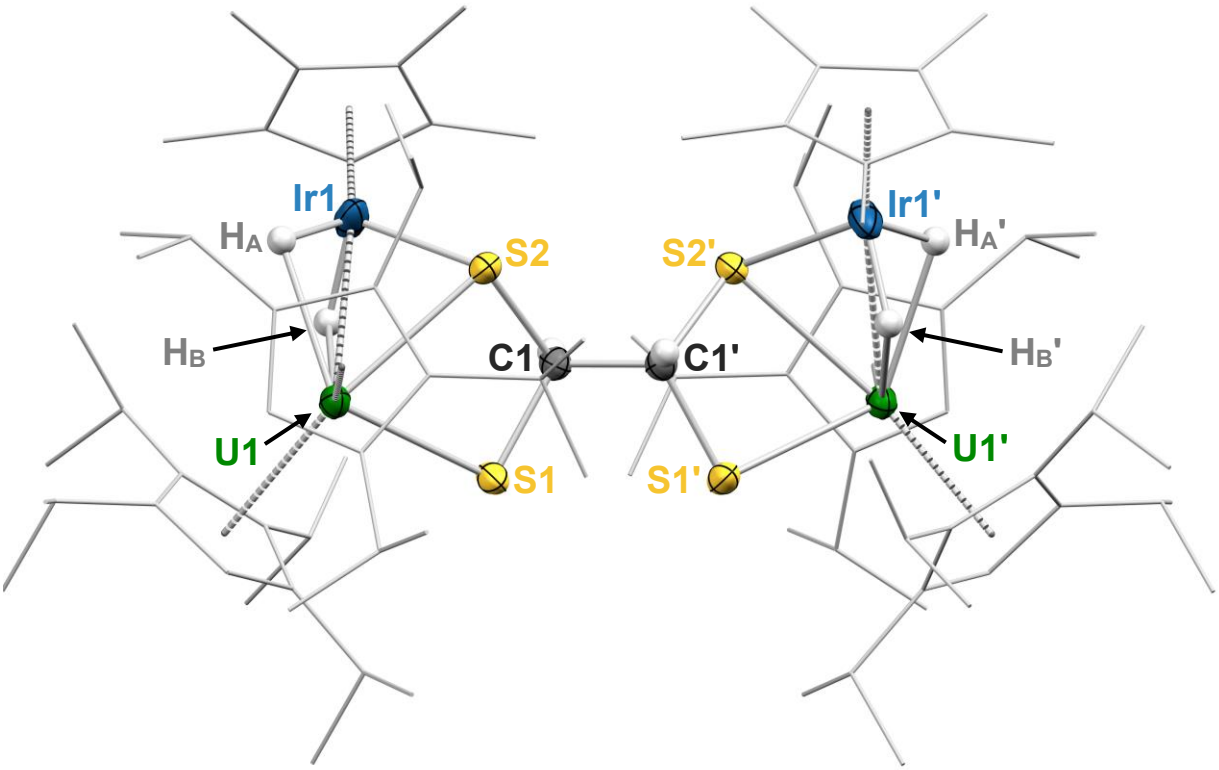

Figure 5.2 ORTEP diagram of **5.2**, with ellipsoids drawn at the 50% probability level. Hydrogen atoms of the Cp* and ^{iPr4}Cp ligands have been eliminated, and the ligands have been wireframed for clarity. Selected bond distances (Å) and angles (°): U1–Ir1 3.1382(6), U1–H_A 2.41(6), U1–H_B 2.52(7), Ir1–H_A 1.60(6), Ir1–H_B 1.52(4), U1–S1 2.6618(13), U1–S2 2.8204(13), Ir1–S2 (2.3585(14), C1–C1' 1.543(8), S1–C1–S2 107.3(2).

Each molecule of CS_2, therefore, has been reduced by three electrons in order to form the $C_2S_4H_2^{4-}$ moiety. Two electrons originate from the hydride bond into which CS_2 inserts, while the third is transferred from the U(III) center of **5.1**, which oxidizes to U(IV) in **5.2**. This is further corroborated by the UV-vis/NIR spectra of **5.1** and **5.2** (Figure 5.3). The spectrum of complex **5.1** contains higher intensity, broader NIR absorption features, in line with a U(III) center, compared to the numerous sharp, lower intensity features indicative of a U(IV) species found in the spectrum of **5.2**.[28,29] The iridium oxidation state remains unchanged, with a bridging hydride replaced with a bridging sulfide. Additions of CO_2 were investigated for similar reactivity, but the only metal-containing species observed was Cp*IrH_2(CO), a CO_2 cleavage product observed in several other systems.[20]

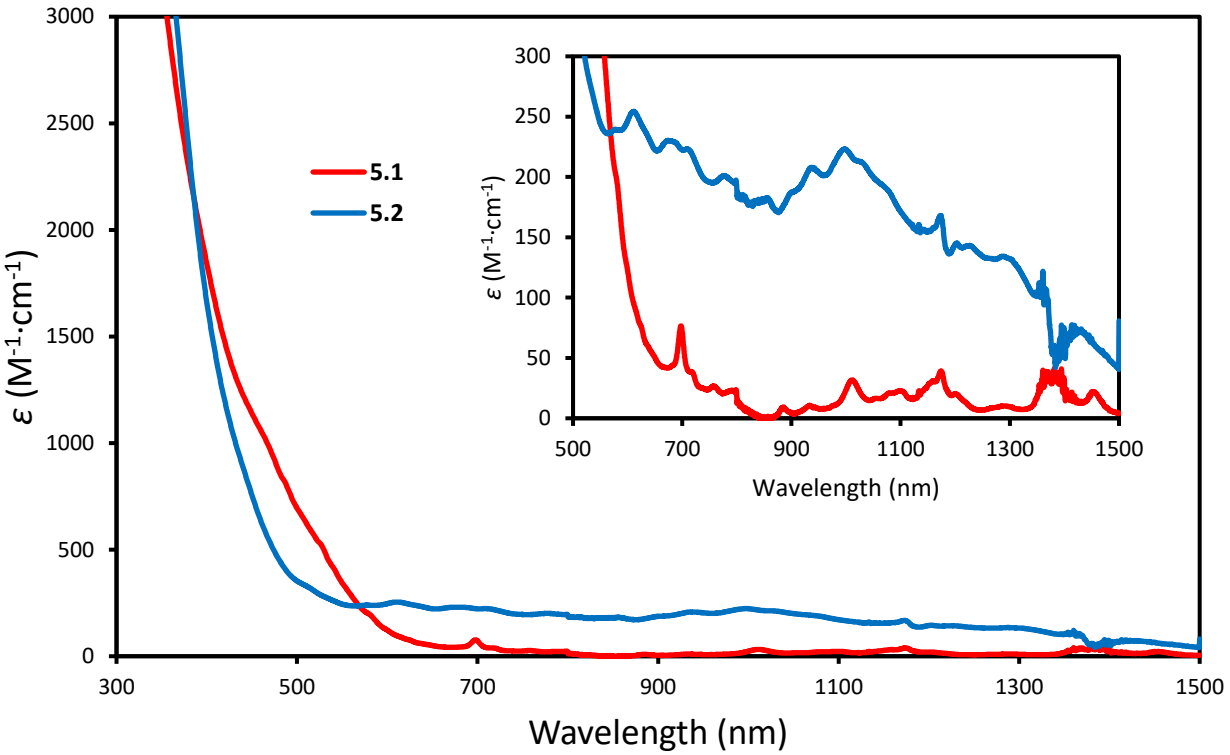

Figure 5.3 UV-vis/NIR spectra of **5.1** and **5.2** in THF, with the inset showing a more detailed view of the spectra between 500 and 1500 nm.

Conclusions

In conclusion, the heterobimetallic U–Ir trihydride **5.1** reduces CS_2 to form an uncommon ethanetetrathiolate fragment *via* C–C coupling and hydride insertion. These two processes have been observed separately in a number of monometallic systems. Uranium complexes have been demonstrated to reduce CS_2 to numerous anionic fragments such as CS_2^{2-}, CS_3^{2-}, $C_2S_4^{2-}$, $C_2S_4^{4-}$, $C_3S_5^{2-}$, etc.[30–41] Notably, in all cases the CS_2 reduction or coupling products remain partially unsaturated. The insertion of CS_2 into metal-hydride bonds is documented for both transition metal and alkali-earth metal systems, resulting in the formation of metal dithioformate complexes.[42–46] However, for actinide–hydride bonds, CS_2 insertion is without precedent, and CO_2 insertion is rare.[47,48] Our hydride-supported U–Ir heterobimetallic system combines the reductive C–C coupling of uranium with the hydride insertion of transition metal hydrides, resulting in the conversion of CS_2 to $C_2S_4H_2^{2-}$, highlighting the potential for new reactivity mediated by actinide/transition metal hydrides. Future work will explore the reactivity scope of these unique complexes.

Experimental Procedures

General considerations: Unless otherwise noted, all reactions were performed using standard Schlenk line techniques under an atmosphere of nitrogen, or in an MBraun inert atmosphere glove box under an atmosphere of nitrogen. Glassware and Celite® were stored in an oven at ca. 150 °C for at least 3 h prior to use. Molecular sieves (4 Å) were activated by heating to 200 °C overnight

under vacuum prior to storage in a glovebox. NMR spectra were recorded on Bruker AV-600 and AVB-400 spectrometers. ^{1}H chemical shifts are given relative to residual solvent peaks and are recorded in units of parts per million (ppm). FT-IR samples were prepared as Nujol mulls pressed between KBr plates, with data collected with a Nicolet iS10 FT-IR spectrometer. Melting points were determined using sealed capillaries prepared under nitrogen on an OptiMelt automated melting point system. Elemental analyses were determined at the Microanalytical Facility at the College of Chemistry, University of California, Berkeley.

Materials: Tetrahydrofuran (THF) and *n*-hexane were purified by passage through columns of activated alumina and degassed by sparging with nitrogen. Deuterated solvents were degassed with three freeze-pump-thaw cycles and stored over molecular sieves. Hexamethyldisiloxane (HMDSO) was stirred over CaH_2, distilled, and sparged with nitrogen. Benzylpotassium,[49] Cp^*IrH_4,[50] and $(Cp^{iPr4})_2UI$[23] were synthesized according to literature procedures. CO_2 was sourced from Linde, research grade (4.8 RS, 99.998% purity). All other chemicals were purchased from commercial sources and used as received.

Synthesis of $(Cp^{iPr4})_2U(\mu\text{-}H)_3IrCp^*$ (5.1):
Cp^*IrH_4 (67.8 mg, 0.205 mmol, 1.05 equiv.) and benzyl potassium (27.1 mg, 0.208 mmol, 1.07 equiv.) were added to a 20 mL scintillation vial with THF (4 mL) to generate a solution of $K[Cp^*IrH_3]$. $(Cp^{iPr4})_2UI$ (162.4 mg, 0.195 mmol, 1.00 equiv) was dissolved in THF (4 mL) and added to the $K[Cp^*IrH_3]$ solution, forming a dark green slurry as KI salt crashed out of solution. After stirring at room temperature for 2 h, the solvent was removed *in vacuo*. The crude solid was then triturated with *n*-hexane and the product was extracted with HMDSO, filtered through Celite, and concentrated (1 mL). This solution was cooled to –40 °C, affording dark green crystals (110.9 mg, 51% yield). Mp ca. 197 °C; ^{1}H NMR (600 MHz, C_6D_6): δ 6.32 (s, 12H, broad), 4.39 (s, 15H, Cp*), –6.55 (s, 12 H, broad), –31.04 (s, broad); ^{13}C NMR (600 MHz, C_6D_6): δ 112.3, 39.1, 5.21, 1.69; IR (Nujol mull on KBr): 2033 (m), 1959 (s), 1253 (s), 1180 (m), 1146 (w), 1102 (w), 1058 (m), 1033 (w), 982 (w), 845 (s), 770 (m), 760 (m), 667 (w); Anal. Calcd (%) for $UIrC_{44}H_{76}\bullet 0.5C_6H_{18}OSi_2$: C, 50.56; H, 7.67. Found: C, 50.21; H, 7.62.

Synthesis of 5.2 from CS_2 and 5.1:
Compound **5.1** (29.7 mg, 0.027 mmol, 1.00 equiv.) was dissolved in 2 mL *n*-hexane in a 4 mL shell vial. From an *n*-hexane stock solution containing 20 µL CS_2/1 mL, CS_2 (1.61 µL, 0.027 mmol, 1.00 equiv.) was added to the shell vial containing the solution of **5.1**, which was sealed in a 20 mL scintillation vial. The dark green solution immediately became red. This solution was cooled to –40 °C, affording X-ray quality, highly insoluble red crystals over several crops (10.4 mg, 34% yield). Mp 179-182 °C; ^{1}H NMR (700 MHz, d_8-THF): δ 30.3, 27.7, 25.3, 22.8, 20.7, 18.9, 16.7, 13.7, 6.17, 5.17, –7.33, –11.3, –12.1, –14.0, –21.2, –30.7, –37.3; No ^{13}C NMR spectrum was collected due to compound paramagnetism and insolubility; IR (Nujol mull on KBr): 2040 (s), 1958 (s), 1916 (s), 1309 (w), 1178 (m), 1145 (m), 1102 (m), 1074 (w), 1061 (w), 1030 (m), 979 (w), 924 (w), 775 (m), 700 (w), 662 (m), 535 (w), 508 (w). Anal. Calcd (%) for $U_2Ir_2C_{96}H_{166}S$: C, 49.93; H, 7.42; S, 5.55. Found: C, 50.28; H, 7.42; S, 5.43.

X-ray crystallography data

In a dry nitrogen glovebox, samples of single crystals were coated in Paratone-N oil for transport to the Advanced Light Source (ALS). Crystals were mounted on a MiTeGen 10 μm aperture Dual-Thickness MicroMount loop. X-ray diffraction data for **5.1** and **5.2** were collected at the ALS, Lawrence Berkeley National Lab, Berkeley, CA, station 12.2.1 using a silicon monochromated beam of 17 keV (λ = 0.7288 Å) synchrotron radiation. Data was collected at 100 K, with the crystals cooled by a stream of dry nitrogen. Bruker APEX3 software was used for the data collections, Bruker SAINT v8.37A or V8.38A software was used to conduct the cell refinement and data reduction procedures,[51] and absorption corrections were carried out by a multi-scan method utilizing the SADABS program.[51] CrysAlis Pro was used for the data collections and data processing, including a multi-scan absorption correction applied using the SCALE3 ABSPACK scaling algorithm within CrysAlis Pro. Initial structure solutions were found using direct methods (SHELXT),[52] and refinements were carried out using SHELXL-2014,[53] as implemented by Olex2.[54] Thermal parameters for all non-hydrogen atoms were refined anisotropically. Hydrogen atoms were placed in calculated positions and refined isotropically. Thermal ellipsoid plots were made using Mercury.[55] The structures have been deposited to the Cambridge Crystallographic Data Centre (CCDC) with deposition numbers 2349727 (**5.1**) and 2349728 (**5.2**).

Table 5.1 Crystal data for complexes **5.1** and **5.2**.

Compound	**5.1**	**5.2**
Empirical formula	$C_{47}H_{85}IrO_{0.5}SiU$	$C_{96}H_{166}Ir_2S_4U_2$
Formula weight	1116.46	2308.98
Temperature/K	100.0	100.0
Crystal system	triclinic	monoclinic
Space group	P-1	C2/c
a/Å	12.0803(12)	29.472(3)
b/Å	12.3459(12)	18.083(2)
c/Å	16.9963(17)	17.948(2)
α/°	105.679(4)	90
β/°	96.253(4)	99.352(4)
γ/°	96.290(4)	90
Volume/Å^3	2400.3(4)	9437.7(18)
Z	2	4
ρ_{calc}g/cm^3	1.545	1.625
μ/mm^{-1}	4.541	4.687
F(000)	1108.0	4576.0
Crystal size/mm^3	0.12 × 0.04 × 0.04	0.2 × 0.1 × 0.1
Radiation	synchrotron (λ = 0.7288)	synchrotron (λ = 0.7288)
2Θ range for data collection/°	4.62 to 61.044	4.62 to 54.194
Index ranges	$-16 \le h \le 16$, $-17 \le k \le 17$, $-23 \le l \le 23$	$-36 \le h \le 36$, $-22 \le k \le 22$, $-22 \le l \le 22$
Reflections collected	42447	61141
Independent reflections	13551 [R_{int} = 0.0666, R_{sigma} = 0.0693]	9655 [R_{int} = 0.0560, R_{sigma} = 0.0372]
Data/restraints/parameters	13551/15/535	9655/15/524
Goodness-of-fit on F^2	1.012	1.032
Final R indexes [I>=2σ (I)]	R_1 = 0.0364, wR_2 = 0.0824	R_1 = 0.0336, wR_2 = 0.0800
Final R indexes [all data]	R_1 = 0.0461, wR_2 = 0.0878	R_1 = 0.0389, wR_2 = 0.0831
Largest diff. peak/hole / e Å^{-3}	0.95/–1.19	2.26/–1.32
CSD entry	2349727	2349728

References

(1) Crossley, S. W. M.; Obradors, C.; Martinez, R. M.; Shenvi, R. A. Mn-, Fe-, and Co-Catalyzed Radical Hydrofunctionalizations of Olefins. *Chem. Rev.* **2016**, *116* (15), 8912–9000. https://doi.org/10.1021/acs.chemrev.6b00334.

(2) Eberhardt, N. A.; Guan, H. Nickel Hydride Complexes. *Chem. Rev.* **2016**, *116* (15), 8373–8426. https://doi.org/10.1021/acs.chemrev.6b00259.

(3) Esteruelas, M. A.; Oro, L. A. Dihydrogen Complexes as Homogeneous Reduction Catalysts. *Chem. Rev.* **1998**, *98* (2), 577–588. https://doi.org/10.1021/cr970322u.

(4) Jordan, A. J.; Lalic, G.; Sadighi, J. P. Coinage Metal Hydrides: Synthesis, Characterization, and Reactivity. *Chem. Rev.* **2016**, *116* (15), 8318–8372. https://doi.org/10.1021/acs.chemrev.6b00366.

(5) Cook, T. R.; Dogutan, D. K.; Reece, S. Y.; Surendranath, Y.; Teets, T. S.; Nocera, D. G. Solar Energy Supply and Storage for the Legacy and Nonlegacy Worlds. *Chem. Rev.* **2010**, *110* (11), 6474–6502. https://doi.org/10.1021/cr100246c.

(6) Appel, A. M.; Bercaw, J. E.; Bocarsly, A. B.; Dobbek, H.; DuBois, D. L.; Dupuis, M.; Ferry, J. G.; Fujita, E.; Hille, R.; Kenis, P. J. A.; Kerfeld, C. A.; Morris, R. H.; Peden, C. H. F.; Portis, A. R.; Ragsdale, S. W.; Rauchfuss, T. B.; Reek, J. N. H.; Seefeldt, L. C.; Thauer, R. K.; Waldrop, G. L. Frontiers, Opportunities, and Challenges in Biochemical and Chemical Catalysis of CO_2 Fixation. *Chem. Rev.* **2013**, *113* (8), 6621–6658. https://doi.org/10.1021/cr300463y.

(7) Maity, A.; Teets, T. S. Main Group Lewis Acid-Mediated Transformations of Transition-Metal Hydride Complexes. *Chem. Rev.* **2016**, *116* (15), 8873–8911. https://doi.org/10.1021/acs.chemrev.6b00034.

(8) Albinati, A.; Venanzi, L. M. Transition Metal Hydrides as Ligands. *Coord. Chem. Rev.* **2000**, *200–202*, 687–715. https://doi.org/10.1016/S0010-8545(00)00257-5.

(9) Kaltsoyannis, N.; Hay, P. J.; Li, J.; Blaudeau, J.-P.; Bursten, B. E. Theoretical Studies of the Electronic Structure of Compounds of the Actinide Elements. In *The Chemistry of the Actinide and Transactinide Elements*; Morss, L. R., Edelstein, N. M., Fuger, J., Eds.; Springer Dordrecht, 2011.

(10) Baudry, D.; Ephritikhine, M. Synthesis of a Hydride-Rich Uranium-Rhenium Dimer: $[(p\text{-}F\text{-}C_6H_4)_3P]_2ReH_6U(\eta\text{-}C_5H_5)_3$. *J. Organomet. Chem* **1986**, *311* (1), 189–192. https://doi.org/10.1016/0022-328X(86)80231-5.

(11) Cendrowski-Guillaume, S. M.; Lance, M.; Nierlich, M.; Vigner, J.; Ephritikhine, M. New Actinide Hydrogen Transition Metal Compounds. Synthesis of $[K(C_{12}H_{24}O_6)][(\eta\text{-}C_5Me_5)_2(Cl)UH_6Re(PPh_3)_2]$ and the Crystal Structure of Its Benzene Solvate. *J. Chem. Soc., Chem. Commun.* **1994**, No. 14, 1655–1656. https://doi.org/10.1039/C39940001655.

(12) Cendrowski-Guillaume, S. M.; Ephritikhine, M. Synthesis and Reactivity of Hydrogen-Rich Uranium–Rhenium Compounds; an Unsuspected Detrimental Effect of Alkali-Metal Halide on Chemical Metathesis. *J. Chem. Soc., Dalton Trans.* **1996**, No. 8, 1487–1491. https://doi.org/10.1039/DT9960001487.

(13) Ye, C. Z.; Rosal, I. D.; Boreen, M. A.; Ouellette, E. T.; Russo, D. R.; Maron, L.; Arnold, J.; Camp, C. A Versatile Strategy for the Formation of Hydride-Bridged Actinide–Iridium Multimetallics. *Chem. Sci.* **2023**, *14* (4), 861–868. https://doi.org/10.1039/D2SC04903A.

(14) Hayes, J. M.; Deydier, E.; Ujaque, G.; Lledós, A.; Malacea-Kabbara, R.; Manoury, E.; Vincendeau, S.; Poli, R. Ketone Hydrogenation with Iridium Complexes with “Non N–H”

Ligands: The Key Role of the Strong Base. *ACS Catal.* **2015**, *5* (7), 4368–4376. https://doi.org/10.1021/acscatal.5b00613.
(15) Oishi, M.; Kino, M.; Saso, M.; Oshima, M.; Suzuki, H. Early–Late Heterobimetallic Complexes with a Ta–Ir Multiple Bond: Bimetallic Oxidative Additions of C–H, N–H, and O–H Bonds. *Organometallics* **2012**, *31* (13), 4658–4661. https://doi.org/10.1021/om300429u.
(16) Oishi, M.; Oshima, M.; Suzuki, H. A Study on Zr–Ir Multiple Bonding Active for C–H Bond Cleavage. *Inorg. Chem.* **2014**, *53* (13), 6634–6654. https://doi.org/10.1021/ic500258g.
(17) Kita, M. R.; Miller, A. J. M. Cation-Modulated Reactivity of Iridium Hydride Pincer-Crown Ether Complexes. *J. Am. Chem. Soc.* **2014**, *136* (41), 14519–14529. https://doi.org/10.1021/ja507324s.
(18) Lassalle, S.; Jabbour, R.; Schiltz, P.; Berruyer, P.; Todorova, T. K.; Veyre, L.; Gajan, D.; Lesage, A.; Thieuleux, C.; Camp, C. Metal–Metal Synergy in Well-Defined Surface Tantalum–Iridium Heterobimetallic Catalysts for H/D Exchange Reactions. *J. Am. Chem. Soc.* **2019**, *141* (49), 19321–19335. https://doi.org/10.1021/jacs.9b08311.
(19) Pichugov, A. V.; Escomel, L.; Lassalle, S.; Petit, J.; Jabbour, R.; Gajan, D.; Veyre, L.; Fonda, E.; Lesage, A.; Thieuleux, C.; Camp, C. Highly Selective and Efficient Perdeuteration of N-Pentane via H/D Exchange Catalyzed by a Silica-Supported Hafnium-Iridium Bimetallic Complex. *Angew. Chem., Int. Ed.* **2024**, *63* (16), e202400992. https://doi.org/10.1002/anie.202400992.
(20) Escomel, L.; Del Rosal, I.; Maron, L.; Jeanneau, E.; Veyre, L.; Thieuleux, C.; Camp, C. Strongly Polarized Iridium$^{\delta-}$–Aluminum$^{\delta+}$ Pairs: Unconventional Reactivity Patterns Including CO_2 Cooperative Reductive Cleavage. *J. Am. Chem. Soc.* **2021**, *143* (12), 4844–4856. https://doi.org/10.1021/jacs.1c01725.
(21) Morisako, S.; Watanabe, S.; Ikemoto, S.; Muratsugu, S.; Tada, M.; Yamashita, M. Synthesis of A Pincer-IrV Complex with A Base-Free Alumanyl Ligand and Its Application toward the Dehydrogenation of Alkanes. *Angew. Chem., Int. Ed.* **2019**, *58* (42), 15031–15035. https://doi.org/10.1002/anie.201909009.
(22) Boreen, M. A.; Arnold, J. The Synthesis and Versatile Reducing Power of Low-Valent Uranium Complexes. *Dalton Trans.* **2020**, *49* (43), 15124–15138. https://doi.org/10.1039/D0DT03151H.
(23) Boreen, M. A.; Lussier, D. J.; Skeel, B. A.; Lohrey, T. D.; Watt, F. A.; Shuh, D. K.; Long, J. R.; Hohloch, S.; Arnold, J. Structural, Electrochemical, and Magnetic Studies of Bulky Uranium(III) and Uranium(IV) Metallocenes. *Inorg. Chem.* **2019**, *58* (24), 16629–16641. https://doi.org/10.1021/acs.inorgchem.9b02719.
(24) Escomel, L.; Soulé, N.; Robin, E.; Del Rosal, I.; Maron, L.; Jeanneau, E.; Thieuleux, C.; Camp, C. Rational Preparation of Well-Defined Multinuclear Iridium–Aluminum Polyhydride Clusters and Comparative Reactivity. *Inorg. Chem.* **2022**, *61* (15), 5715–5730. https://doi.org/10.1021/acs.inorgchem.1c03120.
(25) Takenaka, Y.; Hou, Z. Lanthanide Terminal Hydride Complexes Bearing Two Sterically Demanding $C_5Me_4SiMe_3$ Ligands. Synthesis, Structure, and Reactivity. *Organometallics* **2009**, *28* (17), 5196–5203. https://doi.org/10.1021/om900453j.
(26) Lassalle, S.; Jabbour, R.; Del Rosal, I.; Maron, L.; Fonda, E.; Veyre, L.; Gajan, D.; Lesage, A.; Thieuleux, C.; Camp, C. Stepwise Construction of Silica-Supported Tantalum/Iridium Heteropolymetallic Catalysts Using Surface Organometallic Chemistry. *J. Catal.* **2020**, *392*, 287–301. https://doi.org/10.1016/j.jcat.2020.10.016.

(27) Lassalle, S.; Petit, J.; Falconer, R. L.; Hérault, V.; Jeanneau, E.; Thieuleux, C.; Camp, C. Reactivity of Tantalum/Iridium and Hafnium/Iridium Alkyl Hydrides with Alkyl Lithium Reagents: Nucleophilic Addition, Alpha-H Abstraction, or Hydride Deprotonation? *Organometallics* **2022**, *41* (13), 1675–1687. https://doi.org/10.1021/acs.organomet.2c00158.
(28) Riedhammer, J.; Aguilar-Calderón, J. R.; Miehlich, M.; Halter, D. P.; Munz, D.; Heinemann, F. W.; Fortier, S.; Meyer, K.; Mindiola, D. J. Werner-Type Complexes of Uranium(III) and (IV). *Inorg. Chem.* **2020**, *59* (4), 2443–2449. https://doi.org/10.1021/acs.inorgchem.9b03229.
(29) Löffler, S. T.; Hümmer, J.; Scheurer, A.; Heinemann, F. W.; Meyer, K. Unprecedented Pairs of Uranium (IV/V) Hydroxido and (IV/V/VI) Oxido Complexes Supported by a Seven-Coordinate Cyclen-Anchored Tris-Aryloxide Ligand. *Chem. Sci.* **2022**, *13* (38), 11341–11351. https://doi.org/10.1039/D2SC02736D.
(30) Brennan, J. G.; Andersen, R. A.; Zalkin, A. Chemistry of Trivalent Uranium Metallocenes: Electron-Transfer Reactions with Carbon Disulfide. Formation of $[(RC_5H_4)_3U]_2[\mu\text{-}\eta^1,\eta^2\text{-}CS_2]$. *Inorg. Chem.* **1986**, *25* (11), 1756–1760. https://doi.org/10.1021/ic00231a007.
(31) Lescop, C.; Arliguie, T.; Lance, M.; Nierlich, M.; Ephritikhine, M. Bispentamethylcyclopentadienyl Uranium(IV) Thiolate Compounds. Synthesis and Reactions with CO_2 and CS_2. *J. Organomet. Chem* **1999**, *580* (1), 137–144. https://doi.org/10.1016/S0022-328X(98)01139-5.
(32) Lam, O. P.; Heinemann, F. W.; Meyer, K. C–C Bond Formation through Reductive Coupling of CS_2 to Yield Uranium Tetrathiooxalate and Ethylenetetrathiolate Complexes. *Angew. Chem., Int. Ed.* **2011**, *50* (26), 5965–5968. https://doi.org/10.1002/anie.201101185.
(33) Lam, O. P.; Castro, L.; Kosog, B.; Heinemann, F. W.; Maron, L.; Meyer, K. Formation of a Uranium Trithiocarbonate Complex via the Nucleophilic Addition of a Sulfide-Bridged Uranium Complex to CS_2. *Inorg. Chem.* **2012**, *51* (2), 781–783. https://doi.org/10.1021/ic202535e.
(34) Lam, O. P.; Franke, S. M.; Heinemann, F. W.; Meyer, K. Reactivity of U–E–U (E = S, Se) Toward CO_2, CS_2, and COS: New Mixed-Carbonate Complexes of the Types U–CO_2E–U (E = S, Se), U–CS_2E–U (E = O, Se), and U–COSSe–U. *J. Am. Chem. Soc.* **2012**, *134* (40), 16877–16881. https://doi.org/10.1021/ja307539w.
(35) Mougel, V.; Camp, C.; Pécaut, J.; Copéret, C.; Maron, L.; Kefalidis, C. E.; Mazzanti, M. Siloxides as Supporting Ligands in Uranium(III)-Mediated Small-Molecule Activation. *Angew. Chem., Int. Ed.* **2012**, *51* (49), 12280–12284. https://doi.org/10.1002/anie.201206955.
(36) Matson, E. M.; Breshears, A. T.; Kiernicki, J. J.; Newell, B. S.; Fanwick, P. E.; Shores, M. P.; Walensky, J. R.; Bart, S. C. Trivalent Uranium Phenylchalcogenide Complexes: Exploring the Bonding and Reactivity with CS_2 in the Tp*$_2$UEPh Series (E = O, S, Se, Te). *Inorg. Chem.* **2014**, *53* (24), 12977–12985. https://doi.org/10.1021/ic5020658.
(37) Camp, C.; Cooper, O.; Andrez, J.; Pécaut, J.; Mazzanti, M. CS_2 Activation at Uranium(III) Siloxide Ate Complexes: The Effect of a Lewis Acidic Site. *Dalton Trans.* **2015**, *44* (6), 2650–2656. https://doi.org/10.1039/C4DT02585G.
(38) Arnold, P. L.; Stevens, C. J.; Bell, N. L.; Lord, R. M.; Goldberg, J. M.; Nichol, G. S.; Love, J. B. Multi-Electron Reduction of Sulfur and Carbon Disulfide Using Binuclear Uranium(III) Borohydride Complexes. *Chem. Sci.* **2017**, *8* (5), 3609–3617. https://doi.org/10.1039/C7SC00382J.

(39) Ward, R. J.; Kelley, S. P.; Lukens, W. W.; Walensky, J. R. Reduction of CO_2 and CS_2 with Uranium(III) Metallocene Aryloxides. *Organometallics* **2022**, *41* (12), 1579–1585. https://doi.org/10.1021/acs.organomet.2c00208.
(40) Wang, S.; Wang, D.; Li, T.; Heng, Y.; Hou, G.; Zi, G.; Walter, M. D. Synthesis, Structure, and Reactivity of the Uranium Bipyridyl Complex [$\{\eta^5$-1,2,4-$(Me_3Si)_3C_5H_2\}_2$U(Bipy)]. *Organometallics* **2022**, *41* (12), 1543–1557. https://doi.org/10.1021/acs.organomet.2c00175.
(41) Heng, Y.; Li, T.; Wang, D.; Hou, G.; Zi, G.; Walter, M. D. Synthesis and Reactivity of the Uranium Bipyridyl Metallocene [η^5-1,3-$(Me_3C)_2C_5H_3]_2$U(Bipy). *Organometallics* **2023**, *42* (1), 91–113. https://doi.org/10.1021/acs.organomet.2c00529.
(42) Field, L. D.; Lawrenz, E. T.; Shaw, W. J.; Turner, P. Insertion of CO_2, CS_2, and COS into Iron(II)−Hydride Bonds. *Inorg. Chem.* **2000**, *39* (25), 5632–5638. https://doi.org/10.1021/ic991399z.
(43) Huang, J.; Chen, J.; Gao, H.; Chen, L. Kinetic Aspects for the Reduction of CO_2 and CS_2 with Mixed-Ligand Ruthenium(II) Hydride Complexes Containing Phosphine and Bipyridine. *Inorg. Chem.* **2014**, *53* (18), 9570–9580. https://doi.org/10.1021/ic500866d.
(44) Whited, M. T.; Zhang, J.; Ma, S.; Nguyen, B. D.; Janzen, D. E. Silylene-Assisted Hydride Transfer to CO_2 and CS_2 at a [P_2Si]Ru Pincer-Type Complex. *Dalton Trans.* **2017**, *46* (43), 14757–14761. https://doi.org/10.1039/C7DT03659K.
(45) Rauch, M.; Parkin, G. Insertion of CS_2 into the Mg–H Bond: Synthesis and Structural Characterization of the Magnesium Dithioformate Complex, [TismPriBenz]Mg(K2-S2CH). *Dalton Trans.* **2018**, *47* (36), 12596–12605. https://doi.org/10.1039/C8DT01947A.
(46) Lanorio, J. P.; Frost, B. J. Insertion Reactions of Heteroallenes (CS_2 and CO_2) into the Ru-H Bond of Cp′Ru(PTA)(PR_3)H Complexes (PTA = 1,3,5-Triaza-7-Phosphaadamantane). *Inorganica Chim. Acta* **2019**, *498*, 119138. https://doi.org/10.1016/j.ica.2019.119138.
(47) Moloy, K. G.; Marks, T. J. The Insertion of Carbon Dioxide into Actinide Alkyl and Hydride Bonds. *Inorganica Chim. Acta* **1985**, *110* (2), 127–131. https://doi.org/10.1016/S0020-1693(00)84568-5.
(48) Higgins, J. A.; Cloke, F. G. N.; Roe, S. M. Synthesis and CO_2 Insertion Chemistry of Uranium(IV) Mixed-Sandwich Alkyl and Hydride Complexes. *Organometallics* **2013**, *32* (19), 5244–5252. https://doi.org/10.1021/om400720m.
(49) Bailey, P. J.; Coxall, R. A.; Dick, C. M.; Fabre, S.; Henderson, L. C.; Herber, C.; Liddle, S. T.; Loroño-González, D.; Parkin, A.; Parsons, S. The First Structural Characterisation of a Group 2 Metal Alkylperoxide Complex: Comments on the Cleavage of Dioxygen by Magnesium Alkyl Complexes. *Chem.─Eur. J.* **2003**, *9* (19), 4820–4828. https://doi.org/10.1002/chem.200305053.
(50) Gilbert, T. M.; Bergman, R. G. Preparation and Reactions of Tetrahydrido(Pentamethylcyclopentadienyl)Iridium: A Novel Iridium(V) Polyhydride. *Organometallics* **1983**, *2* (10), 1458–1460. https://doi.org/10.1021/om50004a037.
(51) APEX2, APEX3, SADABS, TWINABS and SAINT. Bruker AXS. Madison, WI, USA.
(52) Sheldrick, G. M. *SHELXT* – Integrated Space-Group and Crystal-Structure Determination. *Acta Crystallogr A Found Adv* **2015**, *71* (1), 3–8. https://doi.org/10.1107/S2053273314026370.
(53) Sheldrick, G. M. Crystal Structure Refinement with *SHELXL*. *Acta Crystallogr C Struct Chem* **2015**, *71* (1), 3–8. https://doi.org/10.1107/S2053229614024218.

(54) Dolomanov, O. V.; Bourhis, L. J.; Gildea, R. J.; Howard, J. A. K.; Puschmann, H. *OLEX2* : A Complete Structure Solution, Refinement and Analysis Program. *J Appl Crystallogr* **2009**, *42* (2), 339–341. https://doi.org/10.1107/S0021889808042726.
(55) Macrae, C. F.; Bruno, I. J.; Chisholm, J. A.; Edgington, P. R.; McCabe, P.; Pidcock, E.; Rodriguez-Monge, L.; Taylor, R.; van de Streek, J.; Wood, P. A. Mercury CSD 2.0– New Features for the Visualization and Investigation of Crystal Structures. *Journal of Applied Crystallography* **2008**, *41*, 466–470.